DISSERTATION

TRANSFORMATION OF SOIL ORGANIC MATTER IN FOREST FIRE IMPACTED WATERSHEDS ELUCIDATED BY FT-ICR MASS SPECTROMETRY

Submitted by

William Bahureksa

Department of Chemistry

In partial fulfillment of the requirements

For the Degree of Doctor of Philosophy

Colorado State University

Fort Collins, Colorado

Fall 2022

Doctoral Committee:

Advisor: Thomas Borch

Delphine Farmer
Chris Ackerson
Adam Heuberger

ABSTRACT

TRANSFORMATION OF SOIL ORGANIC MATTER IN FOREST FIRE IMPACTED WATERSHEDS ELUCIDATED BY FT-ICR MASS SPECTROMETRY

Soils provide numerous ecosystem services that are essential to life on Earth, including food security, water filtration and purification, and infrastructure for biodiversity. Soil properties (e.g., soil productivity, moisture retention, structure and aggregation, and nutrient supply) that facilitate these services depend on the soil organic matter (SOM), which can be dramatically impacted from ecosystem disturbances such as wildfires. Wildfires can provide benefits to an ecosystem through the cleaning of the forest floor, soil nourishment, and the removal of competitive underbrush. However, wildfires have grown in frequency and severity around the world, and there is great interest in resolving changes to SOM composition under wildfire conditions to secure water resources and recover fire-affected areas. In the following work, Fourier transform ion cyclotron resonance mass spectrometry (FT-ICR MS) was critically evaluated for the analysis of SOM. Data processing methods for FT-ICR MS were investigated to improve compositional analysis. Laboratory-simulated and field-based burn samples were collected and used to investigate changes to water-soluble fractions over progressive series of fire intensity, burn severity, and burn extent gradients.

FT-ICR MS currently achieves the highest mass resolving power in the world, which makes it suitable for the study of complex mixtures with tens of thousands of compounds that are separated by mass on the order of a few electrons. Recent strategies for SOM characterization by FT-ICR MS are critically reviewed, with emphasis on SOM sample collection, preparation, analysis, and data interpretation. Importantly, the range of structures, functionalities, and mass means no technique achieves "complete" characterization, and methods used for processing and visualizing

FT-ICR MS spectra can influence representation and interpretation of data. The complexity of DOM and influence of post-data processing was demonstrated by studying the effect of peak-picking threshold (3σ, 4σ, 5σ, and 6σ) on a Suwannee River Fulvic Acid standard measured by a custom 21 tesla FT-ICR mass spectrometer. Applying a 3σ peak-picking threshold revealed an additional 13,000 peaks that could be assigned compared to a 6σ peak-picking threshold with a difference of only 12 ppb root-mean-square mass error. Furthermore, isobaric overlaps differing by as little as the mass of an electron are identified up to m/z 1000, and ^{18}O and ^{17}O isotopologues were assigned for the first time in DOM at 3σ.

Ecosystem recovery after wildfires in forested watersheds depends on revegetation and soil microbial communities and is therefore limited by the availability of nutrients. The remaining nutrients and substrate available for microbes depends on specific wildfire intensities and are poorly understood. To investigate SOM byproducts during heating and mechanisms that contribute to pyrogenic organic matter (pyOM) formation and mobilization, water-extractable organic matter was extracted from soils heated at discrete temperatures using laboratory microcosms. Relative to the unburnt control, dissolved organic carbon and nitrogen increased at ≥150°C and decreased when ≥450°C. Nitrogen-containing species predominated mass spectra at temperatures >150°C, and mass difference-based analysis suggested that products formed during heating could be used to model transformations along the Maillard reaction pathway.

To investigate the short-term impacts of burn extent on water chemistry and dissolved organic matter (DOM) in fire-affected watersheds, streams originating from catchments of low, moderate, and high burn extent within the area of the Cameron Peak Fire of 2020 were sampled before, during, and after the first large rainstorm following the fire. Water chemistry parameters (DOC, TDN, turbidity) for moderate and high burn extents streams tended to increase during the storm and decrease following the storm in high burn extent streams. Fluorescence indices indicated

that low/moderate burn extent streams exhibited an increase in microbially-derived residues compared to high burn extent. While a substantial portion of DOM species between every stream were common between each event and included labile and aromatic residues during the storm, the low burn extent exhibited the most unique aromatic features after the storm. When chlorinating stream samples to simulate drinking water treatment, the total DBPs were greater in streams of moderate/high burn extents compared to low burn extent. When DBP concentrations were normalized to DOC, the DOM introduced during the storm resulted in fewer DBPs, suggesting the increase in DBP formation is due to increased DOM loading overall rather than increased reactivity of the DOM.

In total, the work presented here contributes to the mechanistic understanding of the residues produced during SOM heating that can be mobilized and impact water chemistry in fire-affected watersheds.

ACKNOWLEDGEMENTS

I am extremely grateful to my advisor, Thomas Borch, who showed me compassion and understanding during one of the most intellectually and emotionally challenging times of my life. I feel lucky to have had such a caring advisor and friend offer me positivity, opportunities, and recognition to help me grow as a scientist and person. Special thanks to Robert B. Young who supported, taught, and inspired curiosity in me and was the best mentor I could have asked for. No amount of tedium, exhaustion, or obligation ever stopped you from taking the time to be compassionate, intelligent, and empathetic when approaching projects and people.

I feel extremely grateful to the friends that I made at Colorado State University (CSU). This includes the Borch group that helped reassure and support me throughout the process, giving me time and critique to improve my work and also a space to chat about science and non-science that helped keep graduate school tolerable. I am thankful of numerous Chemistry graduate students ("the gang") and Soil and Crop graduate students which I could decompress around and often relaxed with to play games, watch movies, and eat food. As our time together became sparser when the program became more intense and the pandemic started, I found myself appreciating these interactions more and feel that many of these relationships will last a lifetime.

Thanks to my family for providing me emotional support and a place to return to. Special thanks to my sister, Lindsay Bahureksa, whose shared experience and unending support gave me confidence in both my ability to succeed, and grace should I fail. Our long conversations helped in processing our habits, lifestyles, and dreams, and I can only hope that things continue to get better for us. I would also like to thank my friends back home for welcoming me and picking up wherever we left off when I would travel back home. Knowing I had such a substantial support network was encouraging and helped push me through to graduation.

Finally, I am appreciative of numerous collaborators that supported my growth as a scientist. I am grateful to Amy Mckenna from the National High Magnetic Field Laboratory who was an important collaborator and mentor during my time at CSU that helped facilitate nearly every project I was involved in and helped encourage and reassure me in my own ability and when stuck in the whirlwind that is ultrahigh resolution mass spectrometry. I am grateful to Benny Chefetz and his lab group who displayed extraordinary kindness and empathy to me during a research trip gone wrong that gave me hope to finish the PhD. I am also grateful to Chuck Rhoades and Tim Fegel for providing so much in terms of sampling, discussion, and feedback on several aspects of my fire related research. I would also like to thank Rachelle Rehberg, Holly Roth, Kevin Thorn, David Hanigan, Kenny Hickenbottom, Jacob VanderRoest, Michael Wilkins, Rene Bioteau, Merritt Logan, and Sean Stokes for their help and collaboration in analyzing and interpreting soil organic matter, fire-induced transformation, data processing, and the many nuances of preparing presentations and publications.

DEDICATION

This work is dedicated to the community that has supported my development and well-being throughout my dissertation.

TABLE OF CONTENTS

CHAPTER 1: INTRODUCTION

1.1 Soil Organic Matter Influences Ecosystem Functions

Soils provide a myriad of ecosystem services that make them essential for life on Earth. This includes food security, water and air filtration and purification, and infrastructure to support biodiversity and mitigate the effects of ecosystem disturbances.[1,2] Soil also acts as the largest dynamic carbon reservoir on Earth,[3] where the amount and type of carbon stored is influenced by the organic inputs (e.g., plant, animal, and microbial), organo-mineral interactions, and environmental conditions (e.g., temperature and precipitation). This results in a mixture of organic inputs at various stages of decomposition that comprises most of the organic carbon found in soils and is referred to as soil organic matter (SOM). Soil properties (e.g., soil productivity,[4,5] moisture retention,[6] structure and aggregation,[7] contaminant regulation,[8] and nutrient supply)[9] depend in part on the SOM present, making the SOM content and characteristics crucial for ecosystem services. These functions make impacts from ecosystem disturbances, such as wildfires, of great interest for protecting SOM and ecosystem functions.

1.2 Studying Organic Mixtures using Ultrahigh Resolution Mass Spectrometry

Studying organic matter composition has been challenging historically due to the number of organic inputs and biotic (e.g., enzymatic)[10,11] and abiotic (e.g., wildfire, sunlight)[12–14] transformations that result in a wide range of molecular weights, structure, functional groups, and heteroatoms comprising the resultant heterogenous SOM mixture.[15–17] The exceptional heterogeneity means that no single measurement technique can provide a "complete" molecular level fingerprint for organic matter samples. The introduction of Fourier transform ion cyclotron resonance mass spectrometry (FT-ICR MS) revolutionized the analysis of complex natural mixtures by providing resolution

sufficient to distinguish tens of thousands of individual molecular weights that can differ by as little as the mass of an electron.[18]

FT-ICR MS application has increased substantially in the last two decades in the analysis of SOM, petroleum, aquatic and marine dissolved organic matter (DOM), biochar and pyOM, and biological substrates.[16,19–25] However, the preparation, specialized instrumentation, ionization selectivity, complexity of the mass spectra, and expertise in data treatment and interpretation needed for FT-ICR MS limits the number of researchers capable of applying FT-ICR MS. Importantly, linking molecules measured in FT-ICR MS to corroborative and statistical methods is key to unlocking a clearer understanding molecular level influences on macro-scale processes.[16] Review and discussion detailing the preparation, ionization, analysis, and interpretation of SOM using FT-ICR MS is presented in Chapter 2.

Given the resolution afforded by FT-ICR MS, differences in experimental conditions (e.g., ionization parameters, ion transfer optics, magnetic field strength, detection cell geometry, calibration, data treatment) can substantially influence the representation of organic matter mixtures and limit the reproducibility of complex organic mixture analysis between FT-ICR instruments. This is demonstrated by Hawkes et al. 2020 that studied a Suwannee River Fulvic Acid (SRFA) standard obtained from the International Humic Substances Society across ten commercial and custom-built FT-ICR mass analyzers, where only ~1000 assigned peaks were common between each instrument despite ~2000 to ~5000 assigned in each.[26,27] The disparity in instrument assignments highlights both the "inaccessible" fraction of DOM that lies under noise or matrix effects and the impact of post-data processing. To investigate the complexity and impact of post-data treatment processes on FT-ICR measurements, peak-picking thresholds (3σ, 4σ, 5σ, and 6σ) were compared using SRFA by the assignment of molecular compositions, mass measurement accuracy, and dynamic range.[28] I hypothesize that if peak-picking thresholds are lowered, the number of assignments and assignable

features in SRFA will increase with a negligible amount of additional mass assignment error using the 21 tesla FT-ICR MS. Results and discussion about the improved sensitivity, resolving power, and range of compositional features afforded by 21 tesla FT-ICR analysis at 3σ are presented in Chapter 3.

1.3 Increasing Wildfires Threaten Watershed Ecosystem Functions

Forested watersheds supply water to millions of people in the United States and abroad every year,[29–32] and are vulnerable to ecosystem disturbances such as wildfires. Wildfires can be beneficial to ecosystems by increasing nutrient availability and through the removal of detritus along the forest floor.[33] However, wildfires continue to grow in frequency and severity around the world,[34,35] and can confer negative effects to soil health (e.g., increased erosion, decreased water permeability) and downstream water quality (e.g., increased suspended solids, nutrients, and pH).[36] Incomplete combustion will transform residues from plants, animals, and SOM into pyrogenic organic matter (pyOM), ranging from slightly charred biomass and SOM to charcoal and soot, based on environmental and wildfire conditions.[37,38] Char and pyOM can remain in soils for decades following the fire, impacting soil properties and ground and surface water health.[39–41] Therefore, understanding how pyOM is formed and cycles through soils is key to evaluating wildfire effects and taking steps towards watershed recovery.

Studies investigating the effects of fire intensity (i.e., heat energy released over time) and burn severity (i.e., amount of organic matter remaining) have indicated shifts in molecular characteristics starting as low as 200°C.[13,14,42] Higher temperatures appear to drive predominant characteristics towards highly condensed aromatic materials, often discussed as black carbon.[13,43,44] Specific biomass burning markers are also used to evaluate pyOM source and composition, such as levoglucosan.[45] However, key knowledge gaps remain connecting the compositional changes at

discrete temperatures with the charring and enhanced mobility of water-extractable organic matter following heating. To probe transformation mechanisms for SOM during heating, a laboratory muffle furnace experiment was conducted on soils heated at discrete temperatures. Changes to composition were investigated using organic carbon and nitrogen analysis, solid-state ^{13}C nuclear magnetic resonance spectroscopy (NMR), and FT-ICR MS. Nitrogenated residues were compared between heating temperatures to model reactions and suggest common pathways for nitrogen transformation. I hypothesize that if soils are heated progressively up to 450°C: (i) the amount of water-extractable and aromatic organic matter will increase compared to an unheated soil, (ii) nitrogen-containing aromatic species will be enriched above 200°C, and (iii) species at consecutive heating temperatures will be related through reactions within the Maillard Reaction pathway. Results and discussion from this study are presented in Chapter 4.

Wildfires will alter physical and chemical soil properties (e.g., water infiltration, structure, density, pH), where streams within fire-affected catchments can exhibit degraded water quality for decades following the fire.[13,46,47]Higher levels of salt, turbidity, nutrients and metals, and pyOM mobilized will require additional treatment or infrastructure that will increase water treatment costs, and negatively impact the amount of water available for agriculture and drinking water.[48] Changes to water chemistry vary depending on the burn severity and extent (i.e., percentage of catchment burned), and precipitation events appear to act as controllers for nutrient and DOM export downstream.[40] However, precipitation can exhibit high spatial and temporal variability throughout a stream catchment, making it challenging to decouple changes to stream water chemistry and the export of pyOM from areas of different burn extent.[49,50] Precursors to toxic disinfection byproducts (DBPs) that can form during DOM chlorination at drinking water treatment facilities also increase with greater burn severity in fire-affected stream waters.[51] To investigate the short-term impacts of precipitation and burn extent on water chemistry and DOM in fire-affected watersheds, streams

within the area of the Cameron Peak Fire of 2020 were sampled before, during, and after the first large summer rainstorm following the fire. Streams were distinguished by catchment burn extent (low: 24% burned area with 14% at moderate-high burn severity, moderate: 70% burned with 38% at burn moderate-high severity, and high: 86% burned with >50% at moderate-high burn severity). DBP formation potential was also evaluated by chlorinating each of the stream water samples used to investigate the effect of the precipitation on DBP precursor mobilization in burned areas. I hypothesize that if wildfire-affected watershed stream catchments are within the area of a storm: (i) stream waters associated with catchments of greater burn extent will exhibit lower water quality during the storm, and (ii) the amount of total DBP precursors will be greater in stream water during the storm. Results and discussion from this study are presented in Chapter 5.

1.4 Publications and Presentations

This dissertation examines the opportunities and challenges of developing and applying FT-ICR MS methods to organic matter (Chapter 2,3), and the effects of heating on water-extractable and dissolved organic matter composition in laboratory and field settings (Chapter 4,5). This dissertation includes work that is either published in peer-reviewed journals or in review. Chapter 2 (Bahureksa et al. 2021) and chapter 4 (Bahureksa et al. 2022) were published in *Environmental Science and Technology*.[16,28] Chapter 3 (Bahureksa et al. 2022) was published in *Analytical Chemistry*.[28] Chapter 5 is in preparation to be submitted to *Environmental Science and Technology*. This research has been presented at the Chemistry Research Seminar (Oct 2020, poster),[24] Graduate Student Showcase (November 2020, poster),[24] ACS Spring National Meeting (April 2021, talk),[16,24] IHSS Virtual Global Conference (August 2021, talk),[16,24] ACS Fall national Meeting (August 2021, talk),[24,28] and the Gordon Research Conference (June 2022, poster). Work with my collaborators also resulted in three co-authored publications: Appendix E was published in *Soil Systems* (Young et al. 2018), Appendix F

was published in *Pest Management* (Rehberg et al. 2021), and Appendix G was published in *Analytical Chemistry* (Roth et al. 2022).[18,52,53] Additionally, two co-authored works are in preparation to be submitted: a manuscript studying the impact of pyrolysis temperature on photodegradation and toxicity of wheatgrass biochar to *Biochar*, and a manuscript studying the efficacy and degradation of a pesticide within an infected citrus grove to *Pest Management*.

CHAPTER 2: SOIL ORGANIC MATTER CHARACTERIZATION BY FOURIER TRANSFORM ION CYCLOTRON RESONANCE MASS SPECTROMETRY: A CRITICAL REVIEW OF SAMPLE PREPARATION, ANALYSIS, AND DATA INTERPRETATION[1]

2.1 Introduction

Soil organic matter (SOM) is the accumulated, decaying debris of biota in the soil. It is both the largest active reservoir of terrestrial organic carbon,[54] and fuel for microbial activity and plant nutrient production, "giving life" to soil through its decay.[55] SOM affects soil structure, moisture retention, ion exchange capacity, and other properties, and it can be studied from many diverse perspectives, from soil health to contaminant transport. Most recently, urgent attention has been given to its relationship with atmospheric CO_2 concentrations and climate change.[56,57]

The sources of SOM are vast and various, including extracellular compounds like root exudates, extracellular enzymes, and extracellular polymeric substances,[58,59] decomposition products from above-ground plant litter, root litter, and microbial necromass,[60–63] and abiotic reaction byproducts. The succession of biotic and abiotic reactions, and the disparate conditions across both spatial and temporal scales,[64,65] create mixtures with chemical diversity that is far more complex than the original biological source materials.[66,67] Recent observations also show that SOM is heterogenous at high spatial resolution,[68,69] and that physical separations (i.e., water extractable, particulate, and mineral-associated organic matter) reflect the formation, persistence and function of SOM in the environment better than operational fractions produced by solubilities under different pH conditions (i.e., humic acids, fulvic acids, and humins.[70,71] A wide range of complementary analytical

[1] This chapter contains material that was reproduced with permission from Bahureksa, W.; Tfaily, M. M.; Boiteau, R. M.; Young, R. B.; Logan, M. N.; McKenna, A. M.; Borch, T.; Young, R. B.; Logan, M. N.; Borch, T. Soil Organic Matter Characterization by Fourier Transform Ion Cyclotron Resonance Mass Spectrometry (FTICR MS): A Critical Review of Sample Preparation, Analysis, and Data Interpretation. *Environ. Sci. Technol.* **2021**, *55* (14), 9637–9656. Copyright 2021, American Chemical Society.

techniques are required to study such a complex and dynamic mixture when it is heterogeneously distributed among different physical environments at nearly every measurable scale (i.e., nm to km).[72]

The introduction of Fourier transform ion cyclotron resonance mass spectrometry (FTICR MS) analysis established a means to reliably detect and resolve individual SOM molecules when studying its composition, distribution, or transformation. FTICR MS achieves sufficient mass resolving power over a wide mass range (from a hundred to several thousand Da) to identify an m/z difference of a single electron, where m is ion mass in daltons (Da) and z is the ion charge.[73] This resolution is capable of separating the closely spaced m/z peaks that are found in a typical SOM mass spectra (Figure 2.1).

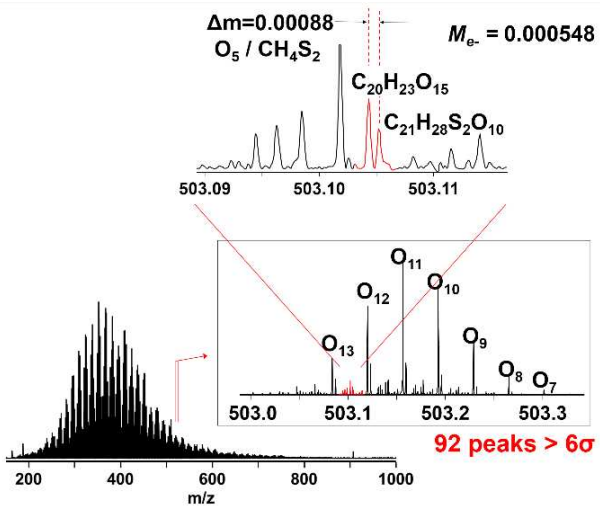

Figure 2.1 FTICR mass spectra of a SOM extract displaying the resolution needed to differentiate unique peaks. The peaks ($C_{20}H_{23}O_{15}$ and $C_{21}H_{28}S_2O_{10}$) differ by 0.00088 m/z, requiring a resolution of ~600,000 (resolution = m/Δm) to separate and assign. The mass of an electron (M_e^-) is provided as reference. Unpublished data from the National Magnetic Field Lab.

However, biases that originate from sample preparation and the chosen analysis conditions make full characterization of any SOM sample difficult, whatever the mass resolving power of the FTICR MS. Due to the diversity of molecular components that comprise SOM, any extraction method will only target a specific fraction and must be tailored to a specific research question to

collect the desired fraction most effectively. Ionization efficiencies vary greatly between molecules of different chemical composition and sample matrices, which complicates the quantitative comparison of SOM mass spectra. Furthermore, once mass spectra are collected, data analysis requires making assumptions to assign reasonable molecular formula to masses, grouping features by calculated indices, and creating visualizations that reflect chemical differences. Robust interpretation relies on critical assessments of the uncertainties introduced during each of these steps.

Importantly, FTICR MS is not, by itself, able to differentiate between isomers, determine molecular structures, or identify functional groups, meaning that FTICR mass spectra are still simplified representations of SOM.[74] FTICR MS provides a qualitative view into a subset of SOM compositional space. However, these data can be further examined using LC-MS and other complementary approaches to identify and characterize specific isomers of interest and contextualize relationships between peaks and samples.

There has been significant progress in overcoming the challenges of organic matter analysis using FTICR MS,[75–77] and the user base of FTICR MS analyses is growing rapidly as techniques for soil organic matter analysis become more standardized. Herein, we aim to provide a comprehensive resource to multidisciplinary researchers interested in applying FTICR MS to obtain molecular level insight to soil organic matter chemistry. Workflows for FTICR MS based SOM analysis will be presented from an experimental design perspective, and potential biases from sample extraction, ionization, and formula assignment methods will be highlighted. Data visualization and exploration methods will also be discussed, with suggested usage to avoid misinterpretations. Finally, techniques complementary to FTICR MS for SOM analysis will be presented with their specific strengths to support more robust conclusions about SOM composition, microbial decomposition pathways and other relevant areas of study (Figure 2.2).

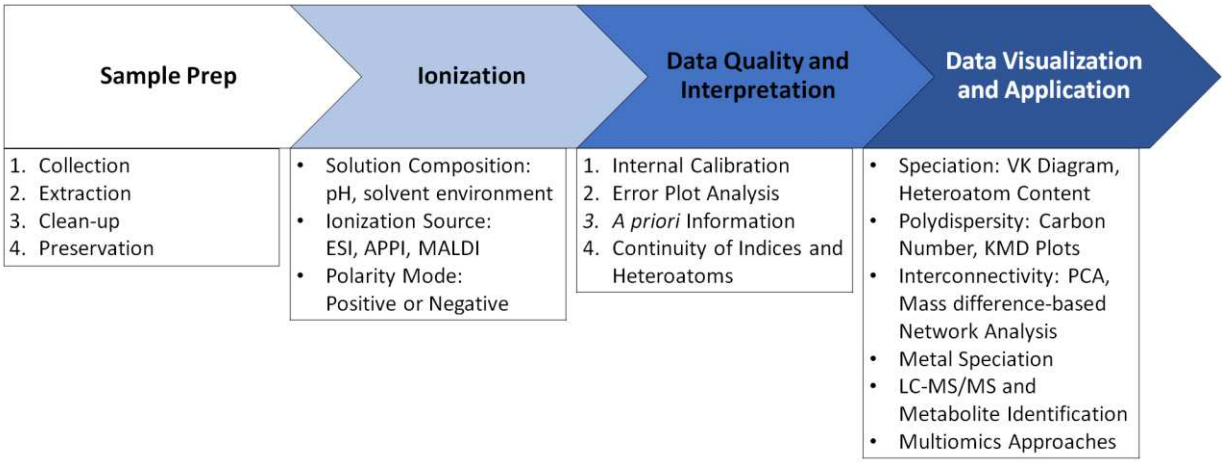

Figure 2.2 Workflow for analysis involving FTICR MS to provide meaningful conclusions about a set of samples.

2.2 Sampling and Extraction of Soil Organic Matter

SOM sampling methodology depends primarily on the scientific focus of the study and which fraction of SOM will provide the most relevant information. The heterogeneity of SOM, soil surfaces, and microenvironments make a single extraction procedure for all SOM features impossible.[78,79] SOM has been historically isolated into fractions operationally defined by their solubility at different pH.[80] While this method continues to be used,[81,82] other fractions of interest can be collected by targeting specific SOM sorption mechanisms. SOM is bound to soil minerals and other organic matter via different mechanisms, from weak electrostatic, hydrophobic, and other nonspecific interactions to strong polar covalent bonds produced by ligand exchange with carboxylic and phenolic functional groups.[78,83] (Figure 2.3) The most commonly used extraction methods include water, alkaline, mineral dissolution, and organic extractions, and each method has been shown to extract different fractions of SOM. Details on specific procedures can be found in Table A.1. Extracted fractions can be related and even complement each other, however they cannot be assumed to be "complete" or truly representative of total SOM as they, by design, only target specific operational fractions defined by the targeted stabilization mechanism.[84] This review outlines

the major extraction methods and the key shortcomings of each that must be considered when collecting samples for FTICR MS.

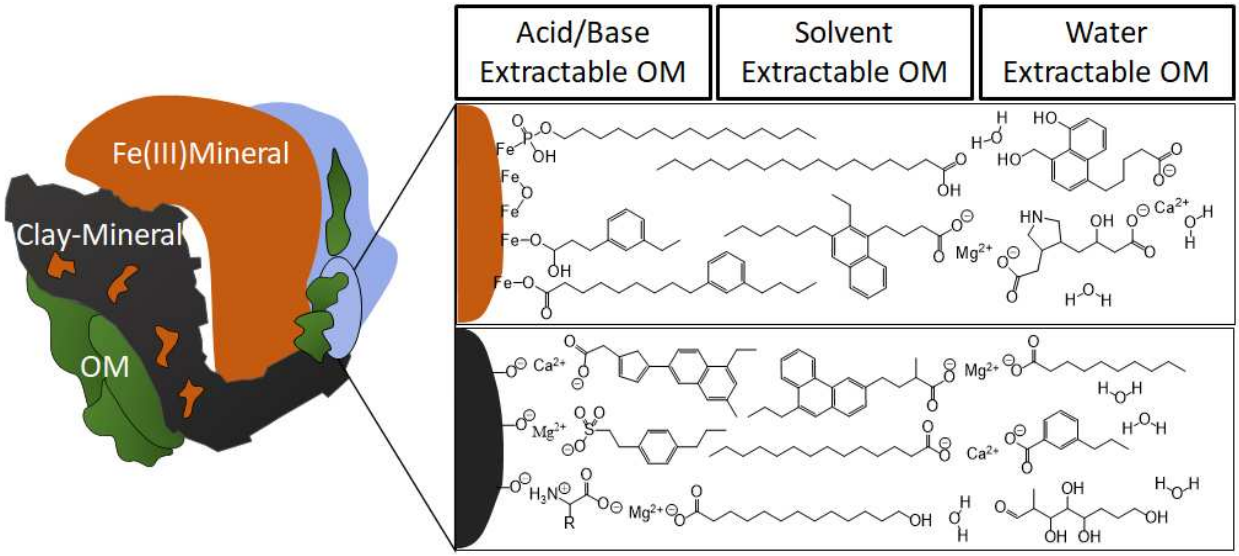

Figure 2.3 Model soil particle depicting an Fe(III) mineral (brown) and clay (black) surface exhibiting various possible interactions with model SOM. The variety of possible interactions will create fractions with varying extractability based on the extraction solution (e.g., acid/base, organic solvent, and water), mineral surface, and intermolecular forces.

2.2.1 Water/polarity-based Extraction

For approximately two decades, water extraction has been used as a collection method for SOM that is released to the soil solutions when equilibrium conditions change.[85] The resulting fraction, referred to as water-extractable SOM (WEOM),[86,87] is closely related to dissolved organic matter (DOM), which is defined operationally by filtration (i.e. passing through 0.4 - 0.6 μm pore sizes)[88] of water-extractable or aquatic organic matter.[89,90] These terms both describe complex natural organic matter and have been shown to be highly related through biomolecular origin and degree of decomposition.[90–93] Therefore, the following discussion on preparation, ionization, and analysis can be similarly applied.

WEOM is considered the most dynamic and bioavailable fraction of SOM and therefore its analysis is highly applicable to a variety of studies.[94–98] The importance and broad application of water extractable SOM is due to its roles in aqueous photochemistry, nutrient cycling, ion

distribution, and pH buffering; in addition to acting as an energy and carbon source for microbes.[99–102] Water extraction is performed with ultrapure water or salt solutions such as potassium sulfate (or potassium chloride) which increases ionic strength, generally improving SOM yield.[85,103–106] Additional alteration of extraction conditions, such as increasing temperature, pressure, or time, have failed to produce significant improvement over leaching or batch extractions at room temperature.[98] Overall, water extractions are easily performed but are generally unable to extract SOM adsorbed to mineral surfaces, hydrophobic molecules, or physically protected SOM, which are important when considering carbon sequestration and mineral-organic interactions.[87,103]

2.2.2 Alkaline Extraction

Alkaline extraction of SOM was first described by Achard in 1786 and has remained relatively unchanged to the current day.[107–110] This extraction is widely used due to its high organic carbon yield usually achieved through the use of 0.1 M NaOH. Alkaline extractions are expected to contain a more diverse range of SOM molecules than WEOM, including molecules that are not hydrophilic under the normal range of *in situ* equilibrium conditions. Alkaline extractions function by deprotonation of acidic functional groups present on SOM, greatly increasing SOM polarity and aqueous solubility.[111] This process's effectiveness relies on the extracting solution having a higher pH than the acidity (*pKa*) of the targeted functional groups (Figure 2.4), and the abundance and distribution of those functional groups in the SOM.[103,111]. The potential for base-catalyzed hydrolysis of SOM collected by alkaline extractions has been debated,[111,112] but many of the extracted features do appear to be identical with other methods.[15,43,113–115] Importantly, any extraction that shifts the *in situ* conditions of the SOM, including alkaline extractions, may produce artifacts or side effects that alter "native" SOM composition, so considering the character and extent of such artifacts is essential to any extraction method.[91,111,112,116] Subject to these considerations, alkaline extractions reach SOM

that is inaccessible to water extractions, and provide a more comprehensive view of SOM composition.[112]

2.2.3 Selective Mineral Dissolution

Study of the role of mineral protection in SOM stability has increased considerably in recent years as mineral-organic associations are thought to increase protection from microbial degradation processes.[91,117] For example, iron oxide minerals are effective sorbents or organic matter through interactions that include co-precipitation, and ligand exchange under more acidic conditions.[118–120] To study these mineral-organic associations directly, mineral dissolving solutions are used to selectively extract SOM associated with those minerals.[118] These extractions function by either reduction, chelation, or dispersion of a mineral phase; resulting in the release of SOM stabilized by that mineral.[87,97,121–123] Example mineral phases include short range order (SRO) Fe(III) oxides, crystalline Fe(III) oxides, aluminum oxides, and aluminosilicate clays among others. Selection of appropriate extraction solutions has been extensively studied in SOM-mineral or mineral cycling studies.[87,103,118,124–126] Not as well characterized is the potential for SOM alteration by extraction conditions or interactions between the DOM and dissolved minerals.[126–128] After dissolution, new SOM-mineral interactions can be inhibited by inclusion of an appropriate buffering or stabilizing agent, such as citrate for Fe^{2+}, that can complex metal ions and prevent re-adsorption or aggregation of extracted SOM.[127,129,130] All mineral extraction will require a cleanup process to remove the extracting chemicals and stabilizing agents that can affect ionization, discussed below. Finally, mineral extractions have the potential to extract compounds that overlap with water extractions and should be noted when comparing extraction yields and spectra.[104,126,131]

2.2.4 Organic Extraction

Soil organic matter is known to contain hydrophobic domains[15] and laboratory studies have indicated that non-selective sorption of DOM contributes substantially to the overall presence of

mineral-organic associations.[53] To study these interactions, it is useful to have an extraction method that targets more hydrophobic domains.

Organic solvents can be more efficient extractors than polar solvents depending on the source material and target fraction (e.g., the hydrophobic domain).[132] Tfaily *et al.* showed that extracted H/C and O/C ratios are influenced by solvent polarity by performing a series of parallel extractions, and in a subsequent study show that low/non-polar solvents detect a greater number of low O/C peaks in FTICR-MS analysis.[94,133] Furthermore, Mckee and Hatcher[134] demonstrated that pyridine extractions of lake sediment isolate a larger range of mass spectral and spectroscopic features compared to other organic and aqueous extractions. Organic extractions can also induce alterations to the SOM, such as esterification following methanol and acetonitrile extraction, that should be considered before usage and when comparing between samples prepared differently.[135] Extraction with organic solvents also dissolves fewer inorganic salts that inhibit SOM ionization compared with aqueous extractions. This is a potentially large benefit as other extractions methods require cleanup that further bias SOM composition.[94]

2.2.5 Sequential Extraction

Extractants can also be applied sequentially to soils to selectively collect SOM bound at different degrees of stabilization. This can be very beneficial when comparing the quantity and characteristics of SOM stabilized by the different mechanisms mentioned above. Lopez-Sangil and Rovira[103] demonstrated this with seven extracting solutions on four soils of varying pH and organic carbon content. Each extractant collected a fraction of SOM but the majority of SOM was collected with sodium tetraborate or sodium pyrophosphate, indicating that cation bridging or chelating interactions predominated, respectively. Tfaily *et al.*[94] also showed that sequential extractions with water followed by different organic solvents resulted in an overall increase in peak counts by 2- to 4-fold. As above, it is possible that extractants overlap in the SOM collected, therefore each extraction

should be performed several times to ensure that as much of the target fraction is extracted as possible before continuing with the next extractant. The additional extracts collected will increase preparation time, however sequential extraction protocol can be tailored to specific research questions based on the mineral-organic associations of interest.

2.2.6 Sample Preservation and Cleanup

Once a soil sample has been collected, it is important to perform an extraction as soon as possible or store the sample to minimize biological degradation of SOM.[136] If extraction soon after sampling is impossible, it is recommended that soil samples be treated as similarly as possible to maintain their comparability, as no storage method can perfectly preserve the *in situ* conditions.[112,129] Before extraction, soil sample storage by freezing or drying should be avoided as both treatments can aggregate the soil or SOM ,[129,137,138] which can alter the structure of the soil matrix, reducing exposure/contact with the extracting chemicals,[129,137,138] and has shown variable carbon yield[129,138] when compared to "wet" or *in situ* samples.

After extraction, long-term storage of SOM extracts is also preferably avoided to minimize post extraction alteration. SOM stability in the extract should be accounted for, but this is easily addressed by sterile filtration, or immediate processing to prepare the samples for FTICR MS. When the extract is aqueous, freezing can provide long-term SOM stability if the solution cannot be sterile filtered, but SOM aggregation can occur so analysis before long-term storage is ideal.[139] The use of acidification or biocides to sterilize sample extracts for storage is also not recommended as there is evidence for alteration of SOM properties.[140,141]

After extraction, SOM often requires concentration and salt removal to make it suitable for FTICR MS analysis. This process is most commonly performed by solid phase extraction (SPE), which utilizes the difference in polarity between small, highly polar inorganic salts and less polar SOM for separation.[142,143] As SPE cartridges use a variety of nonpolar packing material and acidic

functional groups are common, retention of the SOM is assisted by adjusting the extract to around pH 2, resulting in protonation of acidic functional groups, decrease in polarity, and improvement of stationary phase binding, however acidification can cause compositional changes in the SOM.[140,144] Additionally, amino functional groups and N heterocycles can be protonated at low pH, increasing their polarity and preference for cation exchange sorbents.[145]

There are a wide variety of SPE cartridges that retain targeted or broad molecular features, and must be selected based on the design of the experiment.[146] The recovery of SOM from this method is highly variable and depends greatly on the cartridge being used, the origin of the SOM, and the elution procedure,[145,147,148] with recoveries varying between 20 to 90%.[143,149] Addressing the source of variable yields is challenging as there is often no reliable way to identify if the retention or elution were incomplete.[84,143,150]

Alternatives to SPE include ultrafiltration (UF), electrodialysis (ED), and reverse osmosis (RO). Techniques using membranes (i.e., UF and RO) are susceptible to fouling,[151–153] however coupling these techniques with SPE can increase carbon recoveries.[154,155] When coupling SPE with an RO/ED method, Green *et al.*[148] reported near 100% carbon recoveries for marine DOM samples. It is unclear how the higher recovery would affect FTICR MS spectra, and the RO/ED setup costs at least twice as much to perform than SPE.[148] While the combination of methods is still subject to artifacts from procedures in both methods, the improved recovery warrants evaluation for similar performance in extracted SOM.

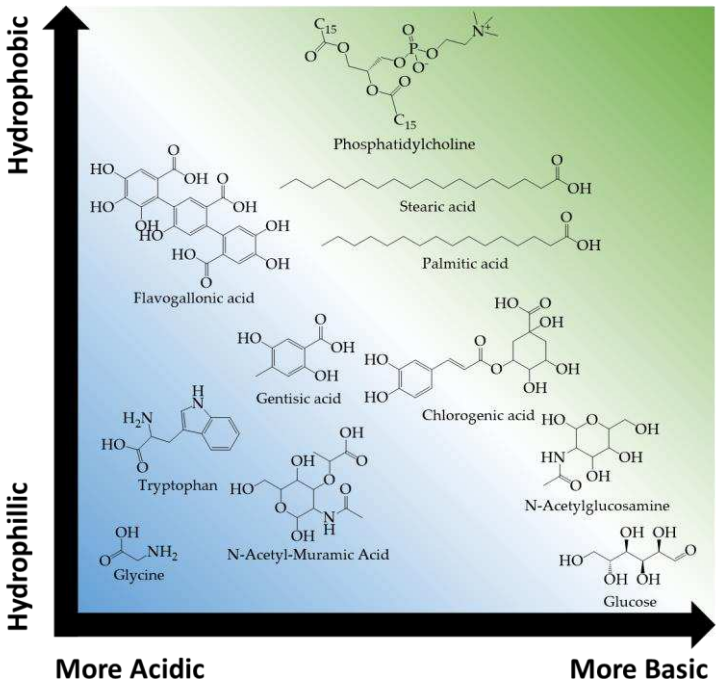

Figure 2.4 Examples of SOM compounds with a variety of functional groups that result in a range of acidity and hydrophobicity, impacting their solubility and ionizability. These features determine their optimal extraction and ionization method. Details on the exact values used to plot these compounds can be found in Table A.2.

2.3 Ionization Techniques and Matrix Effects

Characterization of SOM by any mass spectral technique requires the conversion of nonvolatile analytes from solution to gas phase ions by ionization. All soft ionization techniques are selective, and since OM contains a wide range of polyfunctional species across a wide molecular weight range and ionization potentials, ionization efficiency is determined based on the analyte composition. Different ionization mechanisms preferentially ionize certain components of OM (i.e., functional groups), enhancing their signal and suppressing the signal from other ions, since ionization efficiency depends on acidity/basicity, hydrophobicity, molecular weight, and degree of conjugation. Thus, experimental design begins with a consideration of the selectivity of each ionization technique including the potential need for using multiple techniques for a better understanding of the formulas and features present.[156–158]

2.3.1 Electrospray Ionization

Electrospray ionization (ESI) is the most[159] routinely applied ionization techniques for WEOM components. Ionization is achieved by infusing the analyte (e.g., OM) solution through a positively or negatively charged capillary that generates a fine mist of droplets. Solvent removal, often assisted by heating, yields charged molecular ions. This process is one of the softest methods of ionization and during OM analysis is often assumed to produce intact analyte ions, although some analytes may still undergo in-source fragmentation, particularly at high spray voltages.[160–162]

Ion formation by ESI depends largely on the *pKa* of the analyte as well as the ionization polarity (e.g., negative or positive mode). In negative mode, ions are generally formed by deprotonation or formation of adducts with anions such as Cl^-. Negative ionization efficiency generally correlates inversely with *pKa* and the extent of charge delocalization, such as in conjugated and aromatic chemical structures.[163] Common acidic functional groups in SOM such as carboxylic acids and phenolic groups tend to form negative ions. In positive mode, ions form by protonation or adduct formation with cations such as Na^+, K^+, NH_4^+, or metal ions. Many functional groups in SOM such as amines, alcohols, and carbonyls can be protonated to form cations, and their ionization efficiency is largely correlated with basicity (conjugate acid *pKa*).[164] Thus, positive and negative polarity modes may detect distinct components from a SOM mixture.

Analyte hydrophobicity and molecular size influences ESI efficiency. Hydrophobicity often correlates with higher ionization efficiencies, particularly in aqueous solutions, due to enhanced affinity for the surface of droplets where molecules have a greater probability of being desolvated and charged.[165] ESI sensitivity is often also increased when the analyte is already

ionized in solution (i.e., acidic conditions for basic analytes and basic conditions for acidic analytes),[166] although specific pH effects vary depending on analyte chemistry.[167,168]

Solvent composition influences the relative solubility and droplet surface affinity for polar and nonpolar components, and therefore ionization efficiency.[165,166] Novotny *et al.*[169] demonstrates that different solvent compositions, including neat solvents, efficiently ionize specific fractions and influence the representativeness of a sample spectra. Solvent mixtures commonly used for ESI include water, methanol, and acetonitrile, and can improve ionization efficiency of target molecules[165] and reproducibility of mass spectra[170] by altering the proportion of organic solvent.

Additives, contaminants, salts, and metals can also enhance or suppress ionization by ESI (i.e., introduce matrix effects) and can also dilute feature signals across multiple adducts, discussed further below. Additives can extend the range of compositional features collected[171,172] and enhance the ionization of specific molecular features.[173] In contrast, there are numerous contaminants that can be introduced accidentally during sample collection and preparation that will suppress SOM ionization. This is especially true for surfactants, which preferentially ionize due to their amphiphilic nature and ionizable head groups (Figure 2.5).[53] While the bulk SOM characteristics and most ionizable species will likely still be observable, ionization suppression will limit the number of other peaks that can be detected and assigned near the limit of detection. This can dramatically influence heteroatomic assignments and peak count overall, therefore, it is crucial that materials used for sampling, filtration, and processing prior to collection and sample analysis are tested.

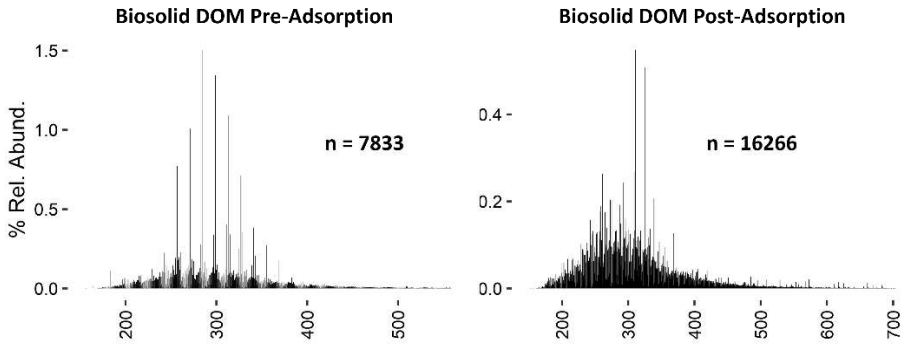

Figure 2.5 FTICR mass spectra collected from biosolid-extracted DOM, pre- and post-sorption to Fe(III)-montmorillonite. Surfactant contaminants present in the native biosolid-extracted DOM were absent after sorption to Fe(III)-montmorillonite. Produced with data obtained from Young *et al.*[53]

The use of micro or nano ESI reduces ion suppression from salts and other species, and improves the ionization efficiency of compounds with less surface affinity, because droplet sizes are reduced and desolvation is enhanced compared to electrospray at higher flow rates.[174] However, high proportions of surfactants or other contaminants can still influence the number of SOM peaks that can be detected and assigned because it remains desirable to limit the number of trapped ions during SOM analysis to prevent adverse effects from space charging[175] (discussed below).

2.3.2 Ionization Techniques for Non-polar and Water-insoluble Soil Organic Matter

While ESI remains the most common ionization technique used for OM analysis, atmospheric pressure photoionization (APPI) offers different ionization mechanisms and selectivity. Using APPI extends the analytical window of FTICR MS to less polar analytes, evidenced by direct comparisons with ESI that display ionization of formulas with lower oxygen content and higher carbon unsaturation.[156,157,176] This will affect heteroatom abundance and peak assignments (Figure 2.6), as less polar nitrogen-containing compounds can be preferentially ionized using positive ion APPI,[177] yet sulfur atoms presumed in polar functional groups are diminished.[156] For positive ion APPI, radical cation ($M^{+\cdot}$) and protonated $[M + H]^{+\bullet}$ species are formed based on ionization energies

of the analyte in respect to the dopant. For negative APPI, analyte ions differ based on electron affinity and include $M^{-\cdot}$, $[M - H]^-$, $[M - X + O]^-$, and $[M + A]^-$ where A is an anion (typically a halogen) and X is H, Cl, or NO_2. Developments and mechanistic discussions of APPI have recently been reviewed.[178]

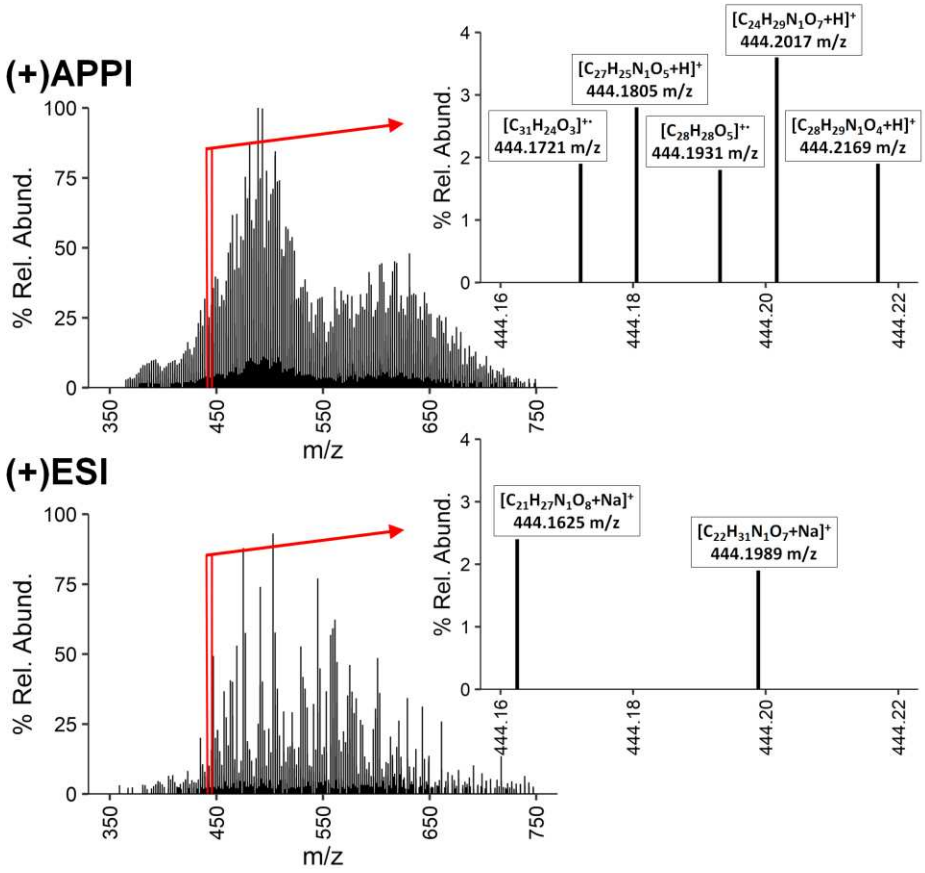

Figure 2.6 FTICR mass spectra of DOM from Lake Drummond (Great Dismal Swamp National Forest, VA, USA). Samples were prepared using C_{18} solid phase extraction and spectra were obtained with atmospheric pressure ionization sources: (+)APPI (top) and (+)ESI (bottom). Spectra display peaks assigned with <1 ppm mass error, where insets indicate molecular formulas unique to each ionization source assigned over 444.16 – 444.22 *m/z*. Produced with data obtained from Hockaday *et al.*[157]

The main benefit of APPI over ESI is the simultaneous formation of gas phase ions from both polar and non-polar compounds. Other benefits include less suppression from salt and solvent effects as charge acquisition occurs differently than in ESI.[179] Comparisons of these methods for lipid analysis suggest that APPI is far more sensitive than ESI, and is particularly useful for studies focusing on condensed aromatics and hydrocarbons within natural organic matter.[180] However, the

additional ionization mechanisms also increase the number of peaks in APPI compared to ESI,[157] increasing the complexity of the mass spectrum and requiring even higher mass resolving power to separate the increased number of isobaric species. The amount of sample required for APPI is also generally higher as injection flow rates can be orders of magnitude larger than in ESI.[156,157,176]

Solid phase samples can also be ionized through desorption techniques, including desorption atmospheric pressure photoionization (DAPPI), laser desorption ionization (LDI), and matrix-assisted laser desorption ionization (MALDI). These techniques allow ordinarily insoluble SOM components to be analyzed directly, such as with the application of DAPPI to pyrolyzed carbon.[181,182] Similar to APPI, LDI and MALDI have been shown to compliment ESI-FTICR MS by ionizing more conjugated and aromatic DOM constituents.[183,184] Mechanisms and substrate selection for LDI and MALDI are reviewed by Zenobi *et al.* and Dreisewerd.[185,186]

Importantly, while using multiple techniques will provide a larger window into the OM compositions present, it is not feasible to use every technique nor can the use of every technique unequivocally ionize every organic residue present in injected samples. Technique and polarity mode should therefore be chosen based on *a priori* knowledge of the sample and target fraction, as ionization parameters can greatly influence sample representation. Additionally, the intensity and m/z distribution are sensitive to instrumental parameters, meaning FTICR MS is not well suited for resolving controversies regarding the size distribution of SOM.

2.4 Analysis and Interpretation of Soil Organic Matter using FTICR MS

When analyzing NOM, FTICR MS typically detects and resolves many thousands of peaks in the m/z range from 150 to 1000 m/z. Molecular formula assignment involves calibrating the mass spectra, computing formulas that fit each mass within the applicable mass error window, and choosing an appropriate assignment when there are conflicts using all available information (e.g., elemental content, and chemical or structural relationships with other formulas).[187] Uncertainty in

assignments rises dramatically with mass and the number of elements[188] as the number of possible formula increases. While automated assignment procedures often select the formula with lowest mass error or smallest number of non-oxygen heteroatoms (i.e., atoms in the ring of a cyclic compound other than carbon or hydrogen atoms), these approaches can sometimes yield incorrect results.[17] Accordingly, various methods, including m/z vs. error[189] and DBE minus O plots[17] can be used to further evaluate dubious or conflicting formula assignments.[190] Following formula assignment, several assumptions will be present in data visualizations and should be carefully considered to avoid misinterpretations. Additional methods, both online and offline to FTICR MS, will be discussed that can provide additional insights into SOM composition, microbial decomposition pathways, and other relevant areas of study.

2.4.1 Mass Calibration

Molecular formula assignment relies on mass error windows, so mass calibration is a critical part of the formula assignment process.[191] External calibration cannot provide better mass accuracy than a few ppm because the number of ions in the ICR cell varies from sample to sample.[192] As a result, complex organic mixture FTICR mass spectra benefit from internal calibration, wherein the ion cyclotron resonance frequency (f) is converted to ion mass-to-charge ratio (m/z) by fitting experimental data spanning the entire detected m/z range (e.g., multiple homologous series) to the relation $m/z = A/f + B/f^2$, to yield root-mean-square mass error as low as ~10-200 ppb.[193]

Savory *et al.* developed a calibration protocol in which the spectrum is divided into dozens of adjoining segments, with separate calibrations applied to each, to eliminate systematic error with respect to m/z, and introduced a third calibration term to minimize systematic error with respect to ion abundance.[189] In addition, Dittmar *et al.* recently reported improved mass accuracy by averaging mass spectral data from independent environmental samples, and increased mass precision through peak alignment during post-detection data processing.[194]

The minimum resolution requirements to adequately analyze a sample composition will change depending on signal-to-noise (S/N) thresholds, the dynamic range of the instrument measurements, digital resolution, and isotopic fine structure.[195] Ideally, the instrument and resolving power should be considered based on *a priori* information as additional constraints, such as inclusion or exclusion of specific heteroatoms, can substantially change the minimum resolving power required.[75] Increasing magnetic field strength will increase mass resolution, dynamic range, and peak non-coalescence.[73,196] Increasing the time-domain acquisition period will also increase resolution, however if sample signal magnitude is low (i.e., sample ions are very low in abundance), instrument noise can also erroneously be assigned.[73] Increasing ion accumulation times can increase sensitivity, however high ion densities in the ICR cell can produce space charge effects that coalesce peaks or alter ion frequencies, adversely affecting both formula assignment and mass accuracy.[73,175,197,198] The limited ion capacity during FTICR MS measurement also means that intensity and m/z distributions are sensitive to instrumental parameters. Molecular weight distributions are better determined in low resolution MS systems like linear ion trap and time-of-flight that also capture lower molecular weights (<200 m/z) efficiently.[20,199] Thresholds for S/N will also strongly affect peak detection and reproducibility. Discussions by Sleighter *et al.*[200] indicate how S/N affects minimum common peak assignments and describes methods to evaluate meaningful differences between samples.

2.4.2 Automated Molecular Formula Assignment

There are a range of tools available for automated molecular formula assignment, including in-house programs (PetroOrg/EnviroOrg at the National High Magnetic Field Laboratory),[201] open-source programs (Formularity, UltraMassExplorer, and ICBM-OCEAN) and publicly-available R or Matlab scripts (MFassignR, CIA, and TRFu).[187,202,203] The Compound Identification Algorithm (CIA) developed by Kujawinski *et al.* computes elemental compositions for low molecular weight compounds (<500 *m/z*), where the potential for conflicting solutions is minimal,[204] and uses a

"formula extension" approach to connect the assigned formulas with higher molecular weight compounds via established chemical and functional group relationships (e.g., CH_2, CH_4 – O, H_2, CO_2 and NH). The existence of these relationships has also been separately established by mass difference and network analyses.[205,206] Mass difference-based network analysis links detected ions by characteristic mass differences, such as the mass of the methylene subunit (CH_2 = 14.01565 amu) or the mass change from nitrosylation (HNO = 31.005814 amu),[206,207] but multiple subunits can be used simultaneously. When plotted as one or more interconnected networks, the resulting plot can seem exceedingly complex because the number of "nodes" is equal to the number of detected ions, and because each node can be connected to other nodes through one or several mass-difference-based "edges" (i.e., subunits) (Figure 2.7). However, subgraphs can be extracted using a subset of the mass differences,[206] and nodes or edges can be colored by sample type, element counts, or other characteristics,[208] to focus on specific features. Mass difference-based network analyses have already been used for diverse purposes including formula assignment,[206] untargeted metabolite profiling,[209,210] and reaction pathway identification.[211] To be clear, the assignment of an elemental composition is insufficient to identify a metabolite, and the occurrence of a specific mass difference can be coincidental in a complex sample.

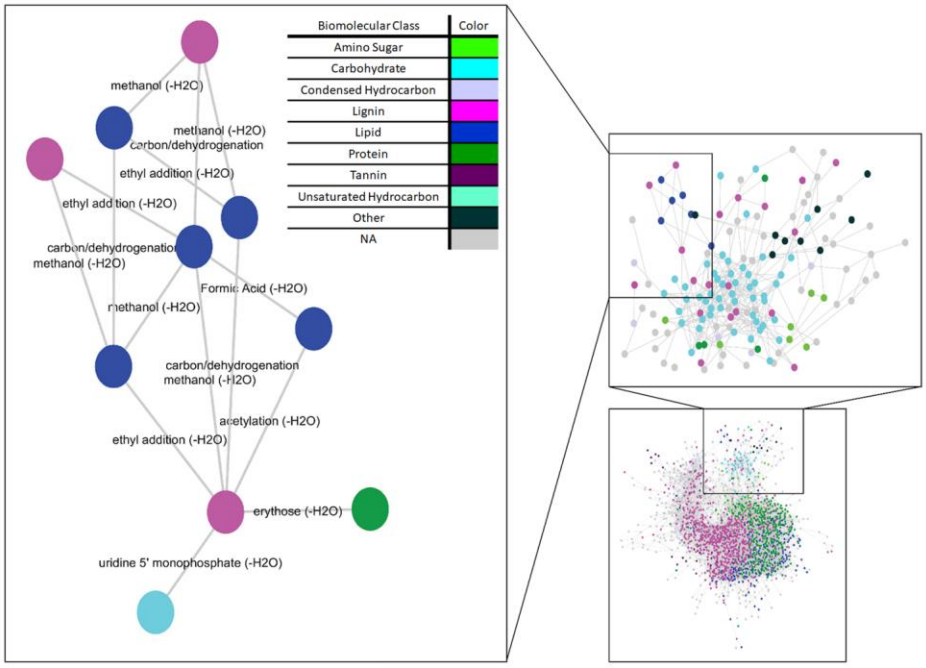

Figure 2.7 Abiotic reactions at low pH occurring in cellulose-like compounds produced by Sphagnum (peat moss), plotted using mass difference-based network analysis to study how plant leachates degrade in soils. Each assigned FTICR MS peak (circle) is colored by a biomolecular class approximation using van Krevelen plot regions and related through different reactions (lines). Produced with data obtained from Fudyma *et al.*[212]

Indeed, some version of formula extension is used in almost every formula assignment algorithm. The CIA algorithm has been incorporated into the freely-available Formularity software platform, which includes an associated database and formula filters based on the "Seven Golden Rules".[213] The CIA component is restricted to C, H, N, O, S and P, but a separate isotopic pattern algorithm (IPA) is available to identify other elements, particularly when they present a strong isotopic signature (e.g., Br, Cl or Hg).[214] ICBM-OCEAN is a server-based tool that integrates published and novel approaches for standardized processing of ultrahigh resolution mass spectrometry data from complex molecular mixtures.[215] Importantly, ICBM-OCEAN incorporates diagnostic and validation tools for each step in data processing, including noise and systematic error reduction and spectra recalibration and alignment, and it has been tested and applied to both FTICR MS and Orbitrap MS for more than 1000 NOM samples.

After automated formula assignment, equivocal assignments (i.e., peaks above S/N with multiple feasible compositions) will generally remain. Molecular formula assignment for equivocal assignments can be highly subjective, therefore different calculated indices and empirical evidence should be used to increase the reliability of manually distinguished assignments wherever applicable. For instance, the selection of heteroatoms during assignment can dramatically alter the number of equivocal assignments (Figure 2.8), however prematurely excluding elements can also result in erroneous assignments.[74] Kendrick mass defect analysis can be used to study patterns in OM assignments, discussed below. Double-bond-equivalents-minus-O (DBE-O) plots are also used that compare equivocal and unequivocal assignments using heteroatoms and oxygen content (Figure 2.9).[188]

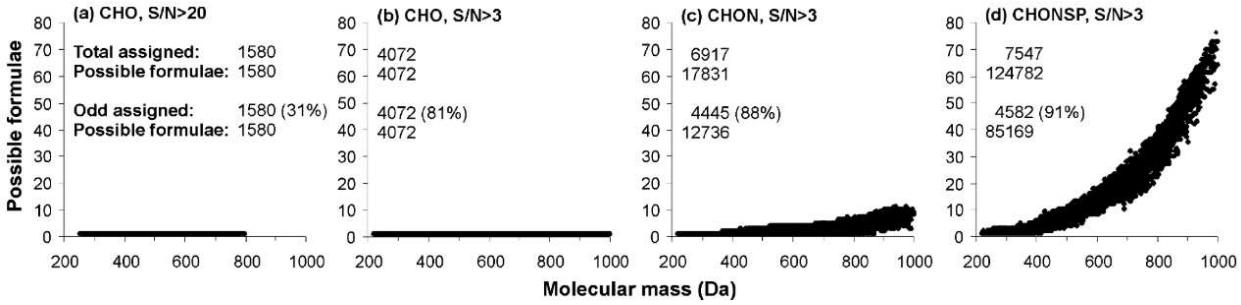

Figure 2.8 Possible formula assignments for peaks at a given molecular mass under different heteroatom and S/N conditions. A) and B): the number of assignments increase as S/N thresholds are lowered. B), C), and D): possible compositions for a given peak increase as the number of heteroatoms included and molecular mass increases. Reproduced from Koch *et al.*[74]

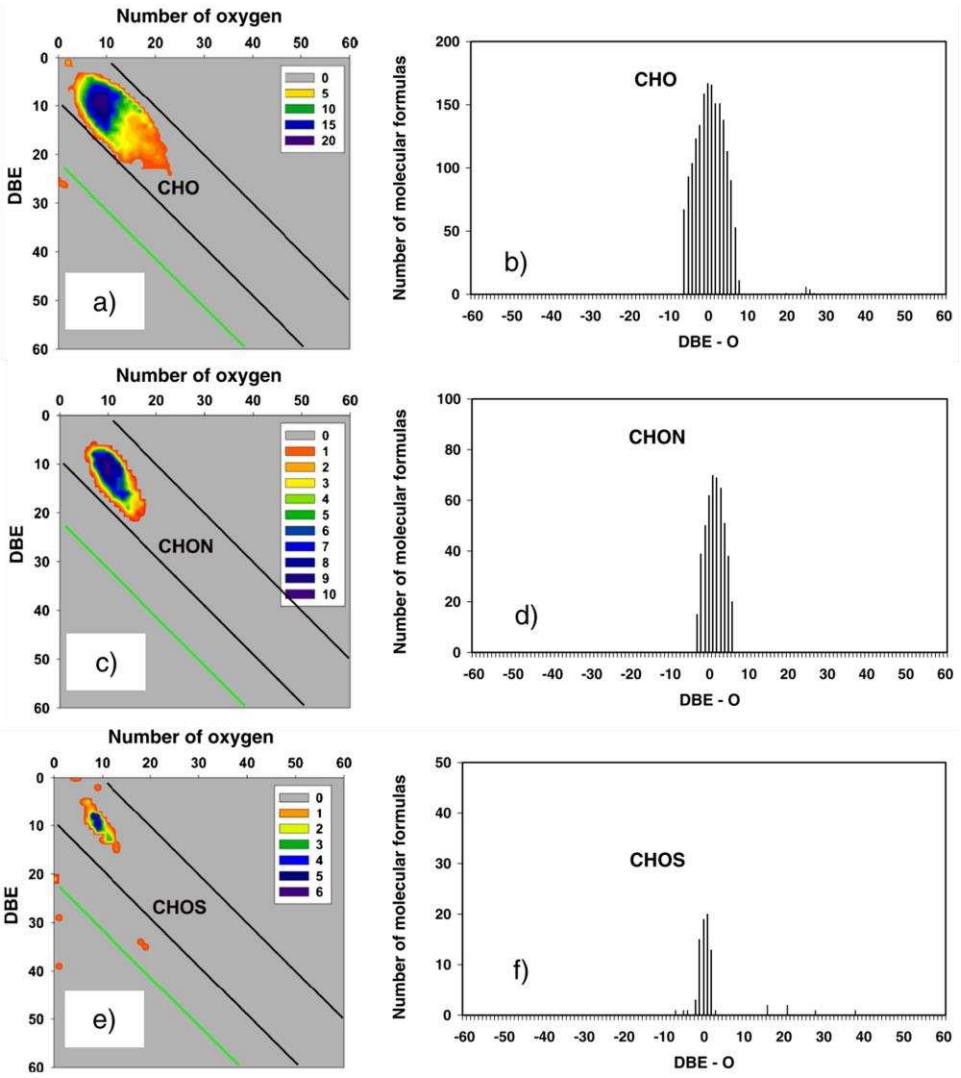

Figure 2.9 Contoured plots of DBE vs. O (a, c, e) and bar graphs of DBE – O vs. number of molecular formulas (b, d, f) for unequivocal assignments in a Suwannee River fulvic acid standard, where color indicates number of m/z values. The positioning and number of m/z values from unequivocal assignments can be compared to equivocal assignments to indicate which compositions have the highest reliability, where reliable equivocal compositions will most frequently lie or overlap within the same regions as unequivocal assignments in the same class. Black lines are to indicate a diagonal range between -10 and 10 DBE – O, and the green line indicates regions where equivocal assignments would be unreliable due to their high hydrophobicity (e.g., black carbon components). Reprinted by permission from Copyright Clearance Center: Springer Nature, Analytical and Bioanalytical Chemistry, Understanding molecular formula assignment of Fourier transform ion cyclotron resonance mass spectrometry data of natural organic matter from a chemical point of view, Peter Herzsprung, Oct. 31 2014.[188]

2.4.3 Visualization and Data Analysis

Once elemental compositions have been assigned, several parameters can be calculated using the stoichiometry of the assigned molecular formulas. These include rings-plus-double-bonds equivalents (RDBE), aromaticity indices (AI_{mod}),[213,216] and the average nominal carbon oxidation state

(NOSC) (Figure 2.10B).[217] NOSC has been used to examine chlorinated disinfection byproduct formation,[218] water solubility,[219] and the biogeochemical reactivity of SOM.[220] Indeed, NOSC makes it possible to calculate the Gibbs free energy (ΔG) provided by the oxidation of a particular compound ($\Delta G°_{Cox}$) given the available electron acceptors and environmental conditions.[221–223] Thus, NOSC and $\Delta G°_{Cox}$ have been used to provide a thermodynamically relevant metric for approximating the energy stored in organic matter, or whether microbial oxidation of OM is thermodynamically favorable under a given set of redox conditions.[224]

Kendrick mass defect (KMD) analysis[225] was initially adopted by the organic matter community as the standard means for visualizing complex mass spectra prior to formula assignment.[226–230] Kendrick plots are generated by plotting nominal mass as a function of KMD, most commonly based on a methylene (CH_2) subunit (Figure 2.10C). In effect, each m/z is normalized by the accurate mass of the subunit (e.g., 14/14.01565 for CH_2 subunits, common to lipid (Figure 2.4), sugar, and lignin derivatives[231]). Afterwards, compounds whose elemental compositions only differ by the number of subunits possess the same KMD value and line up horizontally in the associated KMD plot. KMD analysis on SOM is useful for: i) molecular formula assignment by assisting in assigning molecular formulas at higher m/z ions when there are more formulas that match an exact m/z value, ii) identifying multiply charged ions, and iii) multiply charged polymer ions of plant origin in soils.[232–235]

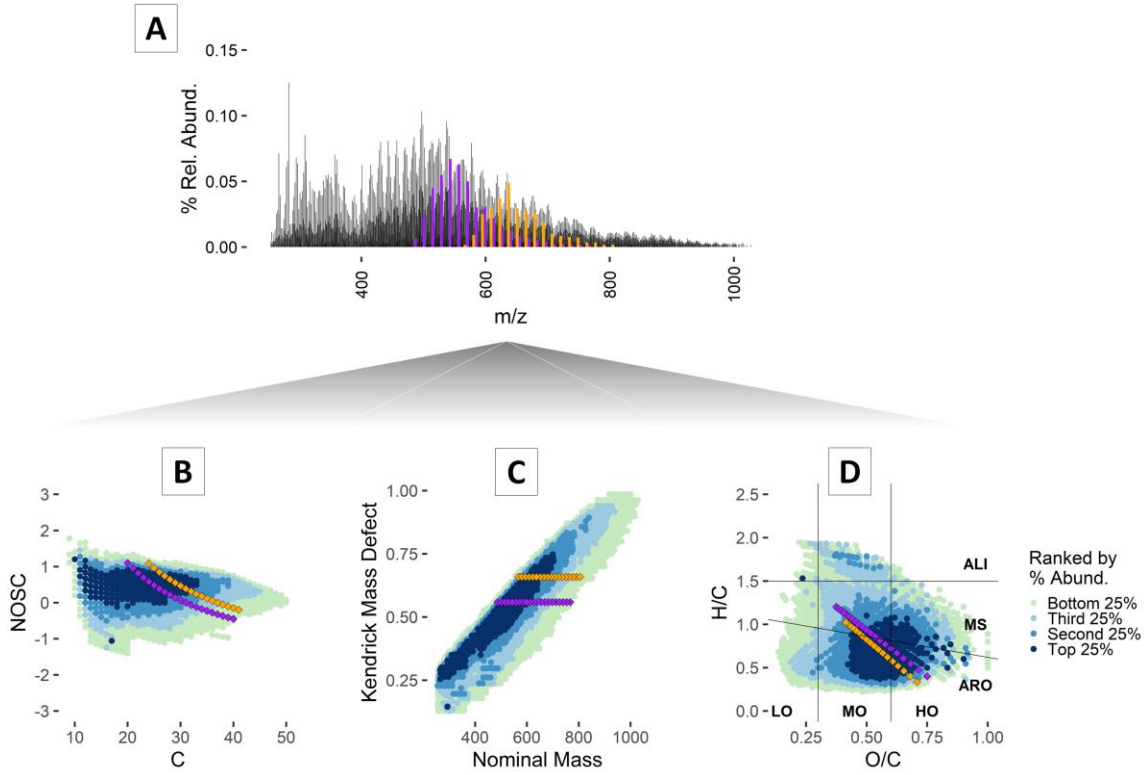

Figure 2.10 The 21T FTICR mass spectrum of Pahokee Peat extracted with pyrophosphate with formula assignment conducted using PetroOrg software[201] to assign 15506 assigned formulas. Two series are highlighted (orange and purple) that represent CH_2 Kendrick mass defect (KMD) series (0.55857 and 0.65806) and are present in each of the plots to illustrate their appearance and patterns through different visualizations: A) mass spectra displaying semi-gaussian abundance distributions, B) nominal oxidation state carbon (NOSC),[217] C) the CH_2 KMD series over the entire mass spectrum, and D) a van Krevelen diagram which sections plot regions indicating oxygen content (LO = low-oxygen, MO = mid-oxygen, HO = high-oxygen content) and degree of saturation (ARO = aromatic,[216] MS = mid-saturated, and ALI = aliphatic[236]). Formulas are colored based on abundance quartiles. Unpublished data from the Borch Lab.

Van Krevelen (VK) diagrams[237] are constructed with assigned formulas using molar ratios of hydrogen-to-carbon (H/C) on the x-axis and oxygen-to-carbon (O/C) on the y-axis (Figure 2.10D). Points can be colored, or a z-axis can be added, to provide additional information such as relative abundances, molecular weights, or elemental classes (e.g., CHO vs. CHNO). VK plots are widely used to make inferences about predominant reaction pathways (e.g., methylation, hydrogenation, condensation), and to estimate the abundance of major compound categories based on the major biogeochemical components of the source material (e.g., lignin-like, lipid-like, or carbohydrate-like), which have characteristic H/C versus O/C ratios.[238–240] However, the boundaries of the compound

classes vary among published studies, and often overlap. Moreover, "lignin-like" components may be derived from non-lignin source materials,[211] or even reflect synthetic chemicals if anthropogenic impacts are present (Figure 2.11), and lignin sources may generate some non-"lignin-like" signatures.[241] Accordingly, while the major compound categories do signify molar ratios similar to well-known biogeochemical classes, they are not reliable indicators of source or structure without additional, complementary information (e.g., on the prevalent reaction pathways).[238] Recent revisions proposed by Rivas *et al.*[242] improves compound classification in biological samples using C/H/O/N/P stoichiometric ratios, but was only tested on different metabolite compositions and omitted "lignin-like" and "condensed hydrocarbon" compounds that could be a major component of soil organic matter.

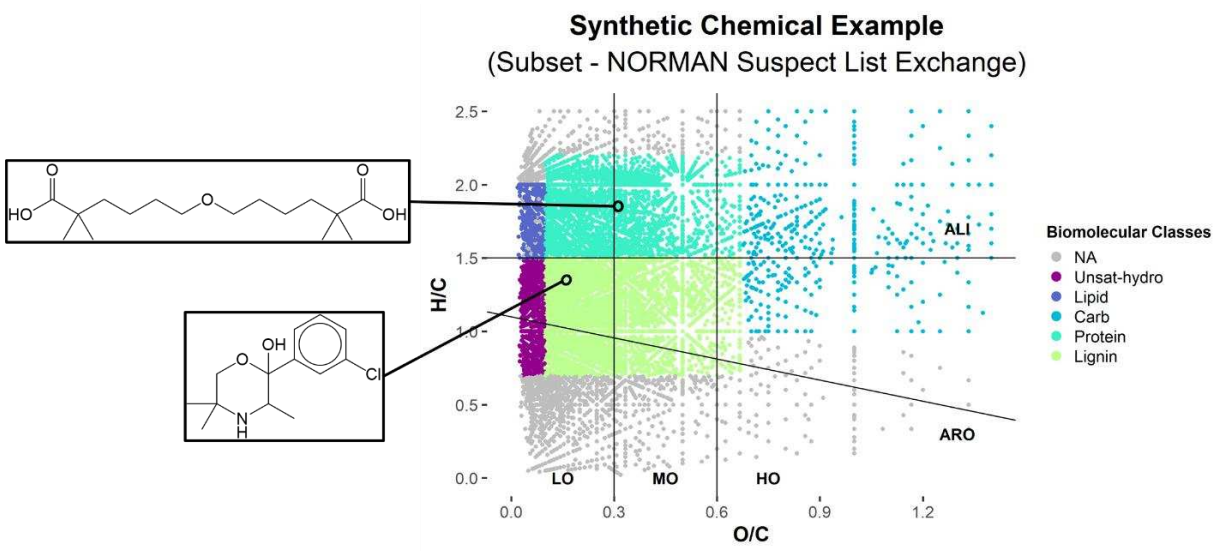

Figure 2.11 NORMAN suspect list exchange[243] plotted onto a VKD with two of the synthetic molecules plotted to demonstrate that assignments unrelated to SOM are still plotted in regions pertaining to specific biomolecular assignments (regions are based on Hockaday 2009).[244]

Regardless of the VK plot limitation, this tool can still provide useful insights into C cycling and changes in soil organic matter composition with perturbation. Users are advised to use O/C and H/C boundaries that are consistent with the chemistry of their sample and carefully interpret their results while acknowledging that these classifications are only putative. Relative abundance values of

different compound classes can also be calculated from count values associated with each observed biomolecule group normalized by the total number of C molecules identified (i.e., number-weighted).[245,246] When comparing multiple samples in side-by-side comparisons or combined analyses, it is important to ensure that systematic biases (e.g., ion suppression or differences in SPE extraction efficiency) are minimized or eliminated, particularly because many SOM constituents are detected at signal intensities close to the detection limit. Molecular weight distribution, heteroatom content, constituent presence or absence, and VKD coverage can all be influenced by these low-intensity signals. Past approaches to eliminate systematic bias include extracting the same number of the most intense signals from every sample,[247] or the formulas common to every sample,[53,248] and then normalizing the extracted signals based on total intensity.

Other visualizations are common in the petroleum and aerosol field for rapid visual comparisons to highlight compositional differences/similarities between samples and can be beneficial to SOM studies.[217,249–251] These include: i) plotting the number of carbons in each formula versus its nominal mass (C versus M), where the molecules are classified into different categories based on their sum of carbon and oxygen atoms (i = C + O), ii) contoured plots of RDBE vs carbon number[252] for members of a single heteroatom class, iii) relative abundance histograms for heteroatom classes, and iv) Kroll diagrams where NOSC is plotted as a function of number of carbons (Figure 2.10B).[248] Kroll diagrams are especially useful when looking at changes in SOM composition under different redox[253] conditions.

When comparing multiple samples, such as DOM from different sources, principle component analysis (PCA)[21,248] and hierarchical clustering analysis (HCA)[254] can be used to group similar samples. PCA takes advantage of the fact that many variables are correlated (e.g., H/C ratios and double bond equivalents), and produces diagrams that group similar samples and show correlations among variables. In one example, PCA was used with intensity-weighted element

number, m/z, H/C, O/C, AI_{mod}, and DBE values to compare the DOM in ten world rivers, associating the intensity-weighted variables with different levels of anthropogenic influence and other watershed characteristics (Figure 2.12).[21] PCA is particularly useful for visualizing the relative similarities and differences of multiple samples, and for identifying the variables that best explain their differences. Importantly, compositional data, such as the %CHO of a DOM sample, are generally not appropriate for PCA.[255] In comparison, HCA uses Bray-Curtis dissimilarity or another distance calculation to perform a series of partitioning calculations that group samples into clusters.[150,256,257] The result is a tree-like dendrogram, where common branches indicate greater similarity.

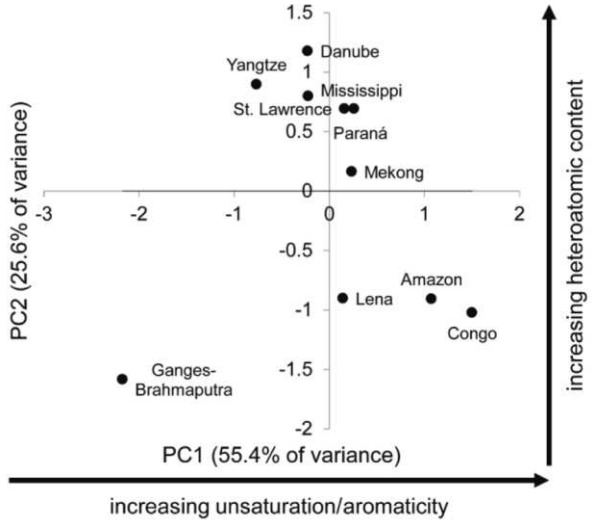

Figure 2.12 Ten rivers around the world were evaluated using FTICR MS and compared with PCA to identify sample groupings. The largest variance originated from the unsaturation/aromaticity and heteroatom content. Reproduced from Wagner *et al.*[21]

2.4.4 Analysis of NOM-Associated Metals

Mineral associated SOM and DOM are known to bind a range of metals and thus control the biogeochemical cycling, mobility, and bioavailability of both toxic metals (e.g., Hg, As, Cd) and essential mineral elements (e.g., Fe, Mn, Zn).[253,258] FTICR MS is particularly well suited for elucidating the speciation of metals and micronutrients that are complexed by or incorporated into

organic molecules that influence their solubility and reactivity. In soils, these elements are often binned into operationally defined fractions based on extraction protocols[259,260] that seek to differentiate water soluble, mineral associated, or bioavailable content. However, understanding the origin and dynamics of these elemental pools requires knowledge of their chemical identity. FTICR MS can resolve diagnostic isotopologues and mass defects that are characteristic of many heteroatoms, including trace metals (e.g. Fe,[261–263] Zn, Cu,[264] Ni, Hg[265]) (Figure 2.13), as well as halogens (Cl, Br, I[266]), thus providing a means to identify the particular SOM components that play a role in the cycling of these elements.

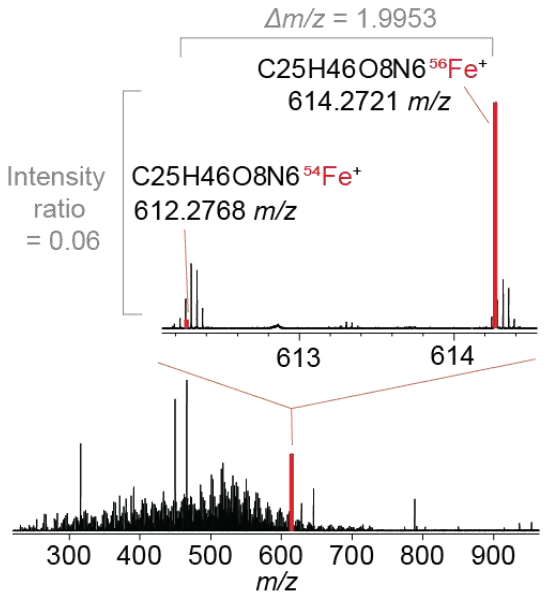

Figure 2.13 Mass spectra in a water extract of SOM that depicts the isotope pattern for a siderophore-Fe complex, Ferrioxamine B. Inset displays the mass and abundance difference indicative of iron complexation. Unpublished data from the Boiteau Lab.

Direct infusion FTICR MS analysis, however, is not well suited to identifying metal-bound molecules in DOM due to the number of peaks that results in unrelated species that mimic mass differences and relative abundances of metals. Furthermore, molecular formula assignments become

more ambiguous as heteroatoms are included in the assignment algorithm (Figure 2.8).[74] Boiteau *et al.*[261] developed a method for confident detection of metal-organic complexes by comparing direct infusion FTICR MS spectra of samples spiked with both natural and rare isotopes of metals of interest, comparing the ratio of features across samples. This was compared to another method based on separation using online HPLC-FTICR MS and detection of isotopologues with coherent elution profiles. While the isotope exchange method required significantly shorter analysis time, nearly twice as many metal-organic species were measured by HPLC-FTICR MS. This highlights how ion suppression is one of the key challenges in overcoming the detection of metal-organic species in complex mixtures.

Techniques such as liquid chromatography hyphenated inductively coupled plasma mass spectrometry (LC-ICPMS) have been used to quantify the various metal species present in DOM samples,[264] and FTICR MS and other high-resolution mass spectrometry techniques have been used to determine the molecular formula of these compounds. This approach has been used to identify and quantify chelating agents of biological origin in soil samples and the chemical form of heavy metal or halogenated contaminants in terrestrial environments.[265] Thus, FTICR MS combined with metal quantification provides insight into the processes that govern the transport, fate, and ecological effects of nutrients and contaminants in soils by providing unprecedented information on elemental speciation.

2.4.5 Fragmentation, Separation, and Metabolomics

While FTICR MS analysis can attribute chemical formulas to molecules within complex SOM mixtures, identifying specific molecular structures such as metabolites or their transformation products requires pairing FTICR MS with chromatographic and fragmentation analyses. Liquid chromatographic separations prior to offline or online FTICR MS has several benefits. The separation of molecules that must otherwise compete for charge reduces the suppression of poorly

ionizing molecules, reducing matrix effects and enabling the detection of a greater number of species.[267–269] In addition, separations can often resolve structural isomers that appear as a single feature with direct infusion FTICR MS (Figure 2.14).[270] These structural variants may have distinct sources, functional groups, and fates in soils, and thus distinguishing between isomers by LC-FTICR MS could be important to decipher processes that form, preserve, and degrade SOM. The chromatographic separation modes generally selected for these analyses are aimed at separating low molecular weight molecules within the m/z range of FTICR MS. Reverse phase liquid chromatography is typically applied to organic matter extracts, often mimicking the mode of retention used during solid phase extraction.[209,261,267,269–272] Hydrophilic interaction chromatography (HILIC), a variant of normal phase chromatography, is also well suited for the separation of polar components of SOM.[273,274] Both separation and ionization are strongly impacted by the choice of mobile phase. Methods commonly employ mass spectrometry grade water, alcohols, and acetonitrile along with volatile pH buffers (e.g., formic acid, acetic acid, ammonium formate, ammonium acetate, or ammonium hydroxide) due to their compatibility with ESI MS. The selectivity of different chromatographic methods for separating DOM has recently been reviewed by Sandon *et al.*[275]

Separation also facilitates the acquisition of tandem MS/MS fragmentation spectra for individual compounds by reducing the number of ions that may appear within a single MS isolation window. Fragment analysis has been used to determine the presence of specific functional groups or structures within DOM and other complex mixtures such as carboxylic acids,[269] sulphates,[276] aromatic archipelagos,[277,278] and metal-binding moieties.[264] MS/MS spectra provide a diagnostic molecular fingerprint that can be compared to the fragmentation spectra of known molecules to facilitate structural elucidation. Libraries of MS/MS fragmentation spectra collected with collision-induced dissociation are ever-growing,[279] and developing computational tools for predicting spectra

of molecular structures *in silico* is an active field of research.[280–282] Longnecker *et al.*[283] coupled LC FTICR MS/MS with *in silico* fragmentation computational tools on *Thalassiosira pseudonana* to study novel, intracellular metabolites, finding that they were related through sulfoquinovosyl head groups. Another developing tool is feature-based molecular networking, which links MS/MS spectra by their spectra similarity, permitting the use of precursor masses and structural information from compounds with library matches to help determine the structures of spectrally similar compounds with no library matches.[284,285] Putative identifications using tools such as *in silico* fragmentation or feature-based molecular networking can be confirmed by comparing retention time and MS/MS spectrum of an authentic compound using the same analytical method used for the soil sample.

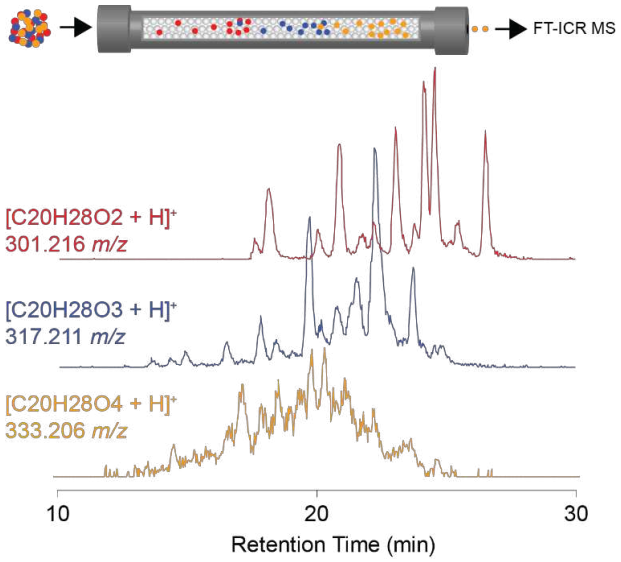

Figure 2.14 Extracted ion chromatograms from an LC-FTICR MS (21T) of a soil water extract. Mass ranges about each m/z were ±0.005 Da, where each trace represents the protonated monoisotopic form of the molecular formula indicated. Peaks separated for each formula represent different isomers. Unpublished data from the Boiteau Lab.

Finally, while they play a significant role in microbial growth,[286–288] essential metabolites with a molecular weight <200 Da such as acetate, pyruvate, amino acids, glucose, fructose, and succinate are typically either outside the optimum mass range of FTICR MS (i.e., 150-1000 m/z) or harder to ionize amongst matrix effects.[146] Gas chromatography mass spectrometry (GC-MS),[289] nuclear magnetic resonance (NMR) spectroscopy,[290,291] and liquid chromatography mass spectrometry (LC-

MS),[274] are the preferred instrumentations to identify these critical small metabolites and their structure in SOM. Recently, Swenson *et al.*[289] used GC-MS to estimate microbial metabolite availability in soils while Martins *et al.*[291] used ^{1}H NMR to measure acetate and methanol metabolite concentrations using samples from the Prairie Pothole Wetlands in North America. Using LC-MS/MS in positive- and negative-ionization modes, Ladd *et al.*[274] were able to identify a wide range of compounds (*e.g.* amino acids, plant/microbial metabolites, sugars, lipids) present in artic soil DOM. Thus, combining multiple analytical techniques can help improve detection and annotation of central and secondary metabolites in SOM important for microbial biogeochemical cycling in soil ecosystems.[223]

Coupling mass spectrometry with microbial techniques (e.g., metaproteomics,[292] community composition profiling[291]) and novel bioinformatics approaches such as correlation networks and metabolite prediction tools[293–296] (Figure 2.15) can also be useful for determining microbial decomposition pathways of OM and gaining insight into relationships between bacterial communities and SOM composition.[132,293,295,297–299] Using FTICR MS, ^{1}H NMR, and community composition, Martins *et al.*[291] found that extremely high sulfate reduction rates and methane fluxes in Prairie Pothole Wetlands were driven by abundant carbon substrates. Graham *et al.*[300] also used FTICR MS, gene expression, and community composition to gain mechanistic insight into hyporheic zone organic matter processing. This multi-omics coupled approach revealed a pronounced phenotypic plasticity in the hyporheic zone microbiome with similar microbiome structure, functional potential, and expression across sediments with dissimilar metabolic rates. Diverse nitrogenous metabolites and biochemical transformations as inferred by FTICR MS appeared to be the significant regulatory factor influencing hyporheic zone organic matter processing.

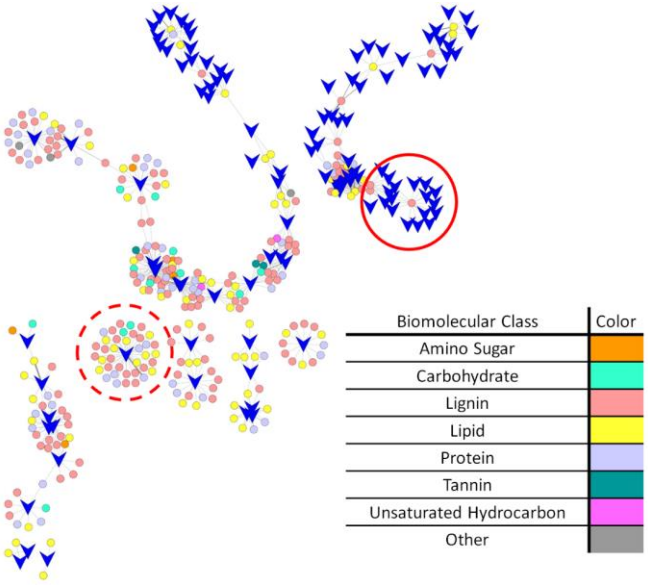

Figure 2.15 Correlation networks between microbial communities (arrowhead) and metabolomic features identified from peaks (colored dots) from FTICR-MS data in peat soil. Pairing metabolomics by FTICR MS with amplicon sequencing can be used to identify how different microbial populations are related by specific biomolecular classes. Arrowheads linked to the same dot indicates that microbial populations are each related through the same peak (solid red circle), and dots surrounding an arrowhead indicates that the associated peaks are unique to that microbial population (dotted red circle). Unpublished data from the Tfaily Lab.

2.4.6 Complementary Spectroscopic Techniques

Molecular characterization of SOM composition and reactivity often relies on combining FTICR MS with complementary analyses that provide additional information on bulk properties, elemental composition, molecular structure, or spatial distribution. The requirements for a 'clean' sample devoid of nonvolatile salts and the challenge of converting analytes into gas phase ions means that there are significant biases that affect signal intensity beyond concentration. The complex nature of SOM makes identifying the diverse range of organic compounds (e.g., lipids, lignin, sugar, fermentation byproducts, charred residues) present in different soil types challenging to analyze. Furthermore, while FTICR MS detects molecular features, direct infusion mass spectra cannot by itself distinguish between structural isomers. Fortunately, additional information from other techniques can be used to attribute molecular formula to functional classes and to particular metabolites. FTICR MS is thus a central component of the analytical suite needed to understand

metabolisms and organic matter transformations in soils. Here, examples utilizing spectroscopic techniques will be presented to illustrate how to utilize them to obtain robust conclusions.

Spectroscopic analyses that distinguish the functional groups and bonding environment of SOM components can provide significant quantitative bulk information that complements the molecular composition information of FTICR MS. NMR is particularly complementary because the major functional groups that comprise organic matter are often well resolved in NMR spectra, although the removal of paramagnetic elements such as iron in the samples is required. In previous studies combining these techniques to study marine and wetland dissolved organic matter, Hertkorn *et al.*[301,302] demonstrated that solid phase extracted DOM exhibited NMR shifts characteristic of aliphatic and carboxyl groups, while FTICR MS showed the abundance of diverse suites of unsaturated CHO, CHNO, CHOS molecules. They synthesized this information into the concept that carboxylic rich alicyclic molecules comprise a major component of DOM. Two-dimensional correlation analysis has been used to link FTICR MS and NMR data across a salinity transect by Abdulla *et al.* 2014.[303] The results of these analyses suggested that CHO compounds correlate strongly with carboxyl-rich compounds observed by H^1 NMR while heteropolysaccharides correlate with mass peaks which contain heteroatoms such as nitrogen, phosphorous and sulfur. DiDonato *et al.* 2016[114] combined solid state ^{13}C NMR and FTICR MS to compare humic acids derived from well aerated versus poorly drained soils. They observed that aerated soils had a higher proportion of condensed mass spectral features, which was corroborated by the higher proportion of aromatic carbon observed by NMR. Together, these results suggested major differences in aliphatic, lignin-like, cyclic, and condensed aromatic classes across soil types (Figure 2.16).

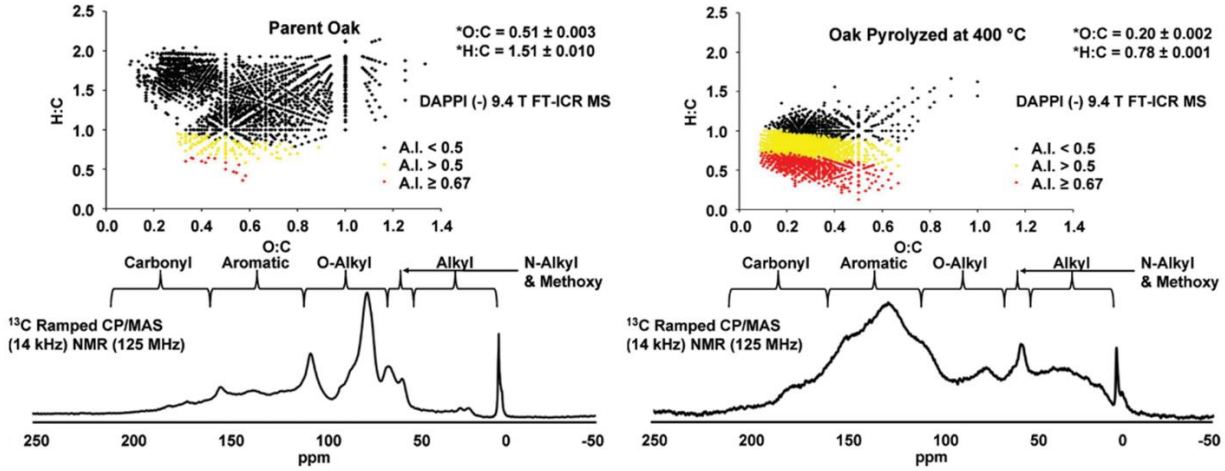

Figure 2.16 Comparisons between unburnt (parent) and pyrolyzed (400°C) oak (*Quercus laurifolia*) using (-)DAPPI FTICR MS with solid-state ^{13}C NMR to corroborate and describe changes to features during pyrolysis. Reproduced from Podgorski *et al.*[181]

Optical measurements have been used and continue to be used to infer organic matter quality through correlations with bulk molecular weight, aromaticity, and humic/fulvic and amino acid content in numerous studies.[304,305] Fourier transform infrared spectroscopy (FTIR) and fluorescence excitation emission spectroscopy (EEMS) can resolve organic functional groups including amide, ester, carbohydrate, phenol, aliphatic and carboxyl functionalities in DOM, and can thus corroborate some compound classes attributed to FTICR MS signals. Hodgkins *et al.*[246] used FTIR and FTIRCR MS to compare peat organic matter structure across a thaw gradient. FTICR MS analysis suggested a trend from larger O/C rich molecules to smaller compounds with lower O/C ratios across the thaw gradient (Figure 2.17).

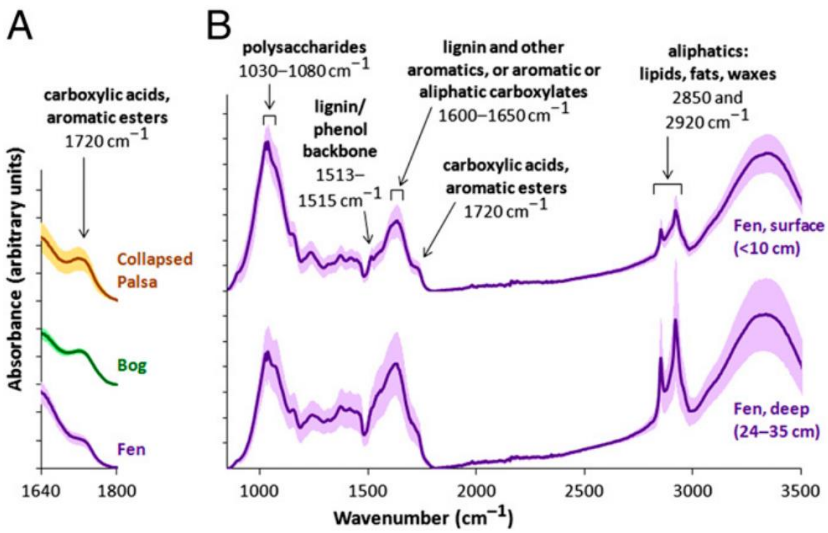

Figure 2.17 Average peat FTIR absorption spectra, with between-site standard errors as shaded areas. Spectra are stacked (i.e., absorbance = 0 at each apparent baseline) and sized to the same vertical scale. (A) Organic acids in incubated peat samples (preincubation) decrease with thaw from collapsed palsas (n = 2) to bogs (n = 3) to fens (including both sedge only and Sphagnum + sedge; n = 4). (B) In fens, humification leads to spectral changes between surface (n = 3) and deep (n = 3) peat. Reproduced from Hodgkins *et al.*[246]

This was consistent with a decrease in hydroxyl rich carbon relative to aliphatic and aromatic in the FTIR spectra suggesting degradation of carbohydrates. Malik *et al.*[306] used FTICR MS and FTIR to characterize the organic matter released from soils after chloroform fumigation extraction, which is commonly used to estimate soil microbial biomass. FTIR analysis confirmed the enrichment of aliphatic CH bonds in the fumigated DOM, which together suggested that fumigation largely increased the recovery of membrane lipids. EEMS detects aromatic fluorescent components of DOM, and these signals are often attributed to functional classes with similar signatures such as lignin phenols, quinones, proteinaceous residues incorporating tryptophan or tyrosine, and refractory humic and fulvic acids. FTICR MS has been used to provide information on the potential molecular identities of these fluorescent agents by correlating the fluorescent signals to the components observed in FTICR MS spectra.[307] EEMS has also been used to differentiate between terrestrial, microbial protein-like, and marine organic matter inputs.[305,308] Together with absorption spectroscopy, they represent inexpensive and fast tools that allow for high throughput. Thus, high-

resolution sampling in both space and time is possible. Both techniques can be done in situ and may be used by remote sensing allowing high-frequency, real-time data collection for understanding ecosystem properties.[309,310] While these measurements are highly suitable for looking at a broad range of extracted material[115] and oxidation states that are more or less bioavailable,[116] these compounds represent only a small fraction of the total organic matter pool.[91,311,312] Thus, for studies that involve microbial communities and microbial pathways, we recommend complimenting optical measurements with either of the above mentioned spectrometric and spectroscopic techniques that allow us to look for individual compounds.

2.5 Future Directions

The strength of FTICR MS as an analytical tool lies in its unrivaled ability to detect individual organic molecules that make up the tremendously complex mixtures found in soils.[193] Despite this, challenges associated with selectivity and the numerous equivocal peak assignments ultimately limits the processing and comparison of samples between studies. The utilization of complementary techniques that reinforce and constrain FTICR MS data are often needed to fully interpret the large and complex FTICR MS datasets. The use of spectroscopy provides highly complementary data on molecular origin or structure.[313]

Experimental design and sample preparation are critical steps because data are mostly qualitative and poorly reproducible across laboratories even on similar samples and within the same experiment on the same instrument.[26,170,200,314] Thus, it is important to ensure standardized protocol that minimizes influences on dependent and independent variables, where numerous biases and considerations are summarized (Table 2.1). Several future developments and needs for the application of FTICR MS to SOM are discussed below.

2.5.1 Unified Sample Preparation

The high chemical diversity of organic compounds in SOM means there is no universal technique for complete and comprehensive extraction, and the resultant analysis and discussion should reflect the limitations of the selected technique to avoid data misrepresentation. Comparisons between studies using different preparations are therefore limited as our understanding of how each preparation alters and isolates the SOM content is still developing.[145,147,148] Characterizing the effects to SOM during preparation would aid in normalizing SOM content against artifacts from preparation, supporting more effective comparisons between data sets. Therefore, a more thorough understanding of the biases introduced during preparation is needed to develop unified sample preparation techniques specific to a target fraction. Standardized protocols for specific sample environments are critical in establishing comparable samples between laboratories and studies.

2.5.2 Automated Internal Calibration

While calibration strategies continue to become more refined in ultrahigh-resolution data, calibration remains dependent on instrument condition and is subject to user input which ultimately contributes to the poor reproducibility across laboratories.[200] Developing automated internal calibration strategies would therefore aid in the consistency and removal of bias during the analysis of FTICR MS samples, such as with the implementation of the ICBM-OCEAN[215] protocol, however procedures remain unique to different laboratories. Standardized SOM processing methods are expected to increase sample reproducibility and provide more opportunity for comparison between datasets.

2.5.3 Investigation of Ionization Techniques

Negative ESI remains the most commonly applied ionization polarity and technique for SOM, and other techniques, such as APPI, are capable of extending the range of ionizable features to less polar and aromatic functionalities. These techniques can be coupled to MS/MS systems for

fragmentation, however collecting MS/MS spectra free from co-isolated precursor fragments has remained a major challenge when fragmenting complex mixtures. Charge acquiring leaving groups such as COO- are abundant during fragmentation of SOM and result in the loss of attributable daughter ions. Structurally informative fragmentation requires the investigation of new solution-based ionization techniques and methods that employ functionality specific ionization. To this end, the development of metal cationization or solvent pH modification methods for specific precursor compounds may provide much higher specificity in the ionizable fraction.

2.5.3 Unified Database Repository

Due to the significant effort required to validate mass spectral features and the large number of features in soil that do not match any fragmentation spectra in databases, comprehensive identification of metabolites in soils remains a major challenge. Therefore, the implementation of a unified database repository using standardized protocol with elemental compositions for SOM datasets worldwide is of great interest for comparisons across temporal and spatial scales in environmental samples. Such repositories could be used to rapidly compare and identify peaks as potential metabolites by linking known and unknown compounds in correlation and network analysis, multi-omics techniques, and fragmentation spectra similarity in targeted analysis.[315] These advances would be critical in conducting statistics using larger datasets, identifying stabilization mechanisms and pathways, and in informing multi-omics approaches in SOM analysis.

Table 2.1. Table of common sources of error/bias during sample preparation and analysis for FTICR MS. Aspects to consider and recommendations are provided.

	Sources of Error/Bias	Considerations and Recommendations
Sample Collection and Preparation	○ Sample Uniformity	○ Ensure samples are well mixed when applicable; analyze pooled samples periodically throughout sample batches to monitor instrument stability and sensitivity.
	○ Contamination	○ Clean sampling equipment (e.g., combusted glass or medical grade polypropylene) prior to sampling
	○ Extraction Methods	○ Using *a priori* knowledge, prepare polar/non-polar/mineral-bound extracts separately to avoid biases in ionization.
		○ Extraction and storage conditions (e.g., pH, temperature, volume of extractant, extraction time) should be consistent across sample sets
	○ Extraction Conditions	○ Artifacts (e.g., byproducts formed during extraction or storage) can be introduced from harsh conditions, conditions should be noted in following spectra and visualizations.
		○ Solvent of choice should be compatible with FTICR MS.
Data Collection and Mass Spectrometry Acquisition Modes	○ Ionization Method Selection	○ Method and mode should target fraction selected during extraction. For bulk SOM, multiple modes provide the largest window into SOM composition.
	○ Sample matrix/instrument variability	○ Quality control strategies and samples (e.g., pooled quality control and standard samples run per analysis session)
		○ S/N should be carefully considered based on the calibration performed (e.g., not set arbitrarily)
Data Pre-processing and Formula Assignment	○ Molecular formula assignment pipeline	○ Heteroatoms included during assignment should be chosen based on *a priori* information.
		○ Exercise caution/manually assign and remove known artifacts (e.g., solvent clusters, extraction byproducts) and contaminants (e.g., surfactants, solvent contaminants) in data post-processing.
	○ Formula assignment quality	○ Assignments should be supervised with quality control strategies (e.g., error plots, continuity in calculated indices/heteroatoms)
Data Visualization	○ Data over-interpretation	○ Data visualization approaches will influence the outcome of the results (e.g., grouping by biomolecular class approximations)
		○ Methods using assigned formulas (e.g., VK diagrams, NOSC vs. C) only approximate features/origin; approximations need support from *a priori* information, experimental design, and complementary analyses.
		○ Formula assignment should not be assumed to represent bulk SOM; only a subset of SOM residues are measured.
		○ Not all indices are appropriate for use in statistical technique.

CHAPTER 3: IMPROVED DYNAMIC RANGE, RESOLVING POWER, AND SENSITIVITY ACHIEVABLE WITH FT-ICR MASS SPECTROMETRY AT 21 T REVEALS THE HIDDEN COMPLEXITY OF NATURAL ORGANIC MATTER[2]

3.1 Introduction

Fourier transform ion-cyclotron resonance mass spectrometry (FT-ICR MS) is the only mass analyzer that can resolve the molecular complexity of natural organic matter at the level of elemental composition assignment and has been applied to a wide range of natural systems (e.g., crude oil, petroleum, weathered oil, biofuels, permafrost, glacial thaw, emerging contaminants, food, and pyrogenic, dissolved, soil, and other natural organic matter).[16,19–25] However, experimental conditions including ionization source configuration, ion accumulation and transfer optics, detection cell geometry, excitation/detection parameters and magnetic field strength present challenges for comparison of complex organic mixtures composition assignment between FT-ICR mass analyzers worldwide.

Recently, Hawkes et. al led an interlaboratory comparison of Suwanee River Fulvic Acid (SRFA),[26] a reference standard produced by the International Humic Substances Society (IHSS), a polydisperse, polyfunctional mixture of organic acids derived from allochthonous plant organic matter (i.e., a mixture of degraded tannins, lignins, carbohydrates, and lipids).[27,112,316,317] SRFA has been widely used as an analytical reference standard in the molecular characterization of dissolved organic matter (DOM) by negative-ion electrospray ionization due to its high acid content, and thus, is one of the widely used standards in analytical method development for complex organic mixture analysis. Most mass spectrometry studies on SRFA couple negative-ion electrospray ionization (ESI)

[2] This chapter contains material that was reproduced with permission from Bahureksa, W.; Borch, T.; Young, R. B.; Weisbrod, C. R.; Blakney, G. T.; Mckenna, A. M. Improved Dynamic Range, Resolving Power, and Sensitivity Achievable with FT-ICR Mass Spectrometry at 21 T Reveals the Hidden Complexity of Natural Organic Matter. *Anal. Chem.* **2022**, *94* (32), 11382–11389. Copyright 2022, American Chemical Society.

to the mass analyzer, where ionization occurs through deprotonation reactions of acid groups.[227] Across ten commercial and custom-built FT-ICR mass analyzers in the study, compositional differences (e.g., H/C and O/C ratios) derived from the number and type of assigned elemental compositions ranged from ~2000 peaks to ~5000 peaks on magnets ranging from 7 T to 15 T, and highlighted disparity in all aspects of the mass analysis, including ion source configuration, ion accumulator/transfer hardware, ICR cell geometry, excitation/detection parameters, external/internal calibration equations, and data processing strategies and software. The resultant peak assignments varied in average oxidation state, saturation, and aromaticity by up to a total of ~15% for peaks common between the FT-ICR MS instruments with even larger differences when considering peaks unique to each instrument. This demonstrates the influence of numerous instrument parameters that limit the measurement of ions and the "true" representation of complex mixtures.

Often, studies compare the molecular signature of DOM from negative-ion ESI FT-ICR MS from a range of marine,[93,318] terrestrial,[90,319] lacustrine,[92,314] and arctic field samples to the IHSS SRFA standard as a control.[320] Stenson, et al. first applied FT-ICR MS at 9.4 tesla to SRFA in 2003, and assigned ~5000 elemental compositions.[227] Since 2003, numerous studies have characterized SRFA, including two interlaboratory comparisons to investigate the impact of various commercial and custom-built FT-ICR mass analyzers (Table 3.1).[26,321] Experimental conditions are crucial at every stage of the FT-ICR MS experiment, including ion source,[322] ion accumulator,[323] ion transfer optics and length,[323,324] rf transfer settings,[323] ICR cell geometry,[325,326] and excitation waveform,[198] in addition to magnetic field strength. Importantly, the type of FT-signal processing can significantly impact the mass spectral data quality, with absorption mode data resulting in ~30% improvement in resolving power compared to magnitude mode.[327,328] Mass accuracy improves significantly through application of an internal "walking" calibration, and results in sub-ppm mass measurement error across

thousands of elemental composition assignments.[189,329] All of the performance metrics of FT-ICR MS improve with higher magnetic field- mass resolving power and acquisition speed linearly, whereas mass accuracy, peak non-coalescence and dynamic range increase quadratically with field strength.[73,330,331] In addition, the higher the magnetic field, the less susceptible an FT-ICR mass analyzer is to ion number-induced frequency shifts (space charge effects)[332] that can impact subsequent peak identification and calibration.[189,333,334]

Table 3.1 Resolving power, dynamic range, and number of elemental compositions assigned in total and in each heteroatom class at each peak-picking threshold for Suwannee River Fulvic Acid (SRFA).

Peaks assigned	Magnet size (T)	Noise Threshold	Resolving Power (x 10^3)	Rrror Range (ppm)	m/z Experimental Range	Assigned Elements	DOI
5000	9.4	Unlisted	200 (at m/z 400)	Varies (<.5 - 1.6)	Unlisted	CHNO Na	10.1021/ac026106p
7547	9.4	>3	Unlisted	<1	Up to 1000	CHNOSP	10.1021/ac061949s
2123	9.4	>3	150 (at m/z 500)	<0.5	0-1000	CHO	10.1021/ac800464g
2551	7	>3, >5	400 (at m/z 400)	<1	150-1000	CHNOSP	10.1016/j.orggeochem.2011.11.007
1549	9.4	>6	750 (at m/z 500)	<1	200-1500	CHNOS	10.1016/j.orggeochem.2013.09.013
8158	21	>3	1,200 (at m/z 367)	<0.5	200-1000	CHNOPS	10.1007/s13361-016-1507-9
900	7	Unlisted	200 (unlisted m/z)	<0.2	200-650	CHON	10.1021/acs.est.6b05140
9000, 12000	9.4, 21	>6	2,700 (at m/z 400)	<0.5	200-1500	CHNOS	10.1021/acs.analchem.7b04159
3050	7	Unlisted	400 (at m/z 400)	<0.5	150-800	CHNOS	10.1002/rcm.8165
3300	9.4	>6	>260 (at m/z 400)	<0.2	200-800	CHNOS	10.1021/acsomega.0c01055
8000	12	>2	1,200 (at m/z 400)	<0.5	150-1000	CHNOS	10.1021/jasms.0c00138
2000 - 5000	9.4	>4	100 – 1,000 (at m/z 401)	~1	150-1000	CHNOS	10.1002/lom3.10364

Peak picking in mass spectrometry establishes the signal magnitude threshold for mass spectral peaks in a spectrum: peaks with signal magnitude above the threshold are considered for elemental composition assignment. Peak-picking at lower noise threshold results in higher peak counts but higher mass error due to peaks with lower S/N ratio, illustrating the trade-off between sensitivity and selectivity in the molecular assignment process. Typical ranges for peak picking thresholds for FT-ICR MS analysis of complex organic mixtures range from three to six times the

average baseline noise level (i.e., 3σ to 6σ).[26,227,335] The definition of limit of detection (LOD), has been defined by the following equation (IUPAC):[336]

$$x_{LOD} = x_{noise} + k\sigma_{noise}$$

Where k is a numerical factor chosen for the desired confidence level. If we consider k = 3 (3σ), peaks above this threshold are identified at the 99.6% confidence interval provided the noise is normally distributed (Gaussian). Practically, this means that for peaks identified at this threshold, 997 instances of 1000 replicate measurements will be true analytes and not random noise fluctuation. Selecting k > 3 limits sensitivity while only enhancing selectivity marginally, as shown by the analysis herein. Previous studies report ~2000 to 7500 elemental composition assignments at 3σ by 9.4 T FT-ICR MS in SRFA,[74,176] whereas comparison at 4σ identified ~2000 to 5000 assignments from ten FT-ICR mass analyzers (7 T to 15 T).[26] At higher noise thresholds from 9.4 T data, ~2500 assignments are reported at 5σ,[170,337] and ~1500 to 9000 at 6σ.[193,240] To date, the highest number of peaks reported on SRFA results from 6σ peak picking and yields ~13,000 elemental composition assignments at ~60 ppb RMS mass error with 21 T FT-ICR MS.[193]

Once resolved and peak-picked, the tens of thousands of mass spectral peaks in a single DOM sample must be internally calibrated to result in sub-ppm mass error for elemental composition assignment. Internal calibration on highly abundant homologous series within the sample itself result in the lowest mass error across a wide molecular weight range.[227,338] Internal calibration is based on the quadratic Ledford equation,[332] though other equations (e.g., linear, polynomial) and the "walking" calibration[189] have also been widely used. Current reports for mass measurement error range from ~25-50 ppb to 2-5 ppm for DOM species by FT-ICR MS.[21,26,90,176,193,321]

Elemental composition assignment software for complex organic mixture FT-ICR MS include open-source software (e.g., UltraMassExplorer,[339] Formularity[214]), open-source R, Python,

C++, or MATLAB molecular formula assignment tools (e.g., CoreMS,[340] CIA,[187] MFAssignR,[202] TRFu[203], ICBM-OCEAN[215]), and molecular formula assignment software (e.g., PetroOrg/EnviroOrg[201], Composer[341]). Each method involves the differentiation of elemental composition assignments based on Kendrick mass defect analysis,[342] elemental composition constraints, mass error, and isotope confirmation to increase reliability.

The custom-built, 21 T FT-ICR mass spectrometer at the NHMFL leads the world in complex mixture analysis, and routinely achieves resolving power in excess of 1,500,000 (at m/z 400), the lowest mass measurement error (10-50 ppb RMS error), and highest dynamic range of any mass analyzer,[18,193,343] fitted with automatic gain control (AGC) to minimize scan to scan variations in ion number,[344,345] and enables identification of species that differ in mass by roughly the mass of an electron.[18,193] The increase in dynamic range (ratio of highest to lowest peak) is critical to simultaneously detect low abundant species and high abundant species without distorting relative ion abundances.[330]

Here, we leverage the high dynamic range, resolving power, resistance to peak coalescence, and maximum number and trapping duration of trapped ions in a 21 T instrument for complex organic mixture analysis.[73] We compare the impact of peak picking threshold (3σ, 4σ, 5σ, and 6σ) on elemental composition assignments, mass measurement accuracy, mass resolving power, and dynamic range for the highest resolving power broadband FT-ICR mass spectrum collected to date on dissolved organic matter, a 6.3 second transient from m/z 200-1200. We identify ^{18}O and ^{17}O isotopologues for highly abundant oxygenated species in a broadband mass spectrum for first time, and report isobaric overlaps on the order of a few electrons that require mass resolving powers only achievable by 21 T FT-ICR MS. Furthermore, we increase mass resolving power by ~30% through absorption mode data processing, leveraging the high dynamic range to provide a molecular

catalogue of a widely utilized reference standard to the analytical community, and the highest performing mass analyzer for complex mixture analysis to date.

3.2 Materials and Methods

3.2.1 FT-ICR Mass Spectrometry of SRFA

Suwannee River Fulvic Acid (SRFA) standard obtained from the IHSS (https://humic-substances.org/the-third-batch-of-suwannee-river-humic-and-fulvic-acids/) was diluted in HPLC grade methanol (JT. Baker Scientific, San Jose, California) without any further modification prior to negative-ion ESI 21 tesla FT-ICR MS analysis.[27,112,316,317]

All solvents were HPLC grade (Sigma-Aldrich Chemical Co., St. Louis, MO) and extracts were ran without further modification by negative ion electrospray ionization. SRFA extracts were analyzed with a custom-built hybrid linear ion trap FT-ICR mass spectrometer equipped with a 21 T superconducting solenoid magnet.[193,343] Sample solution was infused via a microelectrospray source (50 μm i.d. fused silica emitter) at 500 nL/min by a syringe pump.[346] Typical conditions for negative ion formation were: emitter voltage, -2.4-2.9 kV; S-lens RF level: 45% ; and heated metal capillary temperature, 350 ° C. Ions were initially accumulated in an external multipole ion guide (1-5 ms) and released m/z-dependently by a decreasing auxiliary radio frequency potential between the multipole rods and the end-cap electrode. Ions were excited to m/z-dependent radius to maximize the dynamic range and number of observed mass spectral peaks (m/z 200-1500; 32-64%), and excitation and detection were performed on the same pair of electrodes. The dynamically harmonized ICR is operated with 6 V trapping potential. Time-domain transients of 3.1 seconds were acquired with the Predator data station, with 100 time-domain acquisitions averaged for all experiments, which were initiated by a TTL trigger from the commercial Thermo data station. Formulas containing carbon (C), hydrogen (H), oxygen (O), nitrogen (N), and sulfur (S) were assigned using experimentally

measured masses and were converted from the International Union of Pure and Applied Chemistry mass scale to the Kendrick mass scale[225] for rapid identification of homologous series for each heteroatom class (i.e., species with the same $C_cH_hN_nO_oS_s$ content, differing only be degree of alkylation).[338] For each elemental composition, $C_cH_hN_nO_oS_s$, the heteroatom class, type (number of rings plus double bonds to carbon, RDBE = $C - h/2 + n/2 + 1$)[347] and carbon number, c, were tabulated for subsequent generation of heteroatom class relative abundance distributions and graphical relative-abundance weighted images and van Krevelen diagrams. Peaks with signal magnitude greater than 3, 4, 5, and 6 times the baseline root-mean-square (rms) noise at m/z 500 were exported to peak lists, phase-corrected,[348] and internally calibrated on the basis of the "walking" calibration method.[189] Molecular formula assignments and data visualization were performed with PetroOrg © software.[201] Molecular formula assignments with an error >0.4 parts-per-million were discarded, and only heteroatom classes with a combined relative abundance of ≥0.15% of the total were considered.

Dynamic range was calculated by dividing the max peak hieght by the minimum peak height of the most and least abundant peaks assigned, respectively. Resolving power was calculated by averaging the $m/m_{50\%}$ for peaks between m/z 395 – 405. Isobaric overlaps were identified by calculating mass differences among all assigned formulas, and then sorting and filtering them for differences less than $\Delta m/z$ 0.03638. Assignments corresponding to mass differences below $\Delta m/z$ 0.03638 were tabulated and checked to ensure atoms in each overlap were consistent, then experimental averages and standard deviations were calculated for each overlap. The atoms indicated by each overlap were used to calculate the theoretical $\Delta m/z$ and used to compare with the experimental values (Table B.1). Absorption-mode FT-ICR mass spectra files and assigned elemental compositions are publicly available via the Open Science Framework at https://osf.io/zgx3y/ (DOI 10.17605/OSF.IO/ZGX3Y).

3.3 Results and discussion

3.3.1 Resolving Power > 2,000,000 and High Dynamic Range at 21T Identifies New Isobaric Species

Figure 3.1 shows a broadband negative-ion electrospray ionization of SRFA collected on a custom-built 21T FT-ICR mass spectrometer that spans from 200 < *m/z* < 1200, centered at *m/z* 540.[193,335,343] More than 560 scans were signal averaged over a 6.3s acquisition period with signal lasting the entire acquisition period, with achieved resolving power of $m/\Delta m_{50\%}$ (in which $\Delta m_{50\%}$ = mass spectral peak width at half maximum peak height) of 2,250,000 at *m/z* 542. The mass spectral complexity is highlighted in the mass-scale expanded zoom inset of 0.3 Da (542.0 < *m/z* < 542.3).

Figure 3.1 also highlights the improved dynamic range of the 21 T, demonstrated with a mass-scale zoom inset at *m/z* 542 (top right) with peak-picking thresholds annotated at 3σ (red) and 6σ (blue). Peak-picking at three times the baseline noise level (3σ) exports lower abundance peaks to a peak list where isobaric species differ in mass by Δ*m/z* 0.000430 ($[C_{47}H_{32}O_{29}{}^{13}C_2\text{-}H]^{-2}$ and $[C_{24}H_{18}O_{12}S_1{}^{13}C\text{-}H]^{-}$) (top, green arrows)[193] at sub 10 ppb mass error. Furthermore, isobaric species with the same nominal mass (59 Da) that differ in exact mass by 600 μDa (roughly the mass of an electron, 548 μDa), differ in elemental composition by $C_2H_3S_1$ and $N_1O_2{}^{13}C$ are baseline resolved with mass error of +/-100 ppb. A shift in experimental mass difference is likely caused by an unresolved peak or shoulder at high frequency on *m/z* 542.05580.

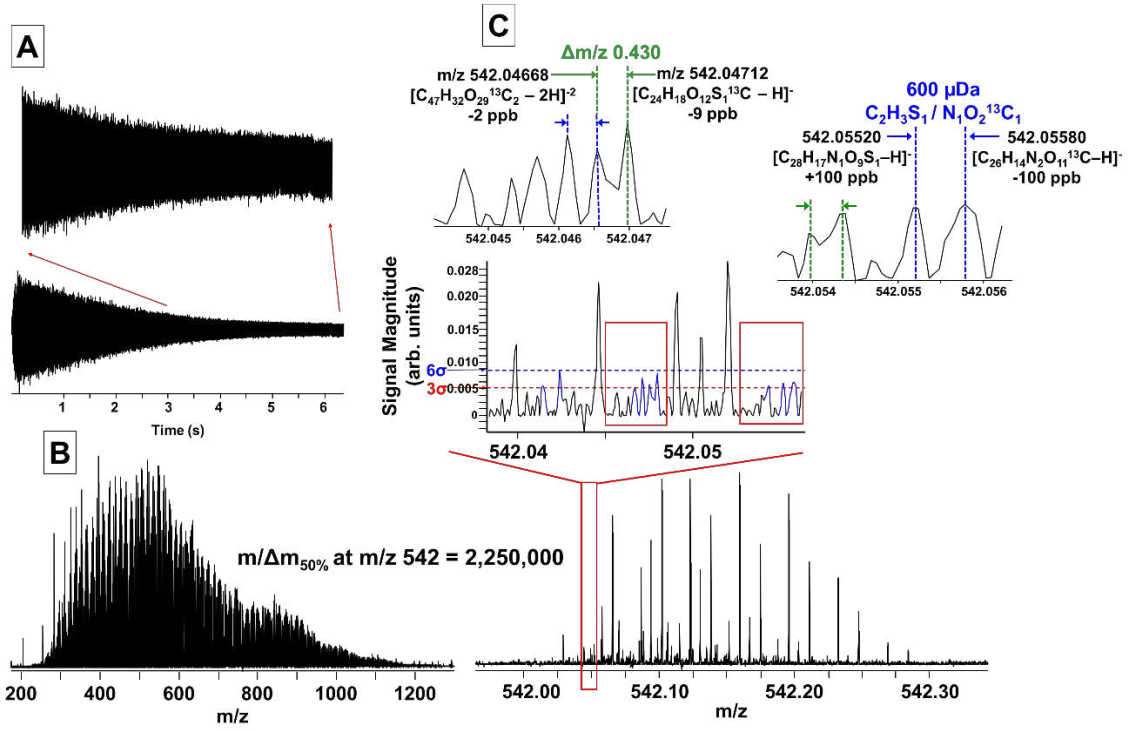

Figure 3.1 Negative-ion ESI 21 tesla FT-ICR mass spectrum of the Suwannee River Fulvic Acid (SRFA) standard with insets depicting mass spectral complexity, resolving power, and dynamic range. (A) Transient signal averaged over 560 scans and a 6.3s acquisition window with a zoomed inset. (B) broadband FT-ICR mass spectrum between m/z 200 – 1200, centered at m/z 542. (C) 300 mDa mass scale-expanded segment from m/z 542.0 – 542.3, with achieved resolving power, $m/\Delta m_{50\%}$ ($\Delta m_{50\%}$ = the full mass spectral peak width at half-maximum peak height) of 2,250,000 at m/z 542.[73] A mass scale-expanded zoom with cutoffs indicated between 3σ (red) and 6σ (blue) is demonstrated within this segment for peaks considered as mass spectral peaks (as opposed to noise). Portions of the spectrum are expanded further in insets for peaks identified in the 3σ between m/z 542.046 – 542.048 and 542.054 – 542.056.

Table 3.2 shows the resolving power (i.e., $m/m_{50\%}$ averaged from peaks between m/z 395 – 405), dynamic range (i.e., the max peak height divided by the minimum peak height of the most and least abundant assigned peaks, respectively), and number of peaks assigned elemental compositions in total and by heteroatom class from the SRFA spectrum at each peak-picking threshold. To date, this mass spectrum represents the highest achieved resolving power for direct infusion mass spectrometry of dissolved organic matter, with achieved resolving power of ~3,000,000 at m/z 400 at each peak-picking threshold. The dynamic range decreases by nearly a factor of 2 between the 3σ and 6σ thresholds (374.2 to 191.7) and impacted the number of formulas assigned: the total number of assignments within the spectrum decreased from 36109 at the 3σ threshold to 23641 at the 6σ

threshold, and disproportionately affected different heteroatom classes. The CHNO assignments decreased by ~45% from the 3σ to the 6σ (from 8776 to 4850), and CHOS assignments decreased by ~63% (from 3840 to 1434). In comparison, the CHO assignments decreased only ~25% at 6σ (from 23097 to 17353). Heteroatom classes with multiple, non-oxygen heteroatoms were even further diminished, where CHNOS assignments decreased by ~99% (396 to 4). This decrease is also apparent in assignments containing multiple nitrogen, seen in Figure B.1.

Table 3.2 Resolving power, dynamic range, and number of elemental compositions assigned in total and in each heteroatom class at each peak-picking threshold for Suwannee River Fulvic Acid (SRFA).

	Resolving Power ($m/\Delta m_{50\%}$) at m/z 400	Dynamic Range	Total	CHO (w/ isotopes and Na adducts)	CHNO (w/ isotopes)	CHOS (w/ isotopes)	CHNOS
3σ	2960218	374.2	36109	23097	8776	3840	396
4σ	2973674	275.6	32855	22736	7425	2541	153
5σ	2993832	238.0	29816	21286	6227	2244	59
6σ	3019947	191.7	23641	17353	4850	1434	4

3.3.2 Resolution and Identification of ^{18}O and ^{17}O isotopologues in Broadband SRFA 21T FT-ICR MS

The high dynamic range, sub-ppm mass error, and > 2,000,000 resolving power of the 21 T enable the first resolution, identification, and isotopic confirmation of oxygen isotopologues in dissolved organic matter. Figure 3.2 shows a zoom inset at m/z 505.09878 that corresponds to the monoisotopic oxygen species $[C_{23}H_{22}O_{13}\text{-}H]^-$. The theoretical mass difference between ^{16}O (natural abundance 99.75%) and ^{17}O (0.038%) is +1.00421 Da and ^{16}O and ^{18}O (0.2%) is +2.00424 Da, and both ^{18}O and ^{17}O isotopologues are detected and assigned. Careful examination of the ^{17}O isotopologues reveals a 0.87 mDa mass difference sufficiently resolved ($m/\Delta m_{50\%}$=2,600,000-2,800,000) between the ^{13}C isotopologue $[C_{22}H_{22}O_{13}{}^{13}C\text{-}H]^-$ (S/N 172, 40 ppb) and ^{17}O $[C_{23}H_{22}O_{12}{}^{17}O\text{-}H]^-$ (S/N 3, 60 ppb).

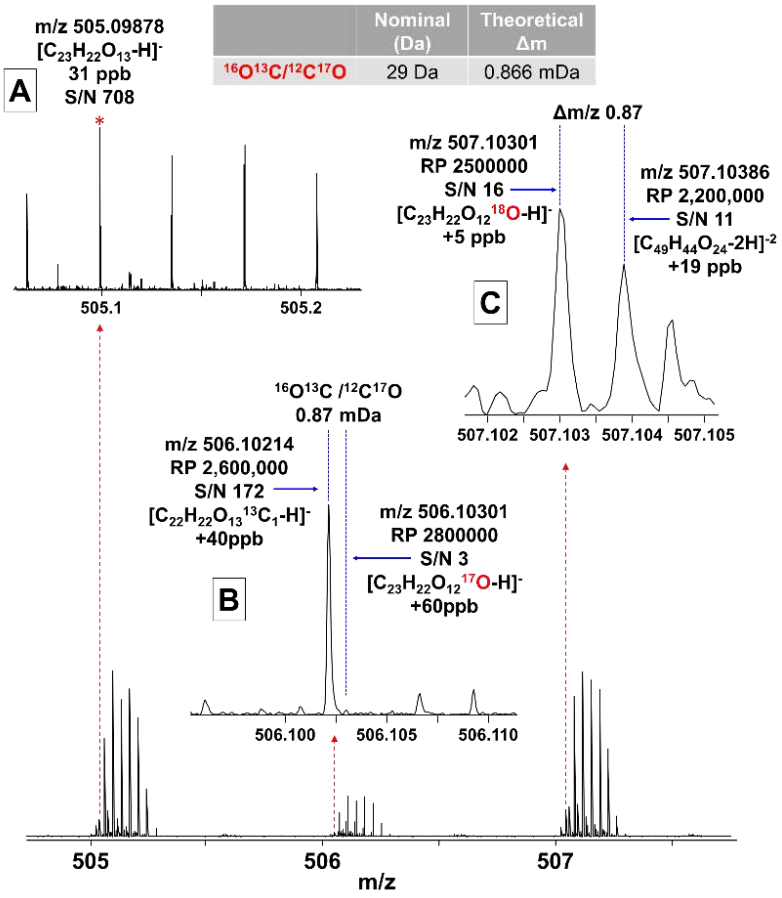

Figure 3.2 Mass-scale expanded inset (bottom) for 505 < *m/z* < 507 from broadband 21 tesla negative-ion ESI FT-ICR mass spectrum of a Suwannee River Fulvic Acid Standard to highlight the resolution and identification of oxygen isotopes that can be confirmed by resolution and detection of ^{13}C, ^{17}O, and ^{18}O isotopologues at sub-ppb mass error. (A) The assignment of the monoisotopic species $[C_{23}H_{22}O_{13}\text{-}H]^-$ at *m/z* 505.09878 and signal-to-noise ratio (S/N) of 708. (B) Assignment of $[C_{22}H_{22}O_{13}{}^{13}C_1\text{-}H]^-$ and $[C_{23}H_{22}O_{12}{}^{17}O\text{-}H]^-$ isotopologues, at a S/N of 172 and 3 respectively, where identification of ^{17}O species for the first time required resolving power > 2,600,000 to resolve isobaric species that differ in elemental composition by $^{12}C^{17}O$ versus $^{16}O^{13}C$, with an experimental mass difference of 0.87 mDa. The theoretical mass difference for $^{12}C^{17}O$ and $^{16}O^{13}C$ is 0.866 mDa. (C) Assignment of the $[C_{23}H_{22}O_{12}{}^{18}O\text{-}H]^-$ isotopologue at a S/N of 16 that is resolved from $[C_{49}H_{44}O_{24}\text{-}2H]^{-2}$ at a S/N of 11.

3.3.3 Peak-picking Influences Isobaric Species Identification

Figure 3.3 shows the number of isobaric overlaps detected from elemental compositions assigned at 3σ, 4σ, 5σ and 6σ from SRFA. Three overlaps are highlighted: $NO_2{}^{13}C/C_2H_3S$ (59 Da nominal mass and differing in theoretical exact mass by 0.71 mDa); $H_2O_3{}^{13}C_2/C_4N_2$ (76 Da nominal mass and differing in theoretical exact mass by 0.96 mDa); and $C_2N_2/H_2O_2{}^{18}O$ (52 Da nominal mass and differing in theoretical exact mass by 1.51 mDa). Each image plots the number of overlaps in

assigned peaks versus the experimental observed mass difference between m/z for isobaric species. The dashed line shows the theoretical mass difference, calculated from the atomic weights. A complete list of all identified isobaric overlaps below a mass difference of m/z 0.03638 can be found in **Table B.1**. The newly identified isobaric overlaps included thousands of assignments that differed by mass on the order of 1-2 electrons (M_{e^-} = 548 μDa),[349] resolved for the first time in SRFA at each peak-picking threshold. For instance, the $NO_2{}^{13}C/C_2H_3S$ overlap was identified most above 3σ (1076 counts), followed by 4σ (882 counts), 5σ (704 counts), and 6σ (506 counts). Interestingly, newly identified isobaric overlaps that included non-oxygen heteroatoms and ^{13}C or ^{18}O isotopes were the most influenced by the peak-picking threshold. This can also be seen in Figure 3.4, where nitrogen- and sulfur-containing overlaps were at a maximum at 3σ and minimum at 6σ. In comparison, the CHO-containing overlaps increased from the 3σ to a maximum at 4σ, and then reached a minimum at 6σ. This is due to the inclusion or exclusion of low abundance heteroatom or isotope-containing assignments that plot between CHO-containing overlaps.

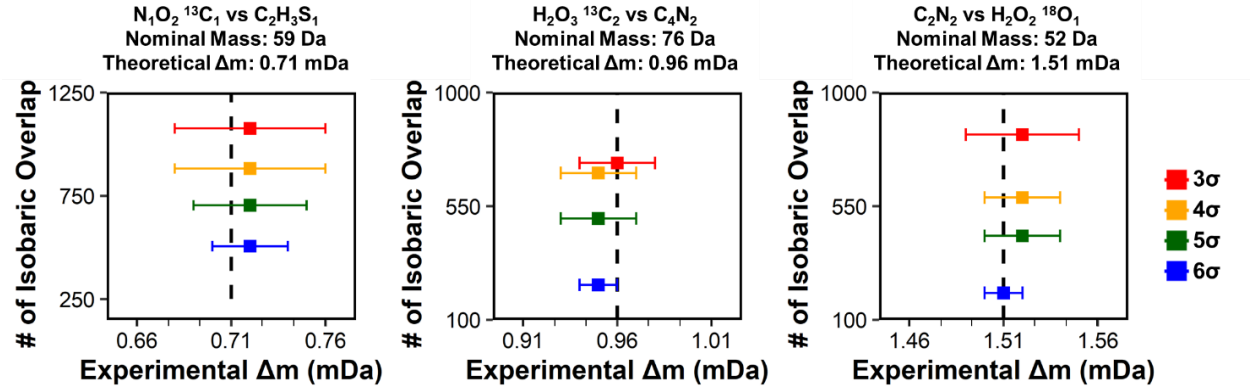

Figure 3.3 Selection of isobaric overlaps identified and counted in each sample, where points are colored by peak-picking threshold. Points correspond to the average mass difference and lines to the associated standard deviation for the counted experimental overlaps. The theoretical mass difference is indicated by the dotted center line in each plot. Each x-axis spans ± 0.0001 Da. For a complete list of isobaric overlaps below a mass difference of m/z 0.03638, see Table B.1.

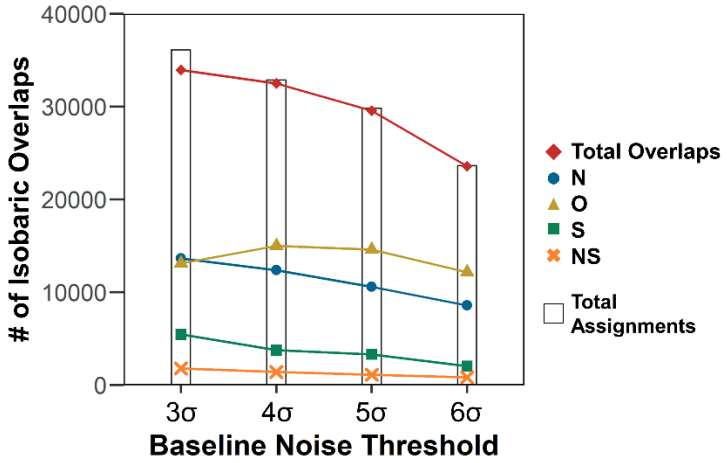

Figure 3.4 Number of isobaric overlaps at each peak-picking threshold in total and separated by the heteroatoms involved in the overlap. Outlined bars indicate the total number of assignments at each peak-picking threshold.

3.3.4 Resolving Power > 2,000,000 Resolves Isobaric Overlaps

Figure 3.5 displays the counts of each isobaric overlap at 3σ from Figure 3.4, separated by m/z bins every m/z 100 (e.g., m/z 300 – 400, m/z 400 – 500). Plots of the isobaric overlaps binned by m/z at 4σ, 5σ, and 6σ can be seen in Figure B.2 and follow a similar distribution. For instance, with the 0.71 mDa isobaric overlap, the minimum counts were on the low ($300 < m/z < 400$) and high ($900 < m/z < 1000$) molecular weight range with 31 (low) and 32 (high) counts. The maximum count occurred in the center of the molecular weight distribution ($500 < m/z < 600$) with 328 counts. This highlights the achieved resolving power at higher m/z that can resolve and identify species that differ in mass on the order of an electron out to ~900-1000 Da. The identification of these species also occurred at high m/z at 5σ and 6σ, but at lower counts. This has been directly compared recently with the m/z 0.000430 mass difference visualized in Figure 3.1, which could not be resolved at m/z ~600 in SRFA on a 9.4 T FT-ICR MS.[193] Isobaric overlaps were identified throughout this study and are well resolved even up to m/z 1000.

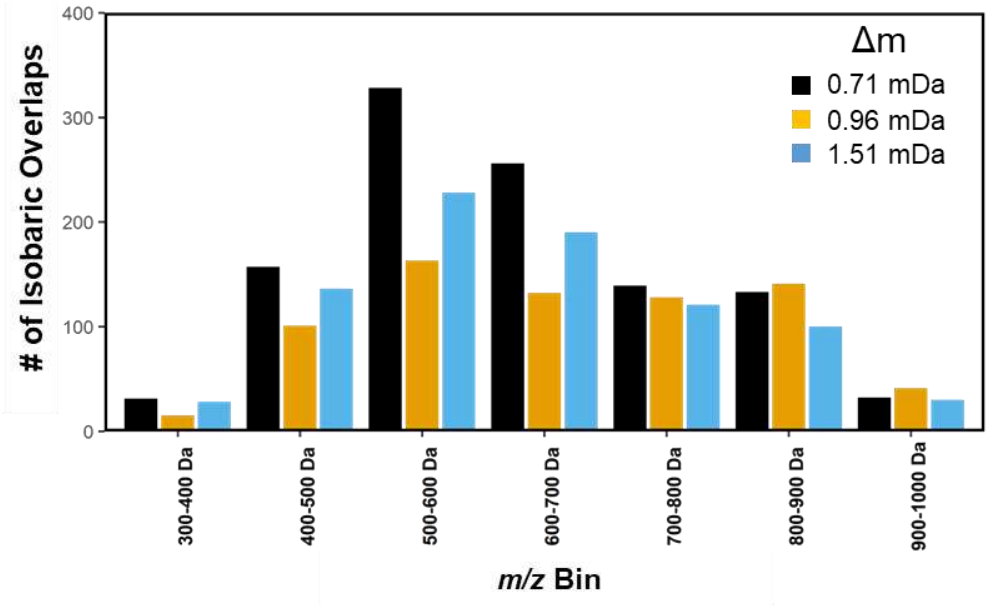

Figure 3.5 Number of isobaric overlaps in SRFA peak-picked at 3σ identified in Figure 3.4 and binned by every m/z 100, up to m/z 1000. Bars are colored by theoretical isobaric overlap that each count was associated with. For the 4σ, 5σ, and 6σ bar plots of the selected isobaric overlaps, see Figure B.2.

3.3.5 Elemental Composition Assignments and RMS Mass Error

The mass measurement error as a function of molecular weight for assignments derived from 3σ, 4σ, 5σ and 6σ is shown in Figure 3.6. At 6σ, more than 23,000 species are assigned with 25 ppb RMS error, whereas 3σ results in a 52% increase in the number of assignments (36,000) with 36 ppb RMS error. This slight increase of 11 ppb in RMS error can be accounted for in the assignment of more species with lower S/N in 3σ. Table 3.3 compiles the number of assignments at each % relative abundance and RMS error for all four datasets. Specifically, ~10,000 more assignments with signal magnitude lower than 25% total relative abundance at 3σ are assigned that have lower S/N and higher mass error (31 ppb) compared to 6σ. Therefore, changes to RMS_{error} can be attributed primarily to the bottom 25% abundance quartile, which includes nitrogen and sulfur species (Table 1). Importantly, even with 21 T FT-ICR MS, lower abundance species can be assigned at 3σ with ~20-40 ppb RMS error and increases compositional information by ~50%.

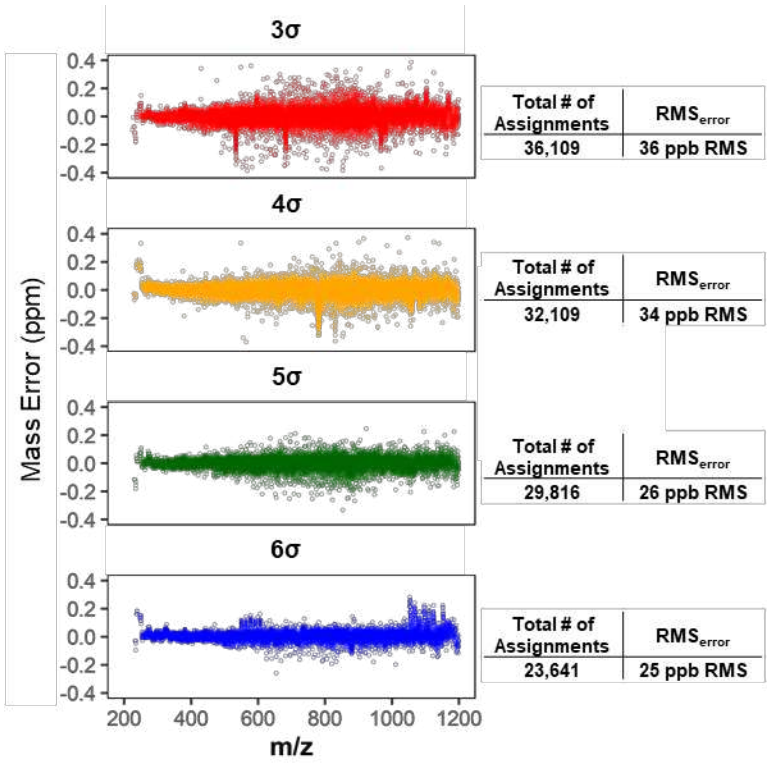

Figure 3.6 Elemental compositions assigned in each of the SRFA samples plotted by mass error versus m/z. RMS_{error} and total number of assignments derived from 3σ, 4σ, 5σ, and 6σ datasets are also tabulated. For assigned peaks by quartile, see Table 3.3.

Table 3.3 Assignments separated by % relative abundance reported with the associated average mass error and total number of assignments with RMS mass error for each peak-picking threshold for SRFA.

	3 S/N		4 S/N		5 S/N		6 S/N	
% R.A.	# assignments	Mass error (ppb)	# assignments	Mass error (ppb)	# assignments	Mass error (ppb)	# assignments	Mass error (ppb)
> 75%	633	12	621	8	608	9	576	9
75-50%	1730	12	1674	10	1620	9	1483	11
25-50%	5179	12	4870	12	4596	10	3873	11
< 25 %	28,567	31	25,690	27	22,992	22	17,609	20
Total	**36,109**	**36 ppb RMS**	**32,109**	**34 ppb RMS**	**29,816**	**26 ppb RMS**	**23,641**	**25 ppb RMS**

3.3.6 Detection at 3σ Extends Compositional Coverage

The increase in detected species impacts the number and compositional coverage of assigned peaks of features based on stoichiometry. This includes van Krevelen diagrams that plot atomic

H/C versus O/C ratio to approximate oxidation state, compositional information to biomolecular precursors,[239,240] and hydrogen deficiency (e.g., DBE, double bond equivalents, number of rings plus double bonds to carbon, DBE = $C - h/2 + n/2 + 1$,[350] or aromaticity index, AI) to approximate biolability.[224]

Figure 3.7A shows H/C versus O/C for neutral species unique to the 3σ when compared to the 6σ. Points are colored by AI: non-aromatic (black, AI ≤ 0.5), aromatic (gold, 0.67 > AI > 0.5), and condensed aromatic (red, AI ≥ 0.67). A total of 12,937 assignments were unique to the 3σ dataset, with 12,933 (99.9%) peaks belonging to the < 25% relative abundance quartile. Species assigned only at 3σ encompass a large compositional space with limits of H/C: ~0.4 – 1.5 and O/C: ~0.2 – 0.8. Figure 3.7B shows the number of unique assignments in the 3σ as a function of DBE. Assignments unique to the 3σ range from 3 to 36 DBE, which highlights the large range of aromaticity only available at 3σ.

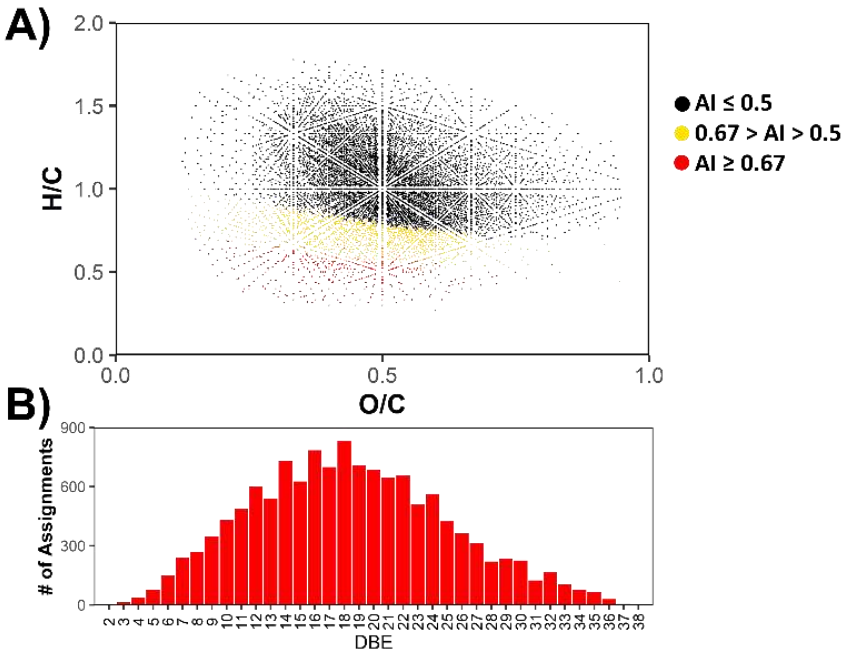

Figure 3.7 Assignments unique to the 3σ plotted by atomic ratios in a van Krevelen diagram and by DBE. A) H/C versus O/C ratios of the assigned molecular formulae in a van Krevelen diagram, where assignments are colored by aromaticity index: non-aromatic (black, AI ≤ 0.5), aromatic (gold, 0.67 > AI > 0.5), and condensed aromatic (red, AI ≥ 0.67). B) number of unique assignments to the 3σ binned by rings-plus-double-bond-equivalents (DBE).

3.4 Conclusions

The SRFA spectrum highlighted here represents a unique experiment in which the highest resolving power, mass measurement accuracy, and dynamic range ever observed for this highly utilized reference material was achieved. Assignment of ^{18}O and ^{17}O isotopologues was enabled by lowering the peak picking threshold and thousands of isobaric overlaps were identified that differed in mass on the order of 1 – 2 electrons. Enhanced sensitivity with respect to peak detection and molecular formula assignment is achieved by lowering the peak detection threshold to 3σ. Lowering the peak detection threshold to 3σ does not appreciably affect selectivity of the measurement in terms of accumulation of false assignments or unidentified peaks ("no-hits"). In fact, setting a more stringent peak picking threshold (>3σ) arbitrarily limits the depth of compositional assignment, effectively leaving high confidence peaks out of the assignment process. Therefore, we recommend using a 3σ peak picking threshold to access a wider suite of species as any calculations based on elemental compositions (e.g., oxidation state, DBE, AI) will more accurately represent the bulk NOM with inclusion of lower abundance species not detected by other mass analyzers and provide a more accurate "true" representation of complex mixtures using FT-ICR MS. These data are provided via the Open Science Framework as reference data for the scientific community for use in their research.

CHAPTER 4: NITROGEN ENRICHMENT DURING SOIL ORGANIC MATTER BURNING AND MOLECULAR EVIDENCE OF MAILLARD REACTIONS[3]

4.1 Introduction

The 2020 wildfire season was the worst wildfire season to date for many regions around the world, including the western United States which burned approximately 10 million acres,[351,352] and Australia which was devasted with over 40 million acres burned.[353] Wildfires are predicted to increase globally,[34,354–356] threatening forested watersheds responsible for supplying drinking water[357–359] to 180 million people in the western United States[29] and many more abroad.[30–32] Alteration of the soil organic matter (SOM) present will adversely affect both water quality downstream and soil properties for years after the fire has subsided.[46,358,360–364] Therefore, understanding how wildfires alter SOM composition following fires is of great interest.

The extent of thermal transformation and loss of SOM, known as burn severity, is commonly assessed by comparing bulk pre-fire SOM, vegetation, and soil properties to post-fire features, including soil microbial communities.[365] Importantly, recovery and revegetation depend on the presence of labile, water-soluble nutrients, such as nitrogen.[366] Nitrogen is a limiting reactant for soil microbial productivity,[367] and soil carbon-to-nitrogen ratios (C/N) inversely correlate to SOM reactivity during microbial metabolism.[368,369] Above 200°C, wildfires can volatilize, transform, and mobilize organic nitrogen,[370] which then leaches from the organic soil layer as water passes through the soil as dissolved organic nitrogen (DON).[53,371] Charred particulate and water-soluble organic matter will be transported downstream from fire-affected watersheds,[372] negatively impacting water quality and even producing toxic effects.[373] Furthermore, the increased formation of toxic nitrogen-

[3] This chapter contains material that was reproduced with permission from (1) Bahureksa, W.; Young, R. B.; McKenna, A. M.; Chen, H.; Thorn, K. A.; Rosario-Ortiz, F. L.; Borch, T. Nitrogen Enrichment during Soil Organic Matter Burning and Molecular Evidence of Maillard Reactions. *Environ. Sci. Technol.* **2022**. Copyright 2022, American Chemical Society.

containing disinfection byproducts (DBPs) has been observed during drinking water treatment downstream of burned areas.[39–41] Therefore, the molecular composition of charred, water-soluble nitrogen species formed during wildfires is of great interest for the recovery of fire-affected watersheds and water quality studies.

Several reviews summarize effects of fire intensity on SOM quantity and quality under both laboratory and field conditions, defining fire intensity as a "specific heating temperature over a fixed interval of time below the soil surface".[37] In brief, heating between 200-250°C results in transformation of biomolecules with concurrent formation of aliphatic, alcohol, carbonyl, and aromatic functionalities, reported by nuclear magnetic resonance (NMR) spectroscopy.[13,14,38,374,375] Carbonization towards more graphitic structures has been observed around 300°C, followed by the near total consumption of SOM and formation of highly condensed aromatic material, often discussed as "dissolved black carbon" when referring to the water-soluble fraction.[13,43,44] Recent models suggest that thermally-altered SOM species contain considerable substitution of aromatic rings with nitrogen (including "dissolved black nitrogen"),[376] oxygen, and sulfur species.[377]

Targeted methods have also been applied to study specific constituents that comprise fire-affected SOM. Residues released by biomolecular components and known pyrolysis products of biomolecules, known as biomass burning markers,[45] have been previously studied using pyrolysis[363,378–382] and derivatization[383–385] prior to gas chromatography mass spectrometry (GCMS), and liquid chromatography mass spectrometry (LCMS)[386,387] on fire-affected organic matter. The precise identity of many charred residues remains elusive, including nitrogen-containing heterocyclic residues (e.g., pyridines, pyrazines, and pyrrole structures). These residues can resemble melanoidins[376,388,389] which typically form through a cascade of reactions associated with the heating of polysaccharides and proteins, referred to as the Maillard reaction pathway.[390] Melanoidin and intermediate Maillard reaction products (MRPs) are frequently discussed as a pathway for both

carbon and nitrogen sequestration following heating in soils,[13,391–394] and may therefore describe nutrient sources in post-wildfire ecosystems.[395,396] Direct measurement of this pathway has not yet been conducted in charred SOM and would require ultrahigh resolution to probe changes to individual residues associated with transformation of SOM.

Fourier transform ion cyclotron resonance mass spectrometry (FTICR MS) routinely achieves the ultrahigh mass resolving power sufficient to separate and accurately assign elemental compositions to ionized components of highly complex mixtures.[16,99,229,251,313] This includes SOM and dissolved organic matter (DOM),[21,87,397–404,92,133,135,143,176,230,247,306] solid and water-soluble char residues,[181,226,320,394,405–409] and petroleum,[20,173,199,277,410,411] where the m/z differences can be as small as the mass of an electron.[73] The characterization of both field[181,394] and laboratory[181,405] produced char have provided insight on molecular level changes to different organic matter substrates induced by heating, however limited information connects compositional changes in charring SOM to changes throughout progressive fire intensity gradients and the enhanced mobility of water-soluble organic nitrogen following a fire.

The soil samples selected for this study originate from Boulder County, CO, USA to simulate SOM from forested watersheds, similar to those affected by the High Park fire in 2012 and Cameron Peak fire in 2020 (northern Colorado).[412] While dissolved organic matter does exhibit unique characteristics that can be used to distinguish different sources,[21] many of its features are remarkably consistent.[413] Dissolved pyrogenic organic matter also has common characteristics that can be observed at numerous sites and locations.[43,320,414] Therefore, these samples were considered representative of soil from similar sites in the western United States and Canada, where forest fires and their effects on ecosystems and watersheds currently generate tremendous interest and concern. Organic carbon quantification[415,416] and solid-state ^{13}C NMR[416] have been previously reported for these samples. Additionally, benzene polycarboxylic acids (BPCAs) and pyridinic analogs were

identified by quadrupole time-of-flight mass spectrometry (QTOF MS) as biomass burning markers (>150°C).[416] These findings only address a fraction of the molecules present during heating, suggesting that ultrahigh-resolution mass spectrometry is required to develop a more complete picture of the compositional changes that occur during heating.

Here, we present a compositional comparison of water-extractable, acidic SOM species produced at discrete temperatures (i.e., 150°C, 250°C, 350°C, 450°C) by negative ESI FT-ICR MS. This study focuses on nitrogen-containing residues due to their enrichment during previous analysis[415] of the samples studied here and importance in ecosystem recovery following fires. We compare and catalogue molecular transformations of nitrogen species in heated SOM at discrete temperatures by FT-ICR MS. Mass difference-based analysis is performed to identify potential reaction products formed during heating and suggest potential pathways in heated SOM as a function of temperature.

4.2 Materials and Methods

4.2.1 Site Description and Sample Processing

Soil samples were collected south of Gross Reservoir in Boulder County at 2,222 m above sea level during the summer of 2016 and correspond to Site H samples in Thurman et al.[416] In brief, triplicate soil samples were collected within 10 m of each other in 1 m^2 transects with a shovel at a depth of 1 - 5 cm after visible litter and vegetation debris were removed. The surrounding overhead vegetation was composed of four main coniferous tree species: ponderosa pine (*Pinus ponderosa*), lodgepole pine (*Pinus contorta*), limber pine (*Pinus flexilis*), and Douglas-fir (*Pseudotsuga menziesii*) varying in density. Understory vegetation for the sampling area included a mix of grasses, forbs, and shrubs; largely dominated by cheatgrass (*Bromus spp.*) and Canada thistle (*Cirsium arvense*). Following sampling, soils were distributed on metal trays 1 cm deep and oven-dried at 100°C for two hours to

eliminate moisture and to suppress the survival of microbial communities present in the soil[417] that may compromise sample integrity during storage. The soil was passed through a 2 mm (No. 10) stainless steel sieve to remove large rocks and through a 0.841mm (No. 20) sieve to remove smaller plant matter before storage.

4.2.2 Simulated Laboratory Heating and Leachate Preparation

Soils were heated in an electric muffle furnace to temperatures of 150ºC, 250ºC, 350ºC, and 450ºC in 90 mL porcelain dish crucibles using a Lindberg/Blue Box Furnace Model BF51442C with a Lindberg Furnace Power Supply Controller Model 59344. To ensure uniformity in soil heating, each soil sample was separated into 10 g per crucible (approximately 0.5 cm high) and heated in batches of 10 crucibles for a total of 100 g soil sample at each temperature. Batches were held at each temperature under atmospheric conditions for 2 hours and cooled to room temperature, then stored in 40 mL amber glass vials at -5 ºC until used. The furnaced samples were then leached for 24 hours in deionized water at 5g soil per liter. Leachates were decanted and filtered using a 0.45 μm glass fiber syringe filter. A portion of the leachates were freeze-dried and used in organic carbon and nitrogen analysis on the solid soil and leachates and is described elsewhere.[416] Additional information on this method to simulate the effects of a wildfire can be found in Appendix C.

Aqueous leachates were fractionated according to Aiken et al.[418] into hydrophobic (XAD-8) and hydrophilic (XAD-4) fractions to facilitate better separation and identification of SOM features and their properties.[16,53] These resins are no longer commercially available, however Supelite DAX resins are suitable substitutes that contain a similar chemistry and porosity.[419,420] In brief, freeze-dried soil leachates were resolubilized in 1 L water and passed through a two-column array using hydrophobic and hydrophilic resins in sequence at a ratio of 2L/200 mL column volume. Both resins retain organic acids containing carboxylic acid, amide, aromatic, phenolic, O-alkyl, and C-alkyl functional groups, with the hydrophilic fraction separating higher concentrations of nitrogen,

carboxylic acid, and O-alkyl carbon but lower aromatic carbon than the hydrophobic fraction.[418] The resins were eluted using 0.1 N NaOH (Certified ACS grade, Fischer Chemical, Pittsburgh, PA) and immediately cation exchanged using an AG MP-50 cation exchange resin to remove Na that was introduced.[418] Alkali solutions can alter organic matter (e.g. by base-catalyzed hydrolysis, oxidation to CO_2 under oxygenated atmospheres); however, a review of studies has indicated that the 0.1 N NaOH used during the XAD elution followed by cation exchange does not appear to alter the sample meaningfully.[112] Samples were then freeze dried and stored. Solid-state ^{13}C NMR of leachate samples are described elsewhere.[416]

4.2.3 FT-ICR MS Analysis

Resin extracts were resolubilized in methanol (HPLC grade, Sigma Aldrich Chemical Co., St. Louis, MO) at 50 ppm carbon concentrations prior to analysis. Each sample solution was infused via a microelectrospray ionization (ESI) source operated in negative mode.[346] DOM extracts were analyzed with a custom-built 9.4 T FT-ICR mass spectrometer and absorption mode mass spectra calibrated and assigned as previously described.[189,421] For a full description of the FTICR MS operating conditions and data processing procedure, see Appendix C. Formulas containing carbon (C), hydrogen (H), oxygen (O), nitrogen (N), and sulfur (S) were assigned using the experimentally measured masses and converted from the International Union of Pure and Applied Chemistry mass scale to the Kendrick mass scale[225] for rapid identification of homologous series for each heteroatom class (i.e., KMD_{CH2} for species differing only be degree of alkylation)[338] using PetroOrg© software.[16,201,213,347] Molecular formula assignments with an error >0.5 parts-per-million were discarded, and only heteroatom ($N_xO_yS_z$) classes with a combined relative abundance of ≥0.15% of the total were considered. Formulas were used to calculate rings-plus-double-bonds (to carbon) equivalents ($RDBE = 1 + c - h/2 + n/2$)[213,347] where c, h, n, o, and s refer to the stoichiometric carbon, hydrogen, oxygen, nitrogen, and sulfur, respectively. Formulas were also used to calculate

modified aromaticity indices (AI_{Mod},)[216,422], which estimate the density of unsaturated carbon after assuming that a portion of the RDBE is not attributable to carbon-carbon bonds (e.g., carbonyl or carboxyl functional groups).

4.3 Results and Discussion

4.3.1 Bulk Heating Effects on Organic Carbon and Nitrogen

Organic carbon and nitrogen content was previously reported for these samples[415,416] and will be used here to support compositional analysis by FT-ICR MS. Table 4.1 shows the total organic carbon (TOC), total organic nitrogen (TON), water-extractable organic carbon (WEOC), water-extractable organic nitrogen (WEON), and inorganic nitrogen measurements collected on each of the heated samples and control (CTRL). The TOC and TON decreased continuously from the control (46.303 ± 0.000 mg TOC/g soil, 2.179 ± 0.004 mg TON/g soil) to 450°C (1.435 ± 0.001 mg TOC/g soil, 0.315 ± 0.000 mg TON/g soil) with increased rates of removal at temperatures >150°C. The WEOC and WEON changed from the control (0.485 ± 0.004 mg WEOC/g soil, 0.032 ± 0.004 mg WEON/g soil) during heating, reaching a maximum at 250°C (2.247 ± 0.036 mg WEOC/g soil, 0.211 ± 0.002 mg WEON/g soil) and minimum at 450°C (0.065 ± 0.002 mg WEOC/g soil, 0.008 ± 0.002 mg WEON/g soil). The difference in magnitude of the water-extractable fraction and total SOM content suggests that most of the SOM was mineralized during heating and thus, did not partition into water at any temperature.

Table 4.1. Organic carbon and nitrogen analysis performed on bulk soil and soil leachate samples after leaching 5 g of soil into 1 L water. Average and standard deviations are reported (n = 3).

Heating Temp. (°C)	TOC (mg C/g soil)	WEOC (mg C/g soil)	TON (mg N/g soil)	WEON (mg N/g soil)	NO_x-N (mg N/g soil)	NH_4-N (mg N/g soil)
CTRL	46.303 ± 0.000	0.485 ± 0.004	2.179 ± 0.000	0.032 ± 0.004	0.0012 ± 0.0004	0.0069 ± 0.0012
150	42.733 ± 0.041	1.342 ± 0.020	2.078 ± 0.002	0.070 ± 0.000	0.0012 ± 0.0003	0.0114 ± 0.0008
250	29.580 ± 0.024	2.247 ± 0.036	2.002 ± 0.001	0.211 ± 0.002	0.0006 ± 0.0001	0.0372 ± 0.0014
350	7.302 ± 0.003	0.714 ± 0.015	1.174 ± 0.000	0.076 ± 0.004	0.0002 ± 0.0001	0.0146 ± 0.0004
450	1.435 ± 0.001	0.065 ± 0.002	0.315 ± 0.000	0.008 ± 0.002	0.0001 ± 0.0002	0.0058 ± 0.0012

Table 4.2 shows the C/N ratios of the total (TOC/TON) and water-extractable (WEOC/WEON) fractions. Both decrease from the control (total: 21.24, water-extractable: 15.16) to 250°C (total: 14.77, water-extractable: 10.63) and further by 450°C (total: 4.56, water-extractable: 8.10). Nitrogen is enriched in both the solid and water-extractable fractions at temperatures ≥250°C. Additionally, the WEOC/WEON does not lower to the same extent as the TOC/TON at 350°C and 450°C, which may indicate that a larger proportion of carbonaceous residues are mineralized directly from the solid phase as opposed to undergoing a reaction that would increase water solubility.

Table 4.2. Carbon-to-nitrogen ratios of the total solid soil (TOC/TON) and water-extractable fraction (WEOC/WEON) from the control (CTRL) and heated soil samples at each temperature.

Temp. (°C)	TOC/TON	WEOC/WEON
CTRL	21.24	15.16
150°C	20.56	19.10
250°C	14.77	10.63
350°C	6.22	9.34
450°C	4.56	8.10

4.3.2 Solid-State ^{13}C NMR Spectroscopy

Solid state CP/MAS and DP/MAS ^{13}C NMR spectra of the hydrophobic acid (XAD-8) and hydrophilic acid (XAD-4) samples were described in detail previously.[416] The CP/MAS spectra are

reproduced in Figure 4.1, and the integrations in Table C.1. In brief, the spectrum of the hydrophobic acid sample at 150°C shows a relative increase in the proportion of the C-alkyl carbon peak (0-60 ppm) above the control. From 150°C to 450°C, there are successive decreases in the C-alkyl carbon, O-alkyl carbon (60-90 ppm), aromatic/acetal carbon (90-110 ppm), and ketone/quinone carbon (190-230 ppm) peaks, and a narrowing of the aromatic carbon (110-190 ppm) and carboxyl/amide (160-190 ppm) carbon peaks. Peptide amides are assumed to have been destroyed by 350°C. The residual aromatic carbon peaks at 131 ppm and carboxylic acid peaks at 172 ppm in the 350°C and 450°C spectra are consistent with the benzene and pyridine carboxylic acids as previously reported[416] among other constituents. The spectra of the hydrophilic acid samples follow a similar pattern from control to 350°C, with the exception that the latter spectrum shows residual C-alkyl and O-alkyl carbon peaks at 30 and 65 ppm, respectively. Comparison of the control hydrophobic and hydrophilic acid spectra shows that water extractable soil carbohydrates preferentially isolate on the XAD-4 resin, indicated by the carbohydrate peaks at 72 and 102 ppm in the hydrophilic acid spectrum. These peaks are significantly reduced in the hydrophilic acid spectra from the 250°C and 350°C samples, confirming destruction of carbohydrate material in the soil at these temperatures.

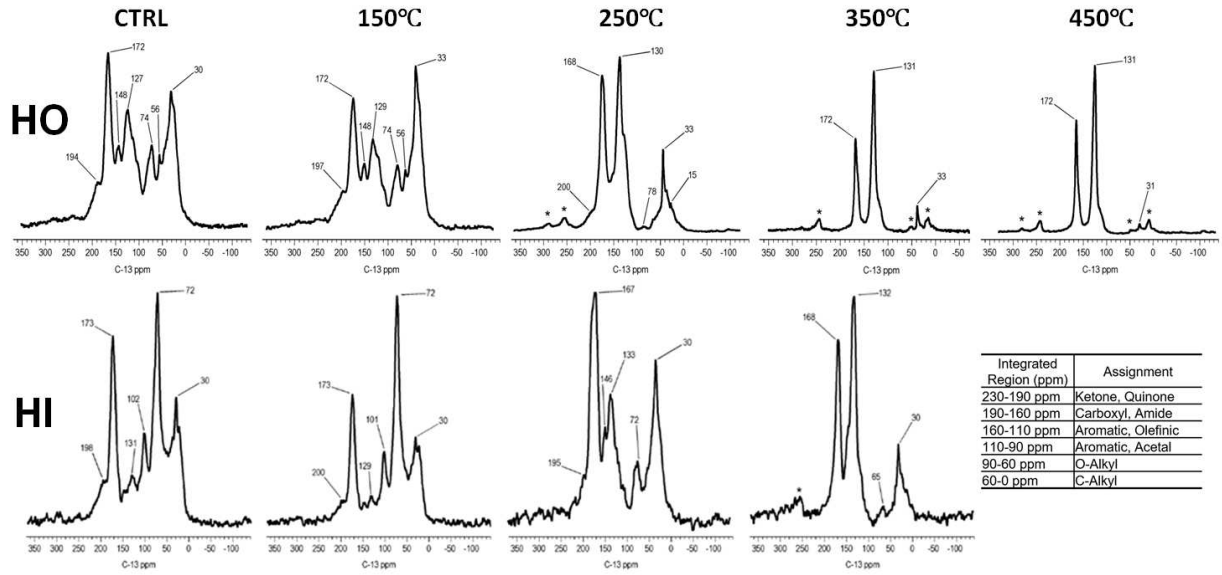

Figure 4.1 Solid State C-13 CP/MAS NMR spectra of the hydrophobic (HO, top) and hydrophilic (HI, bottom) at each temperature and of the control. Contact time = 5 msec; Line Broadening = 100 Hz; Asterisks denote spinning sidebands. The remaining hydrophilic fraction at 450°C was insufficient to collect solid state ^{13}C NMR. Produced with data obtained from Thurman et al.[416]

The quantities of hydrophobic and hydrophilic acid samples isolated (~10-90 mg) were insufficient for analysis of naturally abundant nitrogen by solid state ^{15}N CP/MAS NMR, within reasonable spectrometer accumulation times. However, losses or transformation of nitrogen functionalities with temperature can be inferred from the ^{13}C NMR spectra and are listed in Table 4.3. The forms of nitrogen in soil organic matter, not impacted by fire or heat, may include amines (terminal amino groups of amino acids, amino sugars, primary amines of purine and pyrimidine bases, and primary and secondary aminoquinones), peptides, N-acetylated sugars, the imide and lactam nitrogens of nucleotide bases, and heterocyclic nitrogens such as pyrrole, indole, and imidazole. Carbons alpha to the amine group of amino acids in peptides have ^{13}C chemical shifts in the range from 40 to 65 ppm, while ring carbons bonded to the amine group in amino sugars have chemical shifts in the approximate range from 50 to 60 ppm. These are in the range of sp^3 hybridized carbons that decrease in the ^{13}C NMR spectra of the hydrophobic acid fractions from 150°C to 250°C and have disappeared by 350°C to 450°C. Therefore, removal or transformation of

amino acid, peptide, and amino sugar structures in the soil to leachable aromatic nitrogen compounds or volatile degradation products, including nitrogen gases, is a reasonable inference from these ^{13}C NMR spectra. Nitrogen-containing functionalities encompassed within the 100 to 190 ppm chemical shift region of the residual peaks in the 350°C and 450°C spectra would be limited to non-peptide amide and aromatic heterocyclic structures. Of the water extractable organic matter that sorbs to the XAD-4 resin, the ^{13}C NMR spectra also indicate a decrease, but not total destruction, of amino acid, peptide, and amino sugar structures from 150°C to 350°C (Figure 4.1).

Table 4.3. Chemical shifts associated with nitrogen-containing groups in ^{13}C NMR.

Nitrogen Group	$\delta^{13}C$, ppm
Terminal Amino Acid, Carbon α to Amine Group	40 - 60
Amino Sugar, Ring Carbon Bonded to Amine Group	50-60
Indole Ring Carbons	102-136
Imidazole Ring Carbons	120-138
Purine and Pyrimidine Bases, Ring Carbons	90-170
Peptide Carbonyl	162-178

4.3.3 Proliferation of Nitrogen-containing Heteroatom Classes

Broadband negative ion ESI FT-ICR mass spectra for hydrophobic and hydrophilic fractions as a function of temperature are shown in Figure 4.2 and 4.3. All samples spanned a similar molecular weight range between m/z 150 – 600 with achieved resolving power > 1,500,000 at m/z 400. Figure 4.4 shows the number of assigned formula and percent relative abundance of the CHO (O_x) and CHNO heteroatom classes separated by nitrogen content ($N_{1\text{-}5}O_x$). Counts for each class can be found in Table 4.4, alongside the abundance-weighted average C/N ratios and m/z, discussed below. The CHO and CHNO assigned molecular formulae from the control (hydrophilic: 5518, hydrophobic: 5846) increased slightly at 150°C (hydrophilic: 6149, hydrophobic: 5960) and most at 250°C (hydrophilic: 8770, hydrophobic: 8554). Assignments decreased at 350°C (hydrophilic: 2948, hydrophobic: 3584) and reached a minimum at 450°C (hydrophilic: 1035, hydrophobic: 1734).

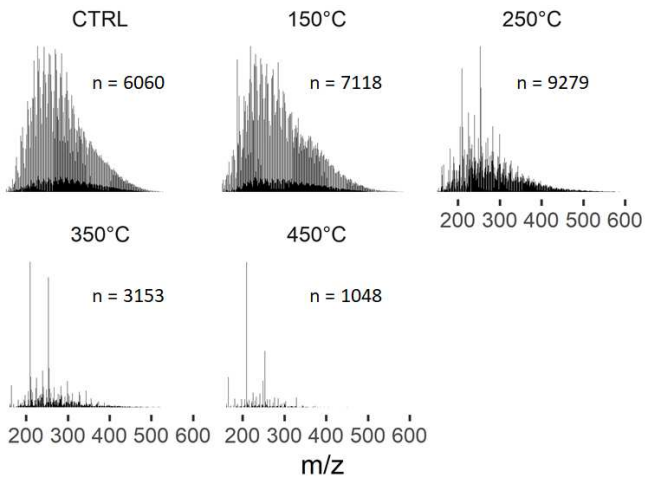

Figure 4.2 FT-ICR mass spectral distribution of all the peaks assigned in from the hydrophilic fraction for the control and heated samples between 150°C and 450°C. Chemical noise and interferences, such as linear alkyl sulfonates,[16] were removed to allow for observation of the molecular weight distribution.

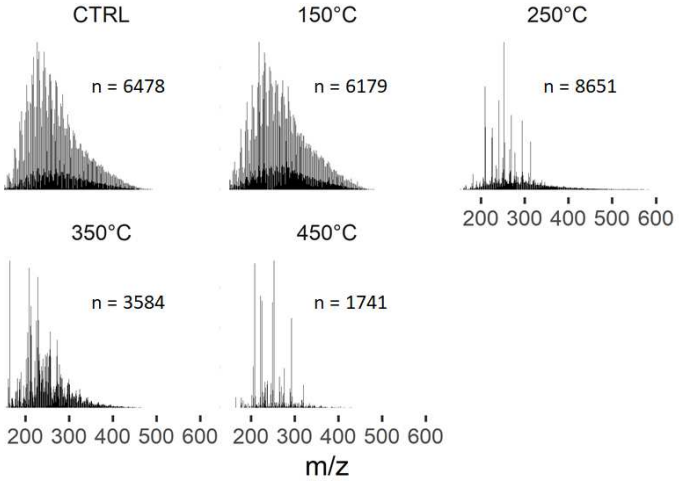

Figure 4.3 Fourier transform ion cyclotron resonance mass spectra collected from the hydrophobic fraction for the control and heated samples between 150°C and 450°C. Chemical noise and interferences, such as linear alkyl sulfonates,[16] were removed to allow for observation of the molecular weight distribution.

Importantly, only the CHNO assignments contributed to the increased formulae at 250°C and remained the largest class, containing over 70% of the formulas assigned at intensities ≥250°C in both fractions (Figure 4.4, top). The percent relative abundance of the heteroatom classes followed a similar trend: class abundances changed slightly below 250°C, after which the CHNO classes in the hydrophilic fraction increased to ~75% and the hydrophobic fraction up to ~50% of

the total abundance at temperatures ≥250°C (Figure 4.4, bottom). Of the CHNO assignments, the $N_{2\text{-}5}O_x$ classes appeared to increase the most in assignments at 250°C. At higher temperatures, all assignments decreased but the $N_{2\text{-}5}O_x$ classes decreased less than the N_1 class, instead increasing or staying relatively the same above 250°C. The increase in $N_{2\text{-}5}O_x$ is also reflected by the average weighted C/N ratio (Table 4.2) that decreased from 250°C to 450°C (hydrophilic: 9.61 to 5.46, hydrophobic: 12.31 to 8.03).

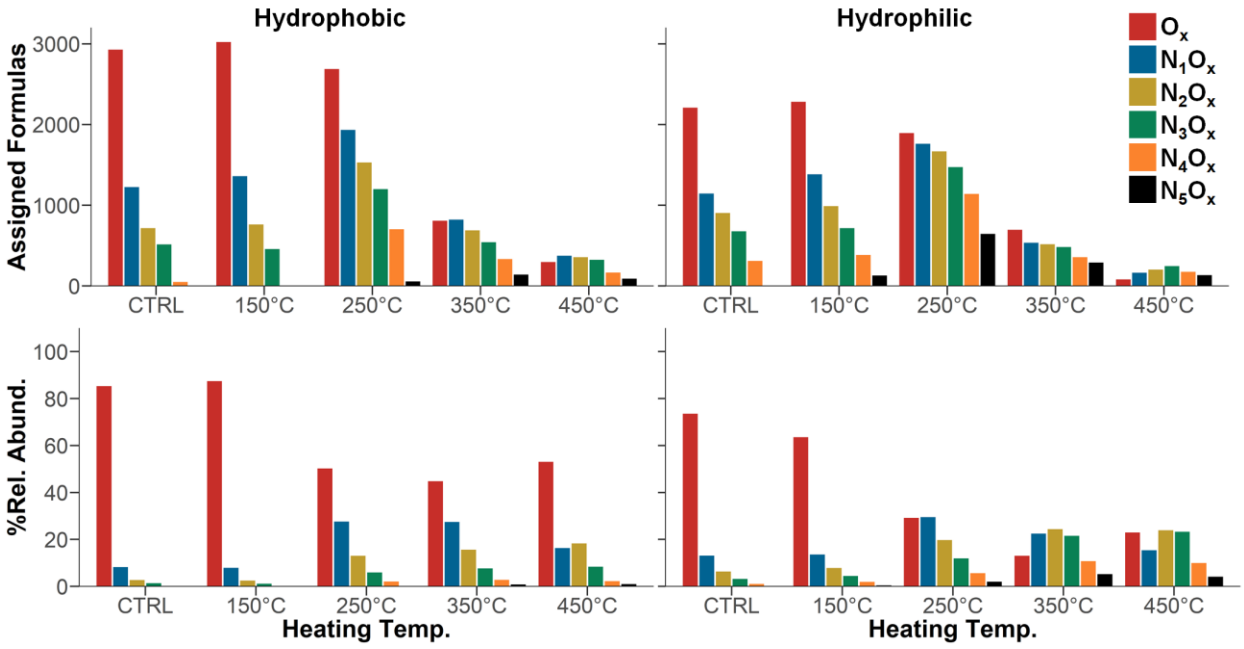

Figure 4.4 Number of assigned molecular formulas (top) and percent relative abundance (bottom) of the CHO and CHNO heteroatom classes at each temperature measured by the 9.4 T FT-ICR MS using negative ESI. CHNO classes are distinguished by nitrogen content ($N_{1\text{-}5}O_x$).

Table 4.4. Molecular formula assignments made in the hydrophilic and hydrophobic fractions collected at each temperature with the corresponding abundance-weighted C/N ratios and average m/z.

Hydrophilic	CHNO	CHO	CHOS	CHNOS	Total #	Weighted Avg. C/N	Weighted Avg. m/z
CTRL	3296	2222	359	183	6060	11.05	293.87
150°C	3868	2281	522	447	7118	9.88	294.31
250°C	6876	1894	119	390	9279	9.61	315.15
350°C	2246	702	136	69	3153	7.01	266.11
450°C	935	100	13	0	1048	5.46	257.63
Hydrophobic	CHNO	CHO	CHOS	CHNOS	Total Formula #	Weighted Avg. C/N	Weighted Avg. m/z
CTRL	2863	2983	230	402	6478	13.01	313.12
150°C	2918	3042	176	43	6179	13.19	316.57
250°C	5843	2711	55	42	8651	12.31	313.83
350°C	2766	818	5	0	3589	10.78	291.32
450°C	1418	316	7	0	1741	8.03	251.37

Despite a similar trend between fractions of increased CHNO assignments and abundance above 150°C, in the hydrophobic fraction, the CHO class remained ~50% of the relative abundance at 350°C and 450°C but was comprised of fewer, highly abundant peaks. These assignments included BPCAs that were previously measured in these samples from 250°C to 450°C and were found to be concentrated in the hydrophobic fraction.[416] Other CHO assignments that are only abundant in the hydrophobic fraction at 350°C and 450°C also appeared to be related by carboxylic acid groups, some matching formulas tentatively identified by Ferrer et al.[423] Pyridinic analogs to BPCAs were also tentatively identified at low concentration in the hydrophilic fraction only,[416] but only corresponded to two assignments in the current study. Interestingly, numerous other CHNO assignments were assigned at high abundance throughout the temperature gradient in the hydrophilic fraction, and to a lesser extent in the hydrophobic fraction, and are explored below.

4.3.4 Speciation of the Water-extractable Nitrogen-containing Residues

The hydrophilic fraction was the focus throughout the rest of this chapter based on the increase in WEON and corresponding increase in CHNO formula assignments that appeared better isolated in the hydrophilic fraction. While generally similar, differences will be noted for the hydrophobic fraction and analogous figures can be found in Appendix C.

Figure 4.5 displays van Krevelen (VK) plots of the CHNO assignments, which can be used to infer changes to saturation and oxygen content throughout the temperature gradient in the hydrophilic fraction (Figure C.1 for the hydrophobic fraction). In the control (CTRL), the CHNO assignments before heating (bottom, third, and second 25% bins) displayed coverage over a large range of H/C (~0.4. to 2.0) and O/C (~0.1 to 1.0) values, typical of a heterogenous WEOM mixture.[53,404,424,425] At 150°C, peaks encompass similar regions to the CTRL and also include additional assignments at H/C > 1, above the ARO line. These mid-saturated and aliphatic CHNO species at 150°C may result from the release of plant, root, and microbial residues that can occur at this temperature.[362,426] At 250°C, CHNO assignments in the aromatic plot region (below the ARO line) increased in abundance and mid-saturated and aliphatic features decreased.

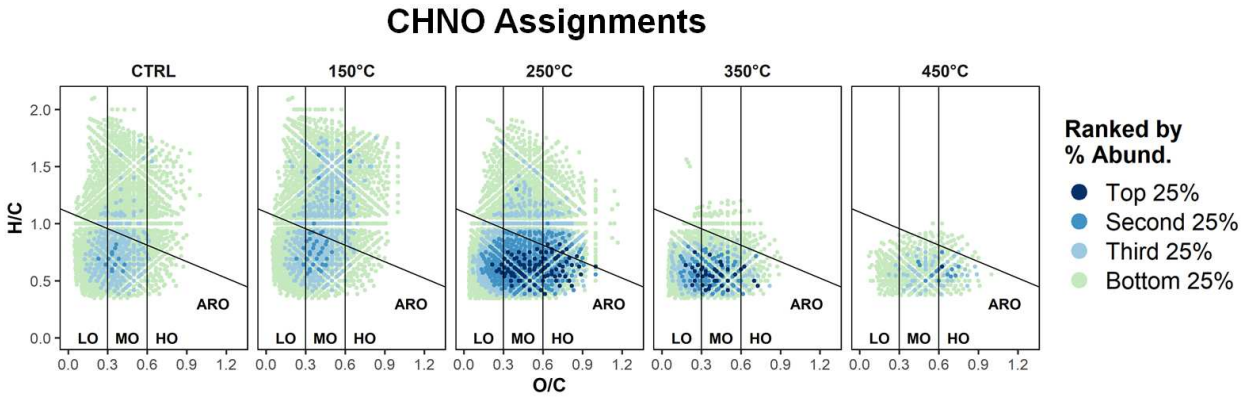

Figure 4.5 Abundance-weighted van Krevelen plots of N_xO_x species derived from negative-ion ESI FT-ICR MS spectra for the unburnt control (CTRL) and heated soil leachates isolated on the hydrophilic resin. Lines were added to each plot to indicate regions where aromatic features predominate ($AI_{Mod} \geq 0.5$, indicated by the ARO line), and relative oxygen density: "LO" = low oxygen density, $O/C \leq 0.3$; "MO" = mid oxygen density, $0.3 < O/C \leq 0.6$; "HO" = high oxygen density, $O/C > 0.6$. Plotted formulas were grouped using their abundances, where the "top 25%" (dark blue points) are 25% of the sample's cumulative abundance comprised of the most abundant formulas, the "second 25%" is the next 25% comprised of the next most abundant formulas, and so on.

The enriched aromatic regions were more pronounced at 350°C and 450°C, with high abundance peaks encompassing a narrower range and fewer assignments. The changes in saturation are also reflected by the RDBE, which is visualized in Figure 4.6 by nitrogen content ($N_{1\text{-}5}O_x$) (Figure C.2 for hydrophobic). While the hydrophilic and hydrophobic fractions were generally

similar, high RDBE peaks (relative to the control) at 350°C and 450°C were only attributed to $N_{2\text{-}5}O_x$ formulas in the hydrophilic fraction. The nitrogen dense assignments exhibited increased abundance and aromaticity during heating, which is in good agreement with the ^{13}C NMR.

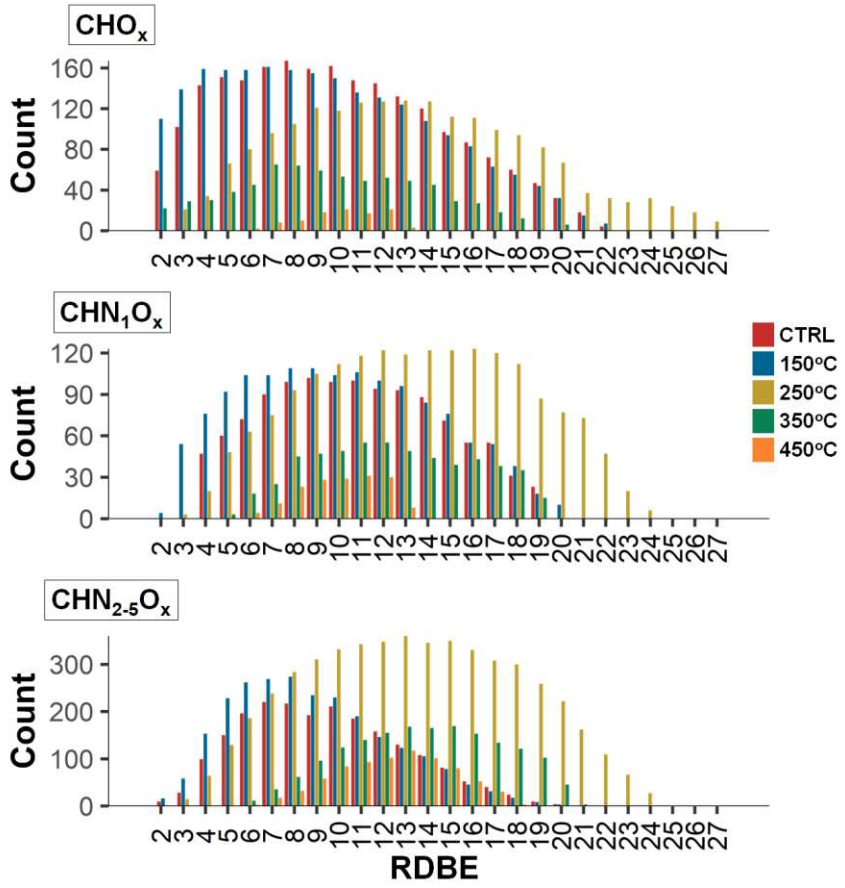

Figure 4.6 Distribution of formula assignments by rings-plus-double-bonds (to carbon) equivalents from the hydrophilic fraction at each temperature. Plots are separated by CHO_x, N_1O_x and $N_{2\text{-}5}O_x$ to distinguish between nitrogen-containing and nitrogen dense assignments. See Figure C.2 for the analogous hydrophobic RDBE plots.

The most abundant O/C regions also appeared to shift during heating. At 250°C, aromatic plot regions were enriched across all O/C but enriched most in mid- and high-oxygen aromatic plot regions. The most abundant aromatic plot region shifted at 350°C to lower O/C, encompassing the low- and mid-oxygen density regions. Finally, at 450°C, abundant peaks were in high-oxygen density regions, and in mid-oxygen regions to a lesser extent, though fewer peaks were present to indicate a

trend. The general shift towards more aromatic assignments is similar in both the CHO and CHNO assignments. As evidenced above in Figure 4.4, CHNO assignments are not prominent below 250ºC

To explore the shift in oxygen content further, Figure 4.7 displays the percent relative abundance of the CHNO classes separated by nitrogen and oxygen ($N_{1-4}O_{2-15}$) (hydrophilic N_5O_{2-15} and hydrophobic fraction in Figure C.3 and C.4, respectively). Features were similar between the control and 150ºC sample, where nitrogen classes were centered around $N_{1-4}O_{5-6}$ or were too low in abundance to detect (i.e., N_5O_x). At 250ºC, the N heteroatom classes increased both in abundance and oxygen number, and several new CHNO classes (N_1O_{13-15}, $N_{2-4}O_{11-14,}$ and N_5O_{3-10}) were assigned. This could indicate multiple oxidation reactions by N- and O-containing species, or condensation reactions among SOM species.

At 350ºC, the abundances of N_xO_{10-15} species decreased greatly or disappeared entirely, and the oxygen numbers of the most abundant N heteroatom classes decreased, now centering around N_1O_{4-5} and $N_{2-5}O_4$. The abundance-weighted average m/z and C/N of the detected peaks also changed more between 250°C and 350°C than at any other temperature transition, decreasing from 315.15 to 266.11 m/z and 9.61 to 7.01 C/N (Table 4.4). This could indicate the loss of O-containing species through dehydration, decarboxylation or other fragmentation reactions. At 450ºC, the most abundant heteroatom classes rose in oxygen number from 350ºC, however each of the class distributions became less uniform. Specific classes appeared enriched at 450ºC (e.g., N_2O_6, N_2O_8), potentially corresponding with specific char products.

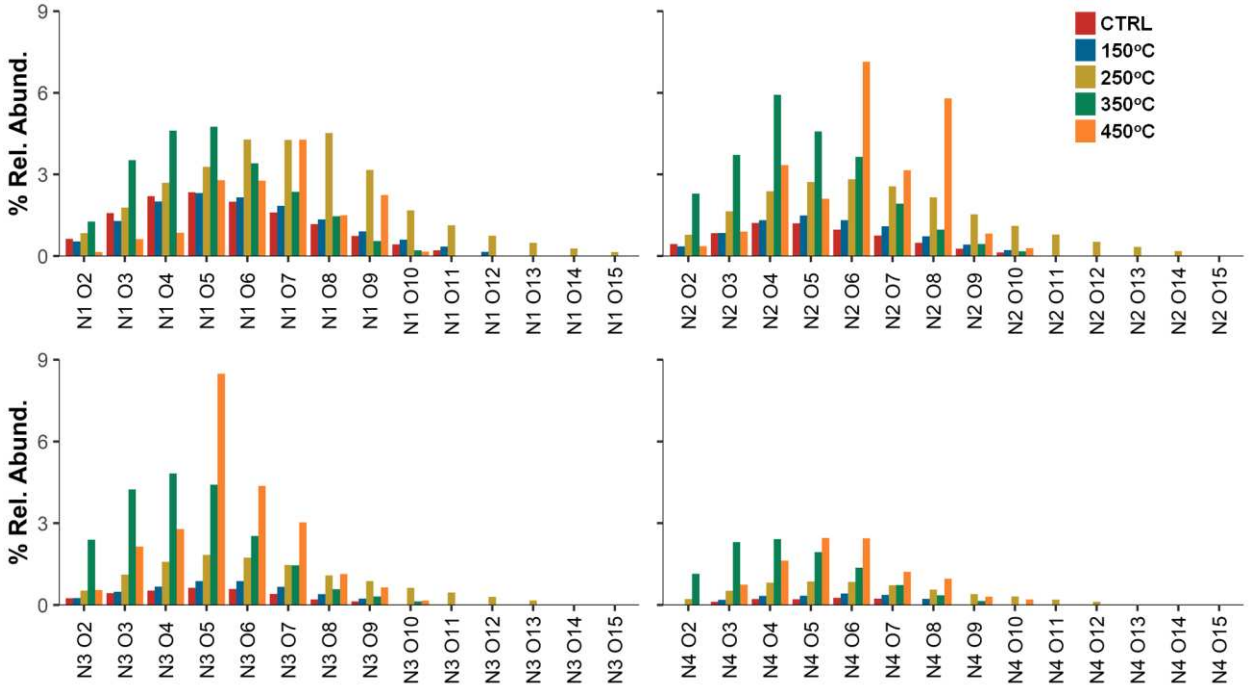

Figure 4.7 Model soil particle depicting an Fe(III) mineral (brown) and clay (black) surface exhibiting various possible interactions with model SOM. The variety of possible interactions will create fractions with varying extractability based on the extraction solution (e.g., acid/base, organic solvent, and water), mineral surface, and intermolecular forces.

While the most abundant N_xO_x class at each temperature differed depending on the amount of nitrogen assigned, the increase and decrease in oxygen content between 150°C and 350°C appeared to occur consistently across every nitrogen class. The trend observed here might suggest the presence of distinct transformations and features in each of the classes, dependent on temperature. In such complex samples, it is difficult to discern whether nitrogen-containing species are persistent once formed, formed continuously as new byproducts through heating, or a combination of both. Similarly, it is difficult to determine if decreasing or disappearing peaks are attributable to new or enriched peaks upon heating, or mineralization. Nevertheless, formation mechanisms that contribute to the observable nitrogen enrichment can be studied if known transformations throughout the temperature gradient can be modeled.

4.3.5 Modeling Maillard Reaction Processes

The Maillard reaction involves the condensation of reducing sugars with amino acids followed by many more reactions, and are well-known in the context of cooking and preparing food.[390] In fact, many Maillard reaction intermediates and fragments, referred to here as Maillard reaction products (MRPs), have been well described and characterized in food chemistry using simple systems.[427–430] Hemmler et al.[211] studied MRPs by heating equimolar mixtures of ribose and glycine at 100°C for up to 10 hours. They reported several findings consistent with the behavior of WEOM in this study, including the enrichment of aromatic nitrogen and increased N_2O_x assignments following heating longer than 4 h, and the presence of several reaction pathways that dominated the MRPs within 6 h. These factors motivated the exploration of Maillard reaction pathways in the current study.

Potential MRPs were identified using a mass difference-based analysis that is depicted in Figure 4.8. Mass differences were computed between peaks based on known Maillard reactions, where potential Maillard "precursor" and "product" peaks were identified going from lower to higher temperatures, respectively, when they differed by the expected mass difference, using the theoretical masses of the assigned formulas (Table C.2). For instance, a peak at 150°C needed to differ from a peak at 250°C by the exact mass of the reaction of interest to be considered a potential MRP. In a complex biogeochemical mixture like SOM, it is possible that some of the expected mass differences will occur by chance, or due to the presence of common structures in SOM molecules. For this reason, the best evidence of potential MRPs comes from (i) product peaks that were not detected at the lower temperature, or (ii) product peaks that were present at both temperatures, but whose abundances increased relative to the corresponding precursor peaks at the higher temperature.

The temperature transitions studied here were CTRL→150°C, 150→250°C, 250→350°C, and 350→450°C. Reactions modeled included amino acid condensations, where glycine (Gly), alanine (Ala), glutamine (Gln), and lysine (Lys) were chosen based on their presence in soil[431] and the contributions of peptidoglycan and other microbial biomass to SOM.[61,63,432,433] Hemmler *et al.*[211] reported that the initial condensation reaction was followed by an extended series of dehydration reactions leading to MRPs with greater degrees of unsaturation and aromaticity, so tentative MRPs were only considered when they occurred in "dehydration series" associated by successive water losses ($n \geq 3$). These were identified in these samples using a modified Kendrick mass defect analysis (KMD_{H2O}) based on the accurate mass of water (IUPAC mass × 18/18.01057),[211,428,434] and can be visualized in Figure 4.9 which plots a subset of dehydration series for N_3O_x assignments.

Ammonia (NH_3) addition was studied as an alternative pathway for nitrogen enrichment, because ammonia was retained here (Table 4.1) and is retained in soil after fires,[435,436] and fire-derived organic matter has been reported to retain ammonia through covalent bond formation.[435] Peaks were also examined for the loss of byproducts specific to the Maillard Reaction pathway (Table C.2), which are referred to here as intermediate reaction products. The intermediate reaction products are identified by the size of the carbon fragment (C#) lost, ranging from C1 (e.g. formic acid) to C6 (e.g. glucosone).[211,428,437] These C# include carbonyl-containing species (e.g., α-hydroketones, α-hydroxyaldehydes) that can react further to form heterocyclic nitrogen.[437] The reactions studied here were not intended to include every possible reaction, but to investigate whether some of the changes in WEOM composition during soil burning could be modeled with time-resolved Maillard reactions previously observed in simpler systems.

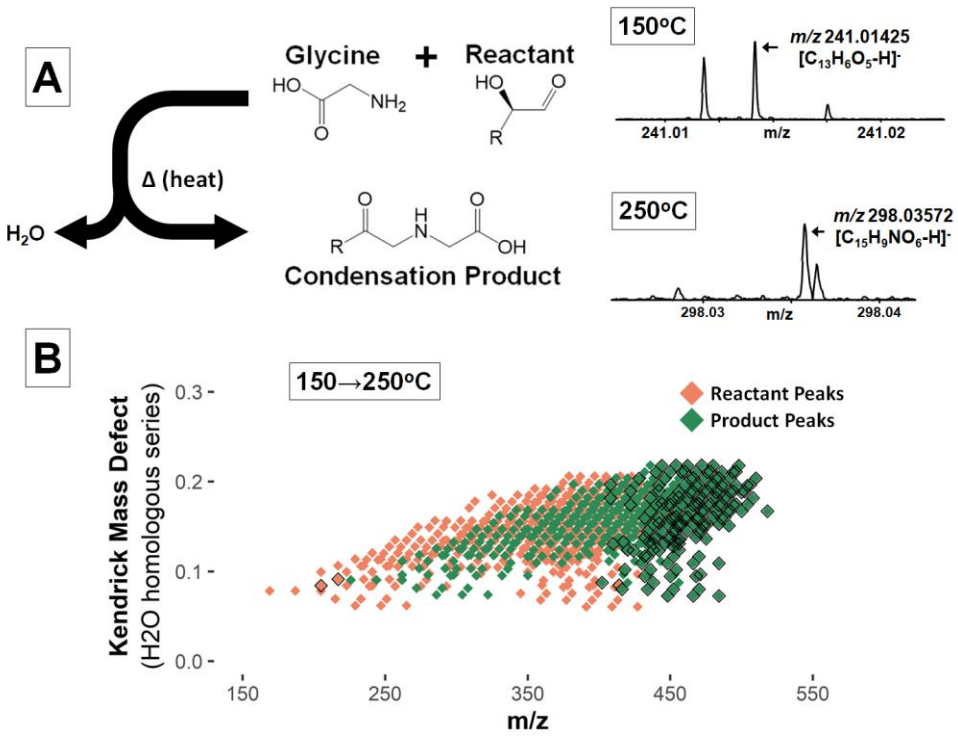

Figure 4.8 Model soil particle depicting an Fe(III) mineral (brown) and clay (black) surface exhibiting various possible interactions with model SOM. The variety of possible interactions will create fractions with varying extractability based on the extraction solution (e.g., acid/base, organic solvent, and water), mineral surface, and intermolecular forces.

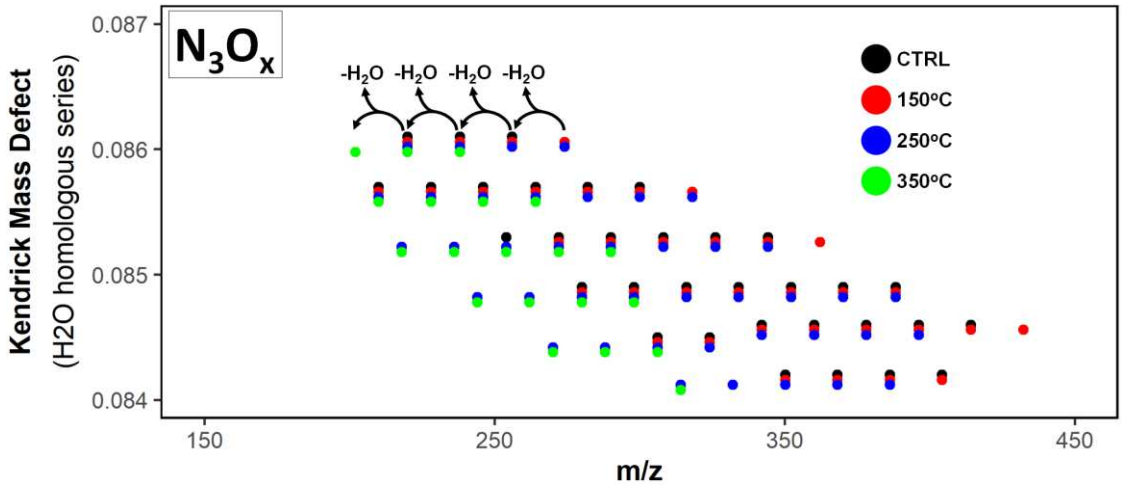

Figure 4.9 Dehydration series for N_3O_x-containing molecular formulas visualized up to 350°C by H_2O Kendrick mass defect (KMD_{H2O}) from the hydrophilic fraction. Data was truncated for ease of visualization, where series with KMD_{H2O} between 0.083 and 0.087 are visualized above. Peaks horizontally plotted by KMD_{H2O} are related by the number of H_2O groups. Points from 450°C were omitted due to the low water-extractable organic matter content and low peak abundances at this temperature.

4.3.6 Molecular Evidence of Maillard Reactions and Ammonia Additions

Figure 4.10 displays the product counts for each of the potential condensation and intermediate reaction pairs. Condensation products and ammonia additions were observed in the CTRL→150°C (8473 total), 150→250°C (10595 total) and 250→350°C (3363 total) temperature transitions (Figure 4.10A). Intermediate reaction products were also found at each of the transitions, and were also highest in the 150→250°C transition (24081 total) (Figure 4.10B). The hydrophobic fraction exhibited similar trends but at lower counts and can be seen in Figure C.5. It is worth noting that, in the hydrophilic fraction, the average m/z of the assigned formulae increased most at 250°C and decreased most at 350°C (Table 4.4).

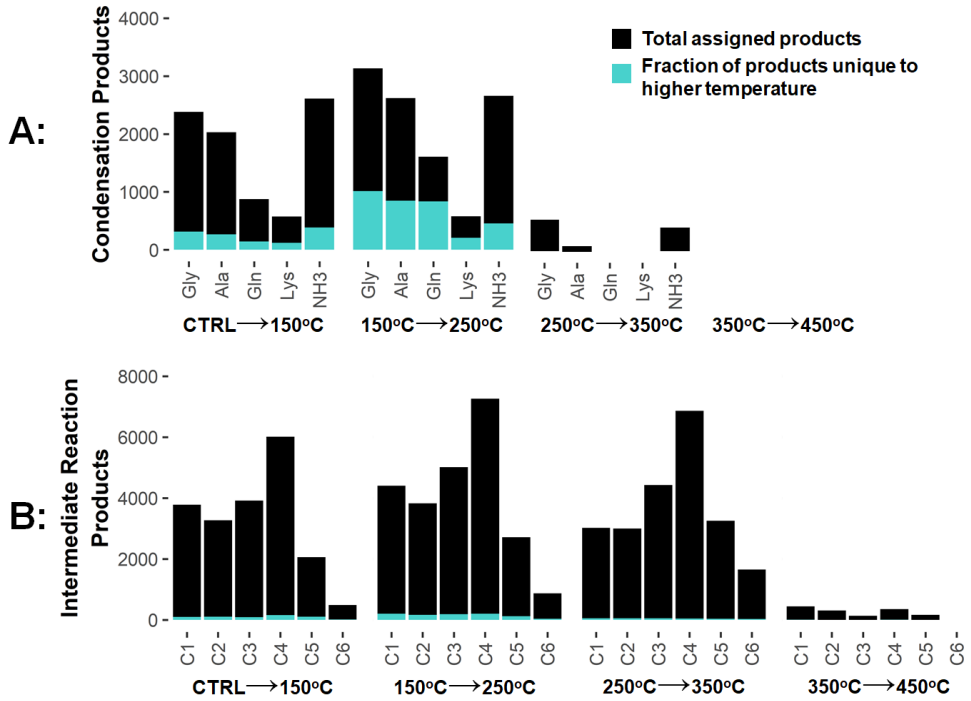

Figure 4.10 Model soil particle depicting an Fe(III) mineral (brown) and clay (black) surface exhibiting various possible interactions with model SOM. The variety of possible interactions will create fractions with varying extractability based on the extraction solution (e.g., acid/base, organic solvent, and water), mineral surface, and intermolecular forces.

The condensation and ammonia addition reaction pairs shared some of the same product peaks and are shown numerically in Venn diagrams in Figure 4.11. This is most prominently

observed in the 150→250°C transition with the Gly and Ala condensation reactions that shared 2065 of their total product peaks (Gly: 3132, Ala: 2619) with each other and ammonia addition pairs. This could indicate that different reactions create product peaks with identical elemental compositions, which is certainly possible in such a complex mixture, but it also highlights the difficulty of evidencing specific reactions in a complex mixture. Importantly, the condensation product peaks also included assignments that were unique to the higher temperature, and unique to only one modeled reaction (Figures 4.10 and C.5). These product peaks present the clearest evidence of specific Maillard reactions in the burned soil systems. They are not dispositive, but they are numerous and consistent with previous observations from much simpler systems.[211] These findings are also supported when considering the loss of carbohydrate signatures by 350°C in the ^{13}C NMR that coincided with the decrease in assigned MRPs. Similarly, the evidence of unique ammonia additions is not dispositive, but they are numerous and their occurrence is consistent with previous reports.[435]

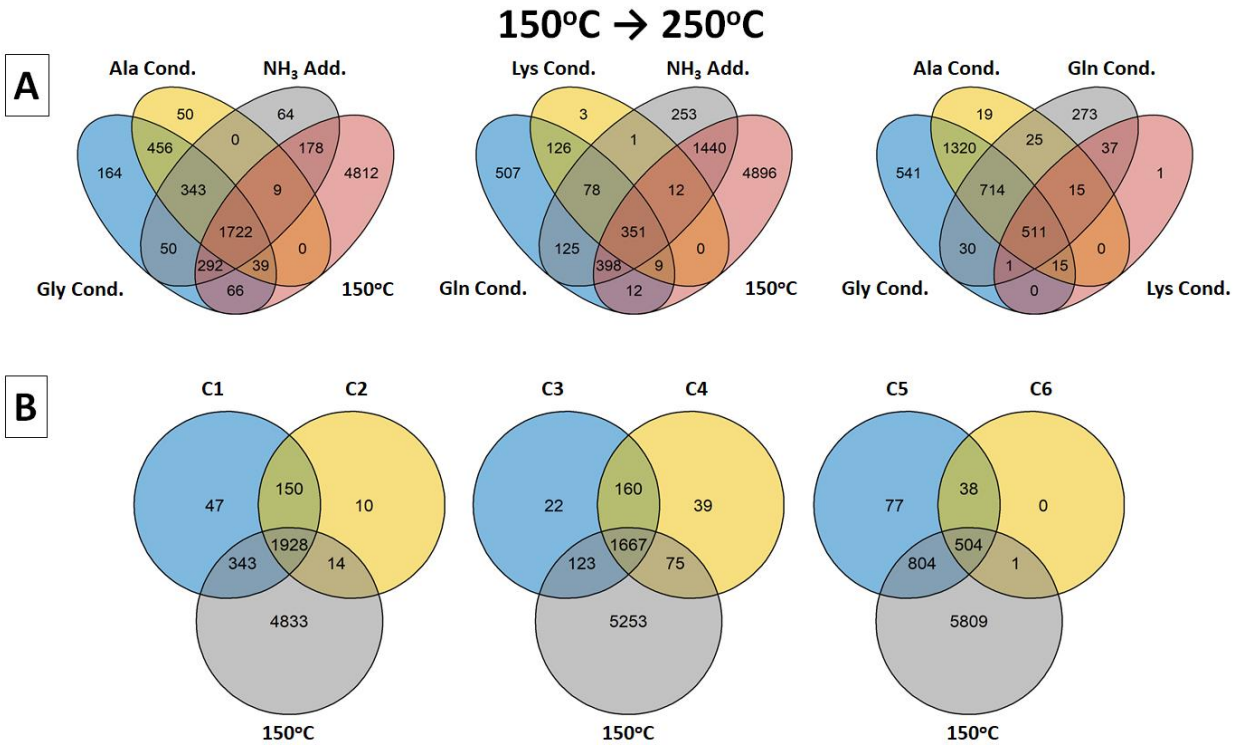

Figure 4.11 Venn diagrams comparing common product peaks of different reaction pairs identified from 150→250°C and assignments made at 150°C to indicate the assignment of compositions unique to 250°C in the hydrophilic fraction. A: comparison of amino acid condensation and ammonia addition products to each other and compositions assigned at 150°C. B: comparison of intermediate reaction products by C# fragments to each other and compositions assigned at 150°C. The C# counts visualized here do not include products shared between C# fragments. Using the top left diagram as an example: (i) peaks corresponding to Gly condensations included 164 unique compositions that were assigned at 250°C and not at 150°C and did not correspond to any products of the NH_3 additions and Ala condensations (blue area). (ii) 456 compositions included products that corresponded to both Gly and Ala condensations but not ammonia and were unique to 250°C (light green area). (iii) 1722 compositions were present at 150°C that corresponded to Gly condensations, Ala condensations, and NH_3 additions (overlapping center area). It should be noted that the intermediate reaction product counts were higher than visible here in the C# Venn diagrams because reactants with common products were only counted once.

In comparison, many of the intermediate reaction products were common to at least one of the other C# reaction pairs or peaks assigned at lower temperatures and are shown numerically in Venn diagrams in Figure 4.11. It seems likely that the high relatedness between the intermediate reaction products and assignments at lower temperatures is due to SOM complexity and the multitude of pathways occurring to individual compounds during heating. Studies[25,211] have reported an exponential increase in MRPs when nitrogen was present during the heating of simple systems, so it seems reasonable that numerous transformations can occur to a single residue. Still, the presence

of intermediate reaction products from 250→350°C and absence of condensation products does correspond with the decreased N_xO_{10-15} and increased N_xO_{3-6} class abundances and lower average m/z.

The presence of shared and uniquely assigned product peaks suggests that products appear to be forming as a function of specific amino acid reactions and also inorganic nitrogen additions. It should be noted that in a study measuring ribose-amino acid products formed during heating at 100°C, Hemmler *et al.*[25] indicated that reactions with Lys produced the most products and had the highest reactivity, and Gly had the lowest, up to N_4O_x. In our study, the order was Gly (3,132) > Ala (2,619) > Gln (1,606) > Lys (580). The discrepancy might originate from differences in source materials and the higher temperatures used, or it might result from confounding mass differences in such a complex material. Ammonia appeared to contribute to the products through inorganic nitrogen addition, but other pathways such as nitration may also be valid for inorganic nitrogen enrichment of WEOM. Finally, reactions between the MRPs formed may contribute to the relative increase of $N_{3-5}O_x$ classes in SOM at above 250°C, but investigation of these reactions or persistent products would require a more precise understanding of the specific MRPs formed during heating.

4.4 Environmental Implications

While the experimental design of this study was a proxy for soil heating in the field, the temperatures used here are reflective of temperatures in the organic soil horizon in mineral soils during wildfires. Low-severity heating (e.g., fast-moving, prescribed fires) can produce temperatures as low as 50°C at 5 cm depths and high-severity heating (e.g., slow-moving, smoldering fires) can reach temperatures of >250°C at up to 10 cm depths with potential to last minutes to several days.[370] Patterns in molecular formulae identified here were not observed up to 450°C, which corresponds to the near total consumption of SOM and WEOM at 450°C in this study and elsewhere.[38,370] Most

residues were removed completely when heating to this temperature, therefore residues from 150°C to 350°C will predominate when studying fire-affected field sites despite the heterogeneity in wildfires intensities. This implies that SOM at specific soil depths within this temperature range will be responsible for what is being leached from soils.

The apparent solubility of the charred organic matter is somewhat contrary to the formation of hydrophobic features[414] and has numerous implications for post-fire watershed and water quality conditions. The mobility of these residues not only removes an organic carbon and nitrogen source at the site of the burn, but the absence of plants and plant nutrient uptake following fires will increase subsurface transport of the WEOM.[438] This removal is associated with an initial pulse of nutrients during the fire and long-term leaching that will influence stream biota metabolism,[439,440] and could correspond to the changes in microbial community structure observed following fires with implications regarding C storage in fire-affected ecosystems.[441] Interestingly, the enriched aromatic CHNO observed here is not considered a reactive precursor for DBP formation during water treatment.[442–444] It is possible that the CHNO fractions containing alkylated amine precursors are not well represented in the samples studied here as the ionization mode used for mass spectrometry was not amenable to basic nitrogen moieties,[18,177] however these groups are often transformed during even moderate heating.[445]

This study employed a laboratory-based heating method to exert the most control over the experimental conditions. The general trend in aromaticity was consistent with other laboratory-[181] and field-based[320,394] SOM chars analyzed by FT-ICR MS. The enriched nitrogen observed here is also common to chars with proteinaceous biomass, such as grasses.[376,405,408,446] While the results of this study focus on a laboratory-simulated microcosm that represents transformations that occur with heating in the field, the observed changes in aromaticity, changes in nitrogen density relative to the oxygen content, and mass-difference analysis provide evidence for SOM-specific

transformations such as Maillard reactions that have been reported in simpler systems. The occurrence of Maillard reaction products here is not definitive evidence of Maillard reactions due to the qualitative analysis by FT-ICR MS, but does support the existence of Maillard reactions when considering existing knowledge of Maillard reactions,[13,25,211,393] the well-known presence of amino acid and carbohydrate functionalities in SOM,[61,63,431–433] and the observed enrichment of N-containing compounds in SOM during heating here and elsewhere.[376,388,391,392]

Without knowledge of the precise precursors present in the SOM, a comprehensive understanding of how the Maillard reaction applies to transformations in heated SOM remains uncertain. However, the evidence presented here suggests that the Maillard reaction pathway can in part describe transformations in heated SOM. Interestingly, the potential MRPs and their reactions appeared to be specific to heat intensity, such that the trends and unique peaks might contribute new N-containing biomass burning markers specific to fire intensity. The introduction of known precursor materials, like specific amino acids, to SOM during controlled heating could more clearly identify product residues that are associated with Maillard reaction pathways.

CHAPTER 5: CHANGES IN DOC AND DBP CHEMISTRY IN A WILDFIRE-IMPACTED WATERSHED FOLLOWING A RAINSTORM

5.1 Introduction

Forest ecosystems in the United States provide numerous ecosystem services (e.g., water resources, soil stabilization and erosion control, climate regulation, and carbon sequestration) which are valued at about $5 trillion a year.[447] Watersheds in the western United States provide water to over 180 million people and are currently pressured by population growth and changing climate.[29,30] There are clear links between water quality and forest disturbance, and projected increases in wildfire size, severity, and frequency are likely to have increasing impacts on aquatic resources and downstream water supply.[34,35] As wildfires continue to grow in frequency and severity, understanding the impacts of wildfires on forested watersheds is critical for securing water resources and protecting ecosystem services.

The degree of combustion varies widely within wildfires due to spatial heterogeneity in fuels (e.g., plants, microbes, litter, soil organic matter (SOM)) and fire behavior and generates a mixture of unburnt, partially, and thoroughly charred pyrogenic organic matter (pyOM). The quantity and composition of pyOM formed will also depend on several watershed features (e.g., soil moisture, topography, vegetation, microbial communities)[13,14,33] and burn severity, defined here as the amount of vegetation and litter consumed and ash present.[37] Soil heating and residual pyOM can generate hydrophobic layers in some soils that decreases post-fire infiltration and increases runoff.[13] The removal of litter and loss of soil structure greatly exacerbates post-fire soil erosion and transport of ash, char, and nutrients.[46] This includes dissolved organic matter (DOM) (i.e., dissolved organic carbon (DOC), dissolved organic nitrogen (DON)) and total dissolved nitrogen (TDN) from surrounding unburnt and fire-affected soils and vegetation.[448–450]

Changes in stream water begin shortly after a fire,[47] often in response to precipitation events. For instance, nitrate, manganese, total suspended solids, chloride, and DOC can increase by orders of magnitude downstream from burned watersheds during storms.[449,451,452] Post-fire summer storms increased various N forms (i.e., nitrate, ammonium, and DON) the first 3 years after fires in the western North American forests.[453,454] General post-fire responses vary with extent and severity of wildfire and both proximity of the storm and fire, but there is also a high degree of spatial and temporal variability within storm events,[451,455] and DOM composition can shift between storm onset and peak discharge.[49,50]

Wildfire-induced changes to stream water composition can adversely impact downstream water treatment, where increases in metals, nutrients, sediment, and DOC require increased filtration and coagulation during treatment.[48,412] Disinfection byproducts (DBPs) formed during chlorination treatment of DOC are regulated by the USEPA due to their toxicity.[456] Wildfire-impacted waters have been shown to contain more DBP precursors compared to unburned areas,[51] and increase from proximal storm events.[412] Post-fire DBP precursors tracked with DOC in Colorado streams affected by the 2002 Hayman fire and were highest in areas with moderate high severity wildfire.[40] Precursors for unregulated DBPs, often highly toxic, N-containing DBPs are also known to increase following high severity wildfire.[40,41,457,458] The majority of aromatic DBPs and DBP precursors formed during forest wildfires remain relatively unknown, and the heterogeneity and complexity of the DOM signature challenges molecular identification and quantification.[459,460]

Characterization of DOM in highly complex surface water samples in post-fire watersheds requires the ability to separate and assign compositions to thousands of ionized species. Fourier transform ion cyclotron resonance mass spectrometry (FT-ICR MS) at 21 tesla achieves the highest mass resolving power and mass accuracy sufficient to separate and assign elemental compositions to tens of thousands of species in SOM and DOM.[16,18,28,99,229,251,313] This makes FT-ICR MS suitable for

complex environmental sample matrices (e.g., DOM,[21,87,399,401–404,92,133,143,230,247,306,397,398] solid and water-soluble char residues,[24,181,320,394,405–409] and petroleum[20,173,199,277,410,411]), where isobaric species differ by the mass of an electron.[28,73] FT-ICR MS applied to characterize organic species in forest soils has catalogued the leaching and degradation of condensed aromatic species derived from charcoal into surrounding pore and stream waters.[461,462] A recent study of DBP formation in surface and groundwater reports that highly aromatic and oxidized residues positively correlate with DBP (i.e., trihalomethane and haloacetonitrile) formation.[463] However, little is known about compositional changes in stream DOM and DBP precursors throughout watershed catchments influenced by wildfire burn extent and precipitation.

The Cameron Peak fire, the largest in Colorado recorded history, burned 208,913 acres in 2020 within the Cache le Poudre and Big Thompson watersheds which deliver agricultural, municipal and industrial water to more than 300,000 residents in Northern Colorado.[464] In this study, stream water chemistry and DOM composition was compared between stream waters originating from catchments at different burn extents before, during, and after the first set of storms following the Cameron Peak fire to investigate the short-term impacts of precipitation and burn extent on water chemistry, DOM character, and DBP formation in fire-affected watersheds.

5.2 Materials and Methods

5.2.1 Site Description and Sample Collection

Sampling took place after the Cameron Peak Fire was extinguished (January 2021). Stream water samples were collected in 2021 before, during, and after the first set of large monsoonal rainstorms: June 15th (pre-storm), August 4th (storm), and October 27th (post-storm). Stream water samples were collected from four catchments that differed by burn extent, defined here as the total area of moderate and high severity burns within a catchment. Burn severity was differentiated using

standard remote sensing approaches.[465] High and moderate severity fires combust and kill most vegetation and organic soil layers[37] and typically generate significant short term watershed responses.[466] Streams were then selected based on the total area of moderate and high severity burns throughout the catchment: South Lone Pine (5,501 acres): 24% burned with 14% at moderate-high severity (Low-BE), Bennett (9,209 acres): 70% burned with 38% at moderate-high severity (Moderate-BE), Fish (3,242 acres): 86% burned with 57% at moderate-high severity (High-BE1), and Little Beaver (11,561 acres): 86% burned with 68% at moderate-high severity (High-BE2). Samples were collected in high density polyethylene sample containers that were cleaned and rinsed in the sample stream prior to collection, then frozen at -4°C until filtered.

5.2.2 Water Chemistry Measurements

Stream samples for dissolved organic carbon (DOC) and total dissolved nitrogen (TDN) analyses were collected in amber borosilicate glass bottles. Prior to use, plastic bottles (high density polyethylene) were triple washed with de-ionized water (SC < 1.0 μS cm^{-1}), and glass bottles were combusted for 1 hour at 500 °C in a muffle furnace. Samples were refrigerated after collection, then DOC and TDN samples were filtered through 0.7μm mesh glass fiber pre-filters (Millipore Corporation, Billerica, MA, USA). Samples were analyzed within 72 hours of collection. Turbidity was measured in 1 L samples using the nephelometric method (HF Scientific, Inc. Micro 100 Turbidimeter).[467] Both DOC and TDN were determined by high-temperature combustion catalytic oxidation using a Shimadzu TOC-V_{CPN} total organic carbon analyzer with a TNM-1 total nitrogen detection unit (Shimadzu Corporation Columbia, MD, USA). Detection limits for DOC and TDN were 0.05 mg L^{-1}.

5.2.3 Spectroscopic Measurements

Stream waters were analyzed using a Horiba Scientific Aqualog (Horiba-Jobin Yvon Scientific Edison, New Jersey, US) with excitation and emission wavelengths from 200-800 nm

at 3 nm intervals and scan times of 2 seconds. Filtered samples were diluted to 5 mg C/L prior to analysis to reduce inner-filter effects and normalize their concentrations. A sealed cuvette of deionized water was used as a blank for each sample run to correct for instrument drift. The samples were corrected for inner-filter effects and Rayleigh scatter was masked using first and second grating orders after spectral analysis. Finally, each spectrum was normalized by the area of the deionized water Raman scattering peak, as determined by the blank.[468] From this, the fluorescence index (FI, Equation 1),[305,469] and humification index were calculated (HIX, Equation 2).[470,471]

$$FI = \frac{emission\ 470nm}{emission\ 520nm}\ at\ 370\ nm\ excitation \qquad \text{(Equation 1)}$$

$$HIX = \frac{\sum_{435\ nm}^{480\ nm} emission}{\sum_{300\ nm}^{345\ nm} emission}\ at\ 254\ nm\ excitation \qquad \text{(Equation 2)}$$

5.2.4 Fourier Transform Ion Cyclotron Resonance Mass Spectrometry

Stream water samples were centrifuged for 10 min at 5000 rpm followed by filtering through a 0.2 μm poly(ether sulfone) filter. Samples were then acidified to pH 2 with trace-metal grade HCl and prepared for FT-ICR MS using solid-phase extraction with styrene-divinylbenzene (SDVB) polymer modified with a proprietary nonpolar surface (Bond Elut PPL, Agilent Technologies). Samples were extracted using methanol (HPLC grade, Sigma Aldrich Chemical Co., St. Louis, MO) to about 50 ppm carbon concentrations and then measured at the National High Magnetic Field Laboratory in Tallahassee, Florida.

Extracts were analyzed with a custom-built hybrid linear ion trap FT-ICR mass spectrometer equipped with a 21 T superconducting solenoid magnet.[193,343] Sample solutions were infused via a microelectrospray source (50 μm i.d. fused silica emitter) at 500 nL/min by a syringe pump.[346] Typical conditions for negative ion formation were: emitter voltage, -2.4-2.9 kV; tube lens, –250 V; and heated metal capillary current, 7 A. Positive mode electrospray ionization was selected based on

the enhanced speciation of nitrogen species in PyOM.[18] Ions were initially accumulated in an external multipole ion guide (1-5 ms) and released m/z-dependently by a decreasing auxiliary radio frequency potential between the multipole rods and the end-cap electrode.[323] Ions were excited to m/z-dependent radius to maximize the dynamic range and number of observed mass spectral peaks (m/z 200-1500; 32-64%), and excitation and detection were performed on the same pair of electrodes.[326] The dynamically harmonized ICR is operated with 6 V trapping potential.[325] Time-domain transients of 3.1 seconds were acquired with the Predator data station, with 100 time-domain acquisitions averaged for all experiments, which were initiated by a TTL trigger from the commercial Thermo data station. Peaks with signal magnitude greater than six times the baseline root-mean-square (rms) noise at m/z 500 were exported to peak lists, phase-corrected,[348] and internally calibrated on the basis of the "walking" calibration method.[189] Experimentally measured masses were converted from the International Union of Pure and Applied Chemistry (IUPAC) mass scale to the Kendrick mass scale for rapid identification of homologous series for each heteroatom class (i.e., species with the same $C_cH_hN_nO_oS_s$ content, differing only be degree of alkylation).[225] Molecular formulae containing carbon (C), hydrogen (H), oxygen (O), nitrogen (N), and sulfur (S) were assigned and visualized with PetroOrg© software.[201] Molecular formula assignments with an error >0.4 parts-per-million were discarded, and only heteroatom classes with a combined relative abundance of ≥0.15% of the total were considered. While isotopes were assigned and used to clarify peak assignments, isotopes and sodiated adducts were omitted in the plots, tables, and discussion here. Assigned elemental formulas of neutral species were used to calculate the double-bond-equivalents (DBE, Equation 3)[216,472] and modified aromaticity indices (AI_{Mod}, Equation 4)[216,472] where C = the number of carbon, O = the number of oxygen, and so on.

$$DBE = 1 + C - O - S - \frac{1}{2}(N + P + H) \qquad \text{(Equation 3)}$$

$$AI_{Mod} = \frac{1+C-O-S-\frac{1}{2}(N+H)}{C-\frac{1}{2}O-N-S} \quad \text{(Equation 4)}$$

Plot regions were indicated based on molecular bonding constraints, where assignments colored as orange and red include aromatic and CA moieties in their structures ($AI_{mod} > 0.5$ and $AI_{mod} \geq 0.67$), respectively. Green points indicate the assignments above the molecular lability boundary (MLB, $H/C \geq 1.5$)[473] that corresponds with generally more labile residues, and grey points represent are mid-saturated (MS) and lie between the more aliphatic MLB and aromatic plot regions. These designations are not all encompassing but have been applied previously and found to be in good agreement in studies with accompanying biological and spectroscopic measurements.[292,474,475]

5.2.5 Disinfection Byproduct Formation Measurements

Disinfection byproduct formation was assessed using uniform formation conditions (UFC).[476] Chlorine demand was initially assessed in each sample by varying the Cl_2:TOC ratio from 1:1 to 2.5:1 in multiple aliquots, and measuring residual chlorine after 24 hours. The chlorine dose which resulted in a residual of 1 ± 0.4 mg/L Cl_2 after 24 hours was selected and repeated on a 70 mL aliquot. After 24 hours, chlorine residual was measured and the sample was then quenched with ascorbic and hydrochloric acid. DBPs were then measured using gas chromatography – electron capture detection (GC-ECD, Agilent 8860). Four THMs, six HANS, and four HAMs, and chloropicrin were quantified using EPA method 551.1. Nine HAAs were quantified using EPA method 552.2.

5.3 Results and Discussion

5.3.1 Stream Water Chemistry Changes with Burn Extent

Streams located within the Cameron Peak Fire perimeter were sampled to elucidate changes to water quality before, during, and following a storm event. Figure 5.1 displays the DOC, TDN, and turbidity for four streams differentiated by burn extent: Low-BE, Moderate-BE, High-BE1, and

High-BE2. Fluorescence spectra were also collected for the samples and used to calculate different indices: the fluorescence index (FI) that approximates DOM source where higher values indicate microbially-derived OM (e.g., extracellular release from bacteria/algae) and lower values indicate terrestrially-derived OM (e.g., decomposing plant matter and SOM);[305,469] and the humification index (HIX) that approximates "humification", where higher values generally indicate more aromatic, phenolic, and carboxylic acid features and correlate with pyOM.[470,471,474] All values plotted in Figure 5.1 can be found in Table 5.1.

In each of the streams, the DOC concentration increased during the storm and then decreased during the post-storm measurement to nearly pre-storm values. The TDN also increased during the storm and decreased during the post-storm event for High-BE1 and High-BE2, but Low-BE and Moderate-BE decreased continuously relative to the pre-storm event. The turbidity increased during the storm for each stream and then decreased during post-storm events for Moderate-BE, High-BE1, and High-BE2. Low-BE was the exception that increased in turbidity at the post-storm event.

The difference in TDN between streams is only distinct during the storm, after which the TDN decreases to a minimum for each stream during the post-storm event. This may result from the mobilization and transportation of organic and inorganic nitrogen that can accumulate in ash and be mobilized during the storm.[376,382,453] While turbidity generally increases with burn extent compared to unburnt watersheds,[36] the turbidity of stream samples here is initially similar at pre-storm. The increasing turbidity in Low-BE might be evidence of progressive erosion and runoff compared to the larger changes driven by the storm at Moderate/High-BE,[477] though erosion can vary substantially within fire-affected and unburnt watersheds.[449,478]

For High-BE1 and High-BE2, the FI increased slightly or stayed relatively the same during the storm and then decreased during the post-storm event to near or below pre-storm values. In

comparison, the FI of Low-BE and Moderate-BE increased continuously. Low-BE FI was lowest at the pre-storm event but resembled High-BE1 and High-BE2 by the post-storm (~1.5), whereas Moderate-BE was greater (~1.6). The HIX was lowest in Low-BE followed by Moderate-BE, High-BE1, and High-BE2. While there was no distinct pattern between events, the HIX was greater in Moderate/High-BE during the storm compared to Low-BE, which stayed approximately the same. By the post-storm event, the Low-BE HIX increased, and Moderate/High-BE decreased to below pre-storm values and Low-BE.

The FI and HIX in the Moderate/High-BE is likely greater than the Low-BE during the pre-storm and storm events because more plant- and SOM-derived residues were removed and more pyOM was present relative to the Low-BE, as opposed to the addition of microbially-derived DOM. The increase in DOC and FI of each stream during the storm also indicates that the DOM mobilized by the storm primarily resembled microbially-derived DOM (to a lesser extent for High-BE2 that stayed the same). While the high burn extent streams decrease in FI during post-storm to near pre-storm values, the increase in FI in low/moderate streams at the post-storm event suggests more microbially-derived DOM.

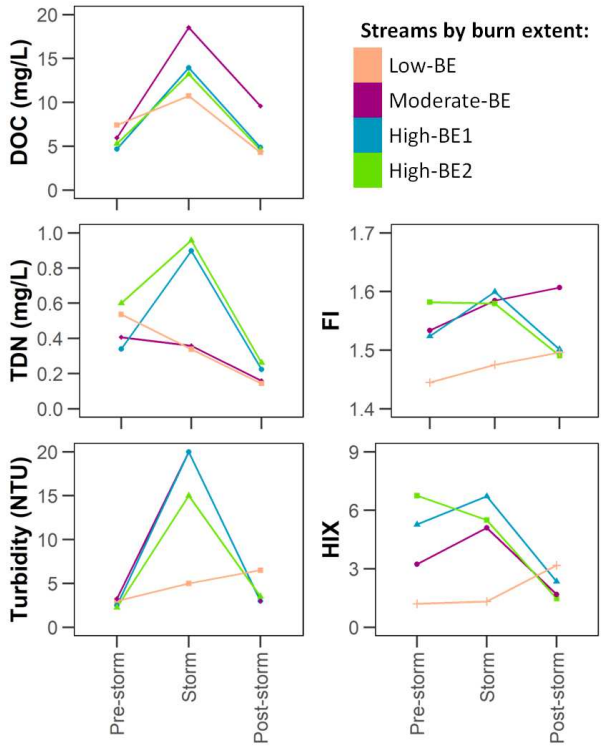

Figure 5.1. Measurements of water chemistry (DOC, TDN, and turbidity) and fluorescence indices (FI and HIX) for each event and stream, colored by burn extent.

Table 5.1. Water chemistry measurements for selected samples used in fluorescence, FT-ICR MS, and DBP analysis

Burn Extent	Event	DOC (mg/L)	TDN (mg/L)	Turbidity (NTU)	SC (µS/cm)	FI	HIX
Low-BE	Pre-storm	7.41	0.54	3.0	45.8	1.186	2.916
	Storm	10.74	0.34	5.0	63.1	1.210	4.062
	Post-storm	4.29	0.14	6.5	53.8	1.214	6.753
Moderate-BE	Pre-storm	5.96	0.41	3.3	111.3	1.273	5.272
	Storm	18.53	0.36	20.0	110.1	1.356	2.762
	Post-storm	9.59	0.16	3.0	128.6	1.303	8.156
High-BE1	Pre-storm	4.68	0.34	2.5	58.2	1.269	3.162
	Storm	13.95	0.90	20.0	91.6	1.348	1.472
	Post-storm	4.87	0.22	3.0	64.6	1.223	2.343
High-BE2	Pre-storm	5.30	0.60	2.3	42.3	1.327	5.915
	Storm	13.21	0.96	15.0	72.3	1.347	7.191
	Post-storm	4.58	0.26	3.5	57.5	1.192	3.173

5.3.2 21 T FT-ICR MS reveals Enriched Nitrogen Heteroatom Classes

Broadband positive-ion 21 tesla ESI FT-ICR mass spectra were collected for DOM at each event (total of 12 FT-ICR mass spectra) and are shown in Figure D.1. All samples spanned a similar mass-to-charge range between m/z 150 – 1000, centered ~m/z 450 – 550 with an achieved resolving power > 1,600,000 at m/z 400 (m/Δm50%, where Δm50% = mass spectral peak width at half-maximum peak height). The total number of assigned species within each heteroatom class is shown in Table 5.2, with the most species assigned in the storm High-BE1 (15,822) and fewest in the pre-storm Low-BE (6741).

Table 5.2. Molecular formula assignments made in each stream water sample separated by heteroatom class with the total number of assignments and relative abundance-weighted average molecular weight.

Sample	Event	CHO (w/ isotopes and Na adducts)	CHNO (w/ isotopes and Na adducts)	CHNOS (w/ isotopes and Na adducts)	CHOS (w/ isotopes and Na adducts)	Total Assignments	R.A.-weighted Average Molecular Weight (Da)
Low-BE	Pre-storm	4421	2320	0	0	6741	463.3595
	Storm	4495	5837	13	8	10353	460.2941
	Post-storm	6369	5702	0	32	12103	478.3879
Moderate-BE	Pre-storm	6361	4902	4	17	11284	480.1371
	Storm	5309	6582	8	8	11907	426.5996
	Post-storm	6403	4833	0	27	11263	486.4058
High-BE1	Pre-storm	6191	4550	0	21	10762	469.3556
	Storm	6208	9546	20	48	15822	434.9716
	Post-storm	4321	4015	8	9	8353	475.7207
High-BE2	Pre-storm	6678	5037	4	23	11742	476.756
	Storm	5380	6175	5	25	11585	435.3853
	Post-storm	5681	4069	0	29	9779	478.7175

During the pre-storm, each stream was predominated by the CHO class which was highest in Low-BE (66%) and lowest in the Moderate-BE (56%), with CHNO comprising the next largest class and was lowest in Low-BE (34%) and highest in Moderate-BE (43%), though Moderate/High-BE streams were within 1% of each other. During the storm, the total assignments in each stream increased or stayed relatively the same and the CHNO class became the largest, increasing to up to 55 – 60% of the total assignments in each stream. This coincided with an increase in DOC and FI

across all streams, indicating that the storm introduced nitrogen-containing species that resembled microbially-derived residues. Interestingly, CHNO species with multiple nitrogen were also enriched during the storm and is demonstrated in Figure 5.2 when separating the CHNO heteroatom class by nitrogen content ($N_{1\text{-}4}O_x$,). This enrichment matches observations following heating ≤450°C in water-extractable organic matter of soils,[24,376] where >450°C resulted in very little organic matter remaining. This suggests that DOM mobilized by the storm may originate primarily from less severely burnt areas in each catchment, regardless of burn extent. The average C/N ratio (calculated only using CHNO assignments, Figure D.2) also differed between burn extents, where Low-BE and Moderate-BE decrease during the storm and the High-BE1 and High-BE2 increase in C/N during the storm. This inverse relationship could be related to the change in predominant features of each stream during the storm, where High-BE1 exhibits the highest number of unique CHNO and largest increase in N_1O_x assignments during the storm and the Low-BE exhibits the largest increase in $N_{2\text{-}4}O_x$ class assignments.

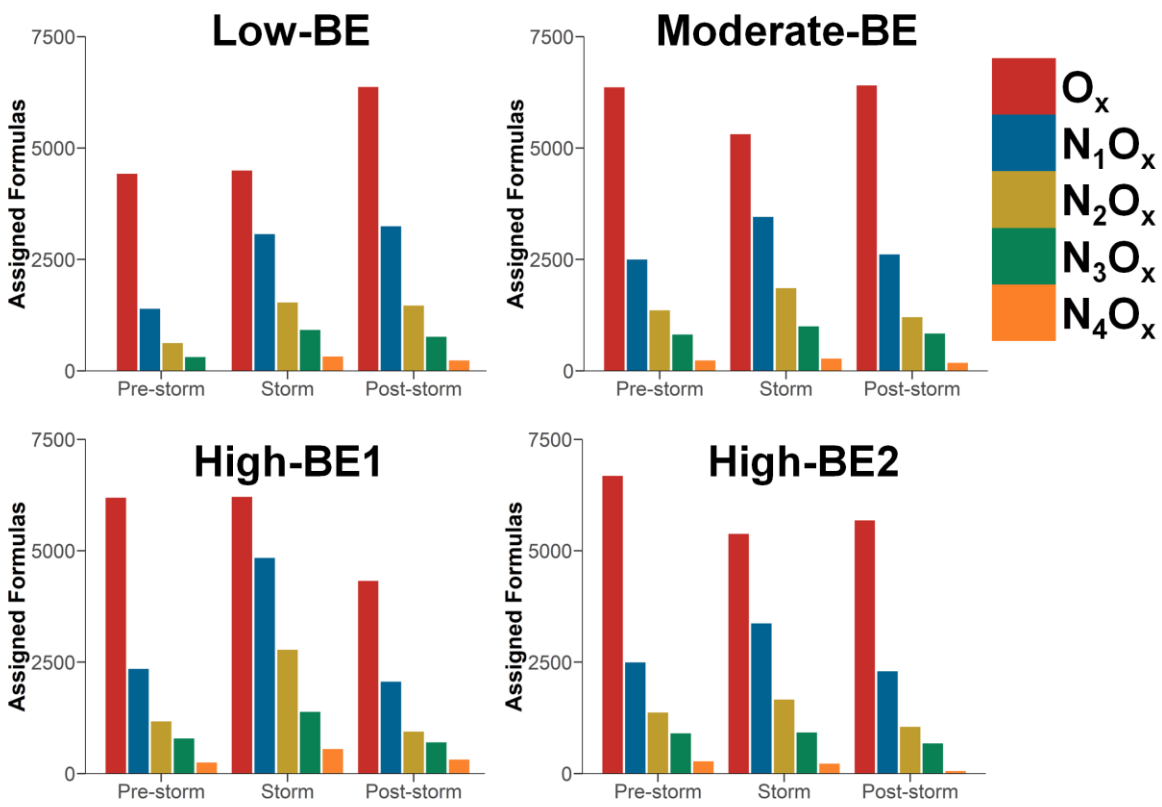

Figure 5.2. Number of assigned molecular formulas of the CHO and CHNO heteroatom classes for each sample and event. CHNO classes are distinguished by nitrogen content ($N_{1\text{-}4}O_x$).

By the post-storm, the CHO class was the largest in each stream but at lower proportions compared to pre-storm (51 – 58%). However, the post-storm Low-BE was the only stream to remain high in CHNO assignments compared to the storm (from 5837 to 5702), where other streams decreased and was most notable in High-BE1 (from 9546 to 4015). The CHO assignments also increased in the Low-BE (from 4495 to 6369) and Moderate-BE (from 5309 to 6403) and, based on the FI during post-storm, may correspond with microbially-derived residues.

5.3.3 Nitrogen Speciation indicates Unique Storm DOM

Figure 5.3 shows van Krevelen diagrams (VKDs) that plot atomic H/C versus O/C ratios for O_x and N_yO_x species derived from positive-ion ESI FT-ICR MS for Low-BE and High-BE1. VKDs provide rapid visualization of qualitative compositional changes between samples that can be used to identify differences in hydrogen saturation and oxygen content.[16] Figure 5.3 is separated by species assigned in all events for a stream (common), followed by peaks that are only identified (unique) in the pre-storm, storm, and post-storm samples. Plot regions were indicated based on molecular bonding constraints, where assignments colored as orange and red likely include aromatic and condensed aromatic (CA) moieties in their structures ($AI_{Mod} > 0.5$ and $AI_{Mod} \geq 0.67$), respectively.[216] Green points indicate assignments above the molecular lability boundary (MLB, $H/C \geq 1.5$)[473] that corresponds with more labile residues. Grey points are mid-saturated (MS) assignments and plot between the MLB and AI_{Mod} plot regions. The number of assignments for each plot region are separated in Table 5.3. Sulfur-containing heteroatom classes (i.e., CHOS, CHNOS) were only minor fractions of the FT-ICR mass spectra and were omitted from this discussion; total counts for elemental composition assignments, separated by heteroatom class, are shown in Table 5.2. Analogous VKDs for Moderate-BE and High-BE2 are shown Figure 5.4 and, while generally similar to High-BE1, differences will be noted below.

In Low-BE (Figure 5.3A), all events shared a fraction of the total peaks near the center of the VKD for both CHO (3877) and CHNO assignments (2289). The number of assignments plotted in each region was highest in order from MS > aromatic > MLB > CA. Unique peak distributions in the pre-storm were also similar amongst samples, where for Low-BE, peaks were mostly centered or towards the edges of the compositional space shared by the common peaks (O/C: 0.0 – 0.8, H/C: 0.4 – 1.7). The unique assignments in each region were highest in order from MS > aromatic > CA > MLB. These observations were similar for the common and unique pre-

storm peaks with the Moderate/High-BE streams (Figure 5.4). Additionally, 5762 peaks were common between every stream and event, and spanned between MS, aromatic, and CA plot regions (Figure 5.5). The common formulas likely originate from similar stream inputs, vegetation, and microbial processing from upstream snowmelt of the sampled watersheds and indicates that there is a common background DOM signature between streams.

During the storm event, unique CHNO assignments increased considerably and plotted over a large compositional space in each stream, densely encompassing and extending the range of H/C values. The Low-BE H/C range increased (H/C: from 0.4 – 1.7 to 0.3 – 1.9) with the greatest number of unique peaks in plot regions in order from MS > MLB > aromatic > CA, which switches aromatic and MLB in order compared with the pre-storm. The enriched plot regions and compositional space exhibited the same pattern in Moderate/High-BE during the storm, where DOM introduced during the storm appeared to be comprised of a diverse suite of aliphatic and aromatic compounds. The number of assignments in the MLB plot region were also greatest in order of High-BE1 > High-BE2 ~ Moderate-BE > Low-BE.

During the post-storm event, Low-BE exhibited a unique spectrum compared to the Moderate/High-BE: the number of unique CHO assignments increased (from 614 to 1999), and the number of unique CHNO assignments stayed similar between storm and post-storm events (from 3547 to 3384). The O/C and H/C range also increase slightly (O/C: from 0.0 – 0.8 to 0.0 – 0.9, H/C: from 0.3 – 1.9 to 0.2 – 1.9). The Low-BE post-storm CHO and CHNO assignments encompassed a large compositional space compared to the common peaks. This differed for the Moderate/High-BE streams where fewer unique species were assigned during the post-storm event. For example, from storm to post-storm for High-BE1, the number of unique CHO and CHNO assignments decreased by an order of magnitude (CHO: from 828 to 85, CHNO: 5170 to 522). The H/C range decreased (H/C: from 0.2 – 2.0 to 0.5 – 1.9).

Changes to DOM composition as a function of burn extent were most distinct during the post-storm, where unique peaks in Moderate/High-BE streams diminished to a fraction of what was unique during the storm. Interestingly, the Low-BE exhibited the highest number of unique CHNO assignments by the post-storm event (3338) of which 2550 of these CHNO assignments were also assigned in the Low-BE storm event. The similarity in nitrogen assignments suggests that even after DOC concentration returns to pre-storm conditions, storm impacts may persist or enact changes that alter post-storm composition to Low-BE stream catchments. For example, the unique peaks in the Low-BE post-storm sample may reflect residues released by plants and microbes "stimulated" by precipitation relative to the higher burn severity samples,[479] but would need further investigation into microbial community structures and additional sample replicates to fully investigate. The unique peaks also correspond with the increasing Low-BE turbidity and FI, though FI values can vary substantially within watersheds.[480]

Table 5.3. Common and unique molecular formula assignments from the pre-storm, storm, and post-storm event in the Low-BE and High-BE categorized by plot regions indicating more labile (MLB), aromatic, condensed aromatic (CA), and mid-saturated (MS) features.

Low-BE	Number of CHO Assignments				Number of CHNO Assignments			
Event	Aromatic	CA	MLB	MS	Aromatic	CA	MLB	MS
Common	586	145	196	2950	194	17	124	1954
Pre-storm	122	76	17	325	7	0	0	23
Storm	50	38	156	370	364	139	604	2440
Post-storm	280	149	252	1318	372	179	470	2363

High-BE1	Number of CHO Assignments				Number of CHNO Assignments			
Event	Aromatic	CA	MLB	MS	Aromatic	CA	MLB	MS
Common	580	138	216	3239	316	51	238	2834
Pre-storm	142	59	0	610	20	1	0	153
Storm	52	101	393	282	446	280	1242	3202
Post-storm	0	0	76	9	21	11	67	423

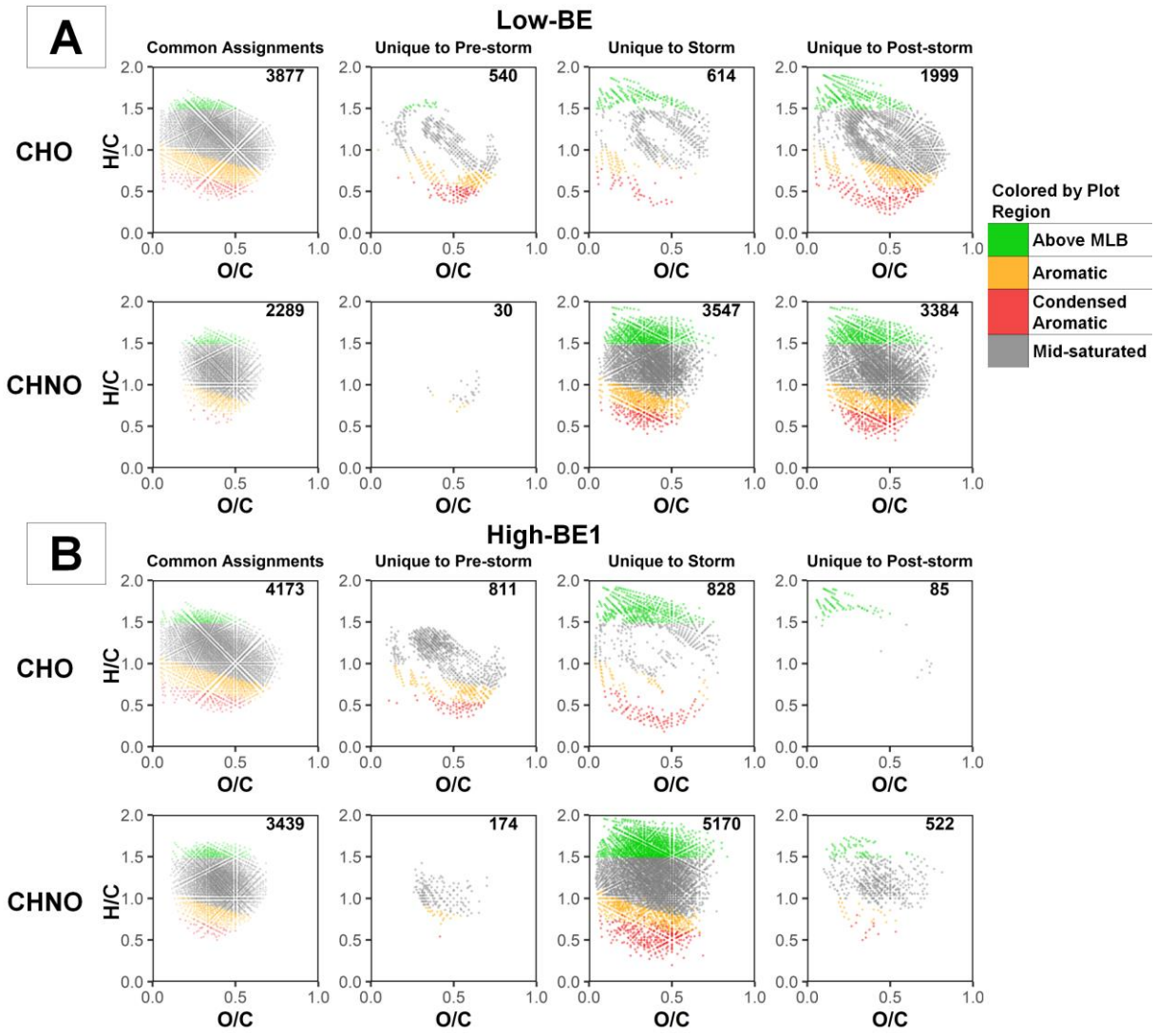

Figure 5.3. Van Krevelen plots of the common and unique species measured in positive-ion ESI FT-ICR MS for Low-BE and High-BE1 burn extent streams across each event. Common assignments were common formulas between all events in a given stream and assignments were considered unique if they were not assigned in the pre-storm spectra (unique peaks in the pre-storm were absent from storm and post-storm). Points are colored based on their compositions where assignments colored as orange and red correspond with aromatic and condensed aromatic (CA) moieties in their structures ($AI_{mod} > 0.5$ and $AI_{mod} \geq 0.67$), respectively.[216] Green points indicate the assignments above the molecular lability boundary (MLB, $H/C \geq 1.5$)[473] that corresponds with more labile residues, and grey points lie outside these boundaries.

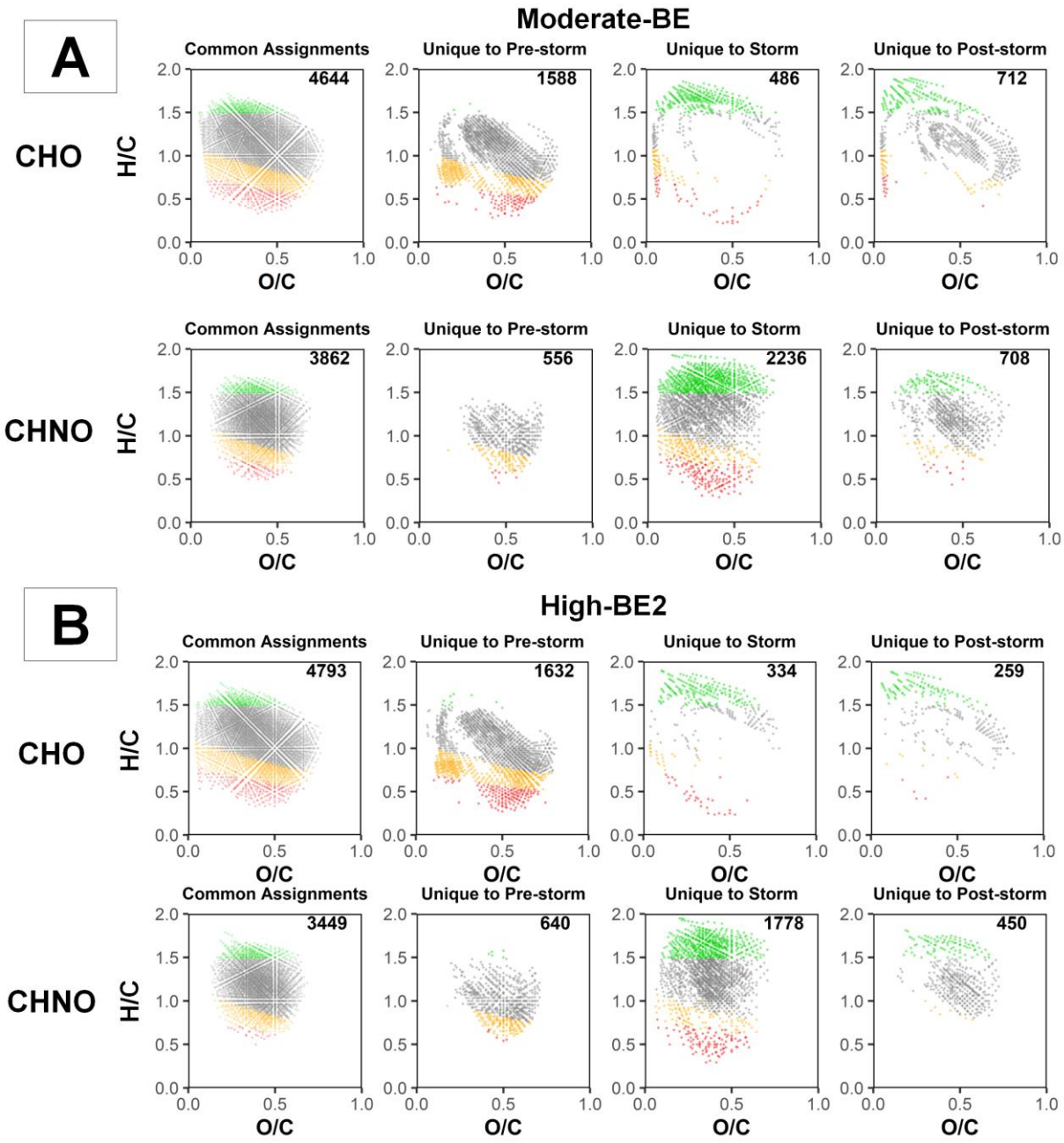

Figure 5.4. Van Krevelen plots of the common and unique species measured in positive-ion ESI FT-ICR MS for Moderate-BE and High-BE2 streams across each event. Common assignments were common between all events in a given stream and assignments were considered unique if they were not assigned in the pre-storm (unique peaks in the pre-storm were absent from storm and post-storm). Points are colored based on their compositions where assignments colored as orange and red include aromatic and condensed aromatic moieties in their structures ($AI_{mod} > 0.5$ and $AI_{mod} \geq 0.67$), respectively.[216] Green points indicate the assignments above the molecular lability boundary (MLB, $H/C \geq 1.5$)[473] that corresponds with more labile residues, and grey points lie outside these boundaries.

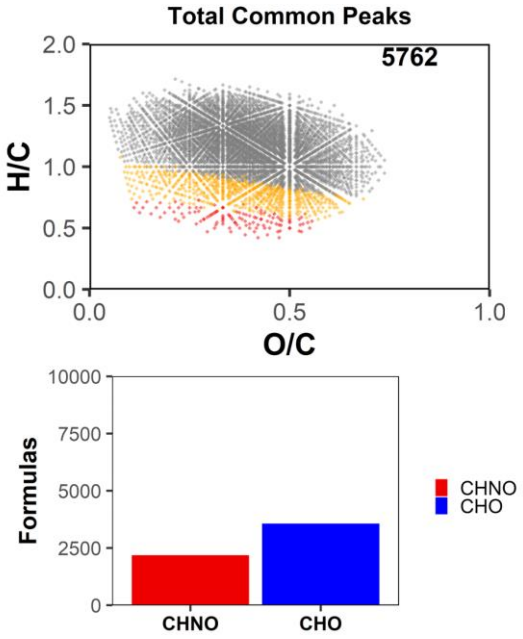

Figure 5.5. Common peaks amongst the FT-ICR mass spectral assignments between every sample stream and event, where assignments colored as orange and red include aromatic and condensed aromatic moieties in their structures ($AI_{mod} > 0.5$ and $AI_{mod} \geq 0.67$), respectively (top).[216] Grey points lie outside these boundaries. Distribution of formulas between CHNO and CHO is also indicated in the bar graph (below).

5.3.4 Storm Impacts DOM Saturation and Oxygen Content

The unique peaks expanded the range of O/C and H/C ratios of the DOM in each stream and some common compositional shifts could be observed by event. To simply illustrate how compositional features shift between each event in every stream, Figure 5.6 shows the relative abundance-weighted average H/C and O/C values from all formula assignments from each stream. The range of compositional space (O/C: 0.36 – 0.41, H/C: 1.11 – 1.19) encompassed is relatively small compared to those in Figure 5.3 and 5.4 and is primarily a function of the common assignments between each stream and event (Figure 5.5). From the pre-storm to storm event, stream DOM exhibited lower average O/C and higher average H/C values across all sites. From the storm to post-storm event, stream DOM exhibited higher O/C and lower H/C values, though the post-storm average O/C and H/C remain higher than pre-storm values in all streams. The similarity in

shifts and relative grouping of the streams during each event is further evidence of a common effect of the storm on each stream, where specific changes to molecular features are explored below.

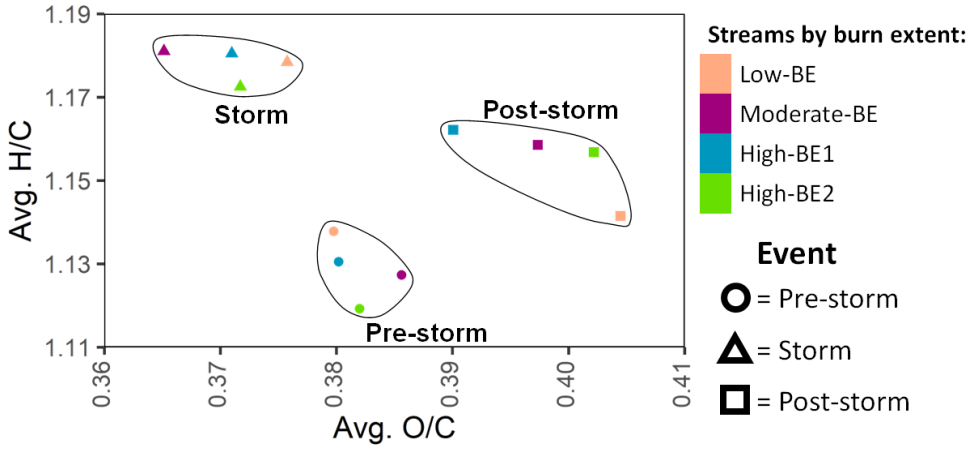

Figure 5.6. Relative abundance-weighted average H/C and O/C ratios for each of the stream samples during each event. Color scale distinguishes streams, where pre-storm (circle), storm (triangle), and post-storm (square) are grouped.

To distinguish features that contribute to the shift in composition, DOM assignments were plotted by double-bond-equivalents (DBE) (Figure 5.7 and D.3) and nominal oxidation state of carbon (NOSC) (Figure 5.8 and D.4). Peaks were grouped by their abundances, where the "top 25%" (dark blue points) are 25% of the sample's cumulative abundance comprised of the most abundant formulas, the "second 25%" is the next 25% comprised of the next most abundant formulas, and so on. Assignments were separated by species in all events for a stream (common), followed by peaks that are only identified (unique) in the pre-storm, storm, and post-storm samples. DBE and NOSC plots for Moderate-BE and High-BE2 are shown in Figure D.3-D.4 and were generally similar to High-BE1 and differences will be noted below.

Figure 5.7 shows the DBE vs. carbon number (C) of assignments in the Low-BE and High-BE1. As noted above, a large background DOM signal is present based on the common assignments that centers at ~10 DBE and ~20 carbon in each stream for both CHO and CHNO assignments.

Unique CHO species during the pre-storm overlapped with some of the common assignments and also included species with higher DBE and carbon number, and unique CHNO species generally fell within the same DBE vs. C range of the common assignments. During the storm, both CHO and CHNO exhibited unique peaks that extended the range of DBE and carbon compared to the pre-storm, but the most abundant unique peaks were centered ~5 DBE and ~15 carbon, decreasing compared to the pre-storm assignments. Like Figure 5.3 and 5.4, the CHNO class of each stream exhibited a more densely occupied compositional space relative to the CHO class during the storm, where the enrichment of low DBE species is consistent with the enrichment of the aliphatic residues in the MLB plot region.

By the post-storm, the unique CHNO species decreased compared to the storm but included more unique species with higher and lower DBE compared to the pre-storm. The most abundant unique CHO peaks also encompassed lower DBE and carbon ranges, though Low/Moderate-BE and High-BE2 exhibited unique but less abundant CHO species up to 26 DBE and 54 carbon. Low-BE was the most similar to its storm event by DBE vs. C range and also retained the most abundant low DBE assignments compared to the other streams.

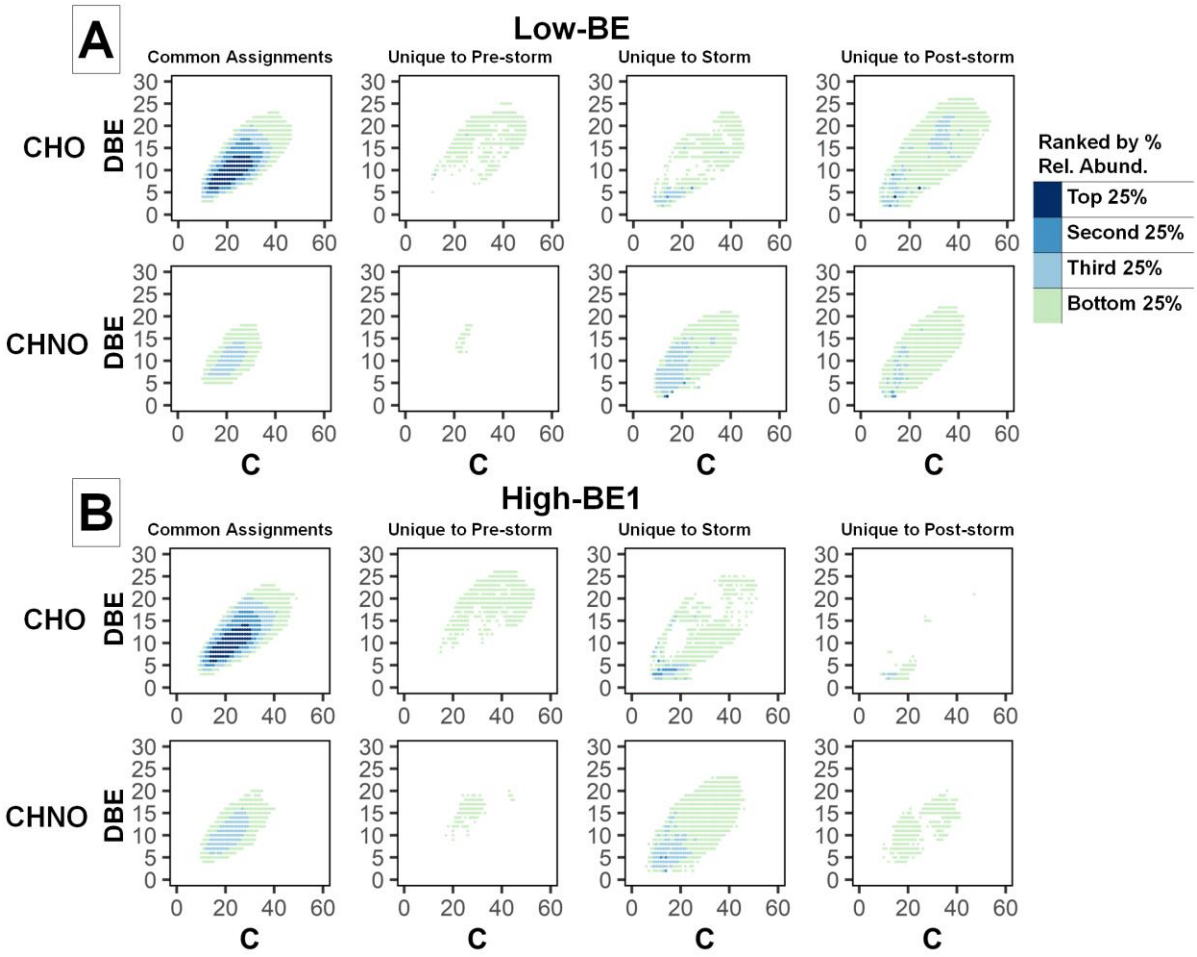

Figure 5.7. Double-bond-equivalents (DBE) of assignments in the Low-BE and High-BE1 streams, separated species in all events for a stream (common), followed by peaks that are only identified (unique) in the pre-storm, storm, and post-storm samples. Peaks were grouped by their abundances, where the "top 25%" (dark blue points) are 25% of the sample's cumulative abundance comprised of the most abundant formulas, the "second 25%" is the next 25% comprised of the next most abundant formulas, and so on.

Figure 5.8 shows the NOSC vs. carbon number (C) of assignments in the Low-BE and High-BE1, separated by species in all events for a stream (common), followed by peaks that are only identified (unique) in the pre-storm, storm, and post-storm samples. The most abundant common CHO assignments centered about NOSC ~-0.5, and the most abundant CHNO assignments centered about NOSC ~ -0.2. Trends were similar between DBE and NOSC during the storm and post-storm: during the storm, the unique CHNO species in each stream were enriched at lower NOSC and displayed a wider NOSC and C range compared to the pre-storm. Fewer abundant high

NOSC CHO species were assigned in the Moderate/High-BE compared to Low-BE, indicating a predominance of smaller, less oxidized CHO species that are reflected by the low O/C values during the storm. During the post-storm, the unique CHO and CHNO species were largely diminished but included more unique species with higher and lower NOSC than the pre-storm. Post-storm Low-BE exhibited a wide distribution of abundant high NOSC CHO species that coincides with the higher average O/C than the other streams.

The post-storm Low-BE displayed a somewhat bimodal CHO distribution centering at ~12 carbon (DBE: ~5, NOSC: ~-0.7) and ~35 carbon (DBE: ~19, NOSC: 0.3), where the higher DBE and NOSC species included unique assignments compared with the Low-BE storm and in other streams. This bimodal distribution indicates that the abundant moieties at Low-BE were split between aliphatic and aromatic features that may represent the presence of both microbially-derived residues and pyOM introduced to the stream by the post-storm. The enrichment of CHO and CHNO species in the MLB plot region with low molecular weight, DBE, and NOSC also appear to resemble a rapidly turned-over metabolite fraction released from soil microbial biomass.[306]

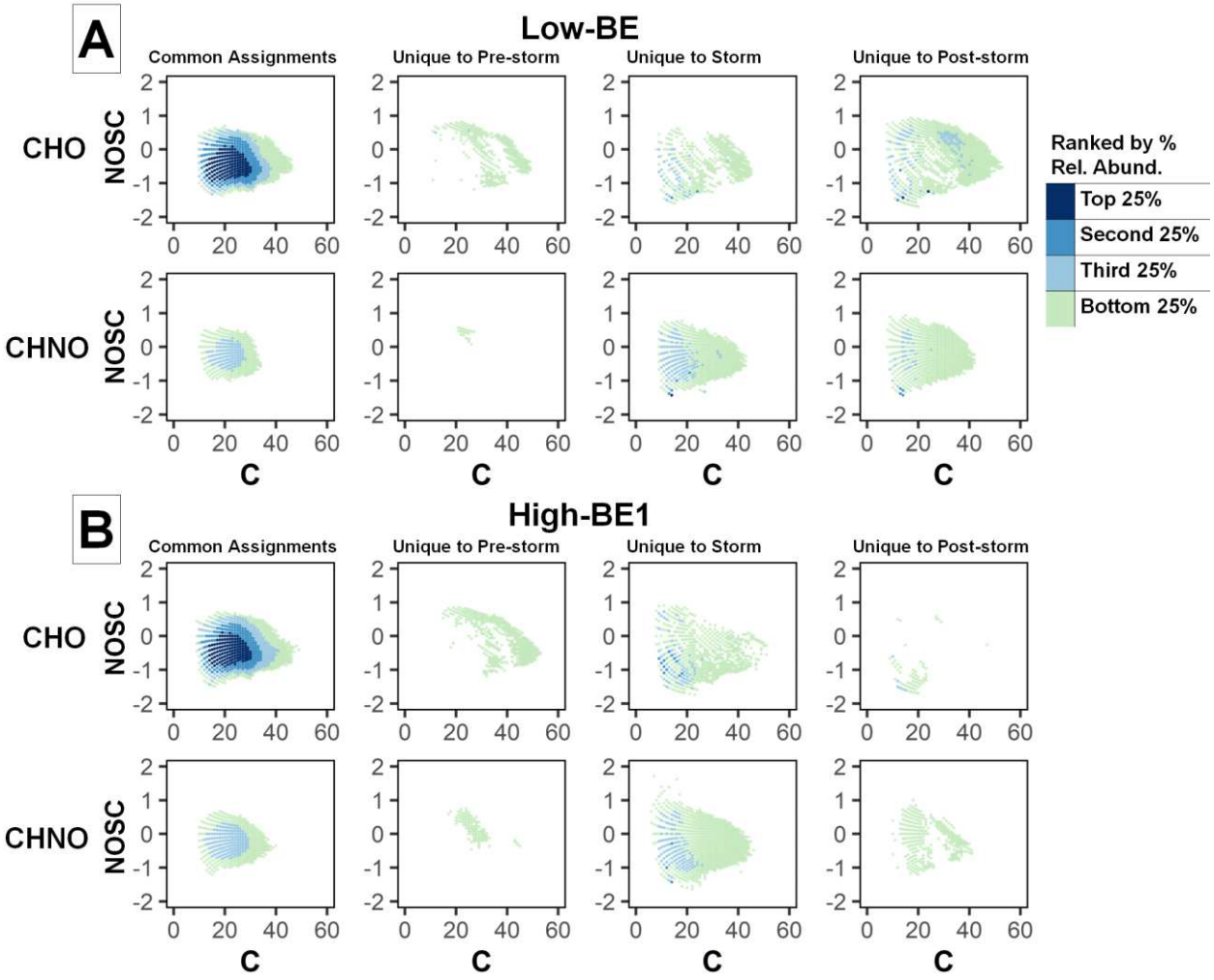

Figure 5.8. The nominal oxidation state of carbon (NOSC) vs. carbon numer for assignments in the Low-BE and High-BE1 streams, separated species in all events for a stream (common), followed by peaks that are only identified (unique) in the pre-storm, storm, and post-storm samples. Peaks were grouped by their abundances, where the "top 25%" (dark blue points) are 25% of the sample's cumulative abundance comprised of the most abundant formulas, the "second 25%" is the next 25% comprised of the next most abundant formulas, and so on.

5.3.5 Change in DOM Character influence Disinfection Byproducts Formed during Storm

To quantitatively determine how the difference in stream DOM composition will influence water quality downstream, stream water samples were chlorinated to measure DBPs, which included trihalomethanes (THM), haloacetonitriles (HAN), haloacetamides (HAM), and haloacetic acids (HAA). Figure 5.9 shows the DBPs formed during each event for Low-BE and High-BE1 by total concentration (Figure 5.9A) and normalized to the DOC of each sample and event (Figure 5.9B). An

analogous plot for Moderate-BE and High-BE2 can be seen in Figure 5.10; concentrations for each DBP identified here for each stream can be seen in Table D.1 and D.2.

While there was no precise trend across events as a function of burn extent, the moderate and high burn extent samples produced greater total DBP concentrations than Low-BE by a factor of ~2. For instance, the total DBP concentration (Figure 5.9A) was greater in High-BE1 compared to Low-BE at every event and is most prominent with chloroform (blue) that is about twice the concentration in High-BE1 compared to Low-BE at every event. Interestingly, DBP concentration normalized to the DOC in Low-BE and High-BE1 (Figure 5.9B) decrease from the pre-storm to storm and increase from the storm to post-storm. These trends for the total and DOC-normalized DBP concentrations are similar across burn extents and DBP classes, though the decrease in DOC-normalized DBP concentrations during the storm were more pronounced in Moderate/High-BE (Figure 5.10).

In Moderate/High-BE streams, the pre- and post-storm DOM formed fewer DBPs compared to the storm when normalized to DOC and reflects a lower reactivity of storm DOM introduced to form DBPs. The storm DOM at Low-BE formed a similar amount of DOC-normalized DBPs between the pre-storm and storm, where DBP precursors appeared to be largely absent for Low-BE and implies a lack a pyOM present during the pre-storm and storm.[463] The Low-BE also exhibited nearly double the DOC-normalized DBPs during the post-storm compared to the storm, and may correspond with unique aromatic and high DBE species (Figure 5.7) that could result from increased erosion (Figure 5.1). The observed increase in DOC and number of unique nitrogenous residues during the storm and post-storm for Low-BE did not correspond with enriched N-DBPs relative to the suite of DBPs measured, though total N-DBPs did trend similarly with the total carbonaceous DBPs through each event (Table D.1 and D.2). This contrasts with studies observing shifts toward more nitrogenous DBPs at higher burn severities both in lab and

field studies.[41,51,412] It is difficult to extrapolate how the burn extents used here compare to heating temperatures in laboratory settings, however the ~2-fold increase in DBPs in Moderate/High-BE compared to Low-BE indicates that DBP formation is greater in watersheds burnt at high severity and extent, matching previous observations.[481] The decrease in DOC-normalized DBPs during the storm indicates that residues introduced during the storm were not predominately reactive with chlorine.

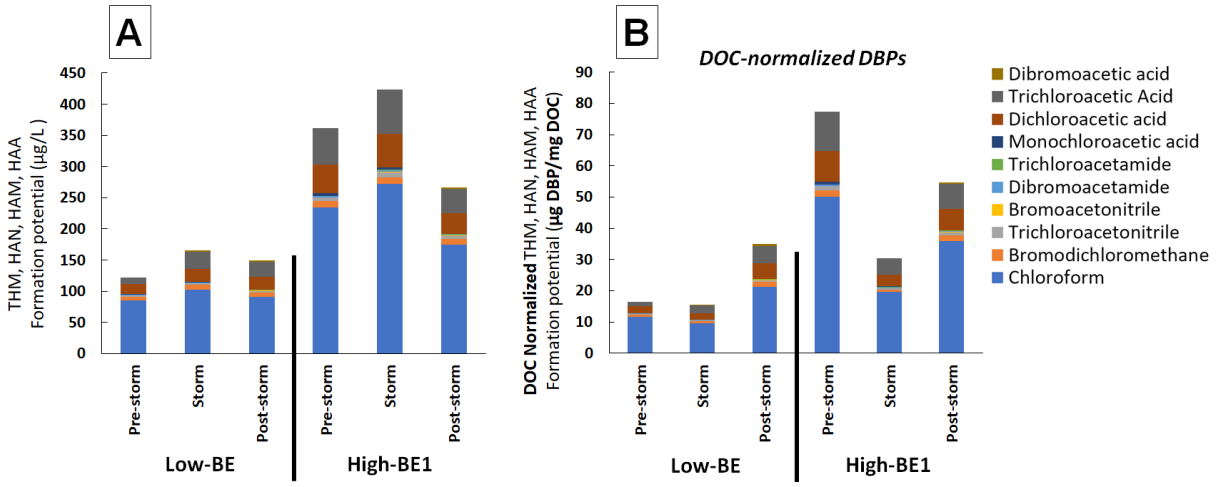

Figure 5.9. Concentration of disinfection byproducts (DBPs) for Low-BE and High-BE burn extent sample streams through each event after chlorination. A: total DBP concentration. B: DOC-normalized DBP concentration. Values for both total (Table D.1) and DOC-normalized (Table D.2) DBPs measured in each sample can be seen in Appendix D.

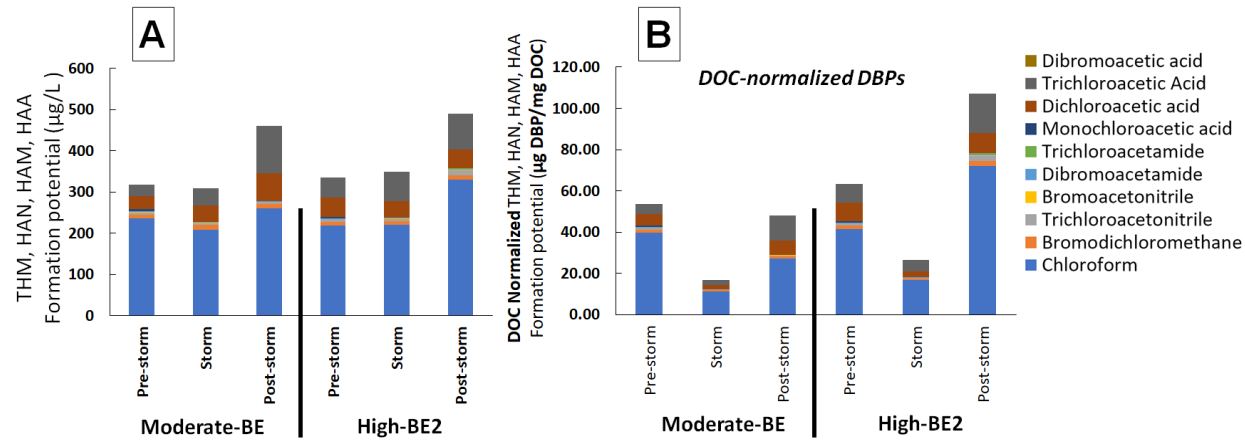

Figure 5.10. Concentration of disinfection byproducts (DBPs) for moderate (BENN) and high (LBEA) burn extent sample streams through each event after chlorination. A: total DBP concentration. B: DOC-normalized DBP concentration. Values for both total (Table D.1) and DOC-normalized (Table D.2) DBPs measured in each sample can be seen in Appendix D.

5.4 Environmental Implications

Although stream discharge in each draining catchment was not measured, seasonality and common environmental inputs throughout the watershed may help explain patterns in water chemistry measurements and DOM composition. For instance, each of the streams studied here contributes to the main stem of the Poudre River, which supplies the city of Fort Collins Municipality. Although there is high variability amongst the burn extents for average turbidities measured here, the range of turbidities fall within the median turbidity measurements along the main stem of the Poudre River from Summer through Fall 2021 (Summer: ~1 – 25, Fall: ~1 – 2 NTU) reported by the City of Fort Collins.[482] These ranges in water chemistry measurements also reflect seasonal hysteresis, defined differences between in-stream analyte concentrations and discharge, which has been demonstrated through Summer and Fall in smaller watersheds.[483] Molecular hysteresis can also influence DOM compositional measurements, where shifts in the predominant molecular characteristics have been measured during the storm onset and peak discharge.[49] As features shared by different streams trend similarly throughout the events, each of the streams appear to be affected similarly by shifts in precipitation and source water.

The enriched CHNO residues during the storm were predominately more saturated and less oxidized and might be related to biomolecules released during low temperature burning.[362,426] The unique nitrogen assignments could also represent labile microbial residues,[484] where the post-storm increase in unique assignments in the Low-BE compared to the other streams might also result from microbes that survived the Cameron Peak Fire at lower severities. A more diverse microbial community would produce a wider range of molecules following precipitation compared to the lower diversity of pyrophilous microorganisms that dominate at higher burn severities,[485] and higher FI values (Figure 5.1) have also been associated with DOM with longer residence times in soil before mobilization.[469] The unique peaks in the Low-BE post-storm sample may also reflect the

plants and microbes "stimulated" by precipitation relative to the higher burn severity streams through a positive feedback loop,[486] but would need further investigation into microbial community structures and additional sample replicates to fully investigate.

Although it is speculative to approximate the extent of pyOM, allochthonous, and autochthonous DOM introduced due to the compositional overlap of DOM sources observed in streams,[16,21,227,487,488] this is the first study noting the lack of DBP precursors mobilized during a storm in streams draining fire-affected catchments. The lack of influence of precipitation on the presence of DBP precursors might also explain persistent pyOM signatures in streams over longer time scales,[35,47] though the water solubility and prolonged leaching of pyOM residues is somewhat disputed due to their aromatic nature.[414] It should be noted that DBP precursors were outside of the m/z range measured using FT-ICR MS in this study, where changes in DBP precursor composition can only be extrapolated here and would require small molecule analysis to confirm. Despite this, the results here reaffirm that short-term declines in water quality will differ based on burn extent in a fire-affected watershed.

CHAPTER 6: SUMMARY

The purpose of the work presented here is to develop and apply methods to better understand the composition and quality of SOM in nature and after wildfires. The research detailed here achieves this by: (I) examining the application of FT-ICR MS as a tool to critically evaluate SOM, (II) developing data processing methods to improve SOM compositional analysis, (III) identifying changes in water-extractable SOM with laboratory heating at discrete heating temperatures, and (IV) measuring changes to water chemistry and DOM as a function of burn severity and extent through a wildfire-affected watershed.

First, a critical review of recent strategies for SOM characterization by FT-ICR MS is presented, with emphasis on SOM sample collection, preparation, analysis, and data interpretation (Chapter 2). The heterogeneity of SOM, soil surfaces, and microenvironments means that no extraction method will capture every fraction of SOM. Fractions of interest can be collected by targeting specific SOM sorption mechanisms, where the most common are water, alkaline, mineral dissolution, and organic extractions. Different ionization techniques must then be considered as each technique exhibits selectivity based on ionization mechanism and analyte composition. The most common ionization technique for SOM and DOM is electrospray ionization in negative mode, though other techniques and positive mode analyses can be applied to probe less acidic, more hydrophobic SOM and DOM residues. After ionization and detection, mass calibration and molecular formula assignment can be completed but numerous assumptions are applied depending on the method. Constraining the data with *a priori* knowledge such as heteroatom content and functional group characteristics can improve formula assignment and visualization substantially. To contextualize qualitative FT-ICR MS results, corroborative elemental, spectroscopic, chromatographic, microbial analyses, and statistical methods are recommended. Future work on FT-ICR MS methods to study SOM would benefit from unified sample preparation, automated internal

calibration, new solution-based ionization techniques, and a unified database repository that would increase the reproducibility and accessibility of FT-ICR MS to probe SOM across a broad range of sample matrixes.

Second, SRFA was measured using a custom built, 21 tesla hybrid linear ion trap FT-ICR mass spectrometer to investigate DOM complexity and the influence of peak-picking threshold on molecular formula assignment (Chapter 3). The effect of peak-picking threshold at 3σ, 4σ, 5σ, and 6σ was compared by number of elemental composition assignments, mass measurement accuracy, and dynamic range across the mass range of m/z 200−1200. More than 36,000 species were assigned with signal magnitude greater than 3σ at root-mean-square mass error of 36 ppb. This is a large improvement over the assignments at 6σ, where over 23,000 species were assigned with signal magnitude greater than 6σ and root-mean-square mass error of 25 ppb. Isobaric overlaps were identified up to m/z 1000 that differed by the mass of a few electrons with the most counts when at 3σ, which included the assignment of ^{18}O and ^{17}O isotopologues. Analyzing at 3σ yielded the widest range of compositional space with unique assignments and aromaticity not detected at higher peak-picking thresholds. Thus, setting more stringent peak-picking thresholds above 3σ may arbitrarily limit molecular formula assignment for high confidence peaks. The additional molecular formulas and features may contribute to the poor reproducibility across different FT-ICR instruments and should be further investigated using retrospective analysis of DOM samples with other matrixes.

Third, water-extractable organic matter from laboratory microcosms of soil burned at discrete temperatures was characterized by FT-ICR MS to study the impacts of fire temperature on SOM and DOM composition (Chapter 4). The amount of water-extractable organic matter changed depending on heating with a maximum at 250°C and minimum at 450°C. The increase in DOC corresponded with a shift towards aromatic nitrogen-containing molecular formulas and exhibited the widest range of aromatic features and oxidation states when at 250°C. Mass difference-based

analysis also suggested that products formed during heating could be modeled using transformations along the Maillard reaction pathway. Reactants and products were paired between consecutive heating temperatures using known amino acids and intermediate carbon fragments, and were identified at every temperatures except 450°C when most DOC was removed. These results describe compositional changes to SOM during heating and identify mechanisms that appear to contribute to pyOM formation. By understanding more about the mechanisms that form pyOM at specific heating intensities, this work enables the identification of patterns in pyOM that could be used characterize precise reactants and temperatures in fire-affected soil.

Finally, streams within the area of the Cameron Peak Fire of 2020 were sampled before, during, and after the first large summer rainstorms following the fire. Streams were distinguished by catchment burn extent and used to investigate the short-term impacts of precipitation and burn extent on water chemistry and DOM in fire-affected watersheds (Chapter 5). Quantitatively, dissolved organic carbon (DOC) increased in every stream during the storm, and turbidity and fluorescence indices varied by burn extent. Many assignments were also common between events and streams, indicating the similarity in source water and DOM inputs regardless of burn extent. Nitrogen species predominated FT-ICR spectra during the storm and corresponded with labile, microbially-derived, and pyrogenic compositions. The unique DOM assignments following the storm decreased by one or two orders of magnitude in every stream except the low burn extent, which could reflect residues release by plants and microbes "stimulated" by precipitation relative to the higher burn severity samples. Chlorination experiments indicated that more than twice the number of DBPs formed from moderate-high burn extents compared to the low burn extent. Interestingly, when DBP concentrations were normalized to DOC, the released DOM formed less DBPs, suggesting the increased in DBP formation is due to increased DOM loading overall rather than increased reactivity of DOM. Thus, pyOM comprises a minor fraction of the storm DOM and

may persist in environments for decades due to the lack of solubility of pyOM observed following precipitation. This work would benefit from small molecule analysis in soils with clearly delineated burn severities to identify the presence of microbial metabolites and DBP precursors.

The work in this dissertation contributes to the mechanistic understanding of the transformation, combustion, and mobilization of SOM following wildfires in forested watersheds. The apparent insolubility of pyOM during precipitation may also explain the long-term persistence and leaching of condensed aromatic residues observed in the streams and soils of fire-affected watersheds and has implications for nutrient cycling and the recovery of fire-impacted watersheds. Within the water-soluble fraction of pyOM, aromatic organic nitrogen moieties were enriched in both laboratory- and field-based fire-affected samples and may contribute to degraded water quality. Studies aiming to bridge the understanding between laboratory-based fire simulations and field studies of wildfires could arrange microcosms with known fuel quantities and temperature throughout a soil column to identify heat penetration and corresponding transformations that influence pyOM characteristics and solubility. Future studies aiming to refine our mechanistic understanding of wildfire transformations on SOM should include samples from different terrestrial ecosystems under similar heating parameters to identify if trends apply across a range of sample matrixes and if modeling approaches can be replicated. Identification of specific molecular precursors to Maillard reaction products or DBPs could also be performed with labeled standards of biomolecules spiked into heated SOM matrixes coupled with small molecule analysis.

REFERENCES

(1) Weil, R.; Brady, N. *The Nature and Properties of Soils. 15th Edition*; 2017.

(2) Smith, P.; Cotrufo, M. F.; Rumpel, C.; Paustian, K.; Kuikman, P. J.; Elliott, J. A.; McDowell, R.; Griffiths, R. I.; Asakawa, S.; Bustamante, M.; House, J. I.; Sobocká, J.; Harper, R.; Pan, G.; West, P. C.; Gerber, J. S.; Clark, J. M.; Adhya, T.; Scholes, R. J.; Scholes, M. C. Biogeochemical Cycles and Biodiversity as Key Drivers of Ecosystem Services Provided by Soils. *SOIL* **2015**, *1* (2), 665–685. https://doi.org/10.5194/soil-1-665-2015.

(3) Scharlemann, J. P. W.; Tanner, E. V. J.; Hiederer, R.; Kapos, V. Global Soil Carbon: Understanding and Managing the Largest Terrestrial Carbon Pool. *Carbon Manag.* **2014**, *5* (1), 81–91. https://doi.org/10.4155/cmt.13.77.

(4) Reeves, D. W. The Role of Soil Organic Matter in Maintaining Soil Quality in Continuous Cropping Systems. *Soil Tillage Res.* **1997**, *43* (1–2), 131–167. https://doi.org/10.1016/S0167-1987(97)00038-X.

(5) Bauer, A.; Black, A. L. Quantification of the Effect of Soil Organic Matter Content on Soil Productivity. *Soil Sci. Soc. Am. J.* **1994**, *58* (1), 185–193. https://doi.org/10.2136/sssaj1994.03615995005800010027x.

(6) Hudson, B. D. Soil Organic Matter and Available Water Capacity. *J. Soil Water Conserv.* **1994**, *49* (2), 189–194. https://doi.org/10.1201/9780429445552-36.

(7) TISDALL, J. M.; OADES, J. M. Organic Matter and Water-stable Aggregates in Soils. *J. Soil Sci.* **1982**, *33* (2), 141–163. https://doi.org/10.1111/j.1365-2389.1982.tb01755.x.

(8) McBride, M.; Sauve, S.; Hendershot, W. Solubility Control of Cu, Zn, Cd and Pb in Contaminated Soils. *Eur. J. Soil Sci.* **1997**, *48* (2), 337–346. https://doi.org/https://doi.org/10.1111/j.1365-2389.1997.tb00554.x.

(9) Tiessen, H.; Cuevas, E.; Chacon, P. The Role of Soil Organic Matter in Sustaining Soil

Fertility. *Nature* **1994**, *371* (6500), 783–785. https://doi.org/10.1038/371783a0.

(10) Kuzyakov, Y.; Blagodatskaya, E. Microbial Hotspots and Hot Moments in Soil: Concept & Review. *Soil Biology and Biochemistry*. 2015, pp 184–199. https://doi.org/10.1016/j.soilbio.2015.01.025.

(11) Kleber, M.; Nico, P. S.; Plante, A.; Filley, T.; Kramer, M.; Swanston, C.; Sollins, P. Old and Stable Soil Organic Matter Is Not Necessarily Chemically Recalcitrant: Implications for Modeling Concepts and Temperature Sensitivity. *Glob. Chang. Biol.* **2011**, *17* (2), 1097–1107. https://doi.org/10.1111/j.1365-2486.2010.02278.x.

(12) Stubbins, A.; Spencer, R. G. M.; Chen, H.; Hatcher, P. G.; Mopper, K.; Hernes, P. J.; Mwamba, V. L.; Mangangu, A. M.; Wabakanghanzi, J. N.; Six, J. Illuminated Darkness: Molecular Signatures of Congo River Dissolved Organic Matter and Its Photochemical Alteration as Revealed by Ultrahigh Precision Mass Spectrometry. *Limnol. Oceanogr.* **2010**, *55* (4), 1467–1477. https://doi.org/10.4319/lo.2010.55.4.1467.

(13) González-Pérez, J. A.; González-Vila, F. J.; Almendros, G.; Knicker, H. The Effect of Fire on Soil Organic Matter—a Review. *Environ. Int.* **2004**, *30* (6), 855–870. https://doi.org/10.1016/j.envint.2004.02.003.

(14) Knicker, H. How Does Fire Affect the Nature and Stability of Soil Organic Nitrogen and Carbon? A Review. *Biogeochemistry* **2007**, *85* (1), 91–118. https://doi.org/10.1007/s10533-007-9104-4.

(15) Masoom, H.; Courtier-Murias, D.; Farooq, H.; Soong, R.; Kelleher, B. P.; Zhang, C.; Maas, W. E.; Fey, M.; Kumar, R.; Monette, M.; Stronks, H. J.; Simpson, M. J.; Simpson, A. J. Soil Organic Matter in Its Native State: Unravelling the Most Complex Biomaterial on Earth. *Environ. Sci. Technol.* **2016**, *50* (4), 1670–1680. https://doi.org/10.1021/acs.est.5b03410.

(16) Bahureksa, W.; Tfaily, M. M.; Boiteau, R. M.; Young, R. B.; Logan, M. N.; McKenna, A. M.;

Borch, T.; Young, R. B.; Logan, M. N.; Borch, T. Soil Organic Matter Characterization by Fourier Transform Ion Cyclotron Resonance Mass Spectrometry (FTICR MS): A Critical Review of Sample Preparation, Analysis, and Data Interpretation. *Environ. Sci. Technol.* **2021**, *55* (14), 9637–9656. https://doi.org/10.1021/acs.est.1c01135.

(17) Herzsprung, P.; Hertkorn, N.; Von Tümpling, W.; Harir, M.; Friese, K.; Schmitt-Kopplin, P. Molecular Formula Assignment for Dissolved Organic Matter (DOM) Using High-Field FT-ICR-MS: Chemical Perspective and Validation of Sulphur-Rich Organic Components (CHOS) in Pit Lake Samples. *Anal. Bioanal. Chem.* **2016**, *408* (10), 2461–2469. https://doi.org/10.1007/s00216-016-9341-2.

(18) Roth, H. K.; Borch, T.; Young, R. B.; Bahureksa, W.; Blakney, G. T.; Nelson, A. R.; Wilkins, M. J.; McKenna, A. M. Enhanced Speciation of Pyrogenic Organic Matter from Wildfires Enabled by 21 T FT-ICR Mass Spectrometry. *Anal. Chem.* **2022**, *94* (6), 2973–2980. https://doi.org/10.1021/acs.analchem.1c05018.

(19) Liberatore, H. K.; Westerman, D. C.; Allen, J. M.; Plewa, M. J.; Wagner, E. D.; McKenna, A. M.; Weisbrod, C. R.; McCord, J. P.; Liberatore, R. J.; Burnett, D. B.; Cizmas, L. H.; Richardson, S. D. High-Resolution Mass Spectrometry Identification of Novel Surfactant-Derived Sulfur-Containing Disinfection Byproducts from Gas Extraction Wastewater. *Environ. Sci. Technol.* **2020**, *54* (15), 9374–9386. https://doi.org/10.1021/acs.est.0c01997.

(20) McKenna, A. M.; Donald, L. J.; Fitzsimmons, J. E.; Juyal, P.; Spicer, V.; Standing, K. G.; Marshall, A. G.; Rodgers, R. P. Heavy Petroleum Composition. 3. Asphaltene Aggregation. *Energy and Fuels* **2013**, *27* (3), 1246–1256. https://doi.org/10.1021/ef3018578.

(21) Wagner, S.; Riedel, T.; Niggemann, J.; Vähätalo, A. V.; Dittmar, T.; Jaffé, R. Linking the Molecular Signature of Heteroatomic Dissolved Organic Matter to Watershed Characteristics in World Rivers. *Environ. Sci. Technol.* **2015**, *49* (23), 13798–13806.

https://doi.org/10.1021/acs.est.5b00525.

(22) Young, R. B.; Pica, N. E.; Sharifan, H.; Chen, H.; Roth, H. K.; Blakney, G. T.; Borch, T.; Higgins, C. P.; Kornuc, J. J.; McKenna, A. M.; Blotevogel, J. PFAS Analysis with Ultrahigh Resolution 21T FT-ICR MS: Suspect and Nontargeted Screening with Unrivaled Mass Resolving Power and Accuracy. *Environ. Sci. Technol.* **2022**, *56* (4), 2455–2465. https://doi.org/10.1021/acs.est.1c08143.

(23) Patzner, M. S.; Logan, M.; McKenna, A. M.; Young, R. B.; Zhou, Z.; Joss, H.; Mueller, C. W.; Hoeschen, C.; Scholten, T.; Straub, D.; Kleindienst, S.; Borch, T.; Kappler, A.; Bryce, C. Microbial Iron Cycling during Palsa Hillslope Collapse Promotes Greenhouse Gas Emissions before Complete Permafrost Thaw. *Commun. Earth Environ.* **2022**, *3* (1), 1–14. https://doi.org/10.1038/s43247-022-00407-8.

(24) Bahureksa, W.; Young, R. B.; McKenna, A. M.; Chen, H.; Thorn, K. A.; Rosario-Ortiz, F. L.; Borch, T. Nitrogen Enrichment during Soil Organic Matter Burning and Molecular Evidence of Maillard Reactions. *Environ. Sci. Technol.* **2022**. https://doi.org/10.1021/acs.est.1c06745.

(25) Hemmler, D.; Roullier-Gall, C.; Marshall, J. W.; Rychlik, M.; Taylor, A. J.; Schmitt-Kopplin, P. Insights into the Chemistry of Non-Enzymatic Browning Reactions in Different Ribose-Amino Acid Model Systems. *Sci. Rep.* **2018**, *8* (1), 1–10. https://doi.org/10.1038/s41598-018-34335-5.

(26) Hawkes, J. A.; D'Andrilli, J.; Agar, J. N.; Barrow, M. P.; Berg, S. M.; Catalán, N.; Chen, H.; Chu, R. K.; Cole, R. B.; Dittmar, T.; Gavard, R.; Gleixner, G.; Hatcher, P. G.; He, C.; Hess, N. J.; Hutchins, R. H. S.; Ijaz, A.; Jones, H. E.; Kew, W.; Khaksari, M.; Palacio Lozano, D. C.; Lv, J.; Mazzoleni, L. R.; Noriega-Ortega, B. E.; Osterholz, H.; Radoman, N.; Remucal, C. K.; Schmitt, N. D.; Schum, S. K.; Shi, Q.; Simon, C.; Singer, G.; Sleighter, R. L.; Stubbins, A.; Thomas, M. J.; Tolic, N.; Zhang, S.; Zito, P.; Podgorski, D. C. An International Laboratory

Comparison of Dissolved Organic Matter Composition by High Resolution Mass Spectrometry: Are We Getting the Same Answer? *Limnol. Oceanogr. Methods* **2020**, *18* (6), 235–258. https://doi.org/10.1002/lom3.10364.

(27) International Humic Substances Society. Isolation of IHSS Samples. https://humic-substances.org/isolation-of-ihss-samples/ (accessed 2021 -06 -06).

(28) Bahureksa, W.; Borch, T.; Young, R. B.; Weisbrod, C. R.; Blakney, G. T.; Mckenna, A. M. Improved Dynamic Range, Resolving Power, and Sensitivity Achievable with FT-ICR Mass Spectrometry at 21 T Reveals the Hidden Complexity of Natural Organic Matter. *Anal. Chem.* **2022**, *94* (32), 11382–11389. https://doi.org/10.1021/acs.analchem.2c02377.

(29) Clifton, C. F.; Forest, U. N.; Roby, K. B.; Forest, L. N.; Contributors, M.; Hansen, W.; Forest, F. M. N.; Hays, P. E.; Mountain, R.; Office, R.; Connor, A.; Forest, C. N.; Leonard, M.; Forest, P. N. Water, Climate Change, and Forests: Watershed Stewardship for a Changing Climate. *For. Manag. Resilience, Adapt. Watershed Prot.* **2012**, No. June, 35–145.

(30) Coogan, S. C. P.; Robinne, F. N.; Jain, P.; Flannigan, M. D. Scientists' Warning on Wildfire — a Canadian Perspective. *Can. J. For. Res.* **2019**, *49* (9), 1015–1023. https://doi.org/10.1139/cjfr-2019-0094.

(31) Price, D. T.; Alfaro, R. I.; Brown, K. J.; Flannigan, M. D.; Fleming, R. A.; Hogg, E. H.; Girardin, M. P.; Lakusta, T.; Johnston, M.; McKenney, D. W.; Pedlar, J. H.; Stratton, T.; Sturrock, R. N.; Thompson, I. D.; Trofymow, J. A.; Venier, L. A. Anticipating the Consequences of Climate Change for Canada's Boreal Forest Ecosystems1. *Environ. Rev.* **2013**, *21* (4), 322–365. https://doi.org/10.1139/er-2013-0042.

(32) Liu, Y.; Stanturf, J.; Goodrick, S. Trends in Global Wildfire Potential in a Changing Climate. *For. Ecol. Manage.* **2010**, *259* (4), 685–697. https://doi.org/10.1016/j.foreco.2009.09.002.

(33) Alcañiz, M.; Outeiro, L.; Francos, M.; Úbeda, X. Science of the Total Environment Effects of

Prescribed Fires on Soil Properties : A Review. *Sci. Total Environ.* **2018**, *613–614*, 944–957. https://doi.org/10.1016/j.scitotenv.2017.09.144.

(34) Ruffault, J.; Curt, T.; Moron, V.; Trigo, R. M.; Mouillot, F.; Koutsias, N.; Pimont, F.; Martin-StPaul, N.; Barbero, R.; Dupuy, J. L.; Russo, A.; Belhadj-Khedher, C. Increased Likelihood of Heat-Induced Large Wildfires in the Mediterranean Basin. *Sci. Rep.* **2020**, *10* (1), 1–9. https://doi.org/10.1038/s41598-020-70069-z.

(35) Williams, A. P.; Livneh, B.; McKinnon, K. A.; Hansen, W. D.; Mankin, J. S.; Cook, B. I.; Smerdon, J. E.; Varuolo-Clarke, A. M.; Bjarke, N. R.; Juang, C. S.; Lettenmaier, D. P. Growing Impact of Wildfire on Western US Water Supply. *Proc. Natl. Acad. Sci. U. S. A.* **2022**, *119* (10), 1–8. https://doi.org/10.1073/pnas.2114069119.

(36) Rhoades, C. C.; Entwistle, D.; Butler, D. The Influence of Wildfire Extent and Severity on Streamwater Chemistry, Sediment and Temperature Following the Hayman Fire, Colorado. *Int. J. Wildl. Fire* **2011**, *20* (3), 430–442. https://doi.org/10.1071/WF09086.

(37) Keeley, J. E. Fire Intensity, Fire Severity and Burn Severity: A Brief Review and Suggested Usage. *Int. J. Wildl. Fire* **2009**, *18*, 116–126. https://doi.org/10.1071/WF07049.

(38) Santín, C.; Doerr, S. H.; Kane, E. S.; Masiello, C. A.; Ohlson, M.; de la Rosa, J. M.; Preston, C. M.; Dittmar, T. Towards a Global Assessment of Pyrogenic Carbon from Vegetation Fires. *Glob. Chang. Biol.* **2016**, *22* (1), 76–91. https://doi.org/10.1111/gcb.12985.

(39) Hohner, A. K.; Terry, L. G.; Townsend, E. B.; Summers, R. S.; Rosario-Ortiz, F. L. Water Treatment Process Evaluation of Wildfire-Affected Sediment Leachates. *Environ. Sci. Water Res. Technol.* **2017**, *3* (2), 352–365. https://doi.org/10.1039/c6ew00247a.

(40) Chow, A. T.; Tsai, K.; Fegel, T. S.; Pierson, D. N.; Rhoades, C. C. Lasting Effects of Wildfire on Disinfection By-Product Formation in Forest Catchments. *J. Environ. Qual.* **2019**, *48* (6), 1826–1834. https://doi.org/10.2134/jeq2019.04.0172.

(41) Wang, J. J.; Dahlgren, R. A.; Erşan, M. S.; Karanfil, T.; Chow, A. T. Wildfire Altering Terrestrial Precursors of Disinfection Byproducts in Forest Detritus. *Environ. Sci. Technol.* **2015**, *49* (10), 5921–5929. https://doi.org/10.1021/es505836m.

(42) Alcañiz, M.; Outeiro, L.; Francos, M.; Farguell, J.; Úbeda, X. Long-Term Dynamics of Soil Chemical Properties after a Prescribed Fire in a Mediterranean Forest (Montgrí Massif, Catalonia, Spain). *Sci. Total Environ.* **2016**, *572*, 1329–1335. https://doi.org/10.1016/j.scitotenv.2016.01.115.

(43) Wagner, S.; Jaffé, R.; Stubbins, A. Dissolved Black Carbon in Aquatic Ecosystems. *Limnol. Oceanogr. Lett.* **2018**. https://doi.org/10.1002/lol2.10076.

(44) Baldock, J. A.; Smernik, R. J. Chemical Composition and Bioavailability of Thermally Altered Pinus Resinosa (Red Pine) Wood. *Org. Geochem.* **2002**, *33* (9), 1093–1109. https://doi.org/10.1016/S0146-6380(02)00062-1.

(45) Wan, X.; Kawamura, K.; Ram, K.; Kang, S.; Loewen, M.; Gao, S.; Wu, G.; Fu, P.; Zhang, Y.; Bhattarai, H.; Cong, Z. Aromatic Acids as Biomass-Burning Tracers in Atmospheric Aerosols and Ice Cores: A Review. *Environmental Pollution*. 2019, pp 216–228. https://doi.org/10.1016/j.envpol.2019.01.028.

(46) Smith, H. G.; Sheridan, G. J.; Lane, P. N. J.; Nyman, P.; Haydon, S. Wildfire Effects on Water Quality in Forest Catchments: A Review with Implications for Water Supply. *Journal of Hydrology*. January 5, 2011, pp 170–192. https://doi.org/10.1016/j.jhydrol.2010.10.043.

(47) Rodríguez-Cardona, B. M.; Coble, A. A.; Wymore, A. S.; Kolosov, R.; Podgorski, D. C.; Zito, P.; Spencer, R. G. M.; Prokushkin, A. S.; McDowell, W. H. Wildfires Lead to Decreased Carbon and Increased Nitrogen Concentrations in Upland Arctic Streams. *Sci. Rep.* **2020**, *10* (1), 1–9. https://doi.org/10.1038/s41598-020-65520-0.

(48) Emelko, M. B.; Silins, U.; Bladon, K. D.; Stone, M. Implications of Land Disturbance on

Drinking Water Treatability in a Changing Climate: Demonstrating the Need for " Source Water Supply and Protection" Strategies. *Water Res.* **2011**, *45* (2), 461–472. https://doi.org/10.1016/j.watres.2010.08.051.

(49) Wagner, S.; Fair, J. H.; Matt, S.; Hosen, J. D.; Raymond, P.; Saiers, J.; Shanley, J. B.; Dittmar, T.; Stubbins, A. Molecular Hysteresis: Hydrologically Driven Changes in Riverine Dissolved Organic Matter Chemistry During a Storm Event. *J. Geophys. Res. Biogeosciences* **2019**, *124* (4), 759–774. https://doi.org/10.1029/2018JG004817.

(50) Fellman, J. B.; Hood, E.; Behnke, M. I.; Welker, J. M.; Spencer, R. G. M. Stormflows Drive Stream Carbon Concentration, Speciation, and Dissolved Organic Matter Composition in Coastal Temperate Rainforest Watersheds. *J. Geophys. Res. Biogeosciences* **2020**, *125* (9), 1–18. https://doi.org/10.1029/2020JG005804.

(51) Bladon, K. D.; Emelko, M. B.; Silins, U.; Stone, M. Wildfire and the Future of Water Supply. *Environ. Sci. Technol.* **2014**, *48* (16), 8936–8943. https://doi.org/10.1021/es500130g.

(52) Rehberg, R. A.; Trivedi, P.; Bahureksa, W.; Sharp, J. L.; Stokes, S. C.; Menger, R. F.; Borch, T. Quantification of Insecticide Spatial Distribution within Individual Citrus Trees and Efficacy through Asian Citrus Psyllid Reductions under Different Application Methods. *Pest Manag. Sci.* **2021**, *77* (4), 1748–1756. https://doi.org/10.1002/ps.6195.

(53) Young, R.; Avneri-Katz, S.; McKenna, A.; Chen, H.; Bahureksa, W.; Polubesova, T.; Chefetz, B.; Borch, T. Composition-Dependent Sorptive Fractionation of Anthropogenic Dissolved Organic Matter by Fe(III)-Montmorillonite. *Soil Syst.* **2018**, *2* (1), 14. https://doi.org/10.3390/soilsystems2010014.

(54) Paustian, K.; Lehmann, J.; Ogle, S.; Reay, D.; Robertson, G. P.; Smith, P. Climate-Smart Soils. *Nature* **2016**, *532* (7597), 49–57. https://doi.org/10.1038/nature17174.

(55) Janzen, H. H. The Soil Carbon Dilemma: Shall We Hoard It or Use It? *Soil Biol. Biochem.*

2006, *38* (3), 419–424. https://doi.org/10.1016/j.soilbio.2005.10.008.

(56) Schuur, E. A. G.; McGuire, A. D.; Schädel, C.; Grosse, G.; Harden, J. W.; Hayes, D. J.; Hugelius, G.; Koven, C. D.; Kuhry, P.; Lawrence, D. M.; Natali, S. M.; Olefeldt, D.; Romanovsky, V. E.; Schaefer, K.; Turetsky, M. R.; Treat, C. C.; Vonk, J. E. Climate Change and the Permafrost Carbon Feedback. *Nature* **2015**, *520* (7546), 171–179. https://doi.org/10.1038/nature14338.

(57) Stewart, C. E.; Paustian, K.; Conant, R. T.; Plante, A. F.; Six, J. Soil Carbon Saturation: Concept, Evidence and Evaluation. *Biogeochemistry* **2007**, *86* (1), 19–31. https://doi.org/10.1007/s10533-007-9140-0.

(58) Vives-Peris, V.; de Ollas, C.; Gómez-Cadenas, A.; Pérez-Clemente, R. M. Root Exudates: From Plant to Rhizosphere and Beyond. *Plant Cell Rep.* **2020**, *39* (1), 3–17. https://doi.org/10.1007/s00299-019-02447-5.

(59) Kögel-Knabner, I. The Macromolecular Organic Composition of Plant and Microbial Residues as Inputs to Soil Organic Matter: Fourteen Years On. *Soil Biology and Biochemistry*. 2017, pp A3–A8. https://doi.org/10.1016/j.soilbio.2016.08.011.

(60) Poirier, V.; Roumet, C.; Munson, A. D. The Root of the Matter: Linking Root Traits and Soil Organic Matter Stabilization Processes. **2018**. https://doi.org/10.1016/j.soilbio.2018.02.016.

(61) Liang, C.; Amelung, W.; Lehmann, J.; Kästner, M. Quantitative Assessment of Microbial Necromass Contribution to Soil Organic Matter. *Glob. Chang. Biol.* **2019**, *25* (11), 3578–3590. https://doi.org/10.1111/gcb.14781.

(62) Fernandez, C. W.; Kennedy, P. G. Commentary Moving beyond the Black-Box: Fungal Traits, Community Structure, and Carbon. *New Phytol.* **2015**, *205*, 1378–1380. https://doi.org/https://doi.org/10.1111/nph.13289.

(63) Liang, C.; Kästner, M.; Joergensen, R. G. Microbial Necromass on the Rise: The Growing

Focus on Its Role in Soil Organic Matter Development. *Soil Biology and Biochemistry*. 2020. https://doi.org/10.1016/j.soilbio.2020.108000.

(64) Piccolo, A. The Supramolecular Structure of Humic Substances: A Novel Understanding of Humus Chemistry and Implications in Soil Science. *Adv. Agron.* **2002**, *75*, 57–134. https://doi.org/10.1016/s0065-2113(02)75003-7.

(65) Lehmann, J.; Hansel, C. M.; Kaiser, C.; Kleber, M.; Maher, K.; Manzoni, S.; Nunan, N.; Reichstein, M.; Schimel, J. P.; Torn, M. S.; Wieder, W. R.; Kögel-Knabner, I. Persistence of Soil Organic Carbon Caused by Functional Complexity. *Nat. Geosci.* **2020**, *13* (8), 529–534. https://doi.org/10.1038/s41561-020-0612-3.

(66) Hertkorn, N.; Ruecker, C.; Meringer, M.; Gugisch, R.; Frommberger, M.; Perdue, E. M.; Witt, M.; Schmitt-Kopplin, P. High-Precision Frequency Measurements: Indispensable Tools at the Core of the Molecular-Level Analysis of Complex Systems. *Anal. Bioanal. Chem.* **2007**, *389* (5), 1311–1327. https://doi.org/10.1007/s00216-007-1577-4.

(67) Schmitt-Kopplin, P.; Hemmler, D.; Moritz, F.; Gougeon, R. D.; Lucio, M.; Meringer, M.; Müller, C.; Harir, M.; Hertkorn, N. Systems Chemical Analytics: Introduction to the Challenges of Chemical Complexity Analysis. *Faraday Discuss.* **2019**, *218*, 9–28. https://doi.org/10.1039/c9fd00078j.

(68) Lehmann, J.; Solomon, D.; Kinyangi, J.; Dathe, L.; Wirick, S.; Jacobsen, C. Spatial Complexity of Soil Organic Matter Forms at Nanometre Scales. *Nat. Geosci.* **2008**, *1* (4), 238–242. https://doi.org/10.1038/ngeo155.

(69) Heister, K.; Höschen, C.; Pronk, G. J.; Mueller, C. W.; Kögel-Knabner, I. NanoSIMS as a Tool for Characterizing Soil Model Compounds and Organomineral Associations in Artificial Soils. *J. Soils Sediments* **2012**, *12* (1), 35–47. https://doi.org/10.1007/s11368-011-0386-8.

(70) Lavallee, J. M.; Soong, J. L.; Cotrufo, M. F. Conceptualizing Soil Organic Matter into

Particulate and Mineral-Associated Forms to Address Global Change in the 21st Century. *Glob. Chang. Biol.* **2020**, *26* (1), 261–273. https://doi.org/10.1111/gcb.14859.

(71) Cotrufo, M. F.; Ranalli, M. G.; Haddix, M. L.; Six, J.; Lugato, E. Soil Carbon Storage Informed by Particulate and Mineral-Associated Organic Matter. *Nat. Geosci.* **2019**, *12* (12), 989–994. https://doi.org/10.1038/s41561-019-0484-6.

(72) Young, I. M.; Crawford, J. W. Interactions and Self-Organization in the Soil-Microbe Complex. *Science* **2004**, *304* (5677), 1634–1637. https://doi.org/10.1126/science.1097394.

(73) Marshall, A. G.; Hendrickson, C. L.; Jackson, G. S. Fourier Transform Ion Cyclotron Resonance Mass Spectrometry: A Primer. *Mass Spectrom. Rev.* **1998**, *17*, 1–35. https://doi.org/10.1002/(SICI)1098-2787(1998)17:1<1::AID-MAS1>3.0.CO;2-K.

(74) Koch, B. P.; Dittmar, T.; Witt, M.; Kattner, G. Fundamentals of Molecular Formula Assignment to Ultrahigh Resolution Mass Data of Natural Organic Matter. *Anal. Chem.* **2007**, *79* (4), 1758–1763. https://doi.org/10.1021/ac061949s.

(75) Reemtsma, T. Determination of Molecular Formulas of Natural Organic Matter Molecules by (Ultra-) High-Resolution Mass Spectrometry. Status and Needs. *J. Chromatogr. A* **2009**, *1216* (18), 3687–3701. https://doi.org/10.1016/j.chroma.2009.02.033.

(76) Zhang, X.; Han, J.; Zhang, X.; Shen, J.; Chen, Z.; Chu, W.; Kang, J.; Zhao, S.; Zhou, Y. Application of Fourier Transform Ion Cyclotron Resonance Mass Spectrometry to Characterize Natural Organic Matter. *Chemosphere* **2020**, *260*, 127458. https://doi.org/10.1016/j.chemosphere.2020.127458.

(77) Qi, Y.; Fu, P.; Volmer, D. A. Analysis of Natural Organic Matter via Fourier Transform Ion Cyclotron Resonance Mass Spectrometry: An Overview of Recent Non-Petroleum Applications. *Mass Spectrom. Rev.* **2020**, 1–15. https://doi.org/10.1002/mas.21634.

(78) Kleber, M.; Sollins, P.; Sutton, R. A Conceptual Model of Organo-Mineral Interactions in

Soils: Self-Assembly of Organic Molecular Fragments into Zonal Structures on Mineral Surfaces. *Biogeochemistry* **2007**, *85* (1), 9–24. https://doi.org/10.1007/s10533-007-9103-5.

(79) Bailey, V. L.; Smith, A. P.; Tfaily, M.; Fansler, S. J.; Bond-Lamberty, B. Differences in Soluble Organic Carbon Chemistry in Pore Waters Sampled from Different Pore Size Domains. *Soil Biol. Biochem.* **2017**, *107*, 133–143. https://doi.org/10.1016/j.soilbio.2016.11.025.

(80) Swift, R. S. Organic Matter Characterization. *Methods of Soil Analysis*. January 1, 1996, pp 1011–1069. https://doi.org/https://doi.org/10.2136/sssabookser5.3.c35.

(81) Ikeya, K.; Sleighter, R. L.; Hatcher, P. G.; Watanabe, A. Chemical Compositional Analysis of Soil Fulvic Acids Using Fourier Transform Ion Cyclotron Resonance Mass Spectrometry. *Rapid Commun. Mass Spectrom.* **2020**, *34* (15), 1–11. https://doi.org/10.1002/rcm.8801.

(82) Ikeya, K.; Sleighter, R. L.; Hatcher, P. G.; Watanabe, A. Characterization of the Chemical Composition of Soil Humic Acids Using Fourier Transform Ion Cyclotron Resonance Mass Spectrometry. *Geochim. Cosmochim. Acta* **2015**, *153*, 169–182. https://doi.org/10.1016/j.gca.2015.01.002.

(83) Coward, E. K.; Ohno, T.; Sparks, D. L. Direct Evidence for Temporal Molecular Fractionation of Dissolved Organic Matter at the Iron Oxyhydroxide Interface. *Environ. Sci. Technol.* **2019**, *53* (2), 642–650. https://doi.org/10.1021/acs.est.8b04687.

(84) Chen, M.; Kim, S.; Park, J. E.; Jung, H. J.; Hur, J. Structural and Compositional Changes of Dissolved Organic Matter upon Solid-Phase Extraction Tracked by Multiple Analytical Tools. *Anal. Bioanal. Chem.* **2016**, *408* (23), 6249–6258. https://doi.org/10.1007/s00216-016-9728-0.

(85) Kleber, M.; Eusterhues, K.; Keiluweit, M.; Mikutta, C.; Mikutta, R.; Nico, P. S. Mineral-Organic Associations: Formation, Properties, and Relevance in Soil Environments. *Adv. Agron.* **2015**, *130*, 1–140. https://doi.org/10.1016/bs.agron.2014.10.005.

(86) Schwesig, D.; Göttlein, A.; Haumaier, L.; Blasek, R.; Ilgen, G. Soil Organic Matter Extraction

Using Water at High Temperature and Elevated Pressure (ASE) as Compared to Conventional Methods. *Int. J. Environ. Anal. Chem.* **1999**, *73* (4), 253–268. https://doi.org/10.1080/03067319908032668.

(87) Fox, P. M.; Nico, P. S.; Tfaily, M. M.; Heckman, K.; Davis, J. A. Characterization of Natural Organic Matter in Low-Carbon Sediments: Extraction and Analytical Approaches. *Org. Geochem.* **2017**, *114* (Supplement C), 12–22. https://doi.org/10.1016/j.orggeochem.2017.08.009.

(88) Chantigny, M. H. Dissolved and Water-Extractable Organic Matter in Soils: A Review on the Influence of Land Use and Management Practices. *Geoderma* **2003**, *113* (3–4), 357–380. https://doi.org/10.1016/S0016-7061(02)00370-1.

(89) Melendez-Perez, J. J.; Martínez-Mejía, M. J.; Awan, A. T.; Fadini, P. S.; Mozeto, A. A.; Eberlin, M. N. Characterization and Comparison of Riverine, Lacustrine, Marine and Estuarine Dissolved Organic Matter by Ultra-High Resolution and Accuracy Fourier Transform Mass Spectrometry. *Org. Geochem.* **2016**, *101*, 99–107. https://doi.org/10.1016/j.orggeochem.2016.08.005.

(90) Koch, B. P.; Witt, M.; Engbrodt, R.; Dittmar, T.; Kattner, G. Molecular Formulae of Marine and Terrigenous Dissolved Organic Matter Detected by Electrospray Ionization Fourier Transform Ion Cyclotron Resonance Mass Spectrometry. *Geochim. Cosmochim. Acta* **2005**, *69* (13), 3299–3308. https://doi.org/10.1016/j.gca.2005.02.027.

(91) Schmidt, M. W. I. I.; Torn, M. S.; Abiven, S.; Dittmar, T.; Guggenberger, G.; Janssens, I. A.; Kleber, M.; Kögel-Knabner, I.; Lehmann, J.; Manning, D. A. C. C.; Nannipieri, P.; Rasse, D. P.; Weiner, S.; Trumbore, S. E. Persistence of Soil Organic Matter as an Ecosystem Property. *Nature* **2011**, *478* (7367), 49–56. https://doi.org/10.1038/nature10386.

(92) Kellerman, A. M.; Kothawala, D. N.; Dittmar, T.; Tranvik, L. J. Persistence of Dissolved

Organic Matter in Lakes Related to Its Molecular Characteristics. *Nat. Geosci.* **2015**, *8* (6), 454–457. https://doi.org/10.1038/NGEO2440.

(93) Kellerman, A. M.; Guillemette, F.; Podgorski, D. C.; Aiken, G. R.; Butler, K. D.; Spencer, R. G. M. Unifying Concepts Linking Dissolved Organic Matter Composition to Persistence in Aquatic Ecosystems. *Environ. Sci. Technol.* **2018**, *52* (5), 2538–2548. https://doi.org/10.1021/acs.est.7b05513.

(94) Tfaily, M. M.; Chu, R. K.; Toyoda, J.; Tolić, N.; Robinson, E. W.; Paša-Tolić, L.; Hess, N. J. Sequential Extraction Protocol for Organic Matter from Soils and Sediments Using High Resolution Mass Spectrometry. *Anal. Chim. Acta* **2017**, *972*, 54–61. https://doi.org/10.1016/j.aca.2017.03.031.

(95) Casals, P.; Lopez-Sangil, L.; Carrara, A.; Gimeno, C.; Nogués, S. Autotrophic and Heterotrophic Contributions to Short-Term Soil CO 2 Efflux Following Simulated Summer Precipitation Pulses in a Mediterranean Dehesa. *Global Biogeochem. Cycles* **2011**, *25* (3). https://doi.org/10.1029/2010GB003973.

(96) Casals, P.; Gimeno, C.; Carrara, A.; Lopez-Sangil, L.; Sanz, M. J. Soil CO2 Efflux and Extractable Organic Carbon Fractions under Simulated Precipitation Events in a Mediterranean Dehesa. *Soil Biol. Biochem.* **2009**, *41* (9), 1915–1922. https://doi.org/10.1016/j.soilbio.2009.06.015.

(97) Coward, E. K.; Ohno, T.; Plante, A. F. Adsorption and Molecular Fractionation of Dissolved Organic Matter on Iron-Bearing Mineral Matrices of Varying Crystallinity. *Environ. Sci. Technol.* **2018**, *52* (3), 1036–1044. https://doi.org/10.1021/acs.est.7b04953.

(98) Guigue, J.; Mathieu, O.; Lévêque, J.; Mounier, S.; Laffont, R.; Maron, P. A.; Navarro, N.; Chateau, C.; Amiotte-Suchet, P.; Lucas, Y. A Comparison of Extraction Procedures for Water-Extractable Organic Matter in Soils. *Eur. J. Soil Sci.* **2014**, *65* (4), 520–530.

https://doi.org/10.1111/ejss.12156.

(99) Nebbioso, A.; Piccolo, A. Molecular Characterization of Dissolved Organic Matter (DOM): A Critical Review. *Analytical and Bioanalytical Chemistry*. Springer January 11, 2013, pp 109–124. https://doi.org/10.1007/s00216-012-6363-2.

(100) Zafiriou, O. C.; Joussot-Dubien, J.; Zepp, R. G.; Zika, R. G. Photochemistry of Natural Waters: Many Compounds and Environments Are Affected by Sunlight-Induced Photochemistry. *Environ. Sci. Technol.* **1984**, *18* (12), 358A-371A. https://doi.org/10.1021/es00130a711.

(101) Fisher, S. G.; Likens, G. E. Energy Flow in Bear Brook, New Hampshire: An Integrative Approach to Stream Ecosystem Metabolism. *Ecol. Monogr.* **1973**, *43* (4), 421–439. https://doi.org/10.2307/1942301.

(102) STEWART, A. J.; WETZEL, R. G. DISSOLVED HUMIC MATERIALS - PHOTODEGRADATION, SEDIMENT EFFECTS, AND REACTIVITY WITH PHOSPHATE AND CALCIUM-CARBONATE PRECIPITATION. *Arch. FUR Hydrobiol.* **1981**, *92* (3), 265–286.

(103) Lopez-Sangil, L.; Rovira, P. Sequential Chemical Extractions of the Mineral-Associated Soil Organic Matter: An Integrated Approach for the Fractionation of Organo-Mineral Complexes. *Soil Biol. Biochem.* **2013**, *62*, 57–67. https://doi.org/10.1016/j.soilbio.2013.03.004.

(104) Jones, D. L.; Willett, V. B. Experimental Evaluation of Methods to Quantify Dissolved Organic Nitrogen (DON) and Dissolved Organic Carbon (DOC) in Soil. *Soil Biol. Biochem.* **2006**, *38* (5), 991–999. https://doi.org/10.1016/j.soilbio.2005.08.012.

(105) Mann, B. F.; Chen, H.; Herndon, E. M.; Chu, R. K.; Tolic, N.; Portier, E. F.; Chowdhury, T. R.; Robinson, E. W.; Callister, S. J.; Wullschleger, S. D.; Graham, D. E.; Liang, L.; Gu, B. Indexing Permafrost Soil Organic Matter Degradation Using High-Resolution Mass

Spectrometry. *PLoS One* **2015**, *10* (6). https://doi.org/10.1371/journal.pone.0130557.

(106) Ryan, M. G.; Melillo, J. M.; Ricca, A. A Comparison of Methods for Determining Proximate Carbon Fractions of Forest Litter. *Can. J. For. Res.* **1990**, *20* (2), 166–171. https://doi.org/10.1139/x90-023.

(107) Achard, F. K. Chemische Untersuchung Des Torfs. *Crell's Chem. Ann* **1786**, *2*, 391–403.

(108) Hayes, M. H. B. Solvent Systems for the Isolation of Organic Components from Soils. *Soil Sci. Soc. Am. J.* **2006**, *70* (3), 986–994. https://doi.org/10.2136/sssaj2005.0107.

(109) Schnitzer, M.; Monreal, C. Chapter Three. Quo Vadis Soil Organic Matter Research? A Biological Link to the Chemistry of Humification. *Adv. Agron.* **2011**, *113*, 143–217. https://doi.org/10.1016/B978-0-12-386473-4.00003-8.

(110) Stevenson, F. J. *Humus Chemistry: Genesis, Composition, Reactions*; John Wiley & Sons, 1994.

(111) Kleber, M.; Lehmann, J. Humic Substances Extracted by Alkali Are Invalid Proxies for the Dynamics and Functions of Organic Matter in Terrestrial and Aquatic Ecosystems. *J. Environ. Qual.* **2019**, *48* (2), 207–216. https://doi.org/10.2134/jeq2019.01.0036.

(112) Olk, D. C.; Bloom, P. R.; Perdue, E. M.; McKnight, D. M.; Chen, Y.; Farenhorst, A.; Senesi, N.; Chin, Y.-P.; Schmitt-Kopplin, P.; Hertkorn, N.; Harir, M. Environmental and Agricultural Relevance of Humic Fractions Extracted by Alkali from Soils and Natural Waters. *J. Environ. Qual.* **2019**, *48* (2), 217–232. https://doi.org/10.2134/jeq2019.02.0041.

(113) DiDonato, N.; Hatcher, P. G. Alicyclic Carboxylic Acids in Soil Humic Acid as Detected with Ultrahigh Resolution Mass Spectrometry and Multi-Dimensional NMR. *Org. Geochem.* **2017**, *112*, 33–46. https://doi.org/10.1016/j.orggeochem.2017.06.010.

(114) DiDonato, N.; Chen, H.; Waggoner, D.; Hatcher, P. G. Potential Origin and Formation for Molecular Components of Humic Acids in Soils. *Geochim. Cosmochim. Acta* **2016**, *178*, 210–222. https://doi.org/10.1016/j.gca.2016.01.013.

(115) Kelleher, B. P.; Simpson, A. J. Humic Substances in Soils: Are They Really Chemically Distinct? *Environ. Sci. Technol.* **2006**, *40* (15), 4605–4611. https://doi.org/10.1021/es0608085.

(116) Lehmann, J.; Kleber, M. The Contentious Nature of Soil Organic Matter. *Nature* **2015**, *528* (7580), 0–8. https://doi.org/10.1038/nature16069.

(117) Kogel-Knabner, I. The Macromolecular Organic Composition of Plant and Microbial Residues as Inputs to Soil Organic Matter. *Soil Biol. Biochem.* **2002**, *105*, A3–A8. https://doi.org/10.1016/j.soilbio.2016.08.011.

(118) Coward, E. K.; Thompson, A. T.; Plante, A. F. Iron-Mediated Mineralogical Control of Organic Matter Accumulation in Tropical Soils. *Geoderma* **2017**, *306*, 206–216. https://doi.org/10.1016/j.geoderma.2017.07.026.

(119) Lalonde, K.; Mucci, A.; Ouellet, A.; Gélinas, Y. Preservation of Organic Matter in Sediments Promoted by Iron. *Nature* **2012**, *483* (7388), 198–200. https://doi.org/10.1038/nature10855.

(120) Gu, B.; Schmitt, J.; Chen, Z.; Liang, L.; McCarthy, J. F. Adsorption and Desorption of Natural Organic Matter on Iron Oxide: Mechanisms and Models. *Environ. Sci. Technol.* **1994**, *28* (1), 38–46. https://doi.org/10.1021/es00050a007.

(121) Mehra, O. P. Iron Oxide Removal from Soils and Clays by a Dithionite-Citrate System Buffered with Sodium Bicarbonate. *Clays Clay Miner.* **1958**, *7* (1), 317–327. https://doi.org/10.1346/ccmn.1958.0070122.

(122) Wagai, R.; Mayer, L. M. Sorptive Stabilization of Organic Matter in Soils by Hydrous Iron Oxides. *Geochim. Cosmochim. Acta* **2007**, *71* (1), 25–35. https://doi.org/10.1016/j.gca.2006.08.047.

(123) Chao, T. T.; Zhou, L. Extraction Techniques for Selective Dissolution of Amorphous Iron Oxides from Soils and Sediments. *Soil Sci. Soc. Am. J.* **1983**, *47* (2), 225–232. https://doi.org/10.2136/sssaj1983.03615995004700020010x.

(124) von Lützow, M.; Kögel-Knabner, I.; Ekschmitt, K.; Flessa, H.; Guggenberger, G.; Matzner, E.; Marschner, B. SOM Fractionation Methods: Relevance to Functional Pools and to Stabilization Mechanisms. *Soil Biol. Biochem.* **2007**, *39* (9), 2183–2207. https://doi.org/10.1016/j.soilbio.2007.03.007.

(125) Keil, R. G.; Mayer, L. M. Mineral Matrices and Organic Matter. In *Treatise on Geochemistry: Second Edition*; Elsevier Inc., 2013; Vol. 12, pp 337–359. https://doi.org/10.1016/B978-0-08-095975-7.01024-X.

(126) Wagai, R.; Mayer, L. M.; Kitayama, K.; Shirato, Y. Association of Organic Matter with Iron and Aluminum across a Range of Soils Determined via Selective Dissolution Techniques Coupled with Dissolved Nitrogen Analysis. *Biogeochemistry* **2013**, *112* (1–3), 95–109. https://doi.org/10.1007/s10533-011-9652-5.

(127) Patzner, M. S.; Mueller, C. W.; Malusova, M.; Baur, M.; Nikeleit, V.; Scholten, T.; Hoeschen, C.; Byrne, J. M.; Borch, T.; Kappler, A.; Bryce, C. Iron Mineral Dissolution Releases Iron and Associated Organic Carbon during Permafrost Thaw. *Nat. Commun.* **2020**, *11* (1), 1–11. https://doi.org/10.1038/s41467-020-20102-6.

(128) Lv, J.; Huang, Z.; Christie, P.; Zhang, S. Reducing Reagents Induce Molecular Artifacts in the Extraction of Soil Organic Matter. *ACS Earth Sp. Chem.* **2020**, acsearthspacechem.0c00194. https://doi.org/10.1021/acsearthspacechem.0c00194.

(129) Fisher, B. J.; Faust, J. C.; Moore, O. W.; Peacock, C. L.; März, C. Technical Note: Uncovering the Influence of Methodological Variations on the Extractability of Iron Bound Organic Carbon. *Biogeosciences Discuss.* **2020**, *2020*, 1–23. https://doi.org/10.5194/bg-2020-399.

(130) Daugherty, E. E.; Gilbert, B.; Nico, P. S.; Borch, T. Complexation and Redox Buffering of Iron(II) by Dissolved Organic Matter. *Environ. Sci. Technol.* **2017**, *51* (19), 11096–11104. https://doi.org/10.1021/acs.est.7b03152.

(131) Chen, C.; Thompson, A. The Influence of Native Soil Organic Matter and Minerals on Ferrous Iron Oxidation. *Geochim. Cosmochim. Acta* **2021**, *292*, 254–270. https://doi.org/10.1016/j.gca.2020.10.002.

(132) Xu, J.; Roley, S. S.; Tfaily, M. M.; Chu, R. K.; Tiedje, J. M. Organic Amendments Change Soil Organic C Structure and Microbial Community but Not Total Organic Matter on Sub-Decadal Scales. *Soil Biol. Biochem.* **2020**, *150* (August), 107986. https://doi.org/10.1016/j.soilbio.2020.107986.

(133) Tfaily, M. M.; Chu, R. K.; Tolić, N.; Roscioli, K. M.; Anderton, C. R.; Paša-Tolić, L.; Robinson, E. W.; Hess, N. J. Advanced Solvent Based Methods for Molecular Characterization of Soil Organic Matter by High-Resolution Mass Spectrometry. *Anal. Chem.* **2015**, *87* (10), 5206–5215. https://doi.org/10.1021/acs.analchem.5b00116.

(134) McKee, G. A.; Hatcher, P. G. A New Approach for Molecular Characterisation of Sediments with Fourier Transform Ion Cyclotron Resonance Mass Spectrometry: Extraction Optimisation. *Org. Geochem.* **2015**, *85*, 22–31. https://doi.org/10.1016/j.orggeochem.2015.04.007.

(135) Flerus, R.; Koch, B. P.; Schmitt-Kopplin, P.; Witt, M.; Kattner, G. Molecular Level Investigation of Reactions between Dissolved Organic Matter and Extraction Solvents Using FT-ICR MS. *Mar. Chem.* **2011**, *124* (1–4), 100–107. https://doi.org/10.1016/j.marchem.2010.12.006.

(136) Schwab, K. Effect-Directed Identification of Bioavailable Toxic Organic Compounds in Contaminated Sediments. **2008**.

(137) Raiswell, R.; Canfield, D. E.; Berner, R. A. A Comparison of Iron Extraction Methods for the Determination of Degree of Pyritisation and the Recognition of Iron-Limited Pyrite Formation. *Chem. Geol.* **1994**, *111* (1–4), 101–110. https://doi.org/10.1016/0009-

2541(94)90084-1.

(138) Bartlett, R.; James, B. Studying Dried, Stored Soil Samples - Some Pitfalls. *Soil Sci. Soc. Am. J.* **1980**, *44* (4), 721–724. https://doi.org/10.2136/sssaj1980.03615995004400040011x.

(139) Heinz, M.; Zak, D. Storage Effects on Quantity and Composition of Dissolved Organic Carbon and Nitrogen of Lake Water, Leaf Leachate and Peat Soil Water. *Water Res.* **2018**, *130*, 98–104. https://doi.org/10.1016/j.watres.2017.11.053.

(140) Tfaily, M. M.; Podgorski, D. C.; Corbett, J. E.; Chanton, J. P.; Cooper, W. T. Influence of Acidification on the Optical Properties and Molecular Composition of Dissolved Organic Matter. *Anal. Chim. Acta* **2011**, *706* (2), 261–267. https://doi.org/10.1016/j.aca.2011.08.037.

(141) Retelletti Brogi, S.; Derrien, M.; Hur, J. In-Depth Assessment of the Effect of Sodium Azide on the Optical Properties of Dissolved Organic Matter. *J. Fluoresc.* **2019**, *29* (4), 877–885. https://doi.org/10.1007/s10895-019-02398-w.

(142) Dittmar, T.; Koch, B.; Hertkorn, N.; Kattner, G. A Simple and Efficient Method for the Solid-Phase Extraction of Dissolved Organic Matter (SPE-DOM) from Seawater. *Limnol. Oceanogr. Methods* **2008**, *6* (6), 230–235. https://doi.org/10.4319/lom.2008.6.230.

(143) Li, Y.; Harir, M.; Uhl, J.; Kanawati, B.; Lucio, M.; Smirnov, K. S.; Koch, B. P.; Schmitt-Kopplin, P.; Hertkorn, N. How Representative Are Dissolved Organic Matter (DOM) Extracts? A Comprehensive Study of Sorbent Selectivity for DOM Isolation. *Water Res.* **2017**, *116*, 316–323. https://doi.org/10.1016/j.watres.2017.03.038.

(144) Lam, B.; Baer, A.; Alaee, M.; Lefebvre, B.; Moser, A.; Williams, A.; Simpson, A. J. Major Structural Components in Freshwater Dissolved Organic Matter. *Environ. Sci. Technol.* **2007**, *41* (24), 8240–8247. https://doi.org/10.1021/es0713072.

(145) Stücheli, P. E.; Niggemann, J.; Schubert, C. J. Comparison of Different Solid Phase Extraction Sorbents for the Qualitative Assessment of Dissolved Organic Nitrogen in

Freshwater Samples Using FT-ICR-MS. *J. Limnol.* **2018**, *77* (3), 400–411. https://doi.org/10.4081/jlimnol.2018.1791.

(146) Wang, C.; He, L.; Li, D. W.; Bruschweiler-Li, L.; Marshall, A. G.; Brüschweiler, R. Accurate Identification of Unknown and Known Metabolic Mixture Components by Combining 3D NMR with Fourier Transform Ion Cyclotron Resonance Tandem Mass Spectrometry. *J. Proteome Res.* **2017**, *16* (10), 3774–3786. https://doi.org/10.1021/acs.jproteome.7b00457.

(147) McAdams, B. C.; Aiken, G. R.; McKnight, D. M.; Arnold, W. A.; Chin, Y. P. High Pressure Size Exclusion Chromatography (HPSEC) Determination of Dissolved Organic Matter Molecular Weight Revisited: Accounting for Changes in Stationary Phases, Analytical Standards, and Isolation Methods. *Environ. Sci. Technol.* **2018**, *52* (2), 722–730. https://doi.org/10.1021/acs.est.7b04401.

(148) Green, N. W.; Perdue, E. M.; Aiken, G. R.; Butler, K. D.; Chen, H.; Dittmar, T.; Niggemann, J.; Stubbins, A. An Intercomparison of Three Methods for the Large-Scale Isolation of Oceanic Dissolved Organic Matter. *Mar. Chem.* **2014**, *161*, 14–19. https://doi.org/10.1016/j.marchem.2014.01.012.

(149) Lv, J.; Zhang, S.; Luo, L.; Cao, D. Solid-Phase Extraction-Stepwise Elution (SPE-SE) Procedure for Isolation of Dissolved Organic Matter Prior to ESI-FT-ICR-MS Analysis. *Anal. Chim. Acta* **2016**, *948*, 55–61. https://doi.org/10.1016/j.aca.2016.10.038.

(150) Raeke, J.; Lechtenfeld, O. J.; Wagner, M.; Herzsprung, P.; Reemtsma, T. Selectivity of Solid Phase Extraction of Freshwater Dissolved Organic Matter and Its Effect on Ultrahigh Resolution Mass Spectra. *Environ. Sci. Process. Impacts* **2016**, *18* (7), 918–927. https://doi.org/10.1039/C6EM00200E.

(151) Yamamura, H.; Okimoto, K.; Kimura, K.; Watanabe, Y. Hydrophilic Fraction of Natural Organic Matter Causing Irreversible Fouling of Microfiltration and Ultrafiltration

Membranes. *Water Res.* **2014**, *54*, 123–136. https://doi.org/10.1016/j.watres.2014.01.024.

(152) Zularisam, A. W.; Ahmad, A.; Sakinah, M.; Ismail, A. F.; Matsuura, T. Role of Natural Organic Matter (NOM), Colloidal Particles, and Solution Chemistry on Ultrafiltration Performance. *Sep. Purif. Technol.* **2011**, *78* (2), 189–200. https://doi.org/10.1016/j.seppur.2011.02.001.

(153) Sim, L. N.; Chong, T. H.; Taheri, A. H.; Sim, S. T. V.; Lai, L.; Krantz, W. B.; Fane, A. G. A Review of Fouling Indices and Monitoring Techniques for Reverse Osmosis. *Desalination* **2018**, *434* (December 2017), 169–188. https://doi.org/10.1016/j.desal.2017.12.009.

(154) Vetter, T. A.; Perdue, E. M.; Ingall, E.; Koprivnjak, J. F.; Pfromm, P. H. Combining Reverse Osmosis and Electrodialysis for More Complete Recovery of Dissolved Organic Matter from Seawater. *Sep. Purif. Technol.* **2007**, *56* (3), 383–387. https://doi.org/10.1016/j.seppur.2007.04.012.

(155) Koprivnjak, J. F.; Perdue, E. M.; Pfromm, P. H. Coupling Reverse Osmosis with Electrodialysis to Isolate Natural Organic Matter from Fresh Waters. *Water Res.* **2006**, *40* (18), 3385–3392. https://doi.org/10.1016/j.watres.2006.07.019.

(156) D'Andrilli, J.; Dittmar, T.; Koch, B. P.; Purcell, J. M.; Marshall, A. G.; Cooper, W. T.; Andrilli, J. D.; Dittmar, T.; Koch, B. P.; Purcell, J. M.; Marshall, A. G.; Cooper, W. T. Comprehensive Characterization of Marine Dissolved Organic Matter by Fourier Transform Ion Cyclotron Resonance Mass Spectrometry with Electrospray and Atmospheric Pressure Photoionization. *Rapid Commun. Mass Spectrom.* **2010**, *24* (24), 3567–3577. https://doi.org/10.1002/rcm.

(157) Hockaday, W. C.; Purcell, J. M.; Marshall, A. G.; Baldock, J. A.; Hatcher, P. G. Electrospray and Photoionization Mass Spectrometry for the Characterization of Organic Matter in Natural Waters: A Qualitative Assessment. *Limnol. Oceanogr. Methods* **2009**, *7* (JAN.), 81–95. https://doi.org/10.4319/lom.2009.7.81.

(158) Ohno, T.; Sleighter, R. L.; Hatcher, P. G. Comparative Study of Organic Matter Chemical Characterization Using Negative and Positive Mode Electrospray Ionization Ultrahigh-Resolution Mass Spectrometry. *Anal. Bioanal. Chem.* **2016**, *408* (10), 2497–2504. https://doi.org/10.1007/s00216-016-9346-x.

(159) Fenn, J. B.; Mann, M.; Meng, C. K.; Wong, S. F.; Whitehouse, C. M. Electrospray Ionization-Principles and Practice. *Mass Spectrom. Rev.* **1990**, *9* (1), 37–70. https://doi.org/10.1002/mas.1280090103.

(160) Xu, Y. F.; Lu, W.; Rabinowitz, J. D. Avoiding Misannotation of In-Source Fragmentation Products as Cellular Metabolites in Liquid Chromatography-Mass Spectrometry-Based Metabolomics. *Anal. Chem.* **2015**, *87* (4), 2273–2281. https://doi.org/10.1021/ac504118y.

(161) Gathungu, R. M.; Larrea, P.; Sniatynski, M. J.; Marur, V. R.; Bowden, J. A.; Koelmel, J. P.; Starke-Reed, P.; Hubbard, V. S.; Kristal, B. S. Optimization of Electrospray Ionization Source Parameters for Lipidomics to Reduce Misannotation of In-Source Fragments as Precursor Ions. *Anal. Chem.* **2018**, *90* (22), 13523–13532. https://doi.org/10.1021/acs.analchem.8b03436.

(162) Konermann, L.; Ahadi, E.; Rodriguez, A. D.; Vahidi, S. Unraveling the Mechanism of Electrospray Ionization. *Anal. Chem.* **2013**, *85* (1), 2–9. https://doi.org/10.1021/ac302789c.

(163) Kruve, A.; Kaupmees, K.; Liigand, J.; Leito, I. Negative Electrospray Ionization via Deprotonation: Predicting the Ionization Efficiency. *Anal. Chem* **2014**, *86*, 57. https://doi.org/10.1021/ac404066v.

(164) Oss, M.; Kruve, A.; Herodes, K.; Leito, I. Electrospray Ionization Efficiency Scale of Organic Compound. *Anal. Chem.* **2010**, *82* (7), 2865–2872. https://doi.org/10.1021/ac902856t.

(165) Liigand, J.; Kruve, A.; Leito, I.; Girod, M.; Antoine, R. Effect of Mobile Phase on Electrospray Ionization Efficiency. *J. Am. Soc. Mass Spectrom.* **2014**, *25* (11), 1853–1861.

https://doi.org/10.1007/s13361-014-0969-x.

(166) Kostiainen, R.; Kauppila, T. J. Effect of Eluent on the Ionization Process in Liquid Chromatography-Mass Spectrometry. *J. Chromatogr. A* **2009**, *1216* (4), 685–699. https://doi.org/10.1016/j.chroma.2008.08.095.

(167) Liigand, J.; Laaniste, A.; Kruve, A. PH Effects on Electrospray Ionization Efficiency. *J. Am. Soc. Mass Spectrom.* **2017**, *28* (3), 461–469. https://doi.org/10.1007/s13361-016-1563-1.

(168) Zhou, S.; Cook, K. D. Protonation in Electrospray Mass Spectrometry: Wrong-Way-Round or Right-Way-Round? *J. Am. Soc. Mass Spectrom.* **2000**, *11* (11), 961–966. https://doi.org/10.1016/S1044-0305(00)00174-4.

(169) Novotny, N. R.; Capley, E. N.; Stenson, A. C. Fact or Artifact: The Representativeness of ESI-MS for Complex Natural Organic Mixtures. *J. Mass Spectrom.* **2014**, *49* (4), 316–326. https://doi.org/10.1002/jms.3345.

(170) Kido Soule, M. C.; Longnecker, K.; Giovannoni, S. J.; Kujawinski, E. B. Impact of Instrument and Experiment Parameters on Reproducibility of Ultrahigh Resolution ESI FT-ICR Mass Spectra of Natural Organic Matter. *Org. Geochem.* **2010**, *41* (8), 725–733. https://doi.org/10.1016/j.orggeochem.2010.05.017.

(171) Lobodin, V. V; Juyal, P.; Mckenna, A. M.; Rodgers, R. P.; Marshall, A. G. Tetramethylammonium Hydroxide as a Reagent for Complex Mixture Analysis by Negative Ion Electrospray Ionization Mass Spectrometry. **2013**.

(172) Lobodin, V. V.; Juyal, P.; McKenna, A. M.; Rodgers, R. P.; Marshall, A. G. Lithium Cationization for Petroleum Analysis by Positive Ion Electrospray Ionization Fourier Transform Ion Cyclotron Resonance Mass Spectrometry. *Energy & Fuels* **2014**, *28* (11), 6841–6847. https://doi.org/10.1021/ef501683w.

(173) Lobodin, V. V.; Juyal, P.; McKenna, A. M.; Rodgers, R. P.; Marshall, A. G. Silver

Cationization for Rapid Speciation of Sulfur-Containing Species in Crude Oils by Positive Electrospray Ionization Fourier Transform Ion Cyclotron Resonance Mass Spectrometry. *Energy and Fuels* **2014**, *28* (1), 447–452. https://doi.org/10.1021/ef401897p.

(174) El-Faramawy, A.; Siu, K. W. M.; Thomson, B. A. Efficiency of Nano-Electrospray Ionization. *J. Am. Soc. Mass Spectrom.* **2005**, *16* (10), 1702–1707. https://doi.org/10.1016/j.jasms.2005.06.011.

(175) Marshall, A. G.; Chen, T. 40 Years of Fourier Transform Ion Cyclotron Resonance Mass Spectrometry. *Int. J. Mass Spectrom.* **2015**, *377* (1), 410–420. https://doi.org/10.1016/j.ijms.2014.06.034.

(176) Hertkorn, N.; Frommberger, M.; Witt, M.; Koch, B. P.; Schmitt-Kopplin, P.; Perdue, E. M.; Hertkorn, N., Frommberger, M., Witt, M., Koch, B.P., Schmitt-Kopplin, P., P.; E.M. Natural Organic Matter and the Event Horizon of Mass Spectrometry. *Anal. Chem.* **2008**, *80* (23), 8908–8919. https://doi.org/10.1021/ac800464g.

(177) Podgorski, D. C.; McKenna, A. M.; Rodgers, R. P.; Marshall, A. G.; Cooper, W. T. Selective Ionization of Dissolved Organic Nitrogen by Positive Ion Atmospheric Pressure Photoionization Coupled with Fourier Transform Ion Cyclotron Resonance Mass Spectrometry. *Anal. Chem.* **2012**, *84* (11), 5085–5090. https://doi.org/10.1021/ac300800w.

(178) Kauppila, T. J.; Syage, J. A.; Benter, T. Recent Developments in Atmospheric Pressure Photoionization-Mass Spectrometry. *Mass Spectrom. Rev.* **2015**, *36* (3), 423–449. https://doi.org/10.1002/mas.21477.

(179) Mopper, K.; Stubbins, A.; Ritchie, J. D.; Bialk, H. M.; Hatcher, P. G. Advanced Instrumental Approaches for Characterization of Marine Dissolved Organic Matter: Extraction Techniques, Mass Spectrometry, and Nuclear Magnetic Resonance Spectroscopy. *Chem. Rev.* **2007**, *107* (2), 419–442. https://doi.org/10.1021/cr050359b.

(180) Cai, S.-S.; Syage, J. a. Atmospheric Pressure Photoionization Mass Spectrometry for Analysis of Fatty Acid and Acylglycerol Lipids. *J. Chromatogr. A* **2006**, *1110*, 15–26. https://doi.org/10.1016/j.chroma.2006.01.050.

(181) Podgorski, D. C.; Hamdan, R.; McKenna, A. M.; Nyadong, L.; Rodgers, R. P.; Marshall, A. G.; Cooper, W. T. Characterization of Pyrogenic Black Carbon by Desorption Atmospheric Pressure Photoionization Fourier Transform Ion Cyclotron Resonance Mass Spectrometry. *Anal. Chem.* **2011**, *84* (3), 1281–1287. https://doi.org/10.1021/ac202166x.

(182) Hagemann, N.; Joseph, S.; Schmidt, H. P.; Kammann, C. I.; Harter, J.; Borch, T.; Young, R. B.; Varga, K.; Taherymoosavi, S.; Elliott, K. W.; McKenna, A.; Albu, M.; Mayrhofer, C.; Obst, M.; Conte, P.; Dieguez-Alonso, A.; Orsetti, S.; Subdiaga, E.; Behrens, S.; Kappler, A. Organic Coating on Biochar Explains Its Nutrient Retention and Stimulation of Soil Fertility. *Nat. Commun.* **2017**, *8* (1), 1–11. https://doi.org/10.1038/s41467-017-01123-0.

(183) Cao, D.; Huang, H.; Hu, M.; Cui, L.; Geng, F.; Rao, Z.; Niu, H.; Cai, Y.; Kang, Y. Comprehensive Characterization of Natural Organic Matter by MALDI- and ESI-Fourier Transform Ion Cyclotron Resonance Mass Spectrometry. *Anal. Chim. Acta* **2015**, *866*, 48–58. https://doi.org/10.1016/j.aca.2015.01.051.

(184) Solihat, N. N.; Acter, T.; Kim, D.; Plante, A. F.; Kim, S. Analyzing Solid-Phase Natural Organic Matter Using Laser Desorption Ionization Ultrahigh Resolution Mass Spectrometry. *Anal. Chem.* **2019**, *91* (1), 951–957. https://doi.org/10.1021/acs.analchem.8b04032.

(185) Zenobi, R.; Knochenmuss, R. Ion Formation in Maldi Mass Spectrometry. *Mass Spectrom. Rev.* **1998**, *17* (5), 337–366. https://doi.org/10.1002/(sici)1098-2787(1998)17:5<337::aid-mas2>3.0.co;2-s.

(186) Dreisewerd, K. The Desorption Process in MALDI. *Chemical Reviews*. 2003, pp 395–425. https://doi.org/10.1021/cr010375i.

(187) Kujawinski, E. B.; Behn, M. D. Automated Analysis of Electrospray Ionization Fourier Transform Ion Cyclotron Resonance Mass Spectra of Natural Organic Matter. *Anal. Chem.* **2006**, *78* (13), 4363–4373. https://doi.org/10.1021/ac0600306.

(188) Herzsprung, P.; Hertkorn, N.; von Tümpling, W.; Harir, M.; Friese, K.; Schmitt-Kopplin, P. Understanding Molecular Formula Assignment of Fourier Transform Ion Cyclotron Resonance Mass Spectrometry Data of Natural Organic Matter from a Chemical Point of View. *Anal. Bioanal. Chem.* **2014**, *406* (30), 7977–7987. https://doi.org/10.1007/s00216-014-8249-y.

(189) Savory, J. J.; Kaiser, N. K.; McKenna, A. M.; Xian, F.; Blakney, G. T.; Rodgers, R. P.; Hendrickson, C. L.; Marshall, A. G. Parts-per-Billion Fourier Transform Ion Cyclotron Resonance Mass Measurement Accuracy with a "Walking" Calibration Equation. *Anal. Chem.* **2011**, *83* (5), 1732–1736. https://doi.org/10.1021/ac102943z.

(190) Herzsprung, P.; V. Tümpling, W.; Hertkorn, N.; Harir, M.; Friese, K.; Schmitt-Kopplin, P. High-Field FTICR-MS Data Evaluation of Natural Organic Matter: Are CHON5S2 Molecular Class Formulas Assigned to 13C Isotopic m/z and in Reality CHO Components? *Anal. Chem.* **2015**, *87* (19), 9563–9566. https://doi.org/10.1021/acs.analchem.5b02549.

(191) Sleighter, R. L.; Mckee, G. A.; Liu, Z.; Hatcher, P. G. Naturally Present Fatty Acids as Internal Calibrants for Fourier Transform Mass Spectra of Dissolved Organic Matter. *Limnol. Oceanogr. Methods* **2008**, *6* (6), 246–253. https://doi.org/10.4319/lom.2008.6.246.

(192) Qi, Y.; O'Connor, P. B. Data Processing in Fourier Transform Ion Cyclotron Resonance Mass Spectrometry. *Mass Spectrom. Rev.* **2014**, *33* (5), 333–352. https://doi.org/10.1002/mas.21414.

(193) Smith, D. F.; Podgorski, D. C.; Rodgers, R. P.; Blakney, G. T.; Hendrickson, C. L. 21 Tesla FT-ICR Mass Spectrometer for Ultrahigh-Resolution Analysis of Complex Organic Mixtures.

Anal. Chem. **2018**, *90* (3), 2041–2047. https://doi.org/10.1021/acs.analchem.7b04159.

(194) Merder, J.; Freund, J. A.; Feudel, U.; Niggemann, J.; Singer, G.; Dittmar, T. Improved Mass Accuracy and Isotope Confirmation through Alignment of Ultrahigh-Resolution Mass Spectra of Complex Natural Mixtures. *Anal. Chem.* **2020**, *92* (3), 2558–2565. https://doi.org/10.1021/acs.analchem.9b04234.

(195) G. Marshall, A.; T. Blakney, G.; Chen, T.; K. Kaiser, N.; M. McKenna, A.; P. Rodgers, R.; M. Ruddy, B.; Xian, F. Mass Resolution and Mass Accuracy: How Much Is Enough? *Mass Spectrom.* **2013**, *2* (Special_Issue), S0009–S0009. https://doi.org/10.5702/massspectrometry.S0009.

(196) Marshall, A. G.; Guan, S. Advantages of High Magnetic Field for Fourier Transform Ion Cyclotron Resonance Mass Spectrometry. *Rapid Commun. Mass Spectrom.* **1996**, *10* (14), 1819–1823. https://doi.org/10.1002/(SICI)1097-0231(199611)10:14<1819::AID-RCM686>3.0.CO;2-Z.

(197) Hohenester, U. M.; Barbier Saint-Hilaire, P.; Fenaille, F.; Cole, R. B. Investigation of Space Charge Effects and Ion Trapping Capacity on Direct Introduction Ultra-High-Resolution Mass Spectrometry Workflows for Metabolomics. *J. Mass Spectrom.* **2020**, *55* (10), 1–15. https://doi.org/10.1002/jms.4613.

(198) Kaiser, N. K.; McKenna, A. M.; Savory, J. J.; Hendrickson, C. L.; Marshall, A. G. Tailored Ion Radius Distribution for Increased Dynamic Range in FT-ICR Mass Analysis of Complex Mixtures. *Anal. Chem.* **2013**, *85* (1), 265–272. https://doi.org/10.1021/ac302678v.

(199) McKenna, A. M.; Marshall, A. G.; Rodgers, R. P. Heavy Petroleum Composition. 4. Asphaltene Compositional Space. *Energy and Fuels* **2013**, *27* (3), 1257–1267. https://doi.org/10.1021/ef301747d.

(200) Sleighter, R. L.; Chen, H.; Wozniak, A. S.; Willoughby, A. S.; Caricasole, P.; Hatcher, P. G.

Establishing a Measure of Reproducibility of Ultrahigh-Resolution Mass Spectra for Complex Mixtures of Natural Organic Matter. *Anal. Chem.* **2012**, *84* (21), 9184–9191. https://doi.org/10.1021/ac3018026.

(201) Krajewski, L. C.; Lobodin, V. V.; Johansen, C.; Bartges, T. E.; Maksimova, E. V.; MacDonald, I. R.; Marshall, A. G. Linking Natural Oil Seeps from the Gulf of Mexico to Their Origin by Use of Fourier Transform Ion Cyclotron Resonance Mass Spectrometry. *Environ. Sci. Technol.* **2018**, *52* (3), 1365–1374. https://doi.org/10.1021/acs.est.7b04445.

(202) Schum, S. K.; Brown, L. E.; Mazzoleni, L. R. MFAssignR: Molecular Formula Assignment Software for Ultrahigh Resolution Mass Spectrometry Analysis of Environmental Complex Mixtures. *Environ. Res.* **2020**, *191*, 110114. https://doi.org/https://doi.org/10.1016/j.envres.2020.110114.

(203) Fu, Q.-L. L.; Fujii, M.; Riedel, T. Development and Comparison of Formula Assignment Algorithms for Ultrahigh-Resolution Mass Spectra of Natural Organic Matter. *Anal. Chim. Acta* **2020**, *1125*, 247–257. https://doi.org/https://doi.org/10.1016/j.aca.2020.05.048.

(204) Kim, S.; Rodgers, R. P.; Marshall, A. G. Truly "Exact" Mass: Elemental Composition Can Be Determined Uniquely from Molecular Mass Measurement at ~0.1 MDa Accuracy for Molecules up to ~500 Da. *Int. J. Mass Spectrom.* **2006**, *251* (2-3 SPEC. ISS.), 260–265. https://doi.org/10.1016/j.ijms.2006.02.001.

(205) Kunenkov, E. V.; Kononikhin, A. S.; Perminova, I. V.; Hertkorn, N.; Gaspar, A.; Schmitt-Kopplin, P.; Popov, I. A.; Garmash, A. V.; Nikolaev, E. N. Total Mass Difference Statistics Algorithm: A New Approach to Identification of High-Mass Building Blocks in Electrospray Ionization Fourier Transform Ion Cyclotron Mass Spectrometry Data of Natural Organic Matter. *Anal. Chem.* **2009**, *81* (24), 10106–10115. https://doi.org/10.1021/ac901476u.

(206) Tziotis, D.; Hertkorn, N.; Schmitt-Kopplin, P. Kendrick-Analogous Network Visualisation of

Ion Cyclotron Resonance Fourier Transform Mass Spectra: Improved Options for the Assignment of Elemental Compositions and the Classification of Organic Molecular Complexity. *Eur. J. Mass Spectrom.* **2011**, *17* (4), 415–421. https://doi.org/10.1255/ejms.1135.

(207) Longnecker, K.; Kujawinski, E. B. Using Network Analysis to Discern Compositional Patterns in Ultrahigh-Resolution Mass Spectrometry Data of Dissolved Organic Matter. *Rapid Commun. Mass Spectrom.* **2016**, *30* (22), 2388–2394. https://doi.org/10.1002/rcm.7719.

(208) Zhang, F.; Harir, M.; Moritz, F.; Zhang, J.; Witting, M.; Wu, Y.; Schmitt-Kopplin, P.; Fekete, A.; Gaspar, A.; Hertkorn, N. Molecular and Structural Characterization of Dissolved Organic Matter during and Post Cyanobacterial Bloom in Taihu by Combination of NMR Spectroscopy and FTICR Mass Spectrometry. *Water Res.* **2014**, *57*, 280–294. https://doi.org/https://doi.org/10.1016/j.watres.2014.02.051.

(209) Fudyma, J. D.; Lyon, J.; AminiTabrizi, R.; Gieschen, H.; Chu, R. K.; Hoyt, D. W.; Kyle, J. E.; Toyoda, J.; Tolic, N.; Heyman, H. M.; Hess, N. J.; Metz, T. O.; Tfaily, M. M. Untargeted Metabolomic Profiling of Sphagnum Fallax Reveals Novel Antimicrobial Metabolites. *Plant Direct* **2019**, *3* (11), e00179. https://doi.org/10.1002/pld3.179.

(210) Southam, A. D.; Lange, A.; Al-Salhi, R.; Hill, E. M.; Tyler, C. R.; Viant, M. R. Distinguishing between the Metabolome and Xenobiotic Exposome in Environmental Field Samples Analysed by Direct-Infusion Mass Spectrometry Based Metabolomics and Lipidomics. https://doi.org/10.1007/s11306-014-0693-3.

(211) Hemmler, D.; Roullier-Gall, C.; Marshall, J. W.; Rychlik, M.; Taylor, A. J.; Schmitt-Kopplin, P. Evolution of Complex Maillard Chemical Reactions, Resolved in Time. *Sci. Rep.* **2017**, *7* (1), 3–8. https://doi.org/10.1038/s41598-017-03691-z.

(212) Fudyma, J. D.; Toyoda, J. G.; Chu, R. K.; Weitz, K. K.; Heyman, H. M.; Eder, E.; Hoyt, D. W.; Gieschen, H.; Graf Grachet, N.; Wilson, R. M.; Tfaily, M. M. Sequential Abiotic-biotic

Processes Drive Organic Carbon Transformation in Peat Bogs. *J. Geophys. Res. Biogeosciences* **2016**, 1–6. https://doi.org/10.1029/2020JG006079.

(213) Kind, T.; Fiehn, O. Seven Golden Rules for Heuristic Filtering of Molecular Formulas Obtained by Accurate Mass Spectrometry. *BMC Bioinformatics* **2007**, *8*. https://doi.org/10.1186/1471-2105-8-105.

(214) Tolić, N. T.; Liu, Y.; Liyu, A.; Shen, Y.; Tfaily, M. M.; Kujawinski, E. B.; Longnecker, K.; Kuo, L.-J. J.; Robinson, E. W.; Paš, L.; Tolić, T.; Hess, N. J.; Tolić, N.; Liu, Y.; Liyu, A.; Shen, Y.; Tfaily, M. M.; Kujawinski, E. B.; Longnecker, K.; Kuo, L.-J. J.; Robinson, E. W.; Paša-Tolić, L.; Hess, N. J. Formularity: Software for Automated Formula Assignment of Natural and Other Organic Matter from Ultrahigh-Resolution Mass Spectra. *Anal. Chem.* **2017**, *89* (23), 12659–12665. https://doi.org/10.1021/acs.analchem.7b03318.

(215) Merder, J.; Freund, J. A.; Feudel, U.; Hansen, C. T.; Hawkes, J. A.; Jacob, B.; Klaproth, K.; Niggemann, J.; Noriega-Ortega, B. E.; Osterholz, H.; Rossel, P. E.; Seidel, M.; Singer, G.; Stubbins, A.; Waska, H.; Dittmar, T. ICBM-OCEAN: Processing Ultrahigh-Resolution Mass Spectrometry Data of Complex Molecular Mixtures. *Anal. Chem.* **2020**, *92* (10), 6832–6838. https://doi.org/10.1021/acs.analchem.9b05659.

(216) Koch, B. P.; Dittmar, T. From Mass to Structure: An Aromaticity Index for High-Resolution Mass Data of Natural Organic Matter. *Rapid Commun. Mass Spectrom.* **2006**, *20* (5), 926–932. https://doi.org/10.1002/rcm.2386.

(217) Kroll, J. H.; Donahue, N. M.; Jimenez, J. L.; Kessler, S. H.; Canagaratna, M. R.; Wilson, K. R.; Altieri, K. E.; Mazzoleni, L. R.; Wozniak, A. S.; Bluhm, H.; Mysak, E. R.; Smith, J. D.; Kolb, C. E.; Worsnop, D. R. Carbon Oxidation State as a Metric for Describing the Chemistry of Atmospheric Organic Aerosol. *Nat. Chem.* **2011**, *3* (2), 133–139. https://doi.org/10.1038/nchem.948.

(218) Lavonen, E. E.; Gonsior, M.; Tranvik, L. J.; Schmitt-Kopplin, P.; Köhler, S. J. Selective Chlorination of Natural Organic Matter: Identification of Previously Unknown Disinfection Byproducts. *Environ. Sci. Technol.* **2013**, *47* (5), 2264–2271. https://doi.org/10.1021/es304669p.

(219) Riedel, T.; Biester, H.; Dittmar, T. Molecular Fractionation of Dissolved Organic Matter with Metal Salts. *Environ. Sci. Technol.* **2012**, *46* (8), 4419–4426. https://doi.org/10.1021/es203901u.

(220) LaRowe, D. E.; Van Cappellen, P. Degradation of Natural Organic Matter: A Thermodynamic Analysis. *Geochim. Cosmochim. Acta* **2011**, *75* (8), 2030–2042. https://doi.org/10.1016/j.gca.2011.01.020.

(221) Keiluweit, M.; Nico, P. S.; Kleber, M.; Fendorf, S. Are Oxygen Limitations under Recognized Regulators of Organic Carbon Turnover in Upland Soils? *Biogeochemistry* **2016**, *127* (2–3), 157–171. https://doi.org/10.1007/s10533-015-0180-6.

(222) Graham, E. B.; Tfaily, M. M.; Crump, A. R.; Goldman, A. E.; Bramer, L. M.; Arntzen, E.; Romero, E.; Resch, C. T.; Kennedy, D. W.; Stegen, J. C. Carbon Inputs From Riparian Vegetation Limit Oxidation of Physically Bound Organic Carbon Via Biochemical and Thermodynamic Processes. *J. Geophys. Res. Biogeosciences* **2017**, *122* (12), 3188–3205. https://doi.org/10.1002/2017JG003967.

(223) Wilson, R. M.; Tfaily, M. M. Advanced Molecular Techniques Provide New Rigorous Tools for Characterizing Organic Matter Quality in Complex Systems. *Journal of Geophysical Research: Biogeosciences*. Blackwell Publishing Ltd June 1, 2018, pp 1790–1795. https://doi.org/10.1029/2018JG004525.

(224) Boye, K.; Noël, V.; Tfaily, M. M.; Bone, S. E.; Williams, K. H.; Bargar, J. R. R.; Fendorf, S. Thermodynamically Controlled Preservation of Organic Carbon in Floodplains. *Nat. Geosci.*

2017, *10* (6), 415–419. https://doi.org/10.1038/ngeo2940.

(225) Kendrick, E. A Mass Scale Based on CH2= 14.0000 for High Resolution Mass Spectrometry of Organic Compounds. *Anal. Chem.* **1963**, *35* (13), 2146–2154. https://doi.org/10.1021/ac60206a048.

(226) Kramer, R. W.; Kujawinski, E. B.; Hatcher, P. G. Identification of Black Carbon Derived Structures in a Volcanic Ash Soil Humic Acid by Fourier Transform Ion Cyclotron Resonance Mass Spectrometry. *Environ. Sci. Technol.* **2004**, *38* (12), 3387–3395. https://doi.org/10.1021/es030124m.

(227) Stenson, A. C.; Marshall, A. G.; Cooper, W. T. Exact Masses and Chemical Formulas of Individual Suwannee River Fulvic Acids from Ultrahigh Resolution Electrospray Ionization Fourier Transform Ion Cyclotron Resonance Mass Spectra. *Anal. Chem.* **2003**, *75* (6), 1275–1284. https://doi.org/10.1021/ac026106p.

(228) Kujawinski, E. B.; Del Vecchio, R.; Blough, N. V; Klein, G. C.; Marshall, A. G. Probing Molecular-Level Transformations of Dissolved Organic Matter: Insights on Photochemical Degradation and Protozoan Modification of DOM from Electrospray Ionization Fourier Transform Ion Cyclotron Resonance Mass Spectrometry. In *Marine Chemistry*; 2004; Vol. 92, pp 23–37. https://doi.org/10.1016/j.marchem.2004.06.038.

(229) Sleighter, R. L.; Hatcher, P. G. The Application of Electrospray Ionization Coupled to Ultrahigh Resolution Mass Spectrometry for the Molecular Characterization of Natural Organic Matter. *J. MASS Spectrom. J. Mass Spectrom* **2007**, *42*, 559–574. https://doi.org/10.1002/jms.1221.

(230) Ohno, T.; Parr, T. B.; Gruselle, M. C. I.; Fernandez, I. J.; Sleighter, R. L.; Hatcher, P. G. Molecular Composition and Biodegradability of Soil Organic Matter: A Case Study Comparing Two New England Forest Types. *Environ. Sci. Technol.* **2014**, *48* (13), 7229–7236.

https://doi.org/10.1021/es405570c.

(231) Dier, T. K. F.; Egele, K.; Fossog, V.; Hempelmann, R.; Volmer, D. A. Enhanced Mass Defect Filtering to Simplify and Classify Complex Mixtures of Lignin Degradation Products. *Anal. Chem.* **2016**, *88* (2), 1328–1335. https://doi.org/10.1021/acs.analchem.5b03790.

(232) Sato, H.; Nakamura, S.; Teramoto, K.; Sato, T. Structural Characterization of Polymers by MALDI Spiral-TOF Mass Spectrometry Combined with Kendrick Mass Defect Analysis. *J. Am. Soc. Mass Spectrom.* **2014**, *25* (8), 1346–1355. https://doi.org/10.1007/s13361-014-0915-y.

(233) Glasser, W. G. About Making Lignin Great Again—Some Lessons From the Past . *Frontiers in Chemistry* . 2019, p 565.

(234) Fouquet, T. N. J.; Cody, R. B.; Ozeki, Y.; Kitagawa, S.; Ohtani, H.; Sato, H. On the Kendrick Mass Defect Plots of Multiply Charged Polymer Ions: Splits, Misalignments, and How to Correct Them. *J. Am. Soc. Mass Spectrom.* **2018**, *29* (8), 1611–1626. https://doi.org/10.1007/s13361-018-1972-4.

(235) Liu, Q.; Luo, L.; Zheng, L. Lignins: Biosynthesis and Biological Functions in Plants. *International Journal of Molecular Sciences*. 2018. https://doi.org/10.3390/ijms19020335.

(236) Lv, J.; Zhang, S.; Wang, S.; Luo, L.; Cao, D.; Christie, P. Molecular-Scale Investigation with ESI-FT-ICR-MS on Fractionation of Dissolved Organic Matter Induced by Adsorption on Iron Oxyhydroxides. *Environ. Sci. Technol.* **2016**, *50* (5), 2328–2336. https://doi.org/10.1021/acs.est.5b04996.

(237) Brockman, S. A.; Roden, E. V.; Hegeman, A. D. Van Krevelen Diagram Visualization of High Resolution-Mass Spectrometry Metabolomics Data with OpenVanKrevelen. *Metabolomics* **2018**, *14* (4), 1–5. https://doi.org/10.1007/s11306-018-1343-y.

(238) Kim, S.; Kramer, R. W.; Hatcher, P. G. Graphical Method for Analysis of Ultrahigh-Resolution Broadband Mass Spectra of Natural Organic Matter, the Van Krevelen Diagram.

Anal. Chem. **2003**, *75* (20), 5336–5344. https://doi.org/10.1021/ac034415p.

(239) Minor, E. C.; Swenson, M. M.; Mattson, B. M.; Oyler, A. R. Structural Characterization of Dissolved Organic Matter: A Review of Current Techniques for Isolation and Analysis. *Environ. Sci. Process. Impacts* **2014**, *16* (9), 2064–2079. https://doi.org/10.1039/C4EM00062E.

(240) D'Andrilli, J.; Foreman, C. M.; Marshall, A. G.; McKnight, D. M. Characterization of IHSS Pony Lake Fulvic Acid Dissolved Organic Matter by Electrospray Ionization Fourier Transform Ion Cyclotron Resonance Mass Spectrometry and Fluorescence Spectroscopy. *Org. Geochem.* **2013**, *65*, 19–28. https://doi.org/10.1016/j.orggeochem.2013.09.013.

(241) Waggoner, D. C.; Chen, H.; Willoughby, A. S.; Hatcher, P. G. Formation of Black Carbon-like and Alicyclic Aliphatic Compounds by Hydroxyl Radical Initiated Degradation of Lignin. **2015**. https://doi.org/10.1016/j.orggeochem.2015.02.007.

(242) Rivas-Ubach, A.; Liu, Y.; Bianchi, T. S.; Tolić, N.; Jansson, C.; Paša-Tolić, L. Moving beyond the van Krevelen Diagram: A New Stoichiometric Approach for Compound Classification in Organisms. *Anal. Chem.* **2018**, *90* (10), 6152–6160. https://doi.org/10.1021/acs.analchem.8b00529.

(243) NORMAN Network (2021). NORMAN Suspect List Exchange (NORMAN-SLE) https://www.norman-network.com/nds/SLE/.

(244) Hockaday, W. C.; Purcell, J. M.; Marshall, A. G.; Baldock, J. A.; Hatcher, P. G. Electrospray and Photoionization Mass Spectrometry for the Characterization of Organic Matter in Natural Waters: A Qualitative Assessment. *Limnol. Oceanogr. Methods* **2009**, *7* (1), 81–95. https://doi.org/10.4319/lom.2009.7.81.

(245) Smith, A. P.; Bond-Lamberty, B.; Benscoter, B. W.; Tfaily, M. M.; Hinkle, C. R.; Liu, C.; Bailey, V. L. Shifts in Pore Connectivity from Precipitation versus Groundwater Rewetting Increases Soil Carbon Loss after Drought. *Nat. Commun.* **2017**, *8* (1), 1–11.

https://doi.org/10.1038/s41467-017-01320-x.

(246) Hodgkins, S. B.; Tfaily, M. M.; McCalley, C. K.; Logan, T. A.; Crill, P. M.; Saleska, S. R.; Rich, V. I.; Chanton, J. P. Changes in Peat Chemistry Associated with Permafrost Thaw Increase Greenhouse Gas Production. *Proc. Natl. Acad. Sci. U. S. A.* **2014**, *111* (16), 5819–5824. https://doi.org/10.1073/pnas.1314641111.

(247) Riedel, T.; Zark, M.; Vähätalo, A. V.; Niggemann, J.; Spencer, R. G. M.; Hernes, P. J.; Dittmar, T. Molecular Signatures of Biogeochemical Transformations in Dissolved Organic Matter from Ten World Rivers. *Front. Earth Sci.* **2016**, *4* (September), 1–16. https://doi.org/10.3389/feart.2016.00085.

(248) Avneri-Katz, S.; Young, R. B.; McKenna, A. M.; Chen, H.; Corilo, Y. E.; Polubesova, T.; Borch, T.; Chefetz, B. Adsorptive Fractionation of Dissolved Organic Matter (DOM) by Mineral Soil: Macroscale Approach and Molecular Insight. *Org. Geochem.* **2017**, *103*, 113–124. https://doi.org/10.1016/j.orggeochem.2016.11.004.

(249) Mapolelo, M. M.; Rodgers, R. P.; Blakney, G. T.; Yen, A. T.; Asomaning, S.; Marshall, A. G. Characterization of Naphthenic Acids in Crude Oils and Naphthenates by Electrospray Ionization FT-ICR Mass Spectrometry. *Int. J. Mass Spectrom.* **2011**, *300* (2), 149–157. https://doi.org/https://doi.org/10.1016/j.ijms.2010.06.005.

(250) Mazur, D. M.; Harir, M.; Schmitt-Kopplin, P.; Polyakova, O. V; Lebedev, A. T. High Field FT-ICR Mass Spectrometry for Molecular Characterization of Snow Board from Moscow Regions. *Sci. Total Environ.* **2016**, *557–558*, 12–19. https://doi.org/https://doi.org/10.1016/j.scitotenv.2016.02.178.

(251) Cho, Y.; Ahmed, A.; Islam, A.; Kim, S. Developments in FT-ICR Ms Instrumentation, Ionization Techniques, and Data Interpretation Methods for Petroleomics. *Mass Spectrom. Rev.* **2015**, *34* (2), 248–263. https://doi.org/10.1002/mas.21438.

(252) Jarvis, J. M.; Page-Dumroese, D. S.; Anderson, N. M.; Corilo, Y.; Rodgers, R. P. Characterization of Fast Pyrolysis Products Generated from Several Western USA Woody Species. *Energy and Fuels* **2014**, *28* (10), 6438–6446. https://doi.org/10.1021/ef501714j.

(253) Borch, T.; Kretzschmar, R.; Skappler, A.; Van Cappellen, P.; Ginder-Vogel, M.; Voegelin, A.; Campbell, K. Biogeochemical Redox Processes and Their Impact on Contaminant Dynamics. *Environ. Sci. Technol.* **2010**, *44* (1), 15–23. https://doi.org/10.1021/es9026248.

(254) Brooker, M. R.; Longnecker, K.; Kujawinski, E. B.; Evert, M. H.; Mouser, P. J. Discrete Organic Phosphorus Signatures Are Evident in Pollutant Sources within a Lake Erie Tributary. *Environ. Sci. Technol.* **2018**, *52* (12), 6771–6779. https://doi.org/10.1021/acs.est.7b05703.

(255) Hervé, M. R.; Nicolè, F.; Lê Cao, K. A. Multivariate Analysis of Multiple Datasets: A Practical Guide for Chemical Ecology. *J. Chem. Ecol.* **2018**, *44* (3), 215–234. https://doi.org/10.1007/s10886-018-0932-6.

(256) Hur, M.; Yeo, I.; Park, E.; Kim, Y. H.; Yoo, J.; Kim, E.; No, M.; Koh, J.; Kim, S. Combination of Statistical Methods and Fourier Transform Ion Cyclotron Resonance Mass Spectrometry for More Comprehensive, Molecular-Level Interpretations of Petroleum Samples. *Anal. Chem.* **2010**, *82* (1), 211–218. https://doi.org/10.1021/ac901748c.

(257) Kujawinski, E. B.; Longnecker, K.; Blough, N. V.; Vecchio, R. Del; Finlay, L.; Kitner, J. B.; Giovannoni, S. J. Identification of Possible Source Markers in Marine Dissolved Organic Matter Using Ultrahigh Resolution Mass Spectrometry. *Geochim. Cosmochim. Acta* **2009**, *73* (15), 4384–4399. https://doi.org/10.1016/j.gca.2009.04.033.

(258) Temminghoff, E. J. M.; Van Der Zee, S. E. A. T. M.; De Haan, F. A. M. Copper Mobility in a Copper-Contaminated Sandy Soil as Affected by PH and Solid and Dissolved Organic Matter. *Environ. Sci. Technol.* **1997**, *31* (4), 1109–1115. https://doi.org/10.1021/es9606236.

(259) Lindsay, W. L.; Norvell, W. A. Development of a DTPA Soil Test for Zinc, Iron, Manganese, and Copper. *Soil Sci. Soc. Am. J.* **1978**, *42* (3), 421–428. https://doi.org/10.2136/sssaj1978.03615995004200030009x.

(260) Gleyzes, C.; Tellier, S.; Astruc, M. Fractionation Studies of Trace Elements in Contaminated Soils and Sediments: A Review of Sequential Extraction Procedures. *TrAC - Trends Anal. Chem.* **2002**, *21* (6–7), 451–467. https://doi.org/10.1016/S0165-9936(02)00603-9.

(261) Boiteau, R. M.; Fansler, S. J.; Farris, Y.; Shaw, J. B.; Koppenaal, D. W.; Pasa-Tolic, L.; Jansson, J. K. Siderophore Profiling of Co-Habitating Soil Bacteria by Ultra-High Resolution Mass Spectrometry. *Metallomics* **2019**, *11* (1), 166–175. https://doi.org/10.1039/c8mt00252e.

(262) Waska, H.; Brumsack, H. J.; Massmann, G.; Koschinsky, A.; Schnetger, B.; Simon, H.; Dittmar, T. Inorganic and Organic Iron and Copper Species of the Subterranean Estuary: Origins and Fate. *Geochim. Cosmochim. Acta* **2019**, *259*, 211–232. https://doi.org/10.1016/j.gca.2019.06.004.

(263) Waska, H.; Koschinsky, A.; Ruiz Chancho, M. J.; Dittmar, T. Investigating the Potential of Solid-Phase Extraction and Fourier-Transform Ion Cyclotron Resonance Mass Spectrometry (FT-ICR-MS) for the Isolation and Identification of Dissolved Metal-Organic Complexes from Natural Waters. *Mar. Chem.* **2015**, *173*, 78–92. https://doi.org/10.1016/j.marchem.2014.10.001.

(264) Boiteau, R. M.; Till, C. P.; Ruacho, A.; Bundy, R. M.; Hawco, N. J.; McKenna, A. M.; Barbeau, K. A.; Bruland, K. W.; Saito, M. A.; Repeta, D. J. Structural Characterization of Natural Nickel and Copper Binding Ligands along the US GEOTRACES Eastern Pacific Zonal Transect. *Front. Mar. Sci.* **2016**, *3* (NOV), 243. https://doi.org/10.3389/fmars.2016.00243.

(265) Chen, H.; Johnston, R. C.; Mann, B. F.; Chu, R. K.; Tolic, N.; Parks, J. M.; Gu, B.

Identification of Mercury and Dissolved Organic Matter Complexes Using Ultrahigh Resolution Mass Spectrometry. *Environ. Sci. Technol. Lett* **2017**, *4*, 3. https://doi.org/10.1021/acs.estlett.6b00460.

(266) Xu, C.; Chen, H.; Sugiyama, Y.; Zhang, S.; Li, H. P.; Ho, Y. F.; Chuang, C. Y.; Schwehr, K. A.; Kaplan, D. I.; Yeager, C.; Roberts, K. A.; Hatcher, P. G.; Santschi, P. H. Novel Molecular-Level Evidence of Iodine Binding to Natural Organic Matter from Fourier Transform Ion Cyclotron Resonance Mass Spectrometry. *Sci. Total Environ.* **2013**, *449*, 244–252. https://doi.org/10.1016/j.scitotenv.2013.01.064.

(267) Shen, Y.; Zhao, R.; Tolić, N.; Tfaily, M. M.; Robinson, E. W.; Boiteau, R.; Paša-Tolić, L.; Hess, N. J. Online Supercritical Fluid Extraction Mass Spectrometry (SFE-LC-FTMS) for Sensitive Characterization of Soil Organic Matter. *Faraday Discuss.* **2019**, *218*, 157–171. https://doi.org/10.1039/c9fd00011a.

(268) Rodgers, R. P.; Mapolelo, M. M.; Robbins, W. K.; Chacón-Patiño, M. L.; Putman, J. C.; Niles, S. F.; Rowland, S. M.; Marshall, A. G. Combating Selective Ionization in the High Resolution Mass Spectral Characterization of Complex Mixtures. *Faraday Discuss.* **2019**, *218*, 29–51. https://doi.org/10.1039/c9fd00005d.

(269) Capley, E. N.; Tipton, J. D.; Marshall, A. G.; Stenson, A. C. Chromatographic Reduction of Isobaric and Isomeric Complexity of Fulvic Acids to Enable Multistage Tandem Mass Spectral Characterization. *Anal. Chem.* **2010**, *82* (19), 8194–8202. https://doi.org/10.1021/ac1016216.

(270) Stenson, A. C. Reversed-Phase Chromatography Fractionation Tailored to Mass Spectral Characterization of Humic Substances. *Environ. Sci. Technol.* **2008**, *42* (6), 2060–2065. https://doi.org/10.1021/es7022412.

(271) Boiteau, R. M.; Fitzsimmons, J. N.; Repeta, D. J.; Boyle, E. A. Detection of Iron Ligands in

Seawater and Marine Cyanobacteria Cultures by High-Performance Liquid Chromatography-Inductively Coupled Plasma-Mass Spectrometry. *Anal. Chem.* **2013**, *85* (9), 4357–4362. https://doi.org/10.1021/ac3034568.

(272) Patriarca, C.; Bergquist, J.; Sjöberg, P. J. R.; Tranvik, L.; Hawkes, J. A. Online HPLC-ESI-HRMS Method for the Analysis and Comparison of Different Dissolved Organic Matter Samples. *Environ. Sci. Technol.* **2018**, *52* (4), 2091–2099. https://doi.org/10.1021/acs.est.7b04508.

(273) Woods, G. C.; Simpson, M. J.; Koerner, P. J.; Napoli, A.; Simpson, A. J. HILIC-NMR: Toward the Identification of Individual Molecular Components in Dissolved Organic Matter. *Environ. Sci. Technol.* **2011**, *45* (9), 3880–3886. https://doi.org/10.1021/es103425s.

(274) Ladd, M. P.; Giannone, R. J.; Abraham, P. E.; Wullschleger, S. D.; Hettich, R. L. Evaluation of an Untargeted Nano-Liquid Chromatography-Mass Spectrometry Approach to Expand Coverage of Low Molecular Weight Dissolved Organic Matter in Arctic Soil. *Sci. Rep.* **2019**, *9* (1), 1–13. https://doi.org/10.1038/s41598-019-42118-9.

(275) Sandron, S.; Rojas, A.; Wilson, R.; Davies, N. W.; Haddad, P. R.; Shellie, R. A.; Nesterenko, P. N.; Kelleher, B. P.; Paull, B. Chromatographic Methods for the Isolation, Separation and Characterisation of Dissolved Organic Matter. *Environ. Sci. Process. Impacts* **2015**, *17* (9), 1531–1567. https://doi.org/10.1039/c5em00223k.

(276) Leclair, J. P.; Collett, J. L.; Mazzoleni, L. R. Fragmentation Analysis of Water-Soluble Atmospheric Organic Matter Using Ultrahigh-Resolution FT-ICR Mass Spectrometry. *Environ. Sci. Technol.* **2012**, *46* (8), 4312–4322. https://doi.org/10.1021/es203509b.

(277) Niles, S. F.; Chacón-Patinõ, M. L.; Smith, D. F.; Rodgers, R. P.; Marshall, A. G. Comprehensive Compositional and Structural Comparison of Coal and Petroleum Asphaltenes Based on Extrography Fractionation Coupled with Fourier Transform Ion

Cyclotron Resonance MS and MS/MS Analysis. *Energy and Fuels* **2020**, *34* (2), 1492–1505. https://doi.org/10.1021/acs.energyfuels.9b03527.

(278) Chacón-Patiño, M. L.; Rowland, S. M.; Rodgers, R. P. Advances in Asphaltene Petroleomics. Part 1: Asphaltenes Are Composed of Abundant Island and Archipelago Structural Motifs. *Energy and Fuels* **2017**, *31* (12), 13509–13518. https://doi.org/10.1021/acs.energyfuels.7b02873.

(279) Guijas, C.; Montenegro-Burke, J. R.; Domingo-Almenara, X.; Palermo, A.; Warth, B.; Hermann, G.; Koellensperger, G.; Huan, T.; Uritboonthai, W.; Aisporna, A. E.; Wolan, D. W.; Spilker, M. E.; Benton, H. P.; Siuzdak, G. METLIN: A Technology Platform for Identifying Knowns and Unknowns. *Anal. Chem.* **2018**, *90* (5), 3156–3164. https://doi.org/10.1021/acs.analchem.7b04424.

(280) Dührkop, K.; Fleischauer, M.; Ludwig, M.; Aksenov, A. A.; Melnik, A. V; Meusel, M.; Dorrestein, P. C.; Rousu, J.; Böcker, S. SIRIUS 4: A Rapid Tool for Turning Tandem Mass Spectra into Metabolite Structure Information. *Nat. Methods* **2019**, *16* (4), 299–302. https://doi.org/10.1038/s41592-019-0344-8.

(281) Ruttkies, C.; Schymanski, E. L.; Wolf, S.; Hollender, J.; Neumann, S. MetFrag Relaunched: Incorporating Strategies beyond in Silico Fragmentation. *J. Cheminform.* **2016**, *8* (1), 3. https://doi.org/10.1186/s13321-016-0115-9.

(282) Djoumbou-Feunang, Y.; Pon, A.; Karu, N.; Zheng, J.; Li, C.; Arndt, D.; Gautam, M.; Allen, F.; Wishart, D. S. CFM-ID 3.0: Significantly Improved ESI-MS/MS Prediction and Compound Identification. *Metabolites* **2019**, *9* (4), 72. https://doi.org/10.3390/metabo9040072.

(283) Longnecker, K.; Kujawinski, E. B. Mining Mass Spectrometry Data: Using New Computational Tools to Find Novel Organic Compounds in Complex Environmental

Mixtures. *Org. Geochem.* **2017**, *110*, 92–99. https://doi.org/10.1016/j.orggeochem.2017.05.008.

(284) Wang, M.; Carver, J. J.; Phelan, V. V.; Sanchez, L. M.; Garg, N.; Peng, Y.; Nguyen, D. D.; Watrous, J.; Kapono, C. A.; Luzzatto-Knaan, T.; Porto, C.; Bouslimani, A.; Melnik, A. V.; Meehan, M. J.; Liu, W. T.; Crüsemann, M.; Boudreau, P. D.; Esquenazi, E.; Sandoval-Calderón, M.; Kersten, R. D.; Pace, L. A.; Quinn, R. A.; Duncan, K. R.; Hsu, C. C.; Floros, D. J.; Gavilan, R. G.; Kleigrewe, K.; Northen, T.; Dutton, R. J.; Parrot, D.; Carlson, E. E.; Aigle, B.; Michelsen, C. F.; Jelsbak, L.; Sohlenkamp, C.; Pevzner, P.; Edlund, A.; McLean, J.; Piel, J.; Murphy, B. T.; Gerwick, L.; Liaw, C. C.; Yang, Y. L.; Humpf, H. U.; Maansson, M.; Keyzers, R. A.; Sims, A. C.; Johnson, A. R.; Sidebottom, A. M.; Sedio, B. E.; Klitgaard, A.; Larson, C. B.; Boya, C. A. P.; Torres-Mendoza, D.; Gonzalez, D. J.; Silva, D. B.; Marques, L. M.; Demarque, D. P.; Pociute, E.; O'Neill, E. C.; Briand, E.; Helfrich, E. J. N.; Granatosky, E. A.; Glukhov, E.; Ryffel, F.; Houson, H.; Mohimani, H.; Kharbush, J. J.; Zeng, Y.; Vorholt, J. A.; Kurita, K. L.; Charusanti, P.; McPhail, K. L.; Nielsen, K. F.; Vuong, L.; Elfeki, M.; Traxler, M. F.; Engene, N.; Koyama, N.; Vining, O. B.; Baric, R.; Silva, R. R.; Mascuch, S. J.; Tomasi, S.; Jenkins, S.; Macherla, V.; Hoffman, T.; Agarwal, V.; Williams, P. G.; Dai, J.; Neupane, R.; Gurr, J.; Rodríguez, A. M. C.; Lamsa, A.; Zhang, C.; Dorrestein, K.; Duggan, B. M.; Almaliti, J.; Allard, P. M.; Phapale, P.; Nothias, L. F.; Alexandrov, T.; Litaudon, M.; Wolfender, J. L.; Kyle, J. E.; Metz, T. O.; Peryea, T.; Nguyen, D. T.; VanLeer, D.; Shinn, P.; Jadhav, A.; Müller, R.; Waters, K. M.; Shi, W.; Liu, X.; Zhang, L.; Knight, R.; Jensen, P. R.; Palsson, B.; Pogliano, K.; Linington, R. G.; Gutiérrez, M.; Lopes, N. P.; Gerwick, W. H.; Moore, B. S.; Dorrestein, P. C.; Bandeira, N. Sharing and Community Curation of Mass Spectrometry Data with Global Natural Products Social Molecular Networking. *Nature Biotechnology*. Nature Publishing Group September 8, 2016, pp 828–837. https://doi.org/10.1038/nbt.3597.

(285) Watrous, J.; Roach, P.; Alexandrov, T.; Heath, B. S.; Yang, J. Y.; Kersten, R. D.; Van Der Voort, M.; Pogliano, K.; Gross, H.; Raaijmakers, J. M.; Moore, B. S.; Laskin, J.; Bandeira, N.; Dorrestein, P. C. Mass Spectral Molecular Networking of Living Microbial Colonies. *Proc. Natl. Acad. Sci. U. S. A.* **2012**, *109* (26), 10150. https://doi.org/10.1073/pnas.1203689109.

(286) Pande, S.; Kost, C. Bacterial Unculturability and the Formation of Intercellular Metabolic Networks. *Trends Microbiol.* **2017**, *25* (5), 349–361. https://doi.org/10.1016/j.tim.2017.02.015.

(287) Pinu, F. R.; Granucci, N.; Daniell, J.; Han, T. L.; Carneiro, S.; Rocha, I.; Nielsen, J.; Villas-Boas, S. G. Metabolite Secretion in Microorganisms: The Theory of Metabolic Overflow Put to the Test. *Metabolomics* **2018**, *14* (4), 1–16. https://doi.org/10.1007/s11306-018-1339-7.

(288) Horak, I.; Engelbrecht, G.; van Rensburg, P. J. J.; Claassens, S. Microbial Metabolomics: Essential Definitions and the Importance of Cultivation Conditions for Utilizing Bacillus Species as Bionematicides. *J. Appl. Microbiol.* **2019**, *127* (2), 326–343. https://doi.org/10.1111/jam.14218.

(289) Swenson, T. L.; Jenkins, S.; Bowen, B. P.; Northen, T. R. Untargeted Soil Metabolomics Methods for Analysis of Extractable Organic Matter. *Soil Biol. Biochem.* **2015**, *80*, 189–198. https://doi.org/10.1016/j.soilbio.2014.10.007.

(290) Bhinderwala, F.; Wase, N.; Dirusso, C.; Powers, R. Combining Mass Spectrometry and NMR Improves Metabolite Detection and Annotation. *J. Proteome Res.* **2018**, *17* (11), 4017–4022. https://doi.org/10.1021/acs.jproteome.8b00567.

(291) Dalcin Martins, P.; Hoyt, D. W.; Bansal, S.; Mills, C. T.; Tfaily, M.; Tangen, B. A.; Finocchiaro, R. G.; Johnston, M. D.; McAdams, B. C.; Solensky, M. J.; Smith, G. J.; Chin, Y. P.; Wilkins, M. J. Abundant Carbon Substrates Drive Extremely High Sulfate Reduction Rates and Methane Fluxes in Prairie Pothole Wetlands. *Glob. Chang. Biol.* **2017**, *23* (8), 3107–3120. https://doi.org/10.1111/gcb.13633.

(292) Tfaily, M. M.; Wilson, R. M.; Brewer, H. M.; Chu, R. K.; Heyman, H. M.; Hoyt, D. W.; Kyle, J. E.; Purvine, S. O. Single-Throughput Complementary High-Resolution Analytical Techniques for Characterizing Complex Natural Organic Matter Mixtures. *JoVE (Journal Vis. Exp.* **2019**, No. 143, e59035. https://doi.org/10.3791/59035.

(293) Georgii, E.; Jin, M.; Zhao, J.; Kanawati, B.; Schmitt-Kopplin, P.; Albert, A.; Winkler, J. B.; Schäffner, A. R. Relationships between Drought, Heat and Air Humidity Responses Revealed by Transcriptome-Metabolome Co-Analysis. *BMC Plant Biol.* **2017**, *17* (1), 1–24. https://doi.org/10.1186/s12870-017-1062-y.

(294) Osterholz, H.; Kirchman, D. L.; Niggemann, J.; Dittmar, T. Diversity of Bacterial Communities and Dissolved Organic Matter in a Temperate Estuary. *FEMS Microbiol. Ecol.* **2018**, *94* (8), 1–11. https://doi.org/10.1093/femsec/fiy119.

(295) Zhou, L.; Zhou, Y.; Yao, X.; Cai, J.; Liu, X.; Tang, X.; Zhang, Y.; Jang, K. S.; Jeppesen, E. Decreasing Diversity of Rare Bacterial Subcommunities Relates to Dissolved Organic Matter along Permafrost Thawing Gradients. *Environ. Int.* **2020**, *134* (November 2019), 105330. https://doi.org/10.1016/j.envint.2019.105330.

(296) Djoumbou-Feunang, Y.; Fiamoncini, J.; Gil-de-la-Fuente, A.; Greiner, R.; Manach, C.; Wishart, D. S. BioTransformer: A Comprehensive Computational Tool for Small Molecule Metabolism Prediction and Metabolite Identification. *J. Cheminform.* **2019**, *11* (1), 2. https://doi.org/10.1186/s13321-018-0324-5.

(297) Yao, Q.; Li, Z.; Song, Y.; Wright, S. J.; Guo, X.; Tringe, S. G.; Tfaily, M. M.; Paša-Tolić, L.; Hazen, T. C.; Turner, B. L.; Mayes, M. A.; Pan, C. Community Proteogenomics Reveals the Systemic Impact of Phosphorus Availability on Microbial Functions in Tropical Soil. *Nat. Ecol. Evol.* **2018**, *2* (3), 499–509. https://doi.org/10.1038/s41559-017-0463-5.

(298) Staley, C.; Ferrieri, A. P.; Tfaily, M. M.; Cui, Y.; Chu, R. K.; Wang, P.; Shaw, J. B.; Ansong, C.

K.; Brewer, H.; Norbeck, A. D.; Markillie, M.; do Amaral, F.; Tuleski, T.; Pellizzaro, T.; Agtuca, B.; Ferrieri, R.; Tringe, S. G.; Paša-Tolić, L.; Stacey, G.; Sadowsky, M. J. Diurnal Cycling of Rhizosphere Bacterial Communities Is Associated with Shifts in Carbon Metabolism. *Microbiome* **2017**, *5* (1), 65. https://doi.org/10.1186/s40168-017-0287-1.

(299) Li, H. Y.; Wang, H.; Wang, H. T.; Xin, P. Y.; Xu, X. H.; Ma, Y.; Liu, W. P.; Teng, C. Y.; Jiang, C. L.; Lou, L. P.; Arnold, W.; Cralle, L.; Zhu, Y. G.; Chu, J. F.; Gilbert, J. A.; Zhang, Z. J. The Chemodiversity of Paddy Soil Dissolved Organic Matter Correlates with Microbial Community at Continental Scales. *Microbiome* **2018**, *6* (1), 1–16. https://doi.org/10.1186/s40168-018-0561-x.

(300) Graham, E. B.; Crump, A. R.; Kennedy, D. W.; Arntzen, E.; Fansler, S.; Purvine, S. O.; Nicora, C. D.; Nelson, W.; Tfaily, M. M.; Stegen, J. C. Multi 'omics Comparison Reveals Metabolome Biochemistry, Not Microbiome Composition or Gene Expression, Corresponds to Elevated Biogeochemical Function in the Hyporheic Zone. *Sci. Total Environ.* **2018**, *642*, 742–753. https://doi.org/10.1016/j.scitotenv.2018.05.256.

(301) Hertkorn, N.; Benner, R.; Frommberger, M.; Schmitt-Kopplin, P.; Witt, M.; Kaiser, K.; Kettrup, A.; Hedges, J. I. Characterization of a Major Refractory Component of Marine Dissolved Organic Matter. *Geochim. Cosmochim. Acta* **2006**, *70* (12), 2990–3010. https://doi.org/10.1016/j.gca.2006.03.021.

(302) Hertkorn, N.; Harir, M.; Koch, B. P.; Michalke, B.; Schmitt-Kopplin, P. High-Field NMR Spectroscopy and FTICR Mass Spectrometry: Powerful Discovery Tools for the Molecular Level Characterization of Marine Dissolved Organic Matter. *Biogeosciences* **2013**, *10* (3), 1583–1624. https://doi.org/10.5194/bg-10-1583-2013.

(303) Abdulla, H. A. N.; Hatcher, P. G. Dynamics of Dissolved Organic Matter: A View from Two Dimensional Correlation Spectroscopy Techniques. *J. Mol. Struct.* **2014**, *1069* (1), 313–317.

https://doi.org/10.1016/j.molstruc.2014.03.038.

(304) Weishaar, J. L.; Aiken, G. R.; Bergamaschi, B. A.; Fram, M. S.; Fujii, R.; Mopper, K. Evaluation of Specific Ultraviolet Absorbance as an Indicator of the Chemical Composition and Reactivity of Dissolved Organic Carbon. *Environ. Sci. Technol.* **2003**, *37* (20), 4702–4708. https://doi.org/10.1021/es030360x.

(305) McKnight, D. M.; Boyer, E. W.; Westerhoff, P. K.; Doran, P. T.; Kulbe, T.; Andersen, D. T. Spectrofluorometric Characterization of Dissolved Organic Matter for Indication of Precursor Organic Material and Aromaticity. *Limnol. Oceanogr.* **2001**, *46* (1), 38–48. https://doi.org/10.4319/lo.2001.46.1.0038.

(306) Malik, A. A.; Roth, V. N.; Hébert, M.; Tremblay, L.; Dittmar, T.; Gleixner, G. Linking Molecular Size, Composition and Carbon Turnover of Extractable Soil Microbial Compounds. *Soil Biol. Biochem.* **2016**, *100*, 66–73. https://doi.org/10.1016/j.soilbio.2016.05.019.

(307) Herzsprung, P.; Osterloh, K.; Von Tümpling, W.; Harir, M.; Hertkorn, N.; Schmitt-Kopplin, P.; Meissner, R.; Bernsdorf, S.; Friese, K. Differences in DOM of Rewetted and Natural Peatlands-Results from High-Field FT-ICR-MS and Bulk Optical Parameters. *Sci. Total Environ.* **2017**, *586*, 770–781. https://doi.org/10.1016/j.scitotenv.2017.02.054.

(308) Coble, P. G. Characterization of Marine and Terrestrial DOM in Seawater Using Excitation-Emission Matrix Spectroscopy. *Mar. Chem.* **1996**, *51* (4), 325–346. https://doi.org/10.1016/0304-4203(95)00062-3.

(309) Aiken, G. Fluorescence and Dissolved Organic Matter. In *Aquatic Organic Matter Fluorescence*; Cambridge University Press, 2014; pp 35–74. https://doi.org/10.1017/cbo9781139045452.005.

(310) Ruhala, S. S.; Zarnetske, J. P. Using In-Situ Optical Sensors to Study Dissolved Organic

Carbon Dynamics of Streams and Watersheds: A Review. *Sci. Total Environ.* **2017**, *575*, 713–723. https://doi.org/10.1016/j.scitotenv.2016.09.113.

(311) Rosario-Ortiz, F. L.; Korak, J. A. Oversimplification of Dissolved Organic Matter Fluorescence Analysis: Potential Pitfalls of Current Methods. *Environ. Sci. Technol.* **2017**, *51* (2), 759–761. https://doi.org/10.1021/acs.est.6b06133.

(312) Wünsch, U. J.; Acar, E.; Koch, B. P.; Murphy, K. R.; Schmitt-Kopplin, P.; Stedmon, C. A. The Molecular Fingerprint of Fluorescent Natural Organic Matter Offers Insight into Biogeochemical Sources and Diagenetic State. *Anal. Chem.* **2018**, *90* (24), 14188–14197. https://doi.org/10.1021/acs.analchem.8b02863.

(313) Matilainen, A.; Gjessing, E. T.; Lahtinen, T.; Hed, L.; Bhatnagar, A.; Sillanpää, M. An Overview of the Methods Used in the Characterisation of Natural Organic Matter (NOM) in Relation to Drinking Water Treatment. *Chemosphere* **2011**, *83* (11), 1431–1442. https://doi.org/10.1016/j.chemosphere.2011.01.018.

(314) Brezonik, P. L.; Bloom, P. R.; Sleighter, R. L.; Cory, R. M.; Khwaja, A. R.; Hatcher, P. G. Chemical Differences of Aquatic Humic Substances Extracted by XAD-8 and DEAE-Cellulose. *J. Environ. Chem. Eng.* **2015**, *3* (4), 2982–2990. https://doi.org/10.1016/j.jece.2015.03.004.

(315) Aron, A. T.; Gentry, E. C.; McPhail, K. L.; Nothias, L. F.; Nothias-Esposito, M.; Bouslimani, A.; Petras, D.; Gauglitz, J. M.; Sikora, N.; Vargas, F.; van der Hooft, J. J. J.; Ernst, M.; Kang, K. Bin; Aceves, C. M.; Caraballo-Rodríguez, A. M.; Koester, I.; Weldon, K. C.; Bertrand, S.; Roullier, C.; Sun, K.; Tehan, R. M.; Boya P, C. A.; Christian, M. H.; Gutiérrez, M.; Ulloa, A. M.; Tejeda Mora, J. A.; Mojica-Flores, R.; Lakey-Beitia, J.; Vásquez-Chaves, V.; Zhang, Y.; Calderón, A. I.; Tayler, N.; Keyzers, R. A.; Tugizimana, F.; Ndlovu, N.; Aksenov, A. A.; Jarmusch, A. K.; Schmid, R.; Truman, A. W.; Bandeira, N.; Wang, M.; Dorrestein, P. C.

Reproducible Molecular Networking of Untargeted Mass Spectrometry Data Using GNPS. *Nat. Protoc.* **2020**, *15* (6), 1954–1991. https://doi.org/10.1038/s41596-020-0317-5.

(316) Leenheer, J. A.; Brown, G. K.; Maccarthy, P.; Cabaniss, S. E. Models of Metal Binding Structures in Fulvic Acid from the Suwannee River, Georgia. *Environ. Sci. Technol.* **1998**, *32* (16), 2410–2416. https://doi.org/10.1021/es9708979.

(317) Aiken, G. R. Isolation and Concentration Techniques for Aquatic Humic Substances. In *Humic substances in soil, sediment and water: geochemistry and isolation*; Aiken, G. R., McKnight, D. M., Wershaw, R. L., Maccarthy, P., Eds.; Wiley-Interscience, New York, 1985.

(318) Reemtsma, T.; These, A.; Linscheid, M.; Leenheer, J.; Spitzy, A. Molecular and Structural Characterization of Dissolved Organic Matter from the Deep Ocean by FTICR-MS, Including Hydrophilic Nitrogenous Organic Molecules. *Environ. Sci. Technol.* **2008**, *42* (5), 1430–1437. https://doi.org/10.1021/es7021413.

(319) Kurek, M. R.; Poulin, B. A.; Mckenna, A. M.; Spencer, R. G. M. Deciphering Dissolved Organic Matter: Ionization, Dopant, and Fragmentation Insights via Fourier Transform-Ion Cyclotron Resonance Mass Spectrometry. *Environ. Sci. Technol.* **2020**, *54* (24), 16249–16259. https://doi.org/10.1021/acs.est.0c05206.

(320) Wagner, S.; Dittmar, T.; Jaffé, R. Molecular Characterization of Dissolved Black Nitrogen via Electrospray Ionization Fourier Transform Ion Cyclotron Resonance Mass Spectrometry. *Org. Geochem.* **2015**, *79*, 21–30. https://doi.org/10.1016/j.orggeochem.2014.12.002.

(321) Zherebker, A.; Kim, S.; Schmitt-Kopplin, P.; Spencer, R. G. M.; Lechtenfeld, O.; Podgorski, D. C.; Hertkorn, N.; Harir, M.; Nurfajin, N.; Koch, B.; Nikolaev, E. N.; Shirshin, E. A.; Berezin, S. A.; Kats, D. S.; Rukhovich, G. D.; Perminova, I. V. Interlaboratory Comparison of Humic Substances Compositional Space as Measured by Fourier Transform Ion Cyclotron Resonance Mass Spectrometry (IUPAC Technical Report). *Pure Appl. Chem.* **2020**, *92* (9),

1447–1467. https://doi.org/10.1515/pac-2019-0809.

(322) Chen, Y.; Leach, F. E.; Kaiser, N. K.; Dang, X.; Ibrahim, Y. M.; Norheim, R. V.; Anderson, G. A.; Smith, R. D.; Marshall, A. G. Improved Ion Optics for Introduction of Ions into a 9.4-T Fourier Transform Ion Cyclotron Resonance Mass Spectrometer. *J. Mass Spectrom.* **2015**, *50* (1), 280–284. https://doi.org/10.1002/jms.3523.

(323) Kaiser, N. K.; Savory, J. J.; Hendrickson, C. L. Controlled Ion Ejection from an External Trap for Extended m/z Range in FT-ICR Mass Spectrometry. *J. Am. Soc. Mass Spectrom.* **2014**, *25* (6), 943–949. https://doi.org/10.1007/s13361-014-0871-6.

(324) Wilcox, B. E.; Hendrickson, C. L.; Marshall, A. G. Improved Ion Extraction from a Linear Octopole Ion Trap: SIMION Analysis and Experimental Demonstration. *J. Am. Soc. Mass Spectrom.* **2002**, *13* (11), 1304–1312. https://doi.org/10.1016/S1044-0305(02)00622-0.

(325) Boldin, I. A.; Nikolaev, E. N. Fourier Transform Ion Cyclotron Resonance Cell with Dynamic Harmonization of the Electric Field in the Whole Volume by Shaping of the Excitation and Detection Electrode Assembly. *Rapid Commun. Mass Spectrom.* **2011**, *25* (1), 122–126. https://doi.org/10.1002/rcm.4838.

(326) Chen, T.; Beu, S. C.; Kaiser, N. K.; Hendrickson, C. L. Note: Optimized Circuit for Excitation and Detection with One Pair of Electrodes for Improved Fourier Transform Ion Cyclotron Resonance Mass Spectrometry. *Rev. Sci. Instrum.* **2014**, *85* (6), 66107. https://doi.org/10.1063/1.4883179.

(327) Kilgour, D. P. A.; Wills, R.; Qi, Y.; O'Connor, P. B. Autophaser: An Algorithm for Automated Generation of Absorption Mode Spectra for FT-ICR MS. *Anal. Chem.* **2013**, *85* (8), 3903–3911. https://doi.org/10.1021/ac303289c.

(328) Beu, S. C.; Blakney, G. T.; Quinn, J. P.; Hendrickson, C. L.; Marshall, A. G. Broadband Phase Correction of FT-ICR Mass Spectra via Simultaneous Excitation and Detection. *Anal. Chem.*

2004, *76* (19), 5756–5761. https://doi.org/10.1021/ac049733i.

(329) Wong, R. L.; Amster, I. J. Sub Part-Per-Million Mass Accuracy by Using Stepwise-External Calibration in Fourier Transform Ion Cyclotron Resonance Mass Spectrometry. *J. Am. Soc. Mass Spectrom.* **2006**, *17* (12), 1681–1691. https://doi.org/10.1016/j.jasms.2006.07.019.

(330) Bowman, A. P.; Blakney, G. T.; Hendrickson, C. L.; Ellis, S. R.; Heeren, R. M. A.; Smith, D. F. Ultra-High Mass Resolving Power, Mass Accuracy, and Dynamic Range MALDI Mass Spectrometry Imaging by 21-T FT-ICR MS. *Anal. Chem.* **2020**, *92* (4), 3133–3142. https://doi.org/10.1021/acs.analchem.9b04768.

(331) Marshall, A. G.; Guan, S.; Eyler, J. R. The U.S.A. National High-Magnetic-Field Fourier Transform Ion Cyclotron Resonance Mass Spectrometry Facility. *Rapid Commun. Mass Spectrom.* **1996**, *10* (14), 1814–1818. https://doi.org/10.1002/(SICI)1097-0231(199611)10:14<1814::AID-RCM694>3.0.CO;2-I.

(332) Ledford, E. B.; Rempel, D. L.; Gross, M. L. Space Charge Effects in Fourier Transform Mass Spectrometry. II. Mass Calibration. *Anal. Chem.* **1984**, *56* (14), 2744–2748. https://doi.org/10.1021/ac00278a027.

(333) Xiang, X.; Grosshans, P. B.; Marshall, A. G. Image Charge-Induced Ion Cyclotron Orbital Frequency Shift for Orthorhombic and Cylindrical FT-ICR Ion Traps. *Int. J. Mass Spectrom. Ion Process.* **1993**, *125* (1), 33–43. https://doi.org/10.1016/0168-1176(93)80014-6.

(334) Wong, R. L.; Amster, I. J. Experimental Evidence for Space-Charge Effects between Ions of the Same Mass-to-Charge in Fourier-Transform Ion Cyclotron Resonance Mass Spectrometry. *Int. J. Mass Spectrom.* **2007**, *265* (2–3), 99–105. https://doi.org/10.1016/j.ijms.2007.01.014.

(335) Shaw, J. B.; Lin, T. Y.; Leach, F. E.; Tolmachev, A. V.; Tolić, N.; Robinson, E. W.; Koppenaal, D. W.; Paša-Tolić, L. 21 Tesla Fourier Transform Ion Cyclotron Resonance Mass

Spectrometer Greatly Expands Mass Spectrometry Toolbox. *J. Am. Soc. Mass Spectrom.* **2016**, *27* (12), 1929–1936. https://doi.org/10.1007/s13361-016-1507-9.

(336) IUPAC. *Compendium of Chemical Terminology (the "Gold Book")*, 2nd ed.; McNaught, A. D., Wilkinson, A., Eds.; Blackwell Scientific Publications: Oxford, 1997. https://doi.org/10.1351/goldbook.

(337) Minor, E. C.; Steinbring, C. J.; Longnecker, K.; Kujawinski, E. B. Characterization of Dissolved Organic Matter in Lake Superior and Its Watershed Using Ultrahigh Resolution Mass Spectrometry. *Org. Geochem.* **2012**, *43*, 1–11. https://doi.org/10.1016/j.orggeochem.2011.11.007.

(338) Hughey, C. A.; Hendrickson, C. L.; Rodgers, R. P.; Marshall, A. G.; Qian, K. Kendrick Mass Defect Spectrum: A Compact Visual Analysis for Ultrahigh-Resolution Broadband Mass Spectra. *Anal. Chem.* **2001**, *73* (19), 4676–4681. https://doi.org/10.1021/ac010560w.

(339) Leefmann, T.; Frickenhaus, S.; Koch, B. P. UltraMassExplorer: A Browser-Based Application for the Evaluation of High-Resolution Mass Spectrometric Data. *Rapid Commun. Mass Spectrom.* **2019**, *33* (2), 193–202. https://doi.org/10.1002/rcm.8315.

(340) Corilo, Y. E.; Kew, W. R.; McCue, L. A. EMSL-Computing/CoreMS: CoreMS 1.0.0. **2021**. https://doi.org/10.5281/ZENODO.4641553.

(341) Stranz, D. Composer64 v1. 5.0. *Sierra Anal. Inc* **2015**.

(342) Fouquet, T.; Sato, H. Extension of the Kendrick Mass Defect Analysis of Homopolymers to Low Resolution and High Mass Range Mass Spectra Using Fractional Base Units. *Anal. Chem.* **2017**, *89* (5), 2682–2686. https://doi.org/10.1021/acs.analchem.6b05136.

(343) Hendrickson, C. L.; Quinn, J. P.; Kaiser, N. K.; Smith, D. F.; Blakney, G. T.; Chen, T.; Marshall, A. G.; Weisbrod, C. R.; Beu, S. C. 21 Tesla Fourier Transform Ion Cyclotron Resonance Mass Spectrometer: A National Resource for Ultrahigh Resolution Mass Analysis.

J. Am. Soc. Mass Spectrom. **2015**, *26* (9), 1626–1632. https://doi.org/10.1007/s13361-015-1182-2.

(344) Page, J. S.; Bogdanov, B.; Vilkov, A. N.; Prior, D. C.; Buschbach, M. A.; Tang, K.; Smith, R. D. Automatic Gain Control in Mass Spectrometry Using a Jet Disrupter Electrode in an Electrodynamic Ion Funnel. *J. Am. Soc. Mass Spectrom.* **2005**, *16* (2), 244–253. https://doi.org/10.1016/j.jasms.2004.11.003.

(345) Williams, D. K.; Muddiman, D. C. Parts-per-Billion Mass Measurement Accuracy Achieved through the Combination of Multiple Linear Regression and Automatic Gain Control in a Fourier Transform Ion Cyclotron Resonance Mass Spectrometer. *Anal. Chem.* **2007**, *79* (13), 5058–5063. https://doi.org/10.1021/ac0704210.

(346) Emmett, M. R.; White, F. M.; Hendrickson, C. L.; Shi, D. H.; Marshall, A. G. Application of Micro-Electrospray Liquid Chromatography Techniques to FT-ICR MS to Enable High-Sensitivity Biological Analysis. *J. Am. Soc. Mass Spectrom.* **1998**, *9* (4), 333–340. https://doi.org/10.1016/S1044-0305(97)00287-0.

(347) Vetter, W. F. W. McLafferty, F. Turecek. Interpretation of Mass Spectra. Fourth Edition (1993). University Science Books, Mill Valley, California. *Biol. Mass Spectrom.* **1994**, *23* (6), 379. https://doi.org/10.1002/bms.1200230614.

(348) Xian, F.; Hendrickson, C. L.; Blakney, G. T.; Beu, S. C.; Marshall, A. G. Automated Broadband Phase Correction of Fourier Transform Ion Cyclotron Resonance Mass Spectra. *Anal. Chem.* **2010**, *82* (21), 8807–8812.

(349) Audi, G.; Bersillon, O.; Blachot, J.; Wapstra, A. H. The NUBASE Evaluation of Nuclear and Decay Properties. *Nucl. Phys. A* **2003**, *729* (1), 3–128. https://doi.org/10.1016/j.nuclphysa.2003.11.001.

(350) McLafferty, F. W.; Turecek, F. Interpretation of Mass Spectra; University Science Books: Mill

Valley, CA, 1993; p 371.

(351) NIFC. National Large Incident Year-to-Date Report.

(352) Hoover, K.; Hanson, L. A. Wildfire Statistics. *Congr. Res. Serv.* **2021**, 2.

(353) Nolan, R. H.; Boer, M. M.; Collins, L.; Resco de Dios, V.; Clarke, H.; Jenkins, M.; Kenny, B.; Bradstock, R. A. Causes and Consequences of Eastern Australia's 2019–20 Season of Mega-Fires. *Glob. Chang. Biol.* **2020**, *26* (3), 1039–1041. https://doi.org/https://doi.org/10.1111/gcb.14987.

(354) Walker, X. J.; Baltzer, J. L.; Cumming, S. G.; Day, N. J.; Ebert, C.; Goetz, S.; Johnstone, J. F.; Potter, S.; Rogers, B. M.; Schuur, E. A. G.; Turetsky, M. R.; Mack, M. C. Increasing Wildfires Threaten Historic Carbon Sink of Boreal Forest Soils. *Nature* **2019**, *572* (7770), 520–523. https://doi.org/10.1038/s41586-019-1474-y.

(355) Martin, D. A. At the Nexus of Fire, Water and Society. *Philos. Trans. R. Soc. B Biol. Sci.* **2016**, *371* (1696). https://doi.org/10.1098/rstb.2015.0172.

(356) Goss, M.; Swain, D. L.; Abatzoglou, J. T.; Sarhadi, A.; Kolden, C. A.; Williams, A. P.; Diffenbaugh, N. S. Climate Change Is Increasing the Likelihood of Extreme Autumn Wildfire Conditions across California. *Environ. Res. Lett.* **2020**, *15* (9). https://doi.org/10.1088/1748-9326/ab83a7.

(357) Caldwell, P. V.; Miniat, C. F.; Elliott, K. J.; Swank, W. T.; Brantley, S. T.; Laseter, S. H. Declining Water Yield from Forested Mountain Watersheds in Response to Climate Change and Forest Mesophication. *Glob. Chang. Biol.* **2016**, *22* (9), 2997–3012. https://doi.org/10.1111/gcb.13309.

(358) Ball, G.; Regier, P.; González-Pinzón, R.; Reale, J.; Van Horn, D. Wildfires Increasingly Impact Western US Fluvial Networks. *Nat. Commun.* **2021**, *12* (1), 1–8. https://doi.org/10.1038/s41467-021-22747-3.

(359) Hallema, D. W.; Robinne, F. N.; Bladon, K. D. Reframing the Challenge of Global Wildfire Threats to Water Supplies. *Earth's Futur.* **2018**, *6* (6), 772–776. https://doi.org/10.1029/2018EF000867.

(360) Pellegrini, A. F. A.; Ahlström, A.; Hobbie, S. E.; Reich, P. B.; Nieradzik, L. P.; Staver, A. C.; Scharenbroch, B. C.; Jumpponen, A.; Anderegg, W. R. L.; Randerson, J. T.; Jackson, R. B. Fire Frequency Drives Decadal Changes in Soil Carbon and Nitrogen and Ecosystem Productivity. *Nature* **2018**, *553* (7687), 194–198. https://doi.org/10.1038/nature24668.

(361) Caon, L.; Vallejo, V. R.; Coen, R. J.; Geissen, V. Effects of Wildfire on Soil Nutrients in Mediterranean Ecosystems. *Earth-Science Rev.* **2014**, *139*, 47–58. https://doi.org/10.1016/j.earscirev.2014.09.001.

(362) Mataix-Solera, J.; Cerdà, A.; Arcenegui, V.; Jordán, A.; Zavala, L. M. Fire Effects on Soil Aggregation: A Review. *Earth-Science Rev.* **2011**, *109* (1–2), 44–60. https://doi.org/10.1016/j.earscirev.2011.08.002.

(363) De La Rosa, J. M.; González-Pérez, J. A.; González-Vila, F. J.; Knicker, H. Medium Term Effects of Fire Induced Soil Organic Matter Alterations on Andosols under Canarian Pine (Pinus Canariensis). *J. Anal. Appl. Pyrolysis* **2013**, *104*, 269–279. https://doi.org/10.1016/j.jaap.2013.07.006.

(364) Pereira, P.; Úbeda, X.; Martin, D. A. Fire Severity Effects on Ash Chemical Composition and Water-Extractable Elements. *Geoderma* **2012**, *191*, 105–114. https://doi.org/10.1016/J.GEODERMA.2012.02.005.

(365) D'Andrilli, J.; Junker, J. R.; Smith, H. J.; Scholl, E. A.; Foreman, C. M. DOM Composition Alters Ecosystem Function during Microbial Processing of Isolated Sources. *Biogeochemistry* **2019**, *142* (2), 281–298. https://doi.org/10.1007/s10533-018-00534-5.

(366) Hernández, T.; García, C.; Reinhardt, I. Short-Term Effect of Wildfire on the Chemical,

Biochemical and Microbiological Properties of Mediterranean Pine Forest Soils. *Biol. Fertil. Soils* **1997**, *25* (2), 109–116. https://doi.org/10.1007/s003740050289.

(367) LeBauer, D; Treseder, K. Nitrogen Limitation of Net Primary Productivity. *Ecology* **2008**, *89* (2), 371–379. https://doi.org/https://doi.org/10.1890/06-2057.1.

(368) Hunt, A. P.; Parry, J. D.; Hamilton-Taylor, J. Further Evidence of Elemental Composition as an Indicator of the Bioavailability of Humic Substances to Bacteria. *Limnol. Ocean.* **2000**, *45* (1), 237–241. https://doi.org/10.4319/lo.2000.45.1.0237.

(369) Wiegner, T. N.; Seitzinger, S. P. Seasonal Bioavailability of Dissolved Organic Carbon and Nitrogen from Pristine and Polluted Freshwater Wetlands SO - Limnology & Oceanography. 49(5):1703-1712, 2004 Sep. MH - Bacterial-Growth Efficiency MH - Soil Solution MH - Matter MH - Mineralization. *Limnol. Ocean.* **2004**, *49* (5), 1703–1712.

(370) Neary, D. G.; Klopatek, C. C.; DeBano, L. F.; Ffolliott, P. F. Fire Effects on Belowground Sustainability: A Review and Synthesis. *For. Ecol. Manage.* **1999**, *122* (1–2), 51–71. https://doi.org/10.1016/S0378-1127(99)00032-8.

(371) Scott, E. E.; Rothstein, D. E. The Dynamic Exchange of Dissolved Organic Matter Percolating through Six Diverse Soils. *Soil Biol. Biochem.* **2014**, *69*, 83–92. https://doi.org/10.1016/j.soilbio.2013.10.052.

(372) Ding, Y.; Watanabe, A.; Jaffé, R. Dissolved Black Nitrogen (DBN) in Freshwater Environments. *Org. Geochem.* **2014**, *68*, 1–4. https://doi.org/10.1016/j.orggeochem.2013.12.009.

(373) Smith, C. R.; Buzan, E. M.; Lee, J. W. Potential Impact of Biochar Water-Extractable Substances on Environmental Sustainability. *ACS Sustain. Chem. Eng.* **2013**, *1* (1), 118–126. https://doi.org/10.1021/sc300063f.

(374) Boon, J. J.; Pastorova, I.; Botto, R. E.; Arisz, P. W. Structural Studies on Cellulose Pyrolysis

and Cellulose Chars by PYMS, PYGCMS, FTIR, NMR and by Wet Chemical Techniques. *Biomass and Bioenergy* **1994**. https://doi.org/10.1016/0961-9534(94)00044-T.

(375) Bird, M. I.; Wynn, J. G.; Saiz, G.; Wurster, C. M.; McBeath, A. The Pyrogenic Carbon Cycle. *Annu. Rev. Earth Planet. Sci.* **2015**, *43* (1), 273–298. https://doi.org/10.1146/annurev-earth-060614-105038.

(376) Knicker, H. "Black Nitrogen" - an Important Fraction in Determining the Recalcitrance of Charcoal. *Org. Geochem.* **2010**, *41* (9), 947–950. https://doi.org/10.1016/j.orggeochem.2010.04.007.

(377) Knicker, H.; Hilscher, A.; González-vila, F. J.; Almendros, G. A New Conceptual Model for the Structural Properties of Char Produced during Vegetation Fires. *Org. Geochem.* **2008**, *39* (8), 935–939. https://doi.org/10.1016/j.orggeochem.2008.03.021.

(378) De la Rosa, J. M.; Faria, S. R.; Varela, M. E.; Knicker, H.; González-Vila, F. J.; González-Pérez, J. A.; Keizer, J. Characterization of Wildfire Effects on Soil Organic Matter Using Analytical Pyrolysis. *Geoderma* **2012**, *191*, 24–30. https://doi.org/10.1016/j.geoderma.2012.01.032.

(379) Almendros, G.; Tinoco, P.; De la Rosa, J.-M.; Knicker, H.; González-Pérez, J.-A.; González-Vila, F. J. Selective Effects of Forest Fires on the Structural Domains of Soil Humic Acids as Shown by Dipolar Dephasing 13C NMR and Graphical-Statistical Analysis of Pyrolysis Compounds. *J. Soils Sediments* **2016**, *18* (4), 1303–1313. https://doi.org/10.1007/s11368-016-1595-y.

(380) Campo, J.; Nierop, K. G. J.; Cammeraat, E.; Andreu, V.; Rubio, J. L. Application of Pyrolysis-Gas Chromatography/Mass Spectrometry to Study Changes in the Organic Matter of Macro- and Microaggregates of a Mediterranean Soil upon Heating. *J. Chromatogr. A* **2011**, *1218* (30), 4817–4827. https://doi.org/10.1016/j.chroma.2011.03.038.

(381) Chen, H.; Rhoades, C. C.; Chow, A. T. Characteristics of Soil Organic Matter 14 Years after a Wildfire: A Pyrolysis-Gas-Chromatography Mass Spectrometry (Py-GC-MS) Study. *J. Anal. Appl. Pyrolysis* **2020**, *152* (June), 104922. https://doi.org/10.1016/j.jaap.2020.104922.

(382) Knicker, H.; González-Vila, F. J.; Polvillo, O.; González, J. A.; Almendros, G. Fire-Induced Transformation of C- and N- Forms in Different Organic Soil Fractions from a Dystric Cambisol under a Mediterranean Pine Forest (Pinus Pinaster). *Soil Biol. Biochem.* **2005**, *37* (4), 701–718. https://doi.org/10.1016/j.soilbio.2004.09.008.

(383) Otto, A.; Gondokusumo, R.; Simpson, M. J. Characterization and Quantification of Biomarkers from Biomass Burning at a Recent Wildfire Site in Northern Alberta, Canada. *Appl. Geochemistry* **2006**, *21* (1), 166–183. https://doi.org/10.1016/j.apgeochem.2005.09.007.

(384) Sazawa, K.; Yoshida, H.; Okusu, K.; Hata, N.; Kuramitz, H. Effects of Forest Fire on the Properties of Soil and Humic Substances Extracted from Forest Soil in Gunma, Japan. *Environ. Sci. Pollut. Res.* **2018**, *25* (30), 30325–30338. https://doi.org/10.1007/s11356-018-3011-1.

(385) Orasche, J.; Schnelle-Kreis, J.; Abbaszade, G.; Zimmermann, R. Technical Note: In-Situ Derivatization Thermal Desorption GC-TOFMS for Direct Analysis of Particle-Bound Non-Polar and Polar Organic Species. *Atmos. Chem. Phys.* **2011**, *11* (17), 8977–8993. https://doi.org/10.5194/acp-11-8977-2011.

(386) Piot, C.; Jaffrezo, J. L.; Cozic, J.; Pissot, N.; El Haddad, I.; Marchand, N.; Besombes, J. L. Quantification of Levoglucosan and Its Isomers by High Performance Liquid Chromatography-Electrospray Ionization Tandem Mass Spectrometry and Its Applications to Atmospheric and Soil Samples. *Atmos. Meas. Tech.* **2012**, *5* (1), 141–148. https://doi.org/10.5194/amt-5-141-2012.

(387) Hoffmann, D.; Iinuma, Y.; Herrmann, H. Development of a Method for Fast Analysis of

Phenolic Molecular Markers in Biomass Burning Particles Using High Performance Liquid Chromatography/Atmospheric Pressure Chemical Ionisation Mass Spectrometry. *J. Chromatogr. A* **2007**, *1143* (1–2), 168–175. https://doi.org/10.1016/j.chroma.2007.01.035.

(388) Maie, N.; Knicker, H.; Watanabe, A.; Kimura, M. Heterocyclic N in the Highly Humified Humic Acids Extracted from the Subsoil of Paddy Fields and Surface Ando Soils. *Org. Geochem.* **2006**, *37* (1), 12–19. https://doi.org/10.1016/j.orggeochem.2005.08.020.

(389) Maie, N.; Parish, K. J.; Watanabe, A.; Knicker, H.; Benner, R.; Abe, T.; Kaiser, K.; Jaffé, R. Chemical Characteristics of Dissolved Organic Nitrogen in an Oligotrophic Subtropical Coastal Ecosystem. *Geochim. Cosmochim. Acta* **2006**, *70* (17), 4491–4506. https://doi.org/10.1016/j.gca.2006.06.1554.

(390) de Oliveira, F. C.; Coimbra, J. S. dos R.; de Oliveira, E. B.; Zuñiga, A. D. G.; Rojas, E. E. G. Food Protein-Polysaccharide Conjugates Obtained via the Maillard Reaction: A Review. *Crit. Rev. Food Sci. Nutr.* **2016**, *56* (7), 1108–1125. https://doi.org/10.1080/10408398.2012.755669.

(391) Knicker, H. Soil Organic N - An under-Rated Player for C Sequestration in Soils? *Soil Biology and Biochemistry*. June 2011, pp 1118–1129. https://doi.org/10.1016/j.soilbio.2011.02.020.

(392) Knicker, H. Stabilization of N-Compounds in Soil and Organic-Matter-Rich Sediments - What Is the Difference? *Mar. Chem.* **2004**, *92* (1-4 SPEC. ISS.), 167–195. https://doi.org/10.1016/j.marchem.2004.06.025.

(393) Almendros, G.; Knicker, H.; González-Vila, F. J. Rearrangement of Carbon and Nitrogen Forms in Peat after Progressive Thermal Oxidation as Determined by Solid-State 13C- and 15N-NMR Spectroscopy. *Org. Geochem.* **2003**, *34* (11), 1559–1568. https://doi.org/10.1016/S0146-6380(03)00152-9.

(394) Jiménez-Morillo, N. T.; González-Pérez, J. A.; Almendros, G.; De La Rosa, J. M.; Waggoner, D. C.; Jordán, A.; Zavala, L. M.; González-Vila, F. J.; Hatcher, P. G. Ultra-High Resolution

Mass Spectrometry of Physical Speciation Patterns of Organic Matter in Fire-Affected Soils. *J. Environ. Manage.* **2018**, *225*, 139–147. https://doi.org/10.1016/j.jenvman.2018.07.069.

(395) De la Rosa, J. M.; Knicker, H. Bioavailability of N Released from N-Rich Pyrogenic Organic Matter: An Incubation Study. *Soil Biol. Biochem.* **2011**, *43* (12), 2368–2373. https://doi.org/10.1016/j.soilbio.2011.08.008.

(396) Hilscher, A.; Knicker, H. Carbon and Nitrogen Degradation on Molecular Scale of Grass-Derived Pyrogenic Organic Material during 28 Months of Incubation in Soil. *Soil Biol. Biochem.* **2011**, *43* (2), 261–270. https://doi.org/10.1016/J.SOILBIO.2010.10.007.

(397) Roth, V. N.; Lange, M.; Simon, C.; Hertkorn, N.; Bucher, S.; Goodall, T.; Griffiths, R. I.; Mellado-Vázquez, P. G.; Mommer, L.; Oram, N. J.; Weigelt, A.; Dittmar, T.; Gleixner, G. Persistence of Dissolved Organic Matter Explained by Molecular Changes during Its Passage through Soil. *Nat. Geosci.* **2019**, *12* (9), 755–761. https://doi.org/10.1038/s41561-019-0417-4.

(398) Li, Y.; Harir, M.; Lucio, M.; Kanawati, B.; Smirnov, K.; Flerus, R.; Koch, B. P.; Schmitt-Kopplin, P.; Hertkorn, N. Proposed Guidelines for Solid Phase Extraction of Suwannee River Dissolved Organic Matter. *Anal. Chem.* **2016**, *88* (13), 6680–6688. https://doi.org/10.1021/acs.analchem.5b04501.

(399) Hertkorn, N.; Harir, M.; Cawley, K. M.; Schmitt-Kopplin, P.; Jaffé, R. Molecular Characterization of Dissolved Organic Matter from Subtropical Wetlands: A Comparative Study through the Analysis of Optical Properties, NMR and FTICR/MS. *Biogeosciences* **2016**, *13* (8), 2257–2277. https://doi.org/10.5194/bg-13-2257-2016.

(400) Koch, B. P.; Ludwichowski, K. U.; Kattner, G.; Dittmar, T.; Witt, M. Advanced Characterization of Marine Dissolved Organic Matter by Combining Reversed-Phase Liquid Chromatography and FT-ICR-MS. *Mar. Chem.* **2008**, *111* (3–4), 233–241. https://doi.org/10.1016/j.marchem.2008.05.008.

(401) Romero, C. M.; Engel, R. E.; D'Andrilli, J.; Chen, C.; Zabinski, C.; Miller, P. R.; Wallander, R. Patterns of Change in Permanganate Oxidizable Soil Organic Matter from Semiarid Drylands Reflected by Absorbance Spectroscopy and Fourier Transform Ion Cyclotron Resonance Mass Spectrometry. *Org. Geochem.* **2018**, *120*, 19–30. https://doi.org/10.1016/j.orggeochem.2018.03.005.

(402) O'Donnell, J. A.; Aiken, G. R.; Butler, K. D.; Guillemette, F.; Podgorski, D. C.; Spencer, R. G. M. DOM Composition and Transformation in Boreal Forest Soils: The Effects of Temperature and Organic-Horizon Decomposition State. *J. Geophys. Res. Biogeosciences* **2016**, *121* (10), 2727–2744. https://doi.org/10.1002/2016JG003431.

(403) Patel, K. F.; Tejnecký, V.; Ohno, T.; Bailey, V. L.; Sleighter, R. L.; Hatcher, P. G. Reactive Oxygen Species Alter Chemical Composition and Adsorptive Fractionation of Soil-Derived Organic Matter. *Geoderma* **2021**, *384* (November 2020). https://doi.org/10.1016/j.geoderma.2020.114805.

(404) Gonsior, M.; Zwartjes, M.; Cooper, W. J.; Song, W.; Ishida, K. P.; Tseng, L. Y.; Jeung, M. K.; Rosso, D.; Hertkorn, N.; Schmitt-Kopplin, P. Molecular Characterization of Effluent Organic Matter Identified by Ultrahigh Resolution Mass Spectrometry. *Water Res.* **2011**, *45* (9), 2943–2953. https://doi.org/10.1016/j.watres.2011.03.016.

(405) Smith, C. R.; Sleighter, R. L.; Hatcher, P. G.; Lee, J. W. Molecular Characterization of Inhibiting Biochar Water-Extractable Substances Using Electrospray Ionization Fourier Transform Ion Cyclotron Resonance Mass Spectrometry. *Environ. Sci. Technol.* **2013**, *47* (23), 13294–13302. https://doi.org/10.1021/es4034777.

(406) Song, J.; Li, M.; Fan, X.; Zou, C.; Zhu, M.; Jiang, B.; Yu, Z.; Jia, W.; Liao, Y.; Peng, P. Molecular Characterization of Water- And Methanol-Soluble Organic Compounds Emitted from Residential Coal Combustion Using Ultrahigh-Resolution Electrospray Ionization

Fourier Transform Ion Cyclotron Resonance Mass Spectrometry. *Environ. Sci. Technol.* **2019**, *53* (23), 13607–13617. https://doi.org/10.1021/acs.est.9b04331.

(407) Solihat, N. N.; Yustiawati; Kim, S.; Kim, S. Elucidating Molecular Level Impact of Peat Fire on Soil Organic Matter by Laser Desorption Ionization Fourier Transform Ion Cyclotron Resonance Mass Spectrometry. *Anal. Bioanal. Chem.* **2019**, *411* (27), 7303–7313. https://doi.org/10.1007/s00216-019-02108-2.

(408) Wozniak, A. S.; Goranov, A. I.; Mitra, S.; Bostick, K. W.; Zimmerman, A. R.; Schlesinger, D. R.; Myneni, S.; Hatcher, P. G. Molecular Heterogeneity in Pyrogenic Dissolved Organic Matter from a Thermal Series of Oak and Grass Chars. *Org. Geochem.* **2020**, *148*, 104065. https://doi.org/10.1016/j.orggeochem.2020.104065.

(409) Chen, H.; Tsai, K. P.; Liu, Y.; Tolić, N.; Burton, S. D.; Chu, R.; Karanfil, T.; Chow, A. T. Characterization of Dissolved Organic Matter from Wildfire-Induced Microcystis Aeruginosa Blooms Controlled by Copper Sulfate as Disinfection Byproduct Precursors Using APPI(-) and ESI(-) FT-ICR MS. *Water Res.* **2021**, *189*. https://doi.org/10.1016/j.watres.2020.116640.

(410) Purcell, J. M.; Hendrickson, C. L.; Rodgers, R. P.; Marshall, A. G. Atmospheric Pressure Photoionization Fourier Transform Ion Cyclotron Resonance Mass Spectrometry for Complex Mixture Analysis. *Anal. Chem.* **2006**, *78* (16), 5906–5912. https://doi.org/10.1021/ac060754h.

(411) Jarvis, J. M.; McKenna, A. M.; Hilten, R. N.; Das, K. C.; Rodgers, R. P.; Marshall, A. G. Characterization of Pine Pellet and Peanut Hull Pyrolysis Bio-Oils by Negative-Ion Electrospray Ionization Fourier Transform Ion Cyclotron Resonance Mass Spectrometry. *Energy and Fuels* **2012**, *26* (6), 3810–3815. https://doi.org/10.1021/ef300385f.

(412) Hohner, A. K.; Cawley, K.; Oropeza, J.; Summers, R. S.; Rosario-Ortiz, F. L. Drinking Water Treatment Response Following a Colorado Wildfire. *Water Res.* **2016**, *105*, 187–198.

https://doi.org/10.1016/j.watres.2016.08.034.

(413) Zark, M.; Dittmar, T. Universal Molecular Structures in Natural Dissolved Organic Matter. *Nat. Commun.* **2018**, *9* (1), 1–8. https://doi.org/10.1038/s41467-018-05665-9.

(414) Wagner, S.; Ding, Y.; Jaffé, R. A New Perspective on the Apparent Solubility of Dissolved Black Carbon. *Front. Earth Sci.* **2017**, *5*, 75. https://doi.org/10.3389/feart.2017.00075.

(415) Hohner, A. K.; Rhoades, C. C.; Wilkerson, P.; Rosario-Ortiz, F. L. Wildfires Alter Forest Watersheds and Threaten Drinking Water Quality. *Acc. Chem. Res.* **2019**, *52* (5), 1234–1244. https://doi.org/10.1021/acs.accounts.8b00670.

(416) Thurman, E. M.; Yu, Y.; Ferrer, I.; Thorn, K. A.; Rosario-Ortiz, F. L. Molecular Identification of Water-Extractable Organic Carbon from Thermally Heated Soils: C-13 NMR and Accurate Mass Analyses Find Benzene and Pyridine Carboxylic Acids. *Environ. Sci. Technol.* **2020**, *54* (5), 2994–3001. https://doi.org/10.1021/acs.est.9b05230.

(417) Dunn, P. H.; Barro, S. C.; Poth, M. *SOIL MOISTURE AFFECTS SURVIVAL OF MICROORGANISMS IN HEATED CHAPARRAL SOIL*; 1985; Vol. 17.

(418) Aiken, G. R.; McKnight, D. M.; Thorn, K. A.; Thurman, E. M. Isolation of Hydrophilic Organic Acids from Water Using Nonionic Macroporous Resins. *Org. Geochem.* **1992**, *18* (4), 567–573. https://doi.org/10.1016/0146-6380(92)90119-I.

(419) Peuravuori, J.; Lehtonen, T.; Pihlaja, K. Sorption of Aquatic Humic Matter by DAX-8 and XAD-8 Resins: Comparative Study Using Pyrolysis Gas Chromatography. *Anal. Chim. Acta* **2002**, *471* (2), 219–226. https://doi.org/10.1016/S0003-2670(02)00931-5.

(420) Chow, A. T. Comparison of DAX-8 and XAD-8 Resins for Isolating Disinfection Byproduct Precursors. *J. Water Supply Res. Technol. - AQUA* **2006**, *55* (1), 45–55. https://doi.org/10.2166/aqua.2005.063.

(421) Kaiser, N. K.; Quinn, J. P.; Blakney, G. T.; Hendrickson, C. L.; Marshall, A. G. A Novel 9.4

Tesla FTICR Mass Spectrometer with Improved Sensitivity, Mass Resolution, and Mass Range. *J. Am. Soc. Mass Spectrom.* **2011**, *22* (8), 1343–1351. https://doi.org/10.1007/s13361-011-0141-9.

(422) Melendez-Perez, J. J.; Martínez-Mejia, M. J.; Eberlin, M. N. A Reformulated Aromaticity Index Equation under Consideration for Non-Aromatic and Non-Condensed Aromatic Cyclic Carbonyl Compounds. *Org. Geochem.* **2016**, *95* (February), 29–33. https://doi.org/10.1016/j.orggeochem.2016.02.002.

(423) Ferrer, I.; Thurman, E. M.; Zweigenbaum, J. A.; Murphy, S. F.; Webster, J. P.; Rosario-Ortiz, F. L. Wildfires: Identification of a New Suite of Aromatic Polycarboxylic Acids in Ash and Surface Water. *Sci. Total Environ.* **2021**, *770*. https://doi.org/10.1016/j.scitotenv.2020.144661.

(424) Chen, M.; Kim, S.; Park, J. E.; Kim, H. S.; Hur, J. Effects of Dissolved Organic Matter (DOM) Sources and Nature of Solid Extraction Sorbent on Recoverable DOM Composition: Implication into Potential Lability of Different Compound Groups. *Anal. Bioanal. Chem.* **2016**, *408* (17), 4809–4819. https://doi.org/10.1007/s00216-016-9569-x.

(425) M. Tfaily, M.; Hodgkins, S.; Podgorski, D. C.; Chanton, J. P.; Cooper, W. T. Comparison of Dialysis and Solid-Phase Extraction for Isolation and Concentration of Dissolved Organic Matter Prior to Fourier Transform Ion Cyclotron Resonance Mass Spectrometry. *Anal. Bioanal. Chem.* **2012**, *404* (2), 447–457. https://doi.org/10.1007/s00216-012-6120-6.

(426) Sharma, R. K.; Wooten, J. B.; Baliga, V. L.; Hajaligol, M. R. Characterization of Chars from Biomass-Derived Materials: Pectin Chars. *Fuel* **2001**, *80* (12), 1825–1836. https://doi.org/10.1016/S0016-2361(01)00066-7.

(427) Smuda, M.; Glomb, M. A. Fragmentation Pathways during Maillard-Induced Carbohydrate Degradation. *J. Agric. Food Chem.* **2013**, *61* (43), 10198–10208. https://doi.org/10.1021/jf305117s.

(428) Weenen, H. Reactive Intermediates and Carbohydrate Fragmentation in Maillard Chemistry. *Food Chem.* **1998**, *62* (4), 393–401. https://doi.org/10.1016/S0308-8146(98)00074-0.

(429) Elmore, J. S.; Mottram, D. S. Investigation of the Reaction between Ammonium Sulfide, Aldehydes, and α-Hydroxyketones or α-Dicarbonyls to Form Some Lipid-Maillard Interaction Products Found in Cooked Beef. *J. Agric. Food Chem.* **1997**, *45* (9), 3595–3602. https://doi.org/10.1021/jf970065u.

(430) Henning, C.; Glomb, M. A. Pathways of the Maillard Reaction under Physiological Conditions. *Glycoconj. J.* **2016**, *33* (4), 499–512. https://doi.org/10.1007/s10719-016-9694-y.

(431) Vranova, V.; Zahradnickova, H.; Janous, D.; Skene, K. R.; Matharu, A. S.; Rejsek, K.; Formanek, P. The Significance of D-Amino Acids in Soil, Fate and Utilization by Microbes and Plants: Review and Identification of Knowledge Gaps. *Plant Soil* **2012**, *354* (1–2), 21–39. https://doi.org/10.1007/s11104-011-1059-5.

(432) Moe, L. A. Amino Acids in the Rhizosphere: From Plants to Microbes. *Am. J. Bot.* **2013**, *100* (9), 1692–1705. https://doi.org/10.3732/ajb.1300033.

(433) Miltner, A.; Bombach, P.; Schmidt-Brücken, B.; Kästner, M. SOM Genesis: Microbial Biomass as a Significant Source. *Biogeochemistry* **2012**, *111* (1–3), 41–55. https://doi.org/10.1007/s10533-011-9658-z.

(434) Lund, M. N.; Ray, C. A. Control of Maillard Reactions in Foods: Strategies and Chemical Mechanisms. *J. Agric. Food Chem.* **2017**, *65* (23), 4537–4552. https://doi.org/10.1021/acs.jafc.7b00882.

(435) Hestrin, R.; Torres-Rojas, D.; Dynes, J. J.; Hook, J. M.; Regier, T. Z.; Gillespie, A. W.; Smernik, R. J.; Lehmann, J. Fire-Derived Organic Matter Retains Ammonia through Covalent Bond Formation. *Nat. Commun.* **2019**, *10* (1), 1–8. https://doi.org/10.1038/s41467-019-08401-z.

(436) Prieto-Fernández, Á.; Carballas, M.; Carballas, T. Inorganic and Organic N Pools in Soils Burned or Heated: Immediate Alterations and Evolution after Forest Wildfires. *Geoderma* **2004**, *121* (3–4), 291–306. https://doi.org/10.1016/j.geoderma.2003.11.016.

(437) Yaylayan, V. Classification of the Maillard Reaction: A Conceptual Approach. **1997**, *81* (January), 13–18.

(438) Spencer, C. N.; Gabel, K. O.; Hauer, F. R. Wildfire Effects on Stream Food Webs and Nutrient Dynamics in Glacier National Park, USA. *For. Ecol. Manage.* **2003**, *178* (1–2), 141–153. https://doi.org/10.1016/S0378-1127(03)00058-6.

(439) Roth, V. N.; Dittmar, T.; Gaupp, R.; Gleixner, G. The Molecular Composition of Dissolved Organic Matter in Forest Soils as a Function of PH and Temperature. *PLoS One* **2015**, *10* (3). https://doi.org/10.1371/journal.pone.0119188.

(440) Bostick, K. W.; Zimmerman, A. R.; Goranov, A. I.; Mitra, S.; Hatcher, P. G.; Wozniak, A. S. Biolability of Fresh and Photodegraded Pyrogenic Dissolved Organic Matter From Laboratory-Prepared Chars. *J. Geophys. Res. Biogeosciences* **2021**, *126* (5), 1–17. https://doi.org/10.1029/2020JG005981.

(441) Nelson, A. R.; Narrowe, A. B.; Rhoades, C. C.; Fegel, T. S.; Daly, R. A.; Roth, H. K.; Chu, R. K.; Amundson, K. K.; Geonczy, S. E.; Emerson, J. B.; Young, R. B.; Steindorff, A. S.; Mondo, S. J.; Grigoriev, I. V; Salamov, A.; Borch, T.; Wilkins, M. J. Playing with FiRE: A Genome Resolved View of the Soil Microbiome Responses to High Severity Forest Wildfire. *bioRxiv* **2021**, 2021.08.17.456416. https://doi.org/10.1101/2021.08.17.456416.

(442) Huang, H.; Wu, Q. Y.; Hu, H. Y.; Mitch, W. A. Dichloroacetonitrile and Dichloroacetamide Can Form Independently during Chlorination and Chloramination of Drinking Waters, Model Organic Matters, and Wastewater Effluents. *Environ. Sci. Technol.* **2012**, *46* (19), 10624–10631. https://doi.org/10.1021/es3025808.

(443) Yang, X.; Shen, Q.; Guo, W.; Peng, J.; Liang, Y. Precursors and Nitrogen Origins of Trichloronitromethane and Dichloroacetonitrile during Chlorination/Chloramination. *Chemosphere* **2012**, *88* (1), 25–32. https://doi.org/10.1016/j.chemosphere.2012.02.035.

(444) Chuang, Y. H.; Tung, H. H. Formation of Trichloronitromethane and Dichloroacetonitrile in Natural Waters: Precursor Characterization, Kinetics and Interpretation. *J. Hazard. Mater.* **2015**, *283*, 218–226. https://doi.org/10.1016/j.jhazmat.2014.09.026.

(445) Knicker, H.; Almendros, G.; González-Vila, F. J. J.; Martin, F.; Lüdemann, H.-D. D. 13C-And15N-NMR Spectroscopic Examination of the Transformation of Organic Nitrogen in Plant Biomass during Thermal Treatment. *Soil Biol. Biochem.* **1996**, *28* (8), 1053–1060. https://doi.org/10.1016/0038-0717(96)00078-8.

(446) Smith, C. R.; Hatcher, P. G.; Kumar, S.; Lee, J. W. Investigation into the Sources of Biochar Water-Soluble Organic Compounds and Their Potential Toxicity on Aquatic Microorganisms. *ACS Sustain. Chem. Eng.* **2016**, *4* (5), 2550–2558. https://doi.org/10.1021/acssuschemeng.5b01687.

(447) Apsalyamova, S. O.; Khashir, B. O.; Khuazhev, O. Z.; Tkhagapso, M. B.; Bgane, Y. K. The Economic Value of Forest Ecosystem Services. *J. Environ. Manag. Tour.* **2015**, *6* (2), 291–296. https://doi.org/10.14505/jemt.v6.2(12).01.

(448) Writer, J. H.; Blaine McCleskey, R.; Murphy, S. F. Effects of Wildfire on Source-Water Quality and Aquatic Ecosystems, Colorado Front Range. *IAHS-AISH Publ.* **2012**, *354* (June), 117–122.

(449) Mast, M. A.; Clow, D. W. Effects of 2003 Wildfires on Stream Chemistry in Glacier National Park, Montana. *Hydrol. Process.* **2008**, *22* (26), 5013–5023. https://doi.org/10.1002/hyp.7121.

(450) Revchuk, A. D.; Suffet, I. H. (Mel). Effect of Wildfires on Physicochemical Changes of Watershed Dissolved Organic Matter. *Water Environ. Res.* **2013**, *86* (4), 372–381.

https://doi.org/10.2175/106143013x13736496909671.

(451) Murphy, S. F.; Writer, J. H.; McCleskey, R. B.; Martin, D. A. The Role of Precipitation Type, Intensity, and Spatial Distribution in Source Water Quality after Wildfire. *Environ. Res. Lett.* **2015**, *10* (8). https://doi.org/10.1088/1748-9326/10/8/084007.

(452) Greenbaum, N.; Wittenberg, L.; Malkinson, D.; Inbar, M. Hydrological and Sedimentological Changes Following the 2010-Forest Fire in the Nahal Oren Basin, Mt. Carmel Israel–a Comparison to Pre-Fire Natural Rates. *Catena* **2021**, *196* (August 2020), 104891. https://doi.org/10.1016/j.catena.2020.104891.

(453) Mast, M. A.; Murphy, S. F.; Clow, D. W.; Penn, C. A.; Sexstone, G. A. Water-Quality Response to a High-Elevation Wildfire in the Colorado Front Range. *Hydrol. Process.* **2016**, *30* (12), 1811–1823. https://doi.org/10.1002/hyp.10755.

(454) Uzun, H.; Dahlgren, R. A.; Olivares, C.; Erdem, C. U.; Karanfil, T.; Chow, A. T. Two Years of Post-Wildfire Impacts on Dissolved Organic Matter, Nitrogen, and Precursors of Disinfection by-Products in California Stream Waters. *Water Res.* **2020**, *181*. https://doi.org/10.1016/j.watres.2020.115891.

(455) Moody, J. A.; Martin, D. A. Post-Fire, Rainfall Intensity-Peak Discharge Relations for Three Mountainous Watersheds in the Western USA. *Hydrol. Process.* **2001**, *15* (15), 2981–2993. https://doi.org/10.1002/hyp.386.

(456) U.S. Environmental Protection Agency. National Primary Drinking Water Regulations: Stage 2 Disinfectants and Disinfection Byproducts Rule. *Fed. Regist.* **2006**, *71* (2), 388–493.

(457) Bond, T.; Huang, J.; Templeton, M. R.; Graham, N. Occurrence and Control of Nitrogenous Disinfection By-Products in Drinking Water - A Review. *Water Res.* **2011**, *45* (15), 4341–4354. https://doi.org/10.1016/j.watres.2011.05.034.

(458) Richardson, S. D.; Plewa, M. J.; Wagner, E. D.; Schoeny, R.; DeMarini, D. M. Occurrence,

Genotoxicity, and Carcinogenicity of Regulated and Emerging Disinfection by-Products in Drinking Water: A Review and Roadmap for Research. *Mutat. Res. - Rev. Mutat. Res.* **2007**, *636* (1–3), 178–242. https://doi.org/10.1016/j.mrrev.2007.09.001.

(459) Gonsior, M.; Schmitt-Kopplin, P.; Stavklint, H.; Richardson, S. D.; Hertkorn, N.; Bastviken, D. Changes in Dissolved Organic Matter during the Treatment Processes of a Drinking Water Plant in Sweden and Formation of Previously Unknown Disinfection Byproducts. *Environ. Sci. Technol.* **2014**, *48* (21), 12714–12722. https://doi.org/10.1021/es504349p.

(460) Han, J.; Zhang, X.; Jiang, J.; Li, W. How Much of the Total Organic Halogen and Developmental Toxicity of Chlorinated Drinking Water Might Be Attributed to Aromatic Halogenated DBPs? *Environ. Sci. Technol.* **2021**, *55* (9), 5906–5916. https://doi.org/10.1021/acs.est.0c08565.

(461) Hockaday, W. C.; Grannas, A. M.; Kim, S.; Hatcher, P. G. Direct Molecular Evidence for the Degradation and Mobility of Black Carbon in Soils from Ultrahigh-Resolution Mass Spectral Analysis of Dissolved Organic Matter from a Fire-Impacted Forest Soil. *Org. Geochem.* **2006**, *37* (4), 501–510. https://doi.org/10.1016/j.orggeochem.2005.11.003.

(462) Ide, J.; Ohashi, M.; Köster, K.; Berninger, F.; Miura, I.; Makita, N.; Yamase, K.; Palviainen, M.; Pumpanen, J. Molecular Composition of Soil Dissolved Organic Matter in Recently-Burned and Long-Unburned Boreal Forests. *Int. J. Wildl. Fire* **2020**, *29* (6), 541–547. https://doi.org/10.1071/WF19085.

(463) Milstead, R. P.; Remucal, C. K. Molecular-Level Insights into the Formation of Traditional and Novel Halogenated Disinfection Byproducts. *ACS ES&T Water* **2021**, *1* (8), 1966–1974. https://doi.org/10.1021/acsestwater.1c00161.

(464) U.S. Forest Service. Cameron Peak Fire https://inciweb.nwcg.gov/incident/6964/ (accessed 2022 -08 -28).

(465) Parsons, A.; Robichaud, P. R.; Lewis, S. A.; Napper, C.; Clark, J. T. Field Guide for Mapping Post-Fire Soil Burn Severity. *USDA For. Serv. - Gen. Tech. Rep. RMRS-GTR* **2010**, No. 243, 1–49.

(466) Wilson, C.; Kampf, S. K.; Wagenbrenner, J. W.; MacDonald, L. H. Rainfall Thresholds for Post-Fire Runoff and Sediment Delivery from Plot to Watershed Scales. *For. Ecol. Manage.* **2018**, *430* (November 2017), 346–356. https://doi.org/10.1016/j.foreco.2018.08.025.

(467) APHA. Nephelometric Method—2130b. In *Standard Methods for the Examination of Water and Wastewater*; American Public Health Association: Washington, D.C., 1998; Vol. 20, pp 2.9-2.11. https://doi.org/ISBN 9780875532356.

(468) Cory, R. M.; McKnight, D. M. Fluorescence Spectroscopy Reveals Ubiquitous Presence of Oxidized and Reduced Quinones in Dissolved Organic Matter. *Environ. Sci. Technol.* **2005**, *39* (21), 8142–8149. https://doi.org/10.1021/es0506962.

(469) Johnson, M. S.; Couto, E. G.; Abdo, M.; Lehmann, J. Fluorescence Index as an Indicator of Dissolved Organic Carbon Quality in Hydrologic Flowpaths of Forested Tropical Watersheds. *Biogeochemistry* **2011**, *105* (1), 149–157. https://doi.org/10.1007/s10533-011-9595-x.

(470) Zsolnay, A.; Baigar, E.; Jimenez, M.; Steinweg, B.; Saccomandi, F. Differentiating with Fluorescence Spectroscopy the Sources of Dissolved Organic Matter in Soils Subjected to Drying. *Chemosphere* **1999**, *38* (1), 45–50. https://doi.org/10.1016/S0045-6535(98)00166-0.

(471) Fuentes, M.; González-Gaitano, G.; García-Mina, J. M. The Usefulness of UV-Visible and Fluorescence Spectroscopies to Study the Chemical Nature of Humic Substances from Soils and Composts. *Org. Geochem.* **2006**, *37* (12), 1949–1959. https://doi.org/10.1016/j.orggeochem.2006.07.024.

(472) Koch, B. P.; Dittmar, T. Erratum: From Mass to Structure: An Aromaticity Index for High-

Resolution Mass Data of Natural Organic Matter (Rapid Communications in Mass Spectrometry (2006) 20 (926-932) DOI: 10.1002/Rcm.2386). *Rapid Commun. Mass Spectrom.* **2016**, *30* (1), 250. https://doi.org/10.1002/rcm.7433.

(473) Andrilli, J. D.; Cooper, W. T.; Foreman, C. M.; Marshall, A. G.; D'Andrilli, J.; Cooper, W. T.; Foreman, C. M.; Marshall, A. G.; Andrilli, J. D.; Cooper, W. T.; Foreman, C. M.; Marshall, A. G. An Ultrahigh-Resolution Mass Spectrometry Index to Estimate Natural Organic Matter Lability. *Rapid Commun. Mass Spectrom.* **2015**, *29* (24), 2385–2401. https://doi.org/10.1002/rcm.7400.

(474) Chen, H.; Ersan, M. S.; Tolić, N.; Chu, R. K.; Karanfil, T.; Chow, A. T. Chemical Characterization of Dissolved Organic Matter as Disinfection Byproduct Precursors by UV/Fluorescence and ESI FT-ICR MS after Smoldering Combustion of Leaf Needles and Woody Trunks of Pine (Pinus Jeffreyi). *Water Res.* **2022**, *209* (August 2021). https://doi.org/10.1016/j.watres.2021.117962.

(475) McKenna, A. M.; Chacón-Patiño, M. L.; Chen, H.; Blakney, G. T.; Mentink-Vigier, F.; Young, R. B.; Ippolito, J. A.; Borch, T. Expanding the Analytical Window for Biochar Speciation: Molecular Comparison of Solvent Extraction and Water-Soluble Fractions of Biochar by FT-ICR Mass Spectrometry. *Anal. Chem.* **2021**, *93* (46), 15365–15372. https://doi.org/10.1021/acs.analchem.1c03058.

(476) Summers, R. S.; Hooper, S. M.; Shukairy, H. M.; Solarik, G.; Owen, D. Assessing DBP Yield: Uniform Formation Conditions. *J. AWWA* **1996**, *88* (6), 80–93. https://doi.org/https://doi.org/10.1002/j.1551-8833.1996.tb06573.x.

(477) Hauer, F. R.; Spencer, C. N. Phosphorus and Nitrogen Dynamics in Streams Associated with Wildfire: A Study of Immediate and Longterm Effects. *Int. J. Wildl. Fire* **1998**, *8* (4), 183–198. https://doi.org/10.1071/WF9980183.

(478) Rhoades, C. C.; Entwistle, D.; Butler, D. The Influence of Wildfire Extent and Severity on Streamwater Chemistry, Sediment and Temperature Following the Hayman Fire, Colorado. *Int. J. Wildl. Fire* **2011**, *20* (3), 430–442. https://doi.org/10.1071/WF09086.

(479) Ni, X.; Liao, S.; Wu, F.; Groffman, P. M. Microbial Biomass in Forest Soils under Altered Moisture Conditions: A Review. *Soil Sci. Soc. Am. J.* **2022**, *86* (2), 358–368. https://doi.org/10.1002/saj2.20344.

(480) Andrilli, J. D.; Silverman, V.; Buckley, S.; Rosario-ortiz, F. L. Inferring Ecosystem Function from Dissolved Organic Matter Optical Properties : A Critical Review. **2022**. https://doi.org/10.1021/acs.est.2c04240.

(481) Cawley, K. M.; Hohner, A. K.; Podgorski, D. C.; Cooper, W. T.; Korak, J. A.; Rosario-Ortiz, F. L. Molecular and Spectroscopic Characterization of Water Extractable Organic Matter from Thermally Altered Soils Reveal Insight into Disinfection Byproduct Precursors. *Environ. Sci. Technol.* **2017**, *51* (2), 771–779. https://doi.org/10.1021/acs.est.6b05126.

(482) City of Fort Collins. Water Quality Reports https://www.fcgov.com/utilities/what-we-do/water/water-quality/source-water-monitoring/water-quality-reports.

(483) Ryan, S. E.; Dwire, K. A.; Dixon, M. K. Impacts of Wildfire on Runoff and Sediment Loads at Little Granite Creek, Western Wyoming. *Geomorphology* **2011**, *129* (1–2), 113–130. https://doi.org/10.1016/j.geomorph.2011.01.017.

(484) Osborne, D. M.; Podgorski, D. C.; Bronk, D. A.; Roberts, Q.; Sipler, R. E.; Austin, D.; Bays, J. S.; Cooper, W. T. Molecular-Level Characterization of Reactive and Refractory Dissolved Natural Organic Nitrogen Compounds by Atmospheric Pressure Photoionization Coupled to Fourier Transform Ion Cyclotron Resonance Mass Spectrometry. *Rapid Commun. Mass Spectrom.* **2013**, *27* (8), 851–858. https://doi.org/10.1002/rcm.6521.

(485) Nelson, A. R.; Narrowe, A. B.; Rhoades, C. C.; Fegel, T. S.; Daly, R. A.; Roth, H. K.; Chu, R.

K.; Amundson, K. K.; Young, R. B.; Steindorff, A. S.; Mondo, S. J.; Grigoriev, I. V; Salamov, A.; Borch, T.; Wilkins, M. J. Wildfire-Dependent Changes in Soil Microbiome Diversity and Function. *Nat. Microbiol.* **2022**, *7* (9), 1419–1430. https://doi.org/10.1038/s41564-022-01203-y.

(486) Belnap, J.; Welter, J. R.; Grimm, N. B.; Barger, N.; Ludwig, J. A. Linkages between Microbial and Hydrologic Processes in Arid and Semiarid Watersheds. *Ecology* **2005**, *86* (2), 298–307. https://doi.org/10.1890/03-0567.

(487) Ohno, T.; He, Z.; Sleighter, R. L.; Honeycutt, C. W.; Hatcher, P. G. Ultrahigh Resolution Mass Spectrometry and Indicator Species Analysis to Identify Marker Components of Soil- and Plant Biomass-Derived Organic Matter Fractions. *Environ. Sci. Technol.* **2010**, *44* (22), 8594–8600. https://doi.org/10.1021/es101089t.

(488) Sleighter, R. L.; Hatcher, P. G. Molecular Characterization of Dissolved Organic Matter (DOM) along a River to Ocean Transect of the Lower Chesapeake Bay by Ultrahigh Resolution Electrospray Ionization Fourier Transform Ion Cyclotron Resonance Mass Spectrometry. *Mar. Chem.* **2008**, *110* (3–4), 140–152. https://doi.org/10.1016/j.marchem.2008.04.008.

(489) Liang, C.; Schimel, J. P.; Jastrow, J. D. The Importance of Anabolism in Microbial Control over Soil Carbon Storage. **2017**. https://doi.org/10.1038/nmicrobiol.2017.105.

(490) Schnitzer, M.; Schuppli, P. Method for the Sequential Extraction of Organic Matter from Soils and Soil Fractions. *Soil Sci. Soc. Am. J.* **1989**, *53* (5), 1418–1424. https://doi.org/10.2136/sssaj1989.03615995005300050019x.

(491) Kim, S.; Chen, J.; Cheng, T.; Gindulyte, A.; He, J.; He, S.; Li, Q.; Shoemaker, B. A.; Thiessen, P. A.; Yu, B.; Zaslavsky, L.; Zhang, J.; Bolton, E. E. PubChem 2019 Update: Improved Access to Chemical Data. *Nucleic Acids Res.* **2019**, *47* (D1), D1102–D1109.

https://doi.org/10.1093/nar/gky1033.

(492) MOSES. Altamira LLC, USA and Molecular Networks GmbH, Germany 2020.

(493) Moncelli, M. R.; Becucci, L.; Guidelli, R. The Intrinsic PKa Values for Phosphatidylcholine, Phosphatidylethanolamine, and Phosphatidylserine in Monolayers Deposited on Mercury Electrodes. *Biophys. J.* **1994**, *66* (6), 1969–1980. https://doi.org/10.1016/S0006-3495(94)80990-7.

APPENDICES

Appendix A: Supporting Information for Chapter 2

Table A.1. Common extraction methods used to extract different fractions of soil organic matter with example conditions used in literature.

Extraction	Example extraction	Target SOM fraction	Reference
Water	Ultrapure (18.2 MΩ), 20+ hours extraction time, and 200g/L (soil/solution)[87]	Water soluble SOM, weakly soil particle bound and most bioavailable SOM	[87,94,98]
Alkaline	0.5 M NaOH, 20 h, and 200 g/L (soil/solution)[110]	General SOM and SOM compounds with acidic functional groups	[87,103,104,110]
Mineral dissolution	#1 - 0.1 M dithionite, 16 hours; followed by 0.05 M HCl rinse 1 h; 167 g/L #2 – 0.25 M hydroxylamine hydrochloride, 0.25 M HCl, 50 °C, 1 h, 200 g/L[489]	For extraction #1: short range order Fe(III) oxides and crystalline Fe(III) oxides For extraction #2: short range order Fe(III) oxides	[118,122,123,128]
Organic	1 mL acetonitrile (ACN), 100 mg soil, shaken for 2 hours[133]	Low polarity SOM and SOM with less abundant acidic functional groups	[94,133,135,490]

Table A.2. Log *P* and *pKa* values predicted by PubChem[491] and MOSES[492] (via ChemDraw Professional), respectively, for common biomolecular classes associated with SOM. Structures and features relative to each of the examples is shown in Figure 2.4. *Intrinsic *pKa* was measured for dioleoyl phosphatidylcholine[493]

Name	Class	Log *P*	*pKa1*	*pKa2*	*pKa3*
glucose	Carbohydrate	-2.6	12.294		
N-Acetyl-Muramic Acid	Amino sugar	-2.1	3.408		
N-Acetyl-D-Glucosamine	Amino sugar	-1.7	11.939		
Tryptophan	Amino Acid	-1.1	2.38	9.39	
Tyrosine	Amino Acid	-2.3	2.2	9.11	10.07
Glycine	Amino Acid	-3.2	2.37	9.78	
Dioleoyl phosphatidylcholine	Phospholipid	13.8	4.053*		
Valoneic acid	Tannin derivative	1.5	8.516		
Hexahydroxydiphenic acid	Tannin derivative	0.5	13.939		
Flavogallonic acid	Tannin derivative	1.6	2.593		
Chlorogenic acid	Lignin derivatives	-0.4	8.099		
Sinapic acid	Lignin derivatives	1.5	4.05		
Vanillic acid	Lignin derivatives	1.4	4.0	9.39	
Gentisic acid	Lignin derivatives	1.3	2.766		
Stearic acid	Fatty acid	7.4	4.75		
Palmitic acid	Fatty acid	6.4	4.75		

Appendix B: Supporting Information for Chapter 3

Table B.1. Identified isobaric overlaps below a mass difference of m/z 0.03638 with the count and experimental average overlap and standard deviation at each peak-picking threshold for SRFA.

		3σ		4σ		5σ		6σ	
Isobaric Overlap	Theor. Overlap (mDa)	Count	Avg. Exp. Overlap (mDa)	Count	Avg. Exp. Overlap (mDa)	Count	Avg. Exp. Overlap (mDa)	Count	Avg. Exp. Overlap (mDa)
N_1O_2 $^{13}C_1$ vs $C_2H_3S_1$	0.71	1076	0.72 ± 0.04	882	0.72 ± 0.04	704	0.72 ± 0.03	506	0.72 ± 0.02
H_4S_1 $^{18}O_1$ vs C_1O_1 $^{13}C_2$	0.91	267	0.87 ± 0.02	121	0.87 ± 0.01	113	0.87 ± 0.01	22	0.87 ± 0.01
H_2O_3 $^{13}C_2$ vs C_4N_2	0.96	721	0.96 ± 0.02	681	0.95 ± 0.02	501	0.95 ± 0.02	238	0.95 ± 0.01
C_2N_2 vs H_2O_2 $^{18}O_1$	1.51	833	1.52 ± 0.03	584	1.52 ± 0.02	432	1.52 ± 0.02	206	1.51 ± 0.01
H_3O_3 vs C_2N_1 $^{13}C_1$	1.79	1440	1.79 ± 0.03	1516	1.79 ± 0.03	1330	1.79 ± 0.02	970	1.79 ± 0.02
C_{10} vs $H_6O_4S_1$ $^{18}O_1$	2.16	427	2.2 ± 0.03	121	2.2 ± 0.01	128	2.2 ± 0.01	25	2.2 ± 0.01
C_7 $^{13}C_1$ vs $H_3N_1O_5$	2.23	389	2.17 ± 0.06	355	2.18 ± 0.05	231	2.17 ± 0.05	114	2.17 ± 0.04
O_1 $^{13}C_2$ vs C_2 $^{18}O_1$	2.46	541	2.47 ± 0.02	543	2.47 ± 0.02	619	2.47 ± 0.02	215	2.47 ± 0.01
O_5 vs C_4S_1	2.5	392	2.53 ± 0.08	140	2.57 ± 0.06	106	2.57 ± 0.06	33	2.55 ± 0.04
C_9 vs H_2O_5 $^{13}C_2$	3.07	811	3.08 ± 0.04	905	3.07 ± 0.03	722	3.07 ± 0.02	325	3.07 ± 0.01
N_3 vs $C_1H_1O_1$ $^{13}C_1$	3.13	782	3.18 ± 0.06	377	3.17 ± 0.04	333	3.15 ± 0.04	137	3.14 ± 0.03
$H_1N_1O_1$ vs $^{13}C_1$ $^{18}O_1$	3.3	317	3.3 ± 0.04	185	3.3 ± 0.02	102	3.3 ± 0.02	20	3.3 ± 0.02
H_4S_1 vs C_3	3.37	3402	3.36 ± 0.04	2522	3.36 ± 0.03	2131	3.36 ± 0.03	1404	3.37 ± 0.02
C_4 $^{18}O_1$ vs H_2O_4	3.85	760	3.84 ± 0.04	518	3.84 ± 0.03	464	3.84 ± 0.03	139	3.85 ± 0.01
C_5 vs N_2O_2	4.02	1451	4.01 ± 0.04	980	4.02 ± 0.03	757	4.02 ± 0.02	787	4.02 ± 0.01
$H_1N_1O_2$ $^{13}C_1$ vs C_5	4.08	708	4.08 ± 0.03	1139	4.08 ± 0.03	1072	4.08 ± 0.02	813	4.08 ± 0.02
C_3 $^{13}C_1$ vs $H_3N_1S_1$	4.73	221	4.73 ± 0.02	119	4.74 ± 0.01	51	4.73 ± 0.01	4	4.74 ± 0.01
$H_2N_2O_2$ vs C_3 $^{13}C_2$	4.92	158	4.91 ± 0.03	251	4.91 ± 0.03	156	4.91 ± 0.02	4	4.92 ± 0.02
C_7 vs H_2O_4 $^{18}O_1$	5.53	24	5.57 ± 0.05	4	5.55 ± 0.04	5	5.55 ± 0.03	2	5.53 ± 0
C_2H_1 $^{18}O_1$ vs N_1O_1 $^{13}C_1$	5.64	285	5.64 ± 0.02	348	5.63 ± 0.02	319	5.64 ± 0.02	204	5.64 ± 0.01
H_4O_5 vs C_7	5.87	2014	5.88 ± 0.05	1932	5.89 ± 0.04	1662	5.89 ± 0.04	1489	5.88 ± 0.03
C_2 $^{13}C_2$ vs H_2O_3	6.32	960	6.32 ± 0.05	1456	6.32 ± 0.04	1287	6.32 ± 0.03	480	6.32 ± 0.02
O_1 $^{18}O_1$ vs H_2S_1	6.35	461	6.35 ± 0.04	256	6.35 ± 0.02	268	6.35 ± 0.02	81	6.35 ± 0.01
C_4N_1 vs H_1O_3 $^{13}C_1$	7.15	2083	7.15 ± 0.03	2153	7.15 ± 0.02	1863	7.15 ± 0.02	1612	7.15 ± 0.02

C_2N_2 vs $H_4O_1S_1$	7.86	367	7.87 ± 0.03	265	7.87 ± 0.02	227	7.87 ± 0.02	304	7.87 ± 0.02
C_3O_1 vs $H_2S_1{}^{18}O_1$	8.03	59	8.07 ± 0.03	42	8.07 ± 0.02	31	8.07 ± 0.01	4	8.07 ± 0.01
$H_1{}^{13}C_1$ vs N_1	8.11	3174	8.1 ± 0.03	2865	8.1 ± 0.02	2593	8.1 ± 0.02	2286	8.1 ± 0.01
$O_2{}^{13}C_2$ vs $C_2H_2S_1$	8.82	77	8.83 ± 0.06	169	8.83 ± 0.05	134	8.83 ± 0.03	54	8.83 ± 0.02
C_2H_2 vs $^{13}C_2$	8.94	1228	8.94 ± 0.04	2079	8.93 ± 0.03	1931	8.93 ± 0.03	699	8.94 ± 0.01
N_1O_2 vs $H_1S_1{}^{13}C_1$	9.65	109	9.71 ± 0.06	130	9.7 ± 0.04	122	9.71 ± 0.04	10	9.7 ± 0.03
$H_2O_1{}^{18}O_1$ vs C_3	9.72	360	9.71 ± 0.03	161	9.72 ± 0.02	130	9.71 ± 0.02	29	9.72 ± 0.02
H_4O_3 vs C_2N_2	9.9	187	9.84 ± 0.06	94	9.85 ± 0.04	73	9.85 ± 0.03	39	9.87 ± 0.02
N_2 vs C_1O_1	11.23	289	11.23 ± 0.03	221	11.23 ± 0.02	200	11.23 ± 0.02	371	11.23 ± 0.01
H_2O_1 vs $^{18}O_1$	11.41	43	11.4 ± 0.02	5	11.4 ± 0.01	1	11.42 ± 0	4	11.4 ± 0.01
C_7 vs $H_4O_3S_1$	11.88	217	11.89 ± 0.05	265	11.89 ± 0.03	268	11.89 ± 0.03	273	11.89 ± 0.02
$C_5H_1{}^{13}C_1$ vs N_3O_2	12.13	36	12.11 ± 0.04	26	12.1 ± 0.04	31	12.09 ± 0.04	16	12.1 ± 0.02
$H_2O_2{}^{13}C_2$ vs C_5	12.19	288	12.19 ± 0.05	375	12.2 ± 0.05	371	12.19 ± 0.03	45	12.19 ± 0.02
$H_3N_1O_2$ vs $C_3{}^{13}C_1$	13.02	603	13.03 ± 0.03	535	13.03 ± 0.02	538	13.03 ± 0.02	676	13.03 ± 0.01
C_4 vs O_3	15.26	2676	15.25 ± 0.04	3037	15.25 ± 0.04	3244	15.25 ± 0.03	4188	15.25 ± 0.02
C_2H_3 vs $N_1{}^{13}C_1$	17.05	1	17.07 ± 0	4	16.87 ± 0.17	1	17.05 ± 0	20	17.04 ± 0.01
O_2 vs S_1	17.76	133	17.76 ± 0.04	109	17.76 ± 0.03	102	17.77 ± 0.03	131	17.76 ± 0.01
$H_5O_3{}^{13}C_1$ vs C_2N_3	18	18	17.97 ± 0.08	2	17.93 ± 0.04	9	17.98 ± 0.04	5	17.97 ± 0.03
$C_1H_4S_1$ vs O_3	18.63	5	18.63 ± 0	1	18.63 ± 0	4	18.63 ± 0.01	5	18.63 ± 0
H_4O_2 vs C_3	21.13	1727	21.13 ± 0.04	2069	21.13 ± 0.04	2184	21.13 ± 0.04	2596	21.13 ± 0.03
$H_2{}^{13}C_2$ vs C_1O_1	27.45	4	27.58 ± 0.18	13	27.44 ± 0.02	17	27.45 ± 0.01	2	27.44 ± 0.01
$C_1H_3N_1$ vs $O_1{}^{13}C_1$	28.28	98	28.28 ± 0.05	35	28.28 ± 0.03	32	28.28 ± 0.02	33	28.28 ± 0.01
C_1H_4 vs O_1	36.39	881	36.39 ± 0.06	931	36.38 ± 0.05	954	36.39 ± 0.05	978	36.39 ± 0.04

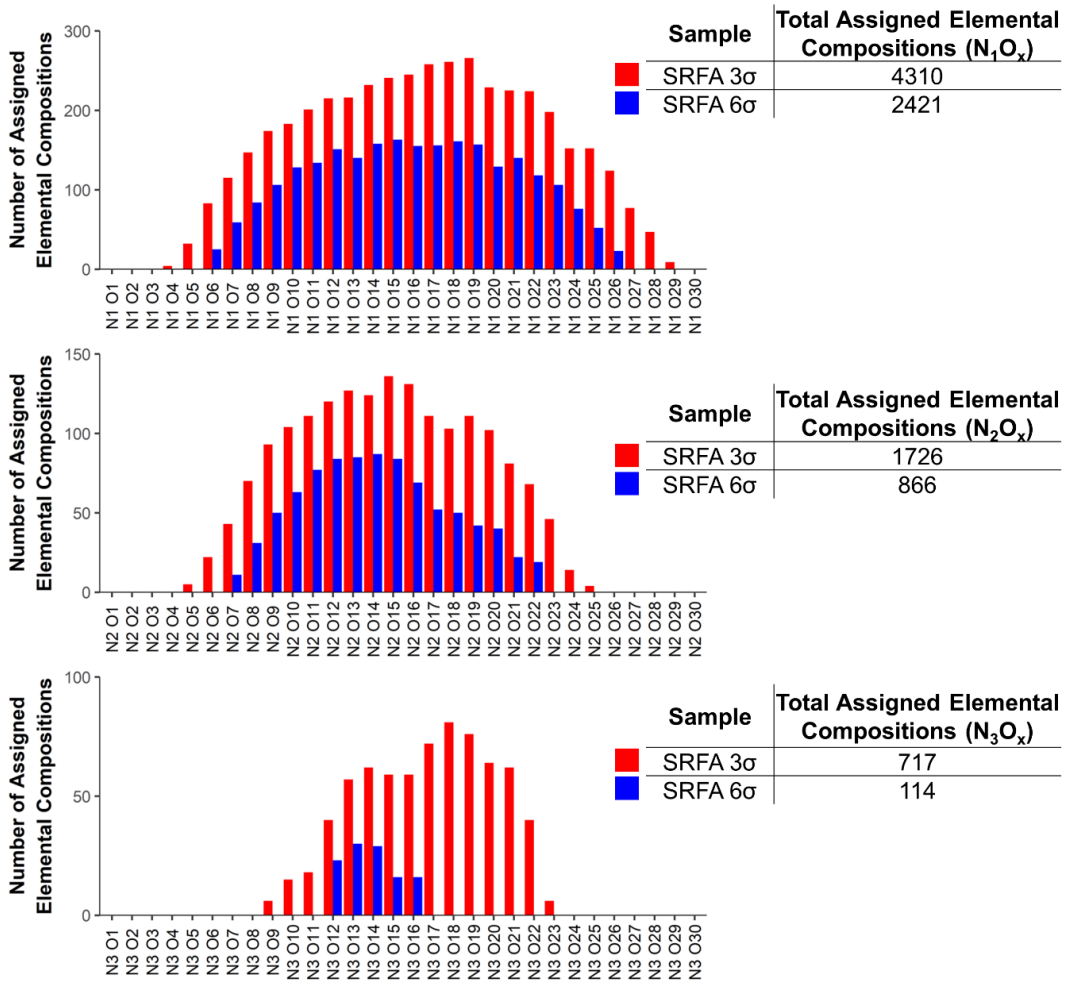

Figure B.1 Number of assigned elemental compositions containing nitrogen atoms separated by nitrogen and oxygen count ($N_{1\text{-}3}O_{1\text{-}30}$) at 3σ and 6σ peak-picking thresholds. The total number of assignments were also separated and tabulated by nitrogen content ($N_{1\text{-}3}$).

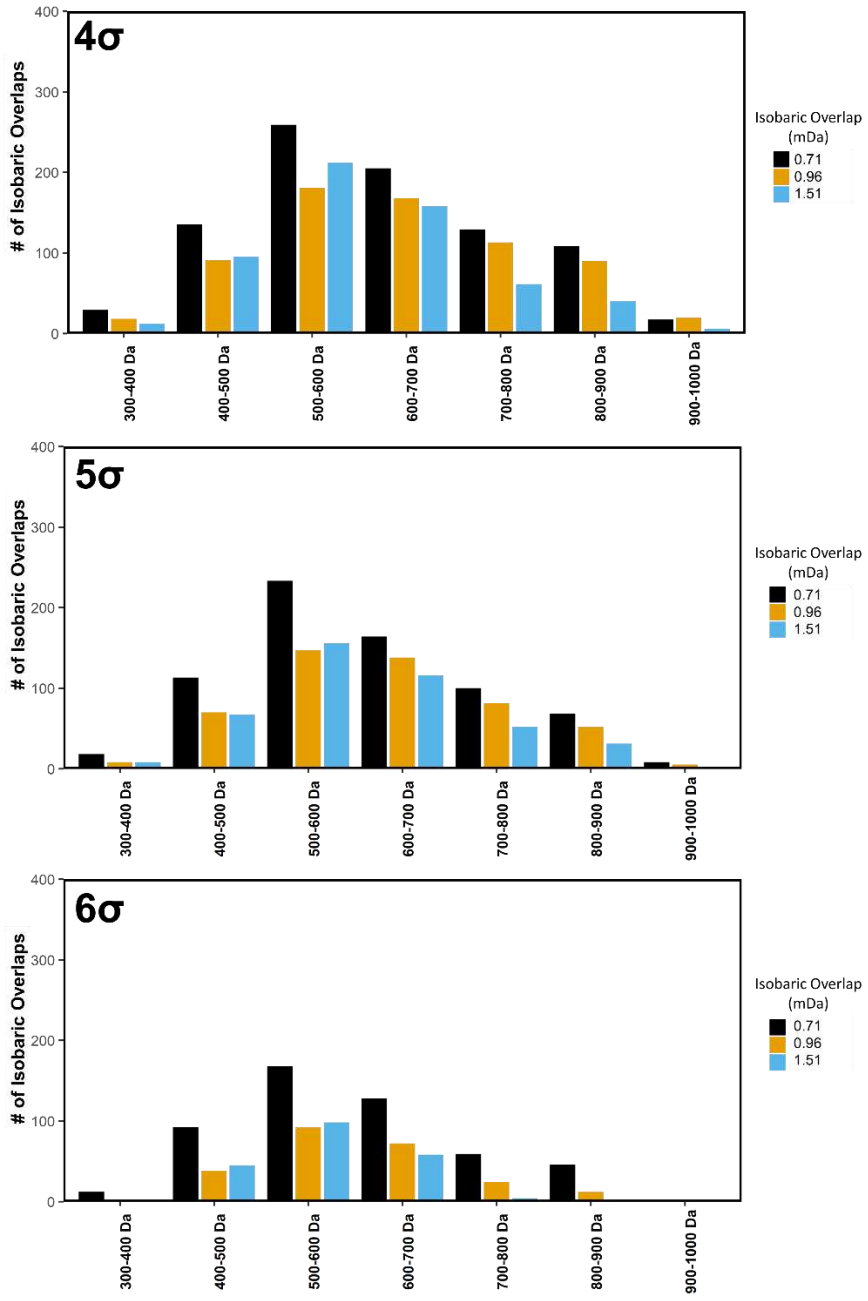

Figure B.2 Number of isobaric overlaps in SRFA peak-picked at 4σ, 5σ, and 6σ identified from Figure 3 and binned by every m/z 100, up to m/z 1000. Bars are colored by theoretical isobaric overlap that each count was associated with.

Appendix C: Supporting Information for Chapter 4

Table C.1. Assignment and peak areas as a percent of total carbon for solid state ^{13}C CP/MAS and DP/MAS spectra of the WEOC isolated in the hydrophobic (XAD-8) fraction. Reproduced from Thurman *et al.*[416]

	230–190 ppm	190–160 ppm	160–110 ppm	110–90 ppm	90–60 ppm	60–0 ppm			
sample	ketone quinone	carboxyl amide quinone	aromatic olefinic	aromatic acetal CHO anomeric	O-alkyl (methoxyl: 58–54 ppm)	C-alkyl (α C to AA's: 40–65 ppm)	sp^2 230–90 ppm	sp^3 90–0 ppm	f_a[a]
					13-CPMAS				
Ctrl	3	18	29	8	13	29	58	42	0.29
150 °C	2	16	27	7	13	35	52	48	0.27
250 °C	1	22	50	6	4	17	79	21	0.50
350 °C		25	64	3	2	6	92	8	0.64
450 °C		29	66	1	13	3	97	3	0.66
					DPMAS				
Ctrl	1	20	28	8	12	30	57	43	0.28
150 °C		15	21	6	4	46	42	58	0.21
250 °C	1	22	40	4	2	30	66	34	0.40
350 °C		26	50	4		18	80	20	0.50
450 °C	1	11	84			4	96	4	0.84

[a] f_a = ^{13}C aromaticity, peak area from 160 to 110 ppm divided by total area.

Table C.2. List of amino acid and fragment molecular weights[a] used when performing mass-difference based analysis including condensation and cleavage[b] reactions common to Maillard reaction pathways.

Reaction	Mass Change	Elemental Change
Dehydration	-18.01057	(-H2O)
Gly Condensation	57.02146	(+C2H3N1O1)
Gly Addition	75.03203	(+C2H5N1O2)
Ala Condensation	71.03711	(+C3H5N1O1)
Gln Condensation	128.05857	(+C5H8N2O2)
Lys Condensation	128.09496	(+C6H12N2O1)
Ammonia Addition	17.02655	(+NH3)
Amidization	-0.98402	(+NH/-O)
F_Formic_acid	-46.00548	(-CH2O2)
F_Formaldehyde	-30.01056	(-CH2O)
F_Acetic_acid_glycoaldehyde	-60.02113	(-C2H4O2)
F_Glyoxal	-58.00548	(-C2H2O2)
F_Glyceraldehyde	-90.03169	(-C3H6O3)
F_Dihydroxyacetone	-90.03169	(-C3H6O3)
F_pyruvaldehyde	-72.02113	(-C3H4O2)
F_Hydroxyacetone	-74.03678	(-C3H6O2)
F_Tetroses	-120.04226	(-C4H8O4)
F_Diacetyl_butanedione	-86.03678	(-C4H6O2)
F_Hydroxybutanal_hydroxybutanone	-88.05243	(-C4H8O2)
F_Furanones	-84.02113	(-C4H4O2)
F_Furan	-68.02621	(-C4H4O)
F_Pentoses_pentuloses_ribulose	-150.05282	(-C5H10O5)
F_Deoxy_deoxyribose	-134.05791	(-C5H10O4)
F_Pyranones	-96.02113	(-C5H4O2)
F_Glucosone	-178.04774	(-C6H10O6)
F_Deoxyglucosone	-162.05282	(-C6H10O5)

[a]Monoisotopic masses were used to calculate mass change

[b]Fragments are denoted with a preceding "F_" and were not differentiated between isomers (i.e. all tetroses were considered the same C4 fragment due to identical fragment formula mass)

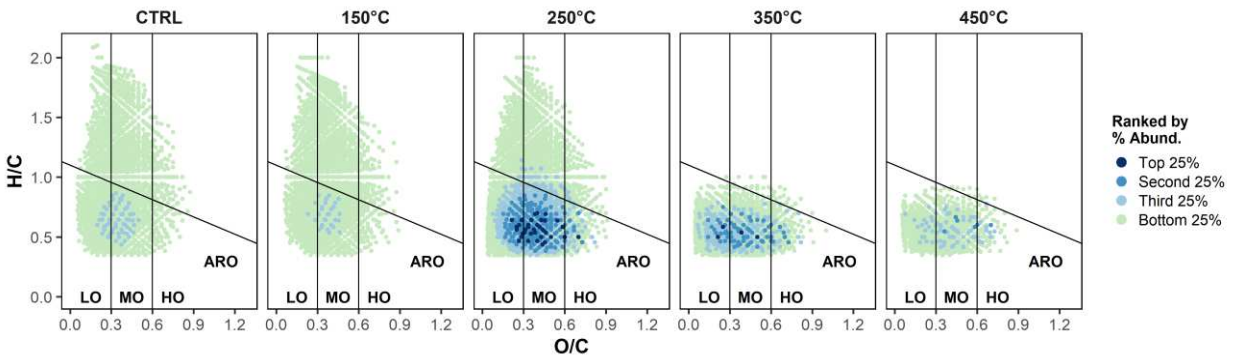

Figure C.1 Abundance-weighted van Krevelen plots of N_xO_x species derived from negative-ion ESI FT-ICR MS spectra for the unburnt control (CTRL) and heated soil leachates isolated on the hydrophobic resin. Lines were added to each plot to indicate regions that contain aromatic features (below AROM line) established using aromaticity indices (AI_{Mod}, outlined by Koch and Dittmar[216] and reformulated by Melendez-Perez et al.[422]), and also oxygen content of the assigned formula: "LO" = low oxygen content, O/C ≤ 0.3; "MO" = mid oxygen content, 0.3 < O/C ≤ 0.6; "HO" = high oxygen content, O/C > 0.6. C: H/C vs. N/C plots of the CHNO assignments along the heating gradient. Plotted formulas were grouped using their abundances, where the "top 25%" (dark blue points) are 25% of the sample's cumulative abundance comprised of the most abundant formulas, the "second 25%" is the next 25% comprised of the next most abundant formulas, and so on.

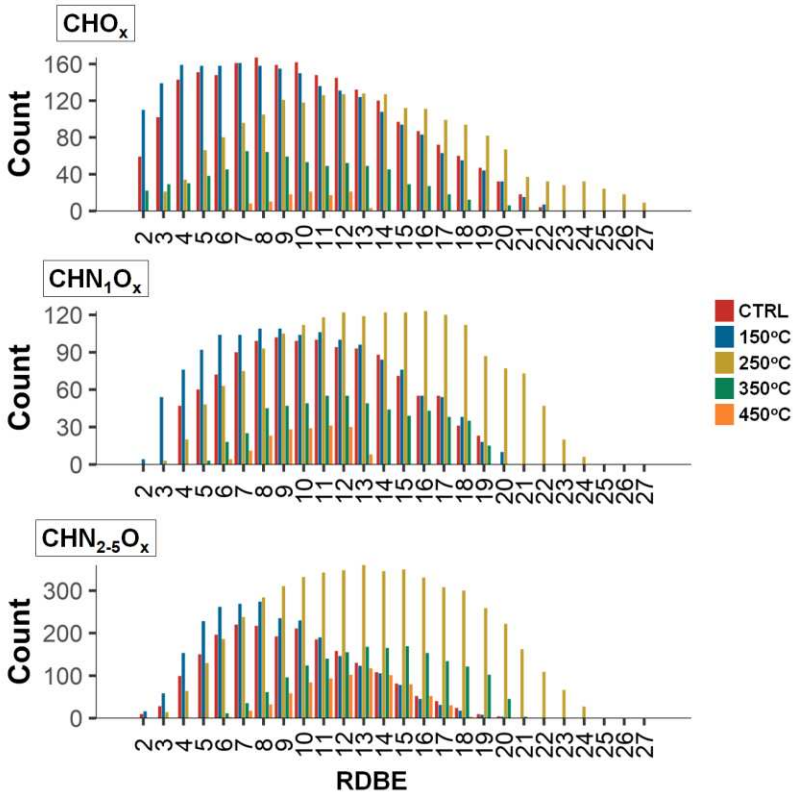

Figure C.2 Abundance-weighted van Krevelen plots of N_xO_x species derived from negative-ion ESI FT-ICR MS spectra for the unburnt control (CTRL) and heated soil leachates isolated on the hydrophobic resin. Lines were added to each plot to indicate regions that contain aromatic features (below AROM line) established using aromaticity indices (AI_{Mod}, outlined by Koch and Dittmar[216] and reformulated by Melendez-Perez et al.[422]), and also oxygen content of the assigned formula: "LO" = low oxygen content, O/C ≤ 0.3; "MO" = mid oxygen content, 0.3 < O/C ≤ 0.6; "HO" = high oxygen content, O/C > 0.6. C: H/C vs. N/C plots of the CHNO assignments along the heating gradient. Plotted formulas were grouped using their abundances, where the "top 25%" (dark blue points) are 25% of the sample's cumulative abundance comprised of the most abundant formulas, the "second 25%" is the next 25% comprised of the next most abundant formulas, and so on.

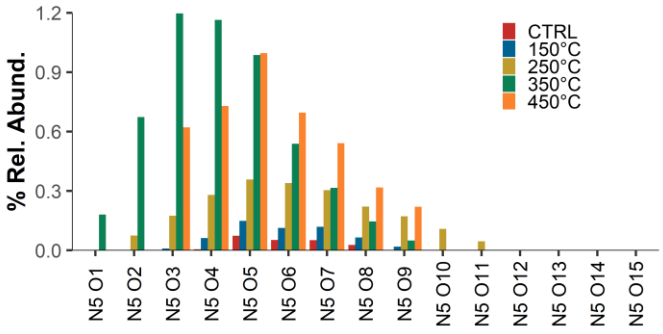

Figure C.3 Relative abundance of CHNO classes in the unburnt (CTRL) and heated (150°C – 450°C) hydrophilic samples separated by nitrogen and oxygen ($N_5O_{2\text{-}15}$) content.

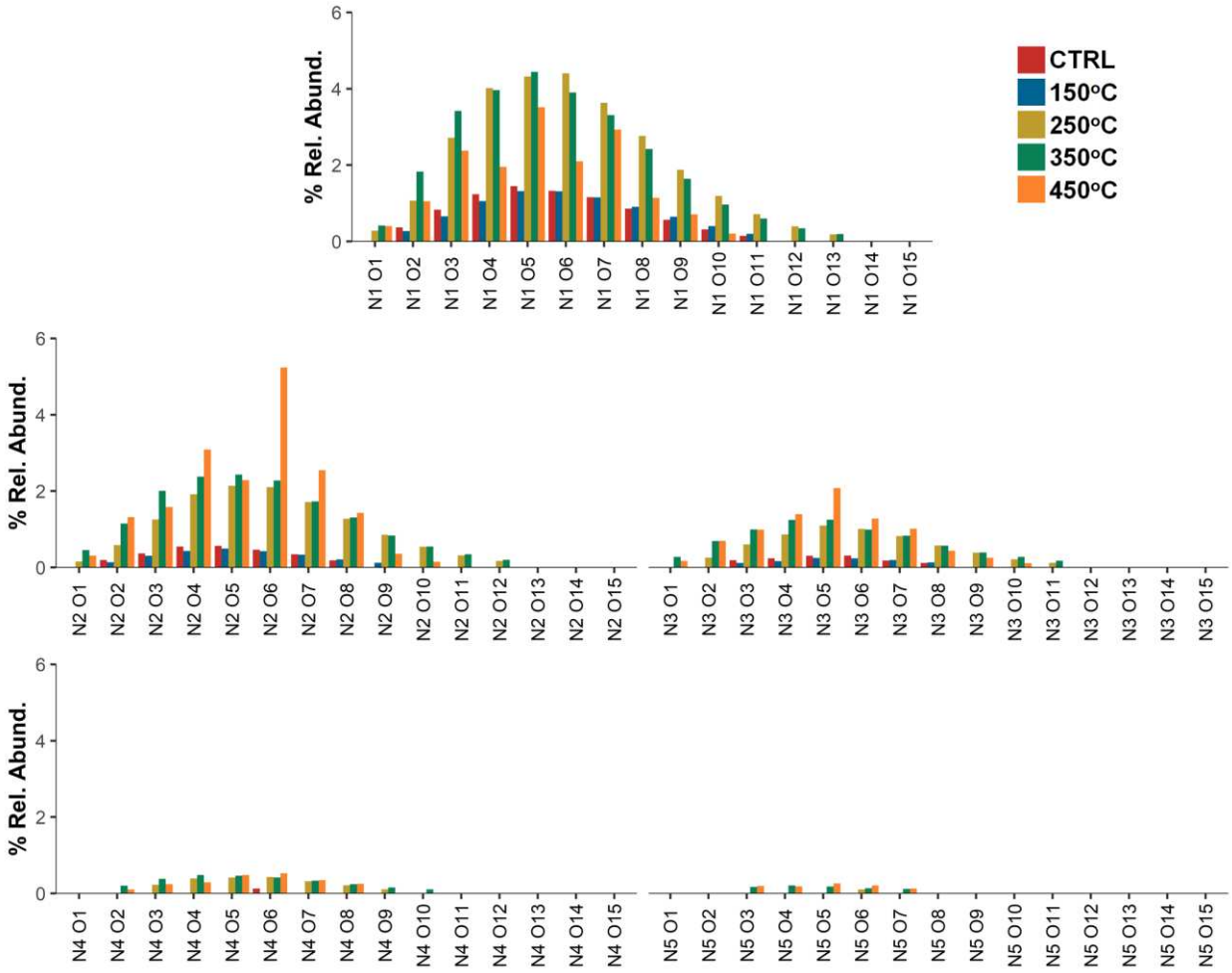

Figure C.4 Relative abundance of CHNO classes in the unburnt (CTRL) and heated (150°C – 450°C) hydrophobic samples separated by nitrogen and oxygen ($N_{1\text{-}5}O_{2\text{-}15}$) content.

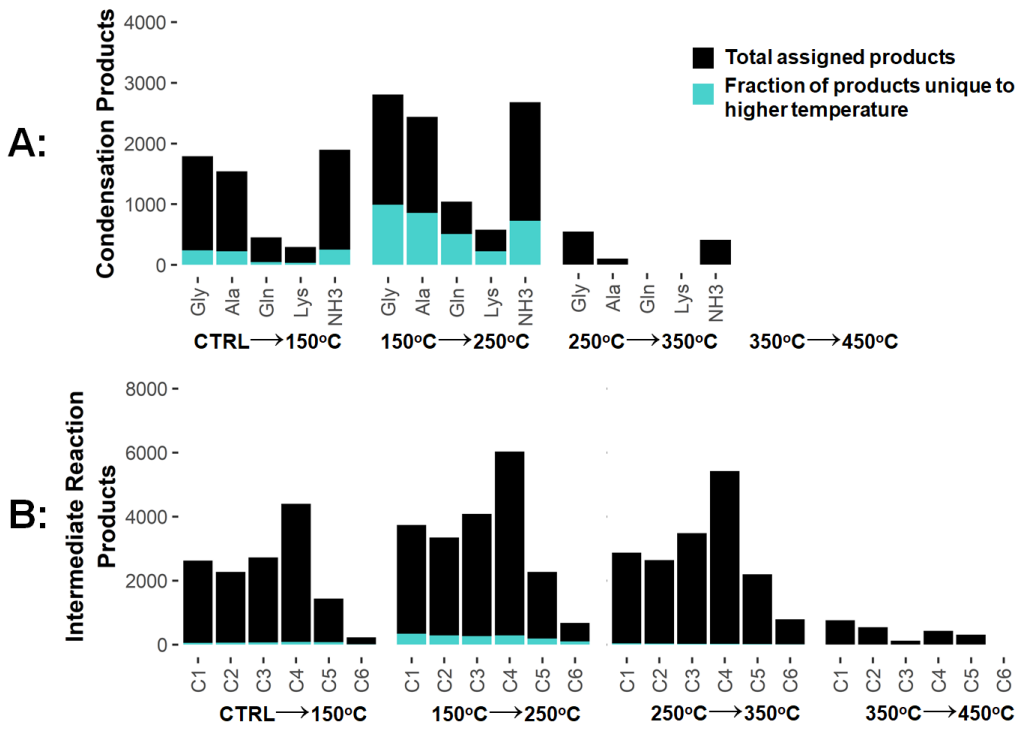

Figure C.5 Number of product assignments matchings reactions with predicted mass differences along the Maillard reaction pathway at each temperature transition from the hydrophobic sample fractions. Blue bars within each plot indicate the number of products that were newly assigned at the higher temperature only. A: Counts for peaks matching amino acid condensation products and also ammonia additions. Peaks matching amino acid condensations were absent from the 350→450°C transition. B: Intermediate reaction products were separated by carbon number (C#) of the fragment lost, ranging from C1 (e.g. formic acid) to C6 (e.g. glucosone). For a complete list of all the amino acid condensation and C# fragment compositions, see Table C.2

Appendix D: Supporting Information for Chapter 5

Table D.1. Total concentration of disinfection byproducts in each stream and event measured when chlorinating using EPA methods 551.1 and 552.2.

	Site	$CHCl_3$	$CHBrCl_2$	CCl_3CN	$BrCH_2CN$	C_2HBr_2N	$C_2H_3Br_2NO$	$C_2H_2Cl_3NO$	$C_2H_3ClO_2$	$C_2H_3BrO_2$	$C_2H_2Cl_2O_2$	$C_2HCl_3O_2$	$C_2H_2Br_2O_2$
Low-BE	Pre-storm	85.70	5.40	1.90	0.60	0.00	0.60	0.00	1.06	0.00	15.96	10.72	0.00
	Storm	102.30	7.60	2.60	0.60	0.00	0.70	0.00	1.23	0.00	21.17	27.44	2.08
	Post-storm	90.90	6.90	2.30	0.60	0.00	0.60	0.80	0.00	0.00	20.84	24.47	2.29
Moderate-BE	Pre-storm	235.70	8.90	5.90	0.90	0.00	2.30	0.00	4.00	0.00	32.75	28.06	0.00
	Storm	207.60	11.80	4.60	1.00	0.00	1.70	0.80	0.00	0.00	40.33	41.75	0.00
	Post-storm	260.50	9.40	5.30	1.00	0.00	2.20	0.00	0.00	0.00	67.21	115.67	0.00
High-BE1	Pre-storm	234.60	9.70	5.60	0.90	0.00	1.70	0.00	4.60	0.00	45.58	59.29	0.00
	Storm	272.60	9.90	7.80	1.10	0.00	2.70	0.80	4.10	0.00	53.09	71.28	0.00
	Post-storm	174.40	9.30	4.90	0.80	0.00	1.40	0.80	0.00	0.00	33.52	39.09	2.25
High-BE2	Pre-storm	218.60	9.30	5.90	0.90	0.00	2.00	0.00	3.33	0.00	46.66	49.25	0.00
	Storm	220.80	8.90	4.90	1.00	0.00	2.20	0.00	0.00	0.00	39.91	72.20	0.00
	Post-storm	329.10	11.30	12.00	1.30	1.90	3.10	0.80	0.00	0.00	45.43	86.47	0.00

*$CHCl_3$ = Chloroform, $CHBrCl_2$ = Bromodichloromethane, CCl_3CN = Trichloroacetonitrile, $BrCH_2CN$ = Bromoacetonitrile, C_2HBr_2N = Dibromoacetonitrile, $C_2H_3Br_2NO$ = Dibromoacetamide, $C_2H_2Cl_3NO$ = Trichloroacetamide, $C_2H_3ClO_2$ = Monochloroacetic acid, $C_2H_3BrO_2$ = Monobromoacetic Acid, $C_2H_2Cl_2O_2$ = Dichloroacetic acid, $C_2HCl_3O_2$ = Trichloroacetic Acid, $C_2H_2Br_2O_2$ = Dibromoacetic acid

Table D.2. DOC-normalized concentration of disinfection byproducts in each stream and event measured when chlorinating using EPA methods 551.1 and 552.2.

	Site	DOC	$CHCl_3$	$CHBrCl_2$	CCl_3CN	$BrCH_2CN$	C_2HBr_2N	$C_2H_3Br_2NO$	$C_2H_2Cl_3NO$	$C_2H_3ClO_2$	$C_2H_3BrO_2$	$C_2H_2Cl_2O_2$	$C_2HCl_3O_2$	$C_2H_2Br_2O_2$
Low-BE	Pre-storm	7.41	11.57	0.73	0.26	0.08	0.00	0.08	0.00	0.14	0.00	2.15	1.45	0.00
	Storm	10.74	9.53	0.71	0.24	0.06	0.00	0.07	0.00	0.11	0.00	1.97	2.55	0.19
	Post-storm	4.29	21.21	1.61	0.54	0.14	0.00	0.14	0.19	0.00	0.00	4.86	5.71	0.53
Moderate-BE	Pre-storm	5.96	39.57	1.49	0.99	0.15	0.00	0.39	0.00	0.67	0.00	5.50	4.71	0.00
	Storm	18.53	11.20	0.64	0.25	0.05	0.00	0.09	0.04	0.00	0.00	2.18	2.25	0.00
	Post-storm	9.59	27.15	0.98	0.55	0.10	0.00	0.23	0.00	0.00	0.00	7.01	12.06	0.00
High-BE1	Pre-storm	4.68	50.15	2.07	1.20	0.19	0.00	0.36	0.00	0.98	0.00	9.74	12.67	0.00
	Storm	13.95	19.54	0.71	0.56	0.08	0.00	0.19	0.06	0.29	0.00	3.81	5.11	0.00
	Post-storm	4.87	35.81	1.91	1.01	0.16	0.00	0.29	0.16	0.00	0.00	6.88	8.03	0.46
High-BE2	Pre-storm	5.30	41.28	1.76	1.11	0.17	0.00	0.38	0.00	0.63	0.00	8.81	9.30	0.00
	Storm	13.21	16.71	0.67	0.37	0.08	0.00	0.17	0.00	0.00	0.00	3.02	5.47	0.00
	Post-storm	4.58	71.92	2.47	2.62	0.28	0.42	0.68	0.17	0.00	0.00	9.93	18.90	0.00

*$CHCl_3$ = Chloroform, $CHBrCl_2$ = Bromodichloromethane, CCl_3CN = Trichloroacetonitrile, $BrCH_2CN$ = Bromoacetonitrile, C_2HBr_2N = Dibromoacetonitrile, $C_2H_3Br_2NO$ = Dibromoacetamide, $C_2H_2Cl_3NO$ = Trichloroacetamide, $C_2H_3ClO_2$ = Monochloroacetic acid, $C_2H_3BrO_2$ = Monobromoacetic Acid, $C_2H_2Cl_2O_2$ = Dichloroacetic acid, $C_2HCl_3O_2$ = Trichloroacetic Acid, $C_2H_2Br_2O_2$ = Dibromoacetic acid

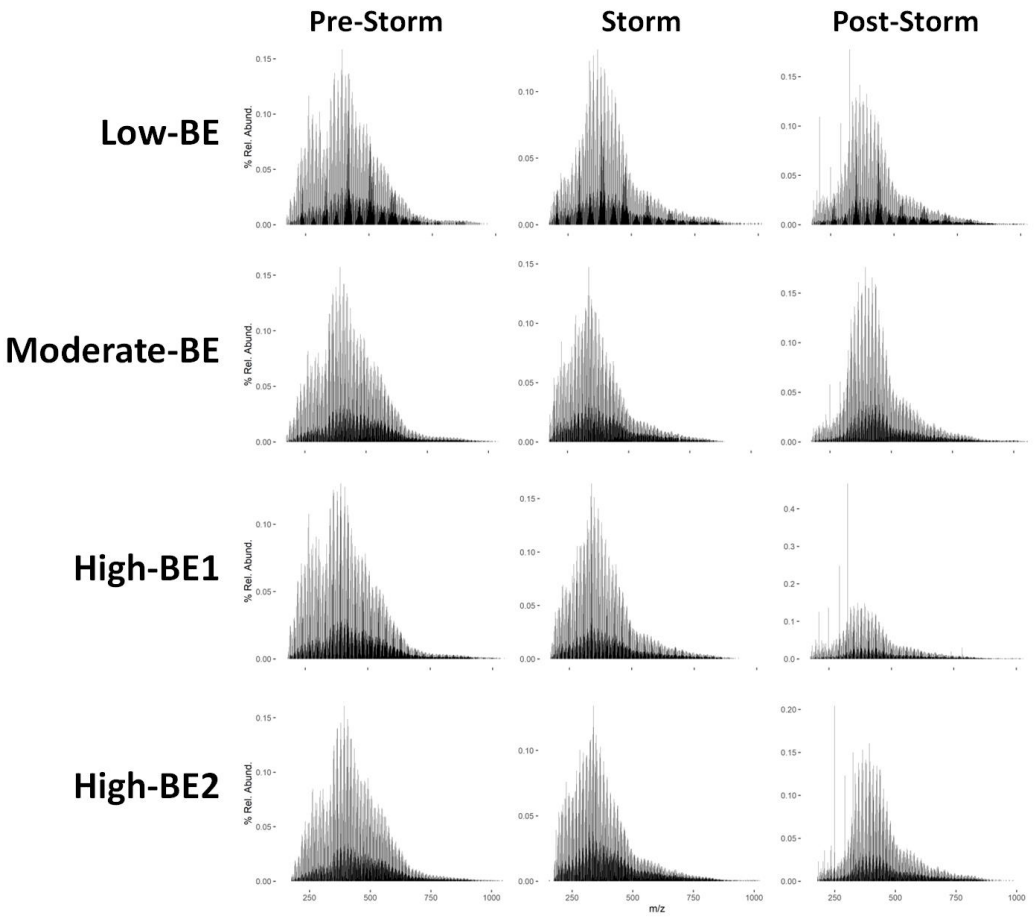

Figure D.1. (+)ESI-FT-ICR mass spectral distribution of all the peaks assigned in each stream and event.

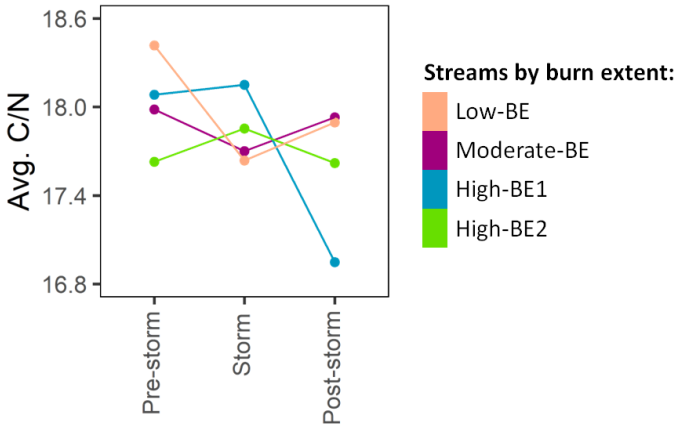

Figure D.2. Average C/N ratios calculated using assignments made in the 21 T (+) ESI FT-ICR MS spectra. Only assignments containing nitrogen were used, and averages were weighted by percent relative abundance.

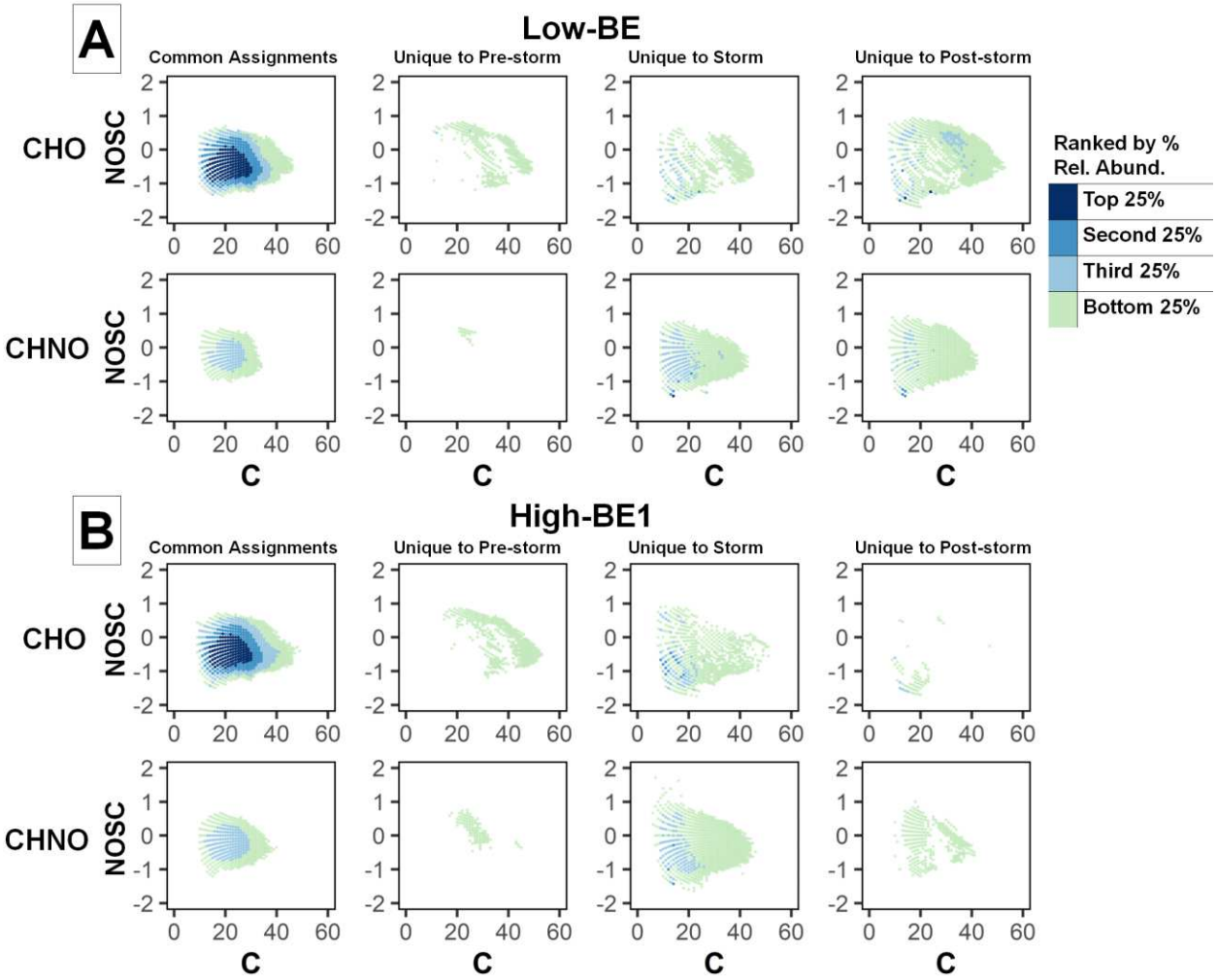

Figure D.3. The nominal oxidation state of carbon (NOSC) vs. carbon numer for assignments in the Low-BE and High-BE1 streams, separated species in all events for a stream (common), followed by peaks that are only identified (unique) in the pre-storm, storm, and post-storm samples. Peaks were grouped by their abundances, where the "top 25%" (dark blue points) are 25% of the sample's cumulative abundance comprised of the most abundant formulas, the "second 25%" is the next 25% comprised of the next most abundant formulas, and so on.

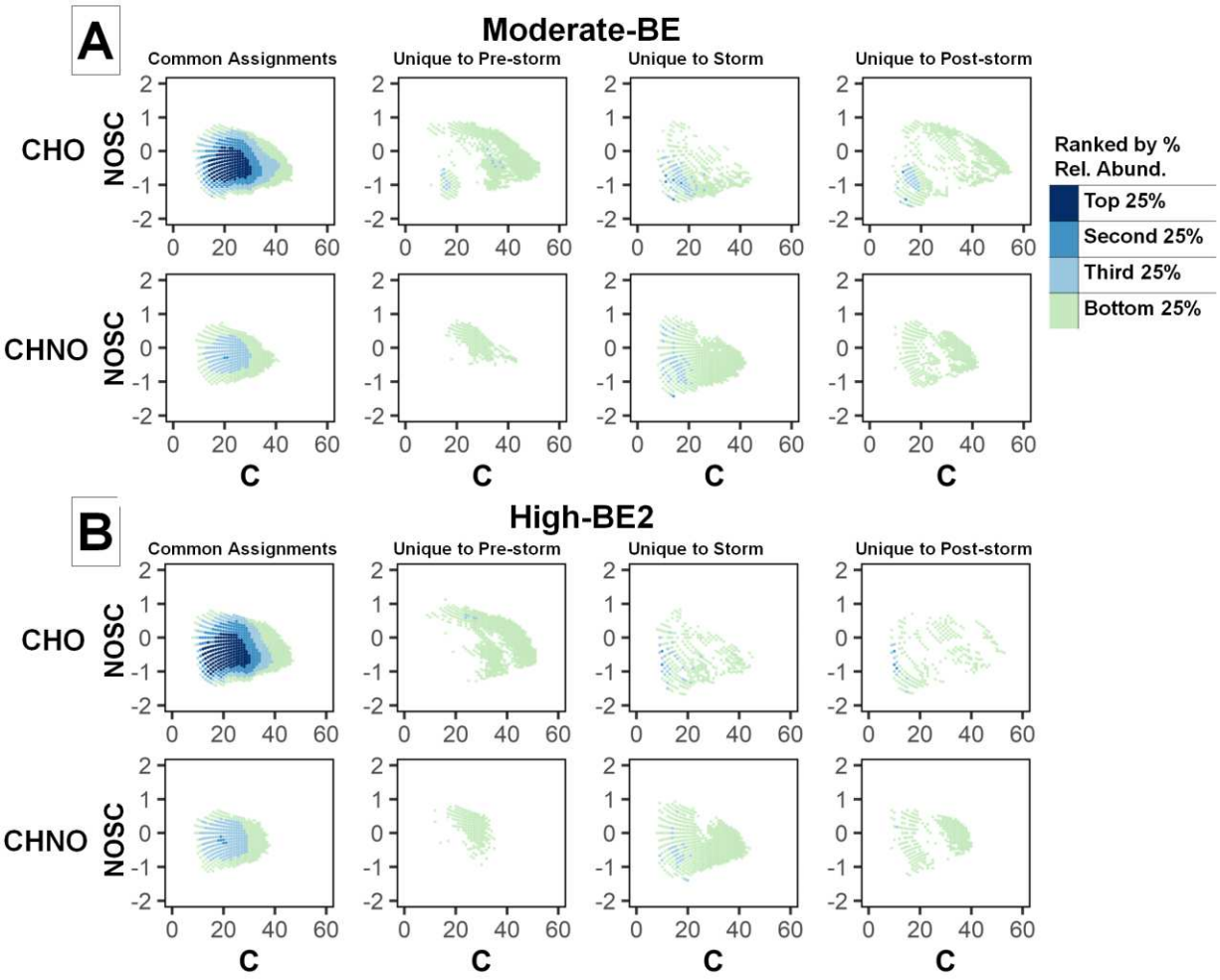

Figure D.4. The nominal oxidation state of carbon (NOSC) vs. carbon numer for assignments in the Low-BE and High-BE1 streams, separated species in all events for a stream (common), followed by peaks that are only identified (unique) in the pre-storm, storm, and post-storm samples. Peaks were grouped by their abundances, where the "top 25%" (dark blue points) are 25% of the sample's cumulative abundance comprised of the most abundant formulas, the "second 25%" is the next 25% comprised of the next most abundant formulas, and so on.

Appendix E: Co-author contributions to Composition-Dependent Sorptive Fractionation Study

Reprinted from Young, R.; Avneri-Katz, S.; McKenna, A.; Chen, H.; Bahureksa, W.; Polubesova, T.; Chefetz, B.; Borch, T. Composition-Dependent Sorptive Fractionation of Anthropogenic Dissolved Organic Matter by Fe(III)-Montmorillonite. *Soil Syst.* **2018**, *2* (1), 14.

My co-author contributions towards this work included data processing, visualization, investigation, and writing/reviewing/editing.

soil systems

MDPI

Article

Composition-Dependent Sorptive Fractionation of Anthropogenic Dissolved Organic Matter by Fe(III)-Montmorillonite

Robert B. Young [1], Shani Avneri-Katz [2], Amy M. McKenna [3], Huan Chen [3], William Bahureksa [4], Tamara Polubesova [2], Benny Chefetz [2] and Thomas Borch [1,4,*]

1 Department of Soil and Crop Sciences, Colorado State University, Fort Collins, CO 80523, USA; robert.b.young@colostate.edu
2 Department of Soil and Water Sciences, Faculty of Agriculture, Food and Environment, The Hebrew University of Jerusalem, Rehovot 7610001, Israel; shani.avneri@mail.huji.ac.il (S.A.-K.); tamara.polubesova@mail.huji.ac.il (T.P.); benny.chefetz@mail.huji.ac.il (B.C.)
3 National High Magnetic Field Laboratory, Florida State University, Tallahassee, FL 32310, USA; mckenna@magnet.fsu.edu (A.M.M.); huan.chen@magnet.fsu.edu (H.C.)
4 Department of Chemistry, Colorado State University, Fort Collins, CO 80523, USA; William.Bahureksa@colostate.edu
* Correspondence: thomas.borch@colostate.edu; Tel.: +1-970-491-6235

Received: 1 December 2017; Accepted: 22 February 2018; Published: 2 March 2018

Abstract: Water transports organic matter through soils, where mineral-organic associations form to retain dissolved organic matter ("DOM"), influencing terrestrial carbon cycling, nutrient availability for plant growth, and other soil organic matter functions. We combined Fourier transform ion cyclotron resonance mass spectrometry with novel data analysis techniques to examine the role of sorptive fractionation in the associations between Fe(III)-montmorillonite and DOM from composted biosolids ("anthropogenic DOM"). To examine the influence of DOM composition on sorption and sorptive fractionation, we used resin-based separation to produce DOM subsamples with different molecular compositions and chemical properties. A large proportion (45 to 64%) of the initial carbon in every DOM solution sorbed to the Fe(III)-montmorillonite. However, when the compositions of the initial solutions were compared to the sorbed organic matter, the computed changes in composition were lower (10 to 32%). In fact, non-selective sorption was more important than selective sorption in every sample, except for the hydrophilic neutral (HiN) fraction, where high nitrogen content and acidic conditions appeared to enhance sorptive fractionation. The results from this study demonstrate that the importance of sorptive fractionation varies with DOM composition and other factors, and that non-selective sorption can contribute substantially to the formation of mineral-organic associations.

Keywords: soil organic matter; dissolved organic carbon; dissolved organic nitrogen; sorption; adsorption; iron; clay; sewage sludge; FT-ICR MS

1. Introduction

Soils are composed of mineral matter, natural organic matter, and voids that are filled with air, water, or both. Soil constituents are transformed under the influence of biota, climate, topography, and other factors to produce cohesive aggregates of soil materials, a range of chemical environments (e.g., reducing and oxidizing) [1,2], and diverse microenvironments teeming with life. Soils have been called the most complicated biomaterial on Earth, and are heterogeneous across all measured scales, from nm to km [3]. Soils contain far more carbon than vegetation and the atmosphere combined [4], evidencing both that carbon turnover times in soils are relatively long, and that soil organic matter plays a key role in terrestrial carbon cycling. Other important soil organic matter functions include

increasing water retention, improving soil structure and aeration, providing nutrients for plant growth, and sequestering contaminants [5,6].

The natural organic matter in soils is derived primarily from plants and microbes [7,8]. Biotic and abiotic processes transform the precursor molecules to various degrees, producing an extremely complex mixture of organic molecules with almost a continuous range of properties and reactivities [9]. Natural organic matter is most abundant in litter layers and upper mineral horizons, and is transported to subsoils in water as dissolved molecules and fine suspended colloids (collectively, "dissolved organic matter" or "DOM") [10,11]. DOM concentrations decrease with depth due to degradation and the formation of mineral-organic associations [12–14]. As a result, most of the DOM produced in terrestrial ecosystems is mineralized or retained in soils [10].

Mineral-organic associations comprise organic matter that is sorbed to minerals or trapped in micro-aggregates [12,13] and co-precipitates [15,16]. The amount of organic matter in such associations varies among soil types, and even among horizons within the same soil [12]. Because mineral-organic associations account for up to 91% of total soil carbon, and have carbon turnover times that average four times longer than free or occluded organic matter [13], a comprehensive understanding of the formation and chemical composition of mineral-organic associations would provide important insights into many soil organic matter functions.

According to the zonal model proposed by Kleber et al. [17], organic matter self-assembles on mineral surfaces in a sequence composed of a "contact zone" at the mineral surface, a "hydrophobic zone" in the middle, and a "kinetic zone" at the organic matter-solution interface where organic matter is loosely retained and exchangeable. This implies that mineral-organic associations include a range of chemical and physical interactions that are not confined to mineral surfaces. In support of this model, Solomon et al. [18] observed a wide range of organic carbon functionalities and inorganic components at the organo-mineral interface, and carbon repository zones that were spatially and compositionally distinct, when examining mineral-organic associations with synchrotron-based scanning x-ray transmission microscopy coupled to near edge x-ray absorption fine structure spectroscopy (STXM-NEXAFS). They suggested that no single binding mechanism could explain mineral-organic associations. Similarly, the combination of chemical force spectroscopy with Fourier transform ion cyclotron resonance mass spectrometry (FT-ICR MS) has revealed that different DOM components adhere to iron oxide surfaces with different strengths [19]. Also, Comprehensive Multiphase nuclear magnetic resonance (NMR) spectroscopy has demonstrated that soil organic matter includes a rigid, hydrophobic interior and a gel-like, hydrated exterior [20]. Finally, nano-scale secondary ion mass spectrometry (NanoSIMS) has shown that new organic matter preferentially attaches to pre-existing mineral-organic associations [21].

On the other hand, carbon accumulation in soils is limited [22,23], and numerous studies have reported the selective fractionation of natural organic matter during sorption to metal oxides and clay minerals [24–27]. This implies that the formation and the chemical composition of mineral-organic associations are influenced by interactions between mineral surfaces and specific DOM components. Recently, Fleury et al. [28] used high resolution Orbitrap mass spectrometry (MS) with batch-equilibrium sorption experiments to examine the selective fractionation of DOM by alumina (an aluminum oxide) and kaolinite (a 1:1 clay with permanently non-charged surfaces). They demonstrated that sorptive fractionation was mineral type-dependent. Specifically, the kaolinite exhibited weak selectivity, which the authors attributed to nonselective hydrogen bonding, and the alumina exhibited strong selectivity for polycyclic aromatic and oxygen-rich compounds, which they attributed to hydrophobic effects and ligand exchange reactions. Similarly, Lv et al. [29] used FT-ICR MS with batch-equilibrium sorption experiments to examine the sorptive fractionation of peat leachates by iron oxides. They observed comparatively weak sorptive fractionation by goethite and lepidocrocite, and strong sorptive fractionation by ferrihydrite, including the preferential sorption of DOM constituents with high O/C ratios, high double-bond equivalent (DBE) values, and low H/C ratios. Finally, Avneri-Katz et al. [30] used FT-ICR MS, resin fractionation, and batch-equilibrium

sorption experiments to examine the sorptive fractionation of DOM from composted biosolids by a mineral soil, and demonstrated that sorptive fractionation was concentration-dependent. Specifically, unsaturated, oxygen-rich DOM components preferentially sorbed to the mineral soil, and selectivity decreased with increasing concentration.

The objective of this study was to examine the role of sorptive fractionation in associations between DOM from composted biosolids (hereafter, "anthropogenic DOM") and Fe(III)-montmorillonite, a 2:1 clay with permanently charged surfaces. FT-ICR MS simultaneously resolves and determines the molecular formulas of thousands of constituents per sample, thus permitting a molecular-level qualitative examination of the differences in complex mixtures such as DOM [31]. We combined FT-ICR MS with novel data analysis techniques to compare the compositions of DOM with the compositions of organic matter sorbed during batch-equilibrium experiments. To examine the influence of DOM composition, we used resin-based separation to produce DOM subsamples with different molecular compositions and chemical properties, separated by hydrophobicity and acidity, and compared the sorption and sorptive fractionation of each structural fraction. We hypothesized that the amount of sorbed organic carbon, and the strength of sorptive fractionation, would depend on the composition of the initial DOM solutions. In particular, we expected the hydrophobic acid (HoA) fraction, which generally contains high carboxyl content [32,33], to sorb most due to the potential for cation bridging and ligand exchange interactions [34,35]. We also expected the samples with the greatest proportion of aromatic and oxygen-rich DOM components to fractionate most. Finally, we hypothesized that the sorbed organic matter would be similar in every experiment due to sorptive fractionation, notwithstanding substantial differences among the initial DOM solutions.

2. Materials and Methods

2.1. Sorbent Preparation

Wyoming Na^+-montmorillonite (SWy, cation exchange capacity = 76.4 meq/100 g) was obtained from the Clay Minerals Society (Chantilly, VA, USA). The <2 μm fraction of SWy was collected by sedimentation with deionized water and enriched with $Fe^{(III)}$, as described by Olshansky et al. [36]. In brief, 6 g aliquots of the <2 μm SWy fraction were agitated with 180 mL of 0.3 M $FeCl_3$ for 2 h at 200 rpm. Next, the SWy was centrifuged at 15,000 g for 10 min, the supernatant was discarded, and the wash procedure was repeated with a fresh $FeCl_3$ solution. After four sequential washes, the Fe-enriched SWy fraction (Fe(III)-montmorillonite) was dialyzed against deionized water in 12–14 K molecular weight cut-off dialysis bags (Medicell International LTD., London, UK) until the dialysate's electrical conductivity and chloride concentration were negligible. The pH of the Fe(III)-montmorillonite suspensions was approximately 3.5, limiting the formation of a separate iron oxide mineral phase [37,38]. After preparation, the Fe(III)-montmorillonite was freeze dried and stored in a desiccator.

2.2. DOM Extraction and Fractionation

Structural fractions of the anthropogenic DOM were prepared as described by Avneri-Katz et al. [30]. In brief, DOM was extracted from commercially available composted biosolids (Kfar Menachem, Dlila Facility, Israel; 50% sewage sludge, 50% tree clippings) by overnight agitation at 200 rpm with a 1:10 (w:v) compost to water ratio. The tree clippings are a carbon source [39], and a bulking agent that absorbs moisture and improves aeration during composting [40].The resulting suspension was centrifuged at 17,000 g for 20 min and filtered through a 0.45 μm Acrodisc Supor membrane (PALL Corp., Ann Arbor, MI, USA). A portion of the resulting anthropogenic DOM was freeze-dried and stored in a desiccator for comparison with the structural fractions.

To produce the structural fractions, the remaining anthropogenic DOM was acidified to pH 3 with 6 M HCl and loaded onto a glass column containing Supelite DAX-8 resin (Supelco, Bellefonte, PA, USA), which selectively retains the hydrophobic fraction [32,41]. The hydrophobic acid (HoA) fraction

was recovered from the DAX-8 resin with 0.1 M NaOH, and the hydrophobic neutral (HoN) fraction was recovered by Soxhlet extraction with methanol for 24 h. The HoN fraction was not recovered in sufficient quantities for replicate experiments. The unretained hydrophilic fraction was loaded sequentially onto glass columns containing cation-exchange (Amberlyst® 15) and anion-exchange (Amberlyst® A21) resins to retain the hydrophilic base (HiB) and hydrophilic acid (HiA) fractions, which could not be recovered in sufficient quantities for further experimentation. The unretained eluent comprised the neutral (HiN) fraction. After preparation, all of the recovered structural fractions were freeze-dried and stored in a desiccator.

2.3. Sorption Experiments

To examine the influence of DOM composition on sorption and sorptive fractionation, batch-equilibrium sorption experiments were conducted using the Fe(III)-montmorillonite, DOM structural fractions, and unfractionated anthropogenic DOM.

To prepare DOM solutions for the sorption experiments, the freeze-dried DOM extracts were dissolved in a background solution prepared with DDW and chloride salts (cations = Ca, K, Mg, and Na, I = 2 mM) to simulate the ionic strength and composition of the original extract from composted biosolids. Prior to DOM addition, the Fe(III)-montmorillonite was agitated in the same background solution at a suspension concentration of 15 g L^{-1} for 2 h at 200 rpm. Next, the DOM solutions were added to the Fe(III)-montmorillonite suspension to produce 3 g L^{-1} clay suspensions with the initial organic C concentrations presented in Table 1. The pH of the resulting samples was approximately 3.5. The resulting samples were agitated at 200 rpm for 48 h at 25 °C, based on preliminary kinetics experiments. After equilibration, the samples were centrifuged at 17,000 g for 10 min, and the supernatants were decanted. Following sedimentation, the Fe(III)-montmorillonite samples were washed with DDW to remove unbound DOM, and the sorbed organic matter was extracted from the mineral-organic associations by agitation with 0.1 M NaOH at a suspension concentration of 15 g L^{-1} for 2 h at 200 rpm. The resulting extracts (each, a "sorbed OM extract") were filtered through a 0.45-µm filter, and were loaded onto a cation-exchange resin (Amberlyst 15), activated with hydrochloric acid (H^+), to remove excess sodium.

Table 1. Initial and sorbed carbon amounts (mean ± std, n = 6) from the batch equilibrium experiments with 3 g L^{-1} Fe(III)-montmorillonite, the anthropogenic DOM, and each structural fraction. Sorbed DOC (%) = 3 g dry clay/L × Sorbed DOC (mg C/g dry clay) ÷ Initial DOC (mg C/L). The HoN fraction was not recovered in sufficient quantities for replicate experiments.

Fraction	Initial DOC (mg C/L)	Sorbed DOC (mg C/g dry clay)	Sorbed DOC (%)
Anthropogenic DOM	54 ± 1	9.8 ± 0.4	54 ± 2
HoA Fraction	55 ± 0.9	11.8 ± 0.5	64 ± 3
HoN Fraction	39	7.6	58
HiN Fraction	14 ± 2	2.1 ± 0.2	45 ± 4

The original DOM solutions and the sorbed OM extracts were examined by total organic carbon (TOC) analysis (VCPH model TOC analyzer, Shimadzu Scientific Instruments, Kyoto, Japan) to determine the masses and the proportions of organic carbon that sorbed to the Fe(III)-montmorillonite during the batch-equilibrium experiments (Table 1). The samples were also analyzed by FT-ICR MS to examine their compositions before and after sorption.

2.4. FT-ICR MS Analysis

2.4.1. Sample Preparation

All of the samples were prepared for FT-ICR MS analysis by solid phase extraction (SPE) following the procedure described by Dittmar et al. [42] and Li et al. [43], with some modifications. In brief, 1 g,

6 mL Bond Elut PPL cartridges (Agilent Technologies, Santa Clara, CA, USA) were conditioned with 18 mL of HPLC grade methanol (Sigma-Aldrich, Rehovot, Israel), followed by 30 mL of 0.01 M HCl. Each DOM sample was acidified to pH ~2.5, and loaded onto the SPE cartridges at masses $\leq$10 mg C. Following sample loading, the SPE cartridges were washed with 12 mL of 0.01 M HCl and dried under N_2 for 3–5 min. Next, the DOM was eluted with 2 mL of HPLC grade methanol, freeze-dried, and stored in a desiccator. Immediately prior to analysis, the freeze-dried DOM samples were dissolved in a 50:50 (v/v) HPLC grade methanol:DDW solution containing 1% (by volume) NH_4OH to enhance the deprotonation of acidic species for negative ion mode electrospray ionization (ESI^-).

2.4.2. Instrumental Analysis

The samples were analyzed with a custom-built passively shielded 9.4 T FT-ICR mass spectrometer [44], equipped with a modular software package for data acquisition (Predator) [45]. Negative ions were generated at atmospheric pressure and were transferred into the mass spectrometer by a tube lens/skimmer at 250 V. The ions were accumulated in an RF-only external quadrupole [46], passed through a mass resolving RF-only quadrupole, and collisionally cooled with helium gas ($\sim 3.5 \times 10^{-6}$ Torr) before transfer by octupole ion guides with capacitively coupled excitation electrodes into a seven-segment cylindrical cell [47,48]. A broadband frequency-sweep ("chirp") excitation (~70 to 720 kHz, 50 Hz/μs sweep rate, 350 $V_{p\text{-}p}$ amplitude) was used for detection. For each sample, 100 time domain transients were coadded, zero-filled, apodized, fast Fourier transformed, and phase-corrected to yield an absorption-mode mass spectrum [49]. The ICR frequencies were converted to m/z using a two-term calibration equation based on quadrupolar trapping potential approximation [50,51]. Peak lists were constructed from peaks of magnitude at least six times greater than the standard deviation of the baseline noise (6σ). Next, the spectra were internally calibrated by a "walking" calibration using the most abundant homologous ion series [52].

2.4.3. Data Analysis

Custom software (PetroOrg©) was used for additional calibration and elemental composition assignment [53]. The m/z values were converted to the Kendrick mass scale [54], assigned an elemental composition ($C_{1\text{-}100}$ $H_{4\text{-}200}$ $N_{0\text{-}5}$ $O_{0\text{-}20}$ $S_{0\text{-}1}$), and grouped by heteroatom class ($O_oN_nS_s$) [55]. For each elemental composition, a modified aromaticity index (ModAI) was computed according to Koch and Dittmar [56]. To compare the structural fractions by composition, principal component analysis was performed on selected categories of the FT-ICR MS data using R software (version 3.4.0) [57] and the FactoMineR package [58].

3. Results

3.1. Sorption by Mass

The amounts and proportions of organic carbon that sorbed to the Fe(III)-montmorillonite are presented in Table 1. The original anthropogenic DOM (54 mg C L^{-1}) and original HoA fraction (55 mg C L^{-1}) contained more organic carbon than the original HoN fraction (39 mg C L^{-1}), and more than 3.5 times the organic carbon in the original HiN fraction (14 mg C L^{-1}). The proportions of organic carbon that sorbed to the Fe(III)-montmorillonite, ordered from most to least, were: HoA fraction (64 ± 3%) > HoN fraction (58%) > anthropogenic DOM (54 ± 2%) > HiN fraction (45 ± 4%). The HiN fraction appeared to exhibit unique sorption behavior, because the amount of sorbed organic matter (mg C/g clay) is usually a linear or decreasing function of DOM concentration (mg C L^{-1}), but the HiN fraction sorbed least on a proportionate basis (45 ± 4%) with the lowest concentration (14 mg C L^{-1}).

3.2. Presence of "Surfactant-Like" Peaks

When the composition of the original and sorbed organic matter samples were examined by FT-ICR MS, several series of "surfactant-like" peaks were evident. Using the Kendrick mass scale [54,55], which assigns the same Kendrick mass defect (KMD) to groups of molecules that differ in elemental composition only by one or more $-CH_2-$ groups (i.e., by alkyl chain length), several sulfur-containing Kendrick series were identified. The surfactant-like series were present in all of the samples, but much less abundant in the sorbed OM extracts (e.g., Supplementary Materials Figure S1). This suggested both that the surfactant-like series were not preferentially sorbed, and that their presence was not caused by laboratory contamination. When the surfactant-like series were highly abundant, ion suppression limited the number of other peaks that could be detected and assigned elemental compositions. As a result, fewer formulas were assigned to the original DOM solutions than their sorbed OM extracts. This was particularly evident in the HoA fraction, when the surfactant-like series were especially abundant.

3.3. Composition-Dependent Sorptive Fractionation

To examine composition-dependent sorptive fractionation, we used FT-ICR MS to identify the formulas that were present both in the original DOM solution and its corresponding sorbed OM extract, and then normalized them to 100% in each sample (hereafter, "Common Formulas"). Formulas that were unique to the original DOM solution or its corresponding sorbed OM extract, due to differences in ion suppression or any other cause, were excluded to ensure that changes in percent abundance were attributable to sorption, and not to differences in the number of assigned formulas. The surfactant-like series were excluded from both samples because they were highly abundant in the original DOM solutions, and much less abundant in the sorbed OM extracts. Without exclusion, they would have dominated the composition of the original DOM solutions, and would have caused the abundances of most other DOM components to appear enhanced in the sorbed OM extracts, masking their sorption behavior relative to each other. The sorption behavior of the surfactant-like series was clear: they tended to remain in solution.

For each sample, the median, mean, and standard deviation of the absolute errors (ppm) of the Common Formula assignments are set forth in Supplementary Materials Table S1. No Common Formula assignment had an absolute error greater than 1 ppm, and no sample had a mean absolute error greater than 0.07 ppm. Except for the HiN fraction (87%), more than 98% of the formulas identified in the original DOM solutions were also identified in their respective sorbed OM extracts. This indicated that the formula assignments for relatively abundant, "unsuppressed" peaks were reproducible, and that most of the identified components in the original DOM solutions were sorbed to the Fe(III)-montmorillonite, at least to some extent. These percentages, like the TOC analysis, suggested that the HiN fraction exhibited unique sorption behavior.

3.3.1. Composition of the Structural Fractions

The van Krevelen diagrams (H/C vs. O/C) in Figure 1 demonstrate that resin-based fractionation produced structural fractions with different molecular compositions, including different relative abundances in the same plot regions. To highlight the Common Formulas that contributed most to the composition of each original sample, the Common Formulas were ranked from most to least abundant and divided into quartiles. The "Top 25%" (dark blue in Figure 1), totaling ~25% of the sample's cumulative abundance, comprised the most abundant Common Formulas. The "Bottom 25%" (light green in Figure 1), also totaling ~25% of the sample's cumulative abundance, comprised the least abundant Common Formulas. Viewed differently, the Top 25% comprised the smallest proportion, and the Bottom 25% comprised the largest proportion, of the total number of Common Formulas in each sample (Supplementary Materials Figure S2). All of the Common Formulas with a ModAI > 0.5 were designated aromatic (AROM) in accordance with Koch and Dittmar [56], and all of the formulas

with H/C ratios $\geq$ 1.5 were designated aliphatic (ALIPH), in accordance with Lv et al. [29] and D'Andrilli et al. [59]. Among the structural fractions, the area of greatest abundance (dark blue in Figure 1) varied, notwithstanding substantial overlap in the center of the van Krevelen diagrams.

To examine the composition of the structural fractions in greater detail, we divided the van Krevelen diagrams into nine discreet regions, illustrated in Supplementary Materials Figure S3, and performed a principal component analysis (PCA) using the samples' cumulative percent abundance in each region (Supplementary Materials Table S2). Specifically, the van Krevelen diagram was divided into aliphatic (ALIPH), aromatic (AROM), and mid saturation (MS) regions, and these regions were subdivided by the degree of oxygenation ("LO" = low oxygen content, O/C $\leq$ 0.3; "MO" = mid oxygen content, 0.3 < O/C $\leq$ 0.6; "HO" = high oxygen content, O/C > 0.6). These categories were created to avoid describing regions of the van Krevelen diagram with reference to lignin, polyphenols and other biomolecules, which can overlap in the same van Krevelen plot region [60,61] and which can become attenuated beyond recognition in natural organic matter [62].

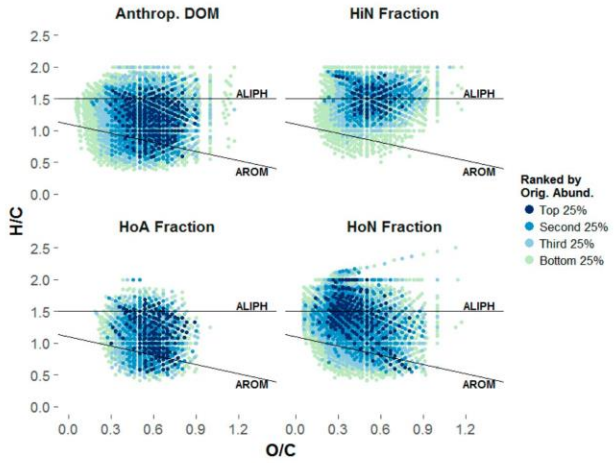

Figure 1. van Krevelen diagrams of the original dissolved organic matter (DOM) solutions. The plotted points represent only the formulas that were present both in the original DOM solution and the corresponding sorbed organic matter extract (Common Formulas). The percent abundances of the Common Formulas in the original DOM solutions were normalized to 100%, ranked from most to least abundant, and divided into quartiles based on their cumulative percent abundances.

According to the PCA (Figure 2), the HoA fraction and the anthropogenic DOM separated from the HiN and HoN fractions along the first principal component ("Dim 1", x axis), primarily because the former group had greater aromatic and MS-HO content, and because the latter group had greater aliphatic content. Along the second principal component ("Dim 2", y axis), the HoN fraction separated from the HiN fraction primarily because the HoN fraction had greater ALIPH-LO and MS-LO content, and because the HiN fraction had greater ALIPH-HO content. The same observations were evident when the cumulative percent abundances of the structural fractions were quantified relative to the anthropogenic DOM in each van Krevelen plot region (Supplementary Materials Figure S4). The HoA fraction did not separate from the anthropogenic DOM in the PCA plots, and differed little from the anthropogenic DOM in Supplementary Materials Figure S4, because their Common Formulas were similarly distributed across the van Krevelen plot regions.

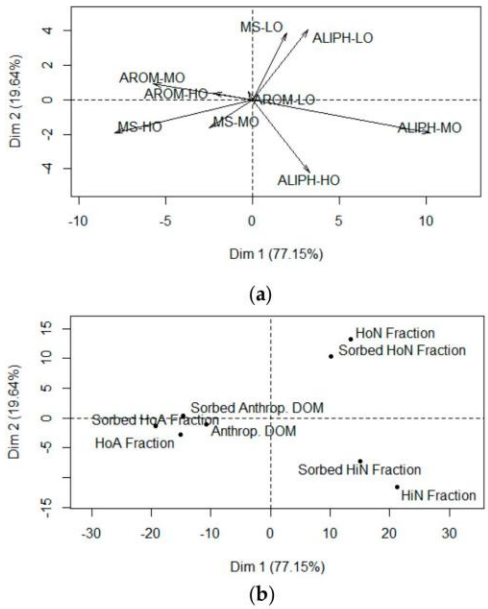

Figure 2. Principal Component Analysis (PCA) plots relating the first and second principal components to (**a**) the nine van Krevelen plot region variables (Supplementary Materials Figure S3), and (**b**) the original and sorbed organic matter samples, considering only the formulas that were present in both the original DOM solutions and their corresponding sorbed organic matter extracts (Common Formulas). "ALIPH" = aliphatic ($H/C \geq 1.5$); "AROM" = aromatic (ModAI > 0.5); "MS" = mid-saturation ($H/C < 1.5$ and ModAI ≤ 0.5); "LO" = low oxygen content ($O/C \leq 0.3$); "MO" = mid-oxygen content ($0.3 < O/C \leq 0.6$); "HO" = high oxygen content ($O/C > 0.6$); "ModAI" = modified aromaticity index.

When the Common Formulas from each structural fraction were compared, 5375 Common Formulas were unique to one structural fraction, 1932 Common Formulas were detected in two of the three structural fractions, and 1283 Common Formulas were detected in all three structural fractions (Supplementary Materials Figure S5). Many of the 1283 Common Formulas that were detected in every structural fraction were abundant in the original, unfractionated anthropogenic DOM sample, suggesting that their structural fractionation was incomplete. For example, 319 Common Formulas composed the Top 25% of the original, unfractionated anthropogenic DOM sample, and 301 of them were detected in every structural fraction. Only 155 Common Formulas were unique to the HoA fraction, presumably because the surfactant-like series suppressed and obscured its low abundance peaks, which were most likely to be completely fractionated.

The structural fractions also differed in elemental composition (Supplementary Materials Table S3). The anthropogenic DOM contained elemental classes in the following order of abundance: CHNO (45.6%) > CHO (27.7%) > CHNOS (16.1%) > CHOS (10.6%). Relative to the anthropogenic DOM, the HoA fraction contained less N content (−10.0%), more CHO content (+7.5%), and more CHOS content (+2.5%), presumably because many sulfur-containing surfactant-like compounds were concentrated in the HoA fraction, notwithstanding the removal of the excluded surfactant-like series (as described in Section 3.3). The HiN fraction contained much more CHNO content (+30.1%), and very little CHOS content (1.4%), when compared to the anthropogenic DOM. Finally, the HoN fraction contained much more CHO content (+21.0%), and much less N content (−30.2%), than the anthropogenic DOM.

3.3.2. Sorptive Fractionation

To identify the occurrence of sorptive fractionation, we subtracted the percent abundance of each Common Formula in the sorbed OM extract from its percent abundance in the original DOM solution. A negative result indicated that sorption was favored, and a positive result indicated that sorption was disfavored. Next, we created a seven-category scale ("Most Sorbed" to "Most Unbound") to describe the degree of sorptive fractionation by the magnitude of the difference in percent abundance (Figure 3). The magnitudes of the individual changes were small, because the total abundance of 100% was divided among thousands of formulas, but the negative and positive results could be summed separately to determine the cumulative compositional changes in each structural fraction (Figure 4a). These cumulative compositional changes were ordered as follows: 32% (HiN fraction) > 18% (HoN fraction) > 14% (HoA fraction) > 10% (anthropogenic DOM).

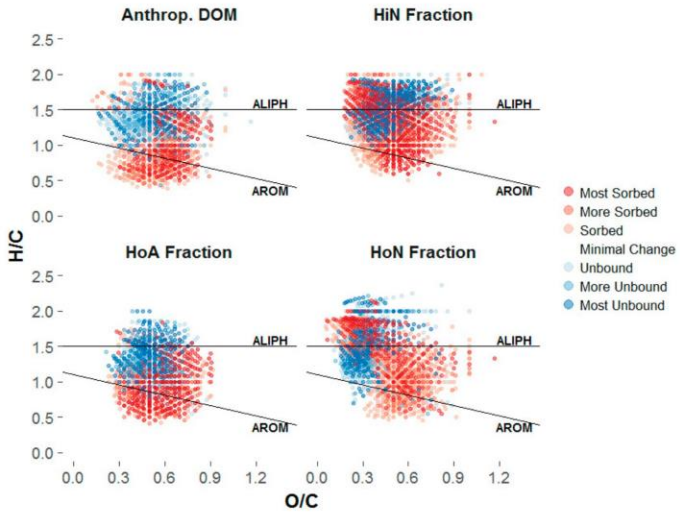

Figure 3. van Krevelen diagrams illustrating the common formulas that were more abundant in the original DOM solutions (Blue), and more abundant in their sorbed organic matter extracts (Red), determined by subtracting the percent abundance of each formula in the sorbed organic matter extract from its percent abundance in the original solution ("Most Sorbed" = Δ abundance < −0.015%; "More Sorbed" = Δ abundance < −0.010%; "Sorbed" = Δ abundance < −0.005%; "Minimal Change"; "Unbound" = Δ abundance > 0.005%; "More Unbound" = Δ abundance > 0.010%; "Most Unbound" = Δ abundance > 0.015%).

When the sorption categories were plotted in van Krevelen diagrams (Figure 3), the patterns of sorptive fractionation were apparent. For example, every sample contained ionizable aromatic and oxygen-rich components that preferentially sorbed to the Fe(III)-montmorillonite. To examine the sorptive fractionation in greater detail, the cumulative changes in each sorption category were divided into elemental compositions (Figure 4b) and van Krevelen plot regions (Figure 5).

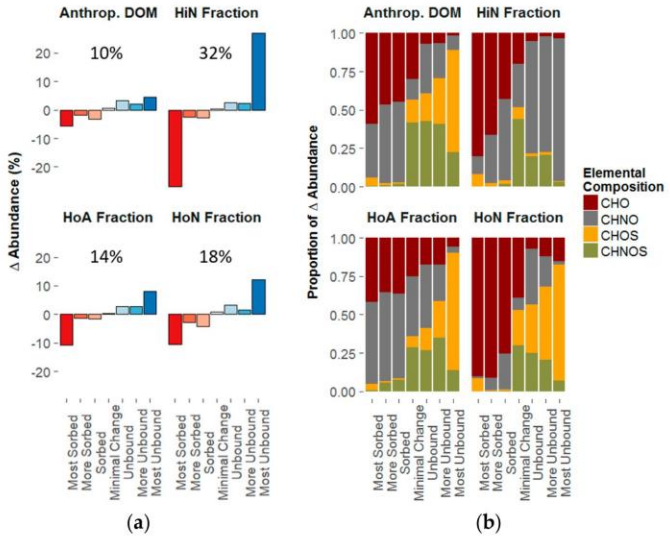

Figure 4. (**a**) Cumulative changes in percent abundance for the sorption categories described in Figure 3. (**b**) Distribution of the cumulative changes in percent abundance according to elemental composition ("Most Sorbed" = Δ abundance < −0.015%; "More Sorbed" = Δ abundance < −0.010%; "Sorbed" = Δ abundance < −0.005%; "Minimal Change"; "Unbound" = Δ abundance > 0.005%; "More Unbound" = Δ abundance > 0.010%; "Most Unbound" = Δ abundance > 0.015%).

In every sample, the ionizable CHO content preferentially sorbed to the Fe(III)-montmorillonite, and the ionizable sulfur-containing content (CHOS and CHNOS) preferentially remained in solution. In contrast, the ionizable CHNO content exhibited variable sorption behavior. In the HiN fraction, where the CHNO content was greatest (75.8%), the CHNO component mostly remained in solution. In the HoA fraction and anthropogenic DOM, where the sulfur-containing content was greatest, the CHNO component mostly sorbed to the Fe(III)-montmorillonite.

When the sorption categories were examined by van Krevelen plot region, the aromatic and MS-HO regions of every sample, and the ALIPH-LO region of the HiN fraction, mostly sorbed to the Fe(III)-montmorillonite. The other plot regions often split with respect to sorption preference, suggesting heterogeneity within the same plot region. For example, the ALIPH-LO and ALIPH-MO content of the HoN fraction were almost evenly split between "Sorbed" and "Unbound".

To examine the interactions between elemental composition and van Krevelen plot region in greater detail, the van Krevelen diagrams in Figure 3 were subdivided by elemental composition (Supplementary Materials Figures S6 through S9). The resulting figures suggest that the heterogeneity in the van Krevelen plot regions was primarily driven by elemental composition. For example, in the aliphatic region of the HiN fraction, where the sulfur-containing content was the lowest, the ionizable CHO content preferentially sorbed to the Fe(III)-montmorillonite, and the ionizable CHNO content tended to remain in solution. Alternatively, in the aliphatic region of the HoN fraction, where the CHNO content was the lowest, the ionizable CHO content preferentially sorbed to the Fe(III)-montmorillonite, and the ionizable sulfur-containing content tended to remain in solution.

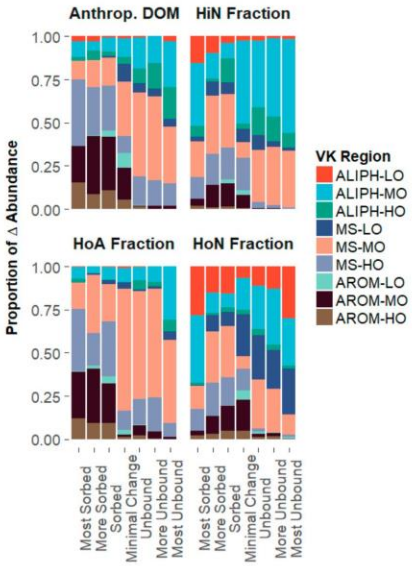

Figure 5. Distribution of the cumulative changes in percent abundance from Figure 4a according to van Krevelen (VK) plot region. "ALIPH" = aliphatic (H/C $\geq$ 1.5); "AROM" = aromatic (ModAI > 0.5); "MS" = mid-saturation (H/C < 1.5 and ModAI $\leq$ 0.5); "LO" = low oxygen content (O/C $\leq$ 0.3); "MO" = mid-oxygen content (0.3 < O/C $\leq$ 0.6); "HO" = high oxygen content (O/C > 0.6); "ModAI" = modified aromaticity index.

During the formula assignment, the maximum number of sulfur atoms was one (1), and the maximum number of nitrogen atoms was five (5). To examine the influence of the number of nitrogen atoms on sorption behavior, the ionizable CHNO content in every sample was subdivided by sorption behavior and the number of nitrogen atoms (Figure 6). In almost every case, preferential sorption to the Fe(III)-montmorillonite decreased as the number of nitrogen atoms increased. This behavior was especially prominent in the HiN fraction, which contained the greatest CHNO content (75.8%) and the lowest sulfur-containing content (6.4%). To examine the influence of the number of oxygen atoms on this behavior, the ionizable CHNO content in the HiN fraction was further subdivided by the number of oxygen atoms (Supplementary Materials Figure S10). When the number of nitrogen atoms exceeded one (1), the ionizable CHNO content in the HiN fraction tended to remain in solution, regardless of oxygen content. In contrast, when the number of nitrogen atoms was equal to one (1), the ionizable CHNO content tended to remain in solution when the number of oxygen atoms was less than or equal to six (6), and preferentially sorbed to the Fe(III)-montmorillonite when the number of oxygen atoms was greater than six (6).

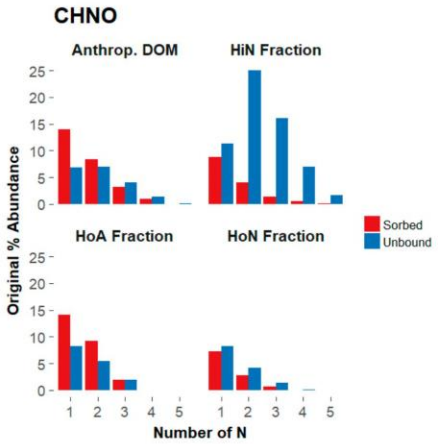

Figure 6. Distribution of CHNO formulas as a function of their original abundance, nitrogen content, and status as "Sorbed" or "Unbound".

4. Discussion

4.1. Composition-Dependent Sorption

According to the TOC data (Table 1), each structural fraction sorbed to the Fe(III)-montmorillonite to a different extent, supporting our hypothesis that the amount of sorbed organic carbon would depend on the composition of the initial DOM solutions. More specifically, 45 to 64% of the initial organic carbon in every sample sorbed to the Fe(III)-montmorillonite. As expected, the HoA fraction sorbed most (64%), presumably due to its high carboxyl content [32,33], the potential for limited ferrihydrite formation [63], the potential for cation bridging and ligand exchange interactions [34,35], and the acidic conditions of the experiments [64].

4.2. Composition-Dependent Sorptive Fractionation

Two findings were required to demonstrate that DOM composition influenced sorptive fractionation by Fe(III)-montmorillonite: (1) the compositions of the original structural fractions had to be different; and, (2) sorptive fractionation had to vary among the structural fractions.

The structural fractions did exhibit unique molecular compositions (Figure 1), even though the anthropogenic DOM was not completely fractionated (Supplementary Materials Figure S5). For example, the anthropogenic DOM and the HoA fraction had greater aromatic and MS-HO content, and the HiN and HoN fractions had greater aliphatic content (Figure 2). Alternatively, from the perspective of elemental composition, the HoN fraction contained the highest CHO content (48.7%) and the lowest CHNO content (24.6%), while the HiN fraction contained the highest CHNO content (75.8%) and the lowest CHO content (17.8%) (Supplementary Materials Table S3).

Sorptive fractionation is evidenced by changes in composition that occur during sorption. If the composition of the sorbed organic matter differs from the composition of the original DOM solution, then sorptive fractionation has occurred. If its composition is considerably different, then strong sorptive fractionation has occurred.

In this study, a major challenge was to characterize the changes in composition when surfactant-like peaks, which are common to sewage treatment wastewater and biosolids [65–68], suppressed the ionization of constituents in the original DOM solutions. We excluded the surfactant-like series, and focused on the relative abundances of DOM constituents that were both

sorbed to the Fe(III)-montmorillonite and present in the original DOM solutions, where most of the ion suppression was occurring. Using this approach, we could not examine every DOM component that sorbed to the Fe(III)-montmorillonite, but we did characterize changes in the abundances of 87 to 99% of the constituents that were identified in the original DOM solutions. These compositional changes are illustrated in Figure 3 and quantified, as much as possible, in Figure 4a. Using this approach, every sample exhibited sorptive fractionation, and the degree of sorptive fractionation varied, supporting our hypothesis that the strength of sorptive fractionation would depend on the composition of the initial DOM solutions.

On the other hand, Figure 2 illustrates that the sorbed organic matter in every experiment resembled the DOM solution from which it came more than it resembled the sorbed organic matter from the other experiments. This contradicts our hypothesis that all of the sorbed organic matter would be similar due to sorptive fractionation, and suggests that most DOM can be retained in mineral-organic associations, subject to changes in environmental conditions [13,69].

4.3. The Influence of Aromaticity, Oxygen Content, and Nitrogen Content on Sorptive Fractionation

Every sample contained ionizable aromatic and oxygen-rich components that preferentially sorbed to the Fe(III)-montmorillonite (Figure 3), as in previous studies [28–30]. However, those constituents did not determine the strength of sorptive fractionation, contrary to expectations. The greatest compositional change occurred in the HiN fraction (32%), which had low aromatic (1.7%) and MS-HO content (9.0%), and the smallest compositional change occurred in the anthropogenic DOM (10%), which had high aromatic (19.2%) and MS-HO (22.8%) content.

The HiN fraction contained the highest CHNO content (75.8%), which exhibited more sorptive fractionation than any other elemental composition (Figure 4; Supplementary Materials Figures S6 through S9). The HiN fraction also contained the highest ALIPH-MO (35.0%) and ALIPH-HO (15.9%) content, and the lowest aromatic content (1.7%). Aliphatic constituents with more than one nitrogen tended to remain in solution (Figure 6), and aliphatic constituents with one nitrogen split according to the number of oxygens. If the number of oxygens was greater than 6, then the aliphatic constituents preferentially sorbed to the Fe(III)-montmorillonite. Otherwise, the aliphatic constituents tended to remain in solution. We suggest that the strong sorptive fractionation of the HiN fraction was caused primarily by nitrogen-rich, non-aromatic DOM, and that the number of oxygens was only important when the number of nitrogens was low (i.e., 0 or 1).

Acidic conditions produce positively charged basic (e.g., amino) functional groups, uncharged acidic (e.g., carboxyl) functional groups, and positively charged surface hydroxyl groups [70]. Furthermore, montmorillonite facilitates cation bridging interactions if saturated with multivalent cations [25,71]. Under these conditions, DOM constituents with positively charged amino groups would tend to remain in solution, uncharged DOM constituents would tend to sorb through hydrophobic, van der Waals, or hydrogen bonding interactions, and highly acidic [72,73] organic functional groups would tend to participate in ligand exchange or cation bridging interactions [34,35,64]. This could explain strong sorptive fractionation in the HiN fraction. The anthropogenic DOM, HoA fraction, and HoN fraction contained greater CHO content (27.7%, 35.2%, and 48.7%, respectively), and exhibited weaker sorptive fractionation.

Similar behavior has been observed in natural systems. Scott and Rothstein [14] recently determined that nitrogen-rich hydrophilic DOM was weakly retained, when compared to hydrophobic DOM, in soil cores from six forests at pH 4.5 to 6.0. In addition, dissolved organic nitrogen concentrations and C:N ratios commonly increase with soil depth [74].

4.4. The Influence of Non-Selective Sorption on the Formation of Mineral-Organic Associations

Among the structural fractions, the HoA fraction sorbed most (64%), but exhibited the smallest composition change (14%). This suggested that non-selective sorption was important. In fact, every sample appeared to exhibit non-selective sorption because the sorbed organic carbon percentage

(Table 1) always exceeded the cumulative compositional change (Figure 4a). To estimate the relative importance of selective and non-selective sorption in every sample, we compared the cumulative compositional change (Figure 4a) to the sorbed organic carbon percentage (Table 1). If the compositional changes appeared to comprise the primary share of the sorbed organic carbon, then selective sorption was deemed more important. If the compositional changes appeared to comprise a minor share of the sorbed organic carbon, then the opposite was true. On this basis, non-selective sorption was more important than selective sorption in every sample except the HiN fraction, notwithstanding the preferential sorption of aromatic and oxygen-rich DOM in every sample, as in previous studies [28–30]. This supports the zonal model [17], and the suggestion that no single binding mechanism can explain mineral-organic associations [18]. It also supports the suggestion that most DOM constituents can be stabilized in mineral-organic associations.

Other studies have reported multiple binding mechanisms and the sorption of various DOM components to cation-enriched clays. Polubesova et al. [35] used resin-based separation, TOC analysis, UV absorbance spectroscopy, and Fourier transform infrared (FT-IR) analysis with batch equilibrium experiments to examine the sorption of anthropogenic DOM to Cu(II)-montmorillonite, Fe(III)-montmorillonite, and crude montmorillonite. For all clays, the HoN fraction sorbed more than the HoA fraction, and both fractions sorbed to the montmorillonite in the following order: Fe(III)-montmorillonite > Cu(II)-montmorillonite > crude montmorillonite. Sorption of the HoN fraction was attributed to higher hydrophobicity, and sorption of the HoA fraction to the Fe(III)-montmorillonite was attributed to a combination of ligand exchange, van der Waals forces, and hydrogen bonding.

Similarly, Genest et al. [75] combined ^{1}H high resolution-magic angle spinning (HR-MAS) NMR spectroscopy with batch-equilibrium experiments to examine the sorption of forest soil DOM, Leonardite humic acid, and peat humic acid to Ca^{2+}-enriched kaolinite and montmorillonite. In addition, they used ^{1}H HR-MAS and solid state ^{13}C NMR spectroscopy to examine whole soils containing kaolinite and montmorillonite. The authors determined that long-chain aliphatic compounds preferentially sorbed to the Ca^{2+}-enriched kaolinite, and that a mixture of aliphatic components and proteins preferentially sorbed to the Ca^{2+}-enriched montmorillonite. In the whole soils, they observed aliphatic components, carbohydrates, and amino acids at the soil–water interface. However, when a more penetrating solvent was used, they also observed aromatic components, implying the existence of hydrophobic, surface-inaccessible domains. Like our study, these findings support the zonal model, and the suggestion that multiple DOM components can be stabilized in mineral-organic associations.

The importance of non-selective sorption is difficult to evaluate during qualitative analyses, which tend to focus on differences in DOM composition. However, the results from this study show that non-selective sorption can contribute substantially to the formation of mineral-organic associations, and thereby influence many soil organic matter functions.

4.5. Additional Environmental Relevance

The use of anthropogenic DOM in this study was environmentally relevant for two reasons. First, composted biosolids are regularly applied to agricultural lands to provide nutrients, enhance soil physical properties, and improve plant yield [76,77]. In the United States, it has been estimated that eight million tons of biosolids are produced each year, and that ~50% is land applied [78]. In addition, Zbytniewski and Buszewski [79] have reported that sewage sludge composting produces organic matter that is structurally similar to soil organic matter. Second, the anthropogenic DOM can serve as a proxy for microbial DOM, which is richer in nitrogen and sulfur-containing constituents than DOM from plant material [80]. In fact, the organic matter in biosolids includes bacterial biomass [81], which might explain the high CHNO content of the anthropogenic DOM.

In addition, the applied experimental conditions were environmentally relevant with respect to acid sulfate soils, which comprise more than 17 million hectares worldwide [82]. These soils form

when sulfide minerals oxidize, producing sulfuric acid and soil pH values < 4. Organic matter addition improves the energy supply for sulfate reducing bacteria, ameliorating the effect of sulfide oxidation, but this improvement depends on the availability of biodegradable organic matter [83,84]. In turn, this availability could be influenced by the formation of mineral-organic associations at low pH.

5. Conclusions

In this study, we combined Fourier transform ion cyclotron resonance mass spectrometry with novel data analysis techniques to examine the role of sorptive fractionation in associations between Fe(III)-montmorillonite and anthropogenic DOM. To examine the influence of DOM composition, we used resin-based separation to produce DOM subsamples with different molecular compositions and chemical properties. A large proportion (45 to 64%) of the initial carbon in every DOM solution sorbed to the Fe(III)-montmorillonite, but each structural fraction sorbed to a different extent, indicating that the amount of sorbed organic carbon depends on DOM composition. Every sample also exhibited sorptive fractionation, and the degree of sorptive fractionation varied, indicating that the strength of sorptive fractionation also depends on DOM composition. Finally, non-selective sorption was more important than selective sorption in every sample except the hydrophilic neutral (HiN) fraction, where high nitrogen content and acidic conditions appeared to enhance sorptive fractionation. This suggests that non-selective sorption can substantially contribute to the formation of mineral-organic associations, and thereby influence a variety of soil organic matter functions.

Supplementary Materials: The following materials are available online at www.mdpi.com/2571-8789/2/1/14/s1: Table S1: Summary statistics for Common Formula assignments; Table S2: Distribution of Common Formulas among van Krevelen plot regions; Table S3: Distribution of Common Formulas among elemental classes; Figure S1: Representative mass spectra for the original and sorbed anthropogenic DOM, before and after exclusion of the surfactant-like series; Figure S2: Distribution of Common Formulas among the quartiles illustrated in Figure 1; Figure S3: Scheme for determining the van Krevelen plot regions; Figure S4: Bar plots demonstrating Common Formula abundances in the van Krevelen plot regions relative to the anthropogenic DOM; Figure S5: Venn diagram illustrating shared Common Formula assignments; Figures S6 through S9: van Krevelen diagrams for each sample illustrating the Common Formulas that were more abundant in the original DOM solutions, and more abundant in their sorbed organic matter extracts, as a function of elemental composition; Figure S10: Bar plots illustrating the status (sorbed or unbound) of the ionizable CHNO content in the HiN fraction as a function of nitrogen and oxygen content.

Acknowledgments: This research was supported by research grants from the U.S. National Science Foundation (grant nos. 1451508 and 1512670), the Israel Science Foundation (grant no. 102/14) and the United States—Israel Binational Agricultural Research and Development Fund (grant nos. US-4551-12 and US-4656-13). The National High Magnetic Field Laboratory is supported by the National Science Foundation Division of Materials Research through DMR-1157490, Florida State University, and the State of Florida.

Author Contributions: B.C., T.B. and T.P. conceived and designed the sorption experiments; S.A.-K. performed the sorption experiments; R.B.Y., A.M.M., H.C. and S.A.-K performed the FT-ICR MS analysis; R.B.Y., A.M.M., H.C., W.B. and S.A.-K. analyzed the data; R.B.Y. and S.A.-K. co-wrote the paper.

Conflicts of Interest: The authors declare no conflict of interest.

References

1. Keiluweit, M.; Nico, P.S.; Kleber, M.; Fendorf, S. Are oxygen limitations under recognized regulators of organic carbon turnover in upland soils? *Biogeochemistry* **2016**, *127*, 157–171. [CrossRef]
2. Boye, K.; Noël, V.; Tfaily, M.M.; Bone, S.E.; Williams, K.H.; Bargar, J.; Fendorf, S. Thermodynamically controlled preservation of organic carbon in floodplains. *Nat. Geosci.* **2017**, *10*, 415–419. [CrossRef]
3. Young, I.M.; Crawford, J.W. Interactions and self-organization in the soil-microbe complex. *Science* **2004**, *304*, 1634–1637. [CrossRef] [PubMed]
4. Lehmann, J.; Kleber, M. The contentious nature of soil organic matter. *Nature* **2015**, *528*, 60–68. [CrossRef] [PubMed]
5. Sparks, D.L. *Environmental Soil Chemistry*; Academic Press: San Diego, CA, USA, 2002.

6. Luthy, R.G.; Aiken, G.R.; Brusseau, M.L.; Cunningham, S.D.; Gschwend, P.M.; Pignatello, J.J.; Reinhard, M.; Traina, S.J.; Weber, W.J.; Westall, J.C. Sequestration of hydrophobic organic contaminants by geosorbents. *Environ. Sci. Technol.* **1997**, *31*, 3341–3347. [CrossRef]
7. Miltner, A.; Bombach, P.; Schmidt-Brucken, B.; Kastner, M. SOM genesis: Microbial biomass as a significant source. *Biogeochemistry* **2012**, *111*, 41–55. [CrossRef]
8. Kallenbach, C.M.; Frey, S.D.; Grandy, A.S. Direct evidence for microbial-derived soil organic matter formation and its ecophysiological controls. *Nat. Commun.* **2016**, *7*, 13630. [CrossRef] [PubMed]
9. Hertkorn, N.; Frommberger, M.; Witt, M.; Koch, B.P.; Schmitt-Kopplin, P.; Perdue, E.M. Natural organic matter and the event horizon of mass spectrometry. *Anal. Chem.* **2008**, *80*, 8908–8919. [CrossRef] [PubMed]
10. Kaiser, K.; Kalbitz, K. Cycling downwards—Dissolved organic matter in soils. *Soil Biol. Biochem.* **2012**, *52*, 29–32. [CrossRef]
11. Nebbioso, A.; Piccolo, A. Molecular characterization of dissolved organic matter (DOM): A critical review. *Anal. Bioanal. Chem.* **2013**, *405*, 109–124. [CrossRef] [PubMed]
12. Kogel-Knabner, I.; Guggenberger, G.; Kleber, M.; Kandeler, E.; Kalbitz, K.; Scheu, S.; Eusterhues, K.; Leinweber, P. Organo-mineral associations in temperate soils: Integrating biology, mineralogy, and organic matter chemistry. *J. Plant Nutr. Soil Sci-Z. Pflanzenernahr. Bodenkund.* **2008**, *171*, 61–82. [CrossRef]
13. Kleber, M.; Eusterhues, K.; Keiluweit, M.; Mikutta, C.; Mikutta, R.; Nico, P.S. Mineral-organic associations: Formation, properties, and relevance in soil environments. In *Advances in Agronomy*; Sparks, D.L., Ed.; Elsevier Academic Press Inc.: San Diego, CA, USA, 2015; Volume 130, pp. 1–140.
14. Scott, E.E.; Rothstein, D.E. The dynamic exchange of dissolved organic matter percolating through six diverse soils. *Soil Biol. Biochem.* **2014**, *69*, 83–92. [CrossRef]
15. Eusterhues, K.; Rennert, T.; Knicker, H.; Kogel-Knabner, I.; Totsche, K.U.; Schwertmann, U. Fractionation of organic matter due to reaction with ferrihydrite: Coprecipitation versus adsorption. *Environ. Sci. Technol.* **2011**, *45*, 527–533. [CrossRef] [PubMed]
16. Chen, C.M.; Dynes, J.J.; Wang, J.; Sparks, D.L. Properties of Fe-organic matter associations via coprecipitation versus adsorption. *Environ. Sci. Technol.* **2014**, *48*, 13751–13759. [CrossRef] [PubMed]
17. Kleber, M.; Sollins, P.; Sutton, R. A conceptual model of organo-mineral interactions in soils: Self-assembly of organic molecular fragments into zonal structures on mineral surfaces. *Biogeochemistry* **2007**, *85*, 9–24. [CrossRef]
18. Solomon, D.; Lehmann, J.; Harden, J.; Wang, J.; Kinyangi, J.; Heymann, K.; Karunakaran, C.; Lu, Y.S.; Wirick, S.; Jacobsen, C. Micro- and nano-environments of carbon sequestration: Multi-element STXM-NEXAFS spectromicroscopy assessment of microbial carbon and mineral associations. *Chem. Geol.* **2012**, *329*, 53–73. [CrossRef]
19. Chasse, A.W.; Ohno, T.; Higgins, S.R.; Amirbahman, A.; Yildirim, N.; Parr, T.B. Chemical force spectroscopy evidence supporting the layer-by-layer model of organic matter binding to iron (oxy)hydroxide mineral surfaces. *Environ. Sci. Technol.* **2015**, *49*, 9733–9741. [CrossRef] [PubMed]
20. Masoom, H.; Courtier-Murias, D.; Farooq, H.; Soong, R.; Kelleher, B.P.; Zhang, C.; Maas, W.E.; Fey, M.; Kumar, R.; Monette, M.; et al. Soil organic matter in its native state: Unravelling the most complex biomaterial on Earth. *Environ. Sci. Technol.* **2016**, *50*, 1670–1680. [CrossRef] [PubMed]
21. Vogel, C.; Mueller, C.W.; Hoschen, C.; Buegger, F.; Heister, K.; Schulz, S.; Schloter, M.; Kogel-Knabner, I. Submicron structures provide preferential spots for carbon and nitrogen sequestration in soils. *Nat. Commun.* **2014**, *5*, 7. [CrossRef] [PubMed]
22. Six, J.; Conant, R.T.; Paul, E.A.; Paustian, K. Stabilization mechanisms of soil organic matter: Implications for C-saturation of soils. *Plant Soil* **2002**, *241*, 155–176. [CrossRef]
23. Guggenberger, G.; Kaiser, K. Dissolved organic matter in soil: Challenging the paradigm of sorptive preservation. *Geoderma* **2003**, *113*, 293–310. [CrossRef]
24. Chorover, J.; Amistadi, M.K. Reaction of forest floor organic matter at goethite, birnessite and smectite surfaces. *Geochim. Cosmochim. Acta* **2001**, *65*, 95–109. [CrossRef]
25. Feng, X.J.; Simpson, A.J.; Simpson, M.J. Chemical and mineralogical controls on humic acid sorption to clay mineral surfaces. *Org. Geochem.* **2005**, *36*, 1553–1566. [CrossRef]
26. Kramer, M.G.; Sanderman, J.; Chadwick, O.A.; Chorover, J.; Vitousek, P.M. Long-term carbon storage through retention of dissolved aromatic acids by reactive particles in soil. *Glob. Chang. Biol.* **2012**, *18*, 2594–2605. [CrossRef]

27. Mitchell, P.J.; Simpson, A.J.; Soong, R.; Oren, A.; Chefetz, B.; Simpson, M.J. Solution-state NMR investigation of the sorptive fractionation of dissolved organic matter by alkaline mineral soils. *Environ. Chem.* **2013**, *10*, 333–340. [CrossRef]
28. Fleury, G.; Del Nero, M.; Barillon, R. Effect of mineral surface properties (alumina, kaolinite) on the sorptive fractionation mechanisms of soil fulvic acids: Molecular-scale ESI-MS studies. *Geochim. Cosmochim. Acta* **2017**, *196*, 1–17. [CrossRef]
29. Lv, J.; Zhang, S.; Wang, S.; Luo, L.; Cao, D.; Christie, P. Molecular-scale investigation with ESI-FT-ICR-MS on fractionation of dissolved organic matter induced by adsorption on iron oxyhydroxides. *Environ. Sci. Technol.* **2016**, *50*, 2328–2336. [CrossRef] [PubMed]
30. Avneri-Katz, S.; Young, R.B.; Mckenna, A.M.; Chen, H.; Corilo, Y.E.; Polubesova, T.; Borch, T.; Chefetz, B. Adsorptive fractionation of dissolved organic matter (DOM) by mineral soil: Macroscale approach and molecular insight. *Org. Geochem.* **2017**, *103*, 113–124. [CrossRef]
31. Minor, E.C.; Steinbring, C.J.; Longnecker, K.; Kujawinski, E.B. Characterization of dissolved organic matter in Lake Superior and its watershed using ultrahigh resolution mass spectrometry. *Org. Geochem.* **2012**, *43*, 1–11. [CrossRef]
32. Chefetz, B.; Hatcher, P.G.; Hadar, Y.; Chen, Y.N. Characterization of dissolved organic matter extracted from composted municipal solid waste. *Soil Sci. Soc. Am. J.* **1998**, *62*, 326–332. [CrossRef]
33. Chefetz, B.; Illani, T.; Schulz, E.; Chorover, J. Wastewater dissolved organic matter: Characteristics and sorptive capabilities. *Water Sci. Technol.* **2006**, *53*, 51–57. [CrossRef] [PubMed]
34. Von Lutzow, M.; Kogel-Knabner, I.; Ekschmitt, K.; Matzner, E.; Guggenberger, G.; Marschner, B.; Flessa, H. Stabilization of organic matter in temperate soils: Mechanisms and their relevance under different soil conditions—A review. *Eur. J. Soil Sci.* **2006**, *57*, 426–445. [CrossRef]
35. Polubesova, T.; Chen, Y.; Navon, R.; Chefetz, B. Interactions of hydrophobic fractions of dissolved organic matter with $Fe^{(3+)}$- and $Cu^{(2+)}$-montmorillonite. *Environ. Sci. Technol.* **2008**, *42*, 4797–4803. [CrossRef] [PubMed]
36. Olshansky, Y.; Polubesova, T.; Chefetz, B. Reconstitution of cutin monomers on smectite surfaces: Adsorption and esterification. *Geoderma* **2014**, *232*, 406–413. [CrossRef]
37. Schwertmann, U. Solubility and dissolution of iron oxides. *Plant Soil* **1991**, *130*, 1–25. [CrossRef]
38. Stefánsson, A. Iron(III) hydrolysis and solubility at 25 °C. *Environ. Sci. Technol.* **2007**, *41*, 6117–6123. [CrossRef] [PubMed]
39. Moretti, S.M.L.; Bertoncini, E.I.; Abreu, C.H. Composting sewage sludge with green waste from tree pruning. *Sci. Agricola* **2015**, *72*, 432–439. [CrossRef]
40. Yanez, R.; Alonso, J.L.; Diaz, M.J. Influence of bulking agent on sewage sludge composting process. *Bioresour. Technol.* **2009**, *100*, 5827–5833. [CrossRef] [PubMed]
41. Amery, F.; Vanmoorleghem, C.; Smolders, E. Adapted DAX-8 fractionation method for dissolved organic matter (DOM) from soils: Development, calibration with test components and application to contrasting soil solutions. *Eur. J. Soil Sci.* **2009**, *60*, 956–965. [CrossRef]
42. Dittmar, T.; Koch, B.; Hertkorn, N.; Kattner, G. A simple and efficient method for the solid-phase extraction of dissolved organic matter (SPE-DOM) from seawater. *Limnol. Oceanogr.-Methods* **2008**, *6*, 230–235. [CrossRef]
43. Li, Y.; Harir, M.; Lucio, M.; Kanawati, B.; Smirnov, K.; Flerus, R.; Koch, B.P.; Schmitt-Kopplin, P.; Hertkorn, N. Proposed guidelines for solid phase extraction of Suwannee River dissolved organic matter. *Anal. Chem.* **2016**, *88*, 6680–6688. [CrossRef] [PubMed]
44. Kaiser, N.K.; Quinn, J.P.; Blakney, G.T.; Hendrickson, C.L.; Marshall, A.G. A novel 9.4 Tesla FTICR mass spectrometer with improved sensitivity, mass resolution, and mass range. *J. Am. Soc. Mass Spectrom.* **2011**, *22*, 1343–1351. [CrossRef] [PubMed]
45. Blakney, G.T.; Hendrickson, C.L.; Marshall, A.G. Predator data station: A fast data acquisition system for advanced FT-ICR MS experiments. *Int. J. Mass Spectrom.* **2011**, *306*, 246–252. [CrossRef]
46. Senko, M.W.; Hendrickson, C.L.; Emmett, M.R.; Shi, S.D.H.; Marshall, A.G. External accumulation of ions for enhanced electrospray ionization Fourier transform ion cyclotron resonance mass spectrometry. *J. Am. Soc. Mass Spectrom.* **1997**, *8*, 970–976. [CrossRef]
47. Kaiser, N.K.; Savory, J.J.; Mckenna, A.M.; Quinn, J.P.; Hendrickson, C.L.; Marshall, A.G. Electrically compensated Fourier transform ion cyclotron resonance cell for complex mixture mass analysis. *Anal. Chem.* **2011**, *83*, 6907–6910. [CrossRef] [PubMed]

48. Tolmachev, A.V.; Robinson, E.W.; Wu, S.; Kang, H.; Lourette, N.M.; Pasa-Tolic, L.; Smith, R.D. Trapped-ion cell with improved DC potential harmonicity for FT-ICR MS. *J. Am. Soc. Mass Spectrom.* **2008**, *19*, 586–597. [CrossRef] [PubMed]
49. Xian, F.; Hendrickson, C.L.; Blakney, G.T.; Beu, S.C.; Marshall, A.G. Automated broadband phase correction of Fourier transform ion cyclotron resonance mass spectra. *Anal. Chem.* **2010**, *82*, 8807–8812. [CrossRef] [PubMed]
50. Shi, S.D.H.; Drader, J.J.; Freitas, M.A.; Hendrickson, C.L.; Marshall, A.G. Comparison and interconversion of the two most common frequency-to-mass calibration functions for Fourier transform ion cyclotron resonance mass spectrometry2. *Int. J. Mass Spectrom.* **2000**, *195–196*, 591–598. [CrossRef]
51. Ledford, E.B.; Rempel, D.L.; Gross, M.L. Space charge effects in Fourier transform mass spectrometry—MASS calibration. *Anal. Chem.* **1984**, *56*, 2744–2748. [CrossRef] [PubMed]
52. Savory, J.J.; Kaiser, N.K.; Mckenna, A.M.; Xian, F.; Blakney, G.T.; Rodgers, R.P.; Hendrickson, C.L.; Marshall, A.G. Parts-per-billion Fourier transform ion cyclotron resonance mass measurement accuracy with a "walking" calibration equation. *Anal. Chem.* **2011**, *83*, 1732–1736. [CrossRef] [PubMed]
53. Corilo, Y.E. *PetroOrg*; The Florida State University: Tallahassee, FL, USA, 2012.
54. Kendrick, E. A mass scale based on CH_2 = 14.0000 for high resolution mass spectrometry of organic compounds. *Anal. Chem.* **1963**, *35*. [CrossRef]
55. Hughey, C.A.; Hendrickson, C.L.; Rodgers, R.P.; Marshall, A.G.; Qian, K.N. Kendrick mass defect spectrum: A compact visual analysis for ultrahigh-resolution broadband mass spectra. *Anal. Chem.* **2001**, *73*, 4676–4681. [CrossRef] [PubMed]
56. Koch, B.P.; Dittmar, T. From mass to structure: An aromaticity index for high-resolution mass data of natural organic matter. *Rapid Commun. Mass Spectrom.* **2006**, *20*, 926–932. [CrossRef]
57. R Core Team. *R: A Language and Environment for Statistical Computing*; R Foundation for Statistical Computing: Vienna, Austria, 2017.
58. Le, S.; Josse, J.; Husson, F. FactoMineR: An R package for multivariate analysis. *J. Stat. Softw.* **2008**, *25*, 1–18. [CrossRef]
59. D'andrilli, J.; Cooper, W.T.; Foreman, C.M.; Marshall, A.G. An ultrahigh-resolution mass spectrometry index to estimate natural organic matter lability. *Rapid Commun. Mass Spectrom.* **2015**, *29*, 2385–2401. [CrossRef] [PubMed]
60. Kuhnert, N.; Dairpoosh, F.; Yassin, G.; Golon, A.; Jaiswal, R. What is under the hump? Mass spectrometry based analysis of complex mixtures in processed food—Lessons from the characterisation of black tea thearubigins, coffee melanoidines and caramel. *Food Funct.* **2013**, *4*, 1130–1147. [CrossRef] [PubMed]
61. Waggoner, D.C.; Chen, H.M.; Willoughby, A.S.; Hatcher, P.G. Formation of black carbon-like and alicyclic aliphatic compounds by hydroxyl radical initiated degradation of lignin. *Org. Geochem.* **2015**, *82*, 69–76. [CrossRef]
62. Hertkorn, N.; Ruecker, C.; Meringer, M.; Gugisch, R.; Frommberger, M.; Perdue, E.M.; Witt, M.; Schmitt-Kopplin, P. High-precision frequency measurements: Indispensable tools at the core of the molecular-level analysis of complex systems. *Anal. Bioanal. Chem.* **2007**, *389*, 1311–1327. [CrossRef] [PubMed]
63. Zhu, M.; Frandsen, C.; Wallace, A.F.; Legg, B.; Khalid, S.; Zhang, H.; Mørup, S.; Banfield, J.F.; Waychunas, G.A. Precipitation pathways for ferrihydrite formation in acidic solutions. *Geochim. Cosmochim. Acta* **2016**, *172*, 247–264. [CrossRef]
64. Gu, B.H.; Schmitt, J.; Chen, Z.H.; Liang, L.Y.; Mccarthy, J.F. Adsorption and desorption of natural organic matter on iron oxide—Mechanisms and models. *Environ. Sci. Technol.* **1994**, *28*, 38–46. [CrossRef] [PubMed]
65. Brunner, P.H.; Capri, S.; Marcomini, A.; Giger, W. Occurrence and behavior of linear alkulbenzenesulfonates, nonylphenol, nonylphenol monophenol and nonylphenol diethoxylates in sewage and sewage sludge treatment. *Water Res.* **1988**, *22*, 1465–1472. [CrossRef]
66. Gonsior, M.; Zwartjes, M.; Cooper, W.J.; Song, W.; Ishida, K.P.; Tseng, L.Y.; Jeung, M.K.; Rosso, D.; Hertkorn, N.; Schmitt-Kopplin, P. Molecular characterization of effluent organic matter identified by ultrahigh resolution mass spectrometry. *Water Res.* **2011**, *45*, 2943–2953. [CrossRef] [PubMed]
67. Cantarero, S.; Prieto, C.A.; Lopez, I. Occurrence of high-tonnage anionic surfactants in Spanish sewage sludge. *J. Environ. Manag.* **2012**, *95*, S149–S153. [CrossRef] [PubMed]

68. Schymanski, E.L.; Singer, H.P.; Longree, P.; Loos, M.; Ruff, M.; Stravs, M.A.; Vidal, C.R.; Hollender, J. Strategies to characterize polar organic contamination in wastewater: Exploring the capability of high resolution mass spectrometry. *Environ. Sci. Technol.* **2014**, *48*, 1811–1818. [CrossRef] [PubMed]
69. Knorr, K.H. DOC-dynamics in a small headwater catchment as driven by redox fluctuations and hydrological flow paths—Are DOC exports mediated by iron reduction/oxidation cycles? *Biogeosciences* **2013**, *10*, 891–904. [CrossRef]
70. Tombacz, E.; Libor, Z.; Illes, E.; Majzik, A.; Klumpp, E. The role of reactive surface sites and complexation by humic acids in the interaction of clay mineral and iron oxide particles. *Org. Geochem.* **2004**, *35*, 257–267. [CrossRef]
71. Arnarson, T.S.; Keil, R.G. Mechanisms of pore water organic matter adsorption to montmorillonite. *Mar. Chem.* **2000**, *71*, 309–320. [CrossRef]
72. Leenheer, J.A.; Wershaw, R.L.; Reddy, M.M. Strong-acid, carboxyl group structures in fulvic acid from the Suwannee River, Georgia. 1. Minor structures. *Environ. Sci. Technol.* **1995**, *29*, 393–398. [CrossRef] [PubMed]
73. Leenheer, J.A.; Wershaw, R.L.; Reddy, M.M. Strong-acid, carboxyl group structures in fulvic acid from the Suwannee River, Georgia. 2. Major structures. *Environ. Sci. Technol.* **1995**, *29*, 399–405. [CrossRef] [PubMed]
74. Bingham, A.H.; Cotrufo, M.F. Organic nitrogen storage in mineral soil: Implications for policy and management. *Sci. Total Environ.* **2016**, *551–552*, 116–126. [CrossRef] [PubMed]
75. Genest, S.C.; Simpson, M.J.; Simpson, A.J.; Soong, R.; Mcnally, D.J. Analysis of soil organic matter at the solid-water interface by nuclear magnetic resonance spectroscopy. *Environ. Chem.* **2014**, *11*, 472–482. [CrossRef]
76. Kinney, C.A.; Furlong, E.T.; Zaugg, S.D.; Burkhardt, M.R.; Werner, S.L.; Cahill, J.D.; Jorgensen, G.R. Survey of organic wastewater contaminants in biosolids destined for land application. *Environ. Sci. Technol.* **2006**, *40*, 7207–7215. [CrossRef] [PubMed]
77. Cogger, C.G.; Forge, T.A.; Neilsen, G.H. Biosolids recycling: Nitrogen management and soil ecology. *Can. J. Soil Sci.* **2006**, *86*, 613–620. [CrossRef]
78. Gray, J.L.; Borch, T.; Furlong, E.T.; Davis, J.G.; Yager, T.J.; Yang, Y.Y.; Kolpin, D.W. Rainfall-runoff of anthropogenic waste indicators from agricultural fields applied with municipal biosolids. *Sci. Total Environ.* **2017**, *580*, 83–89. [CrossRef] [PubMed]
79. Zbytniewski, R.; Buszewski, B. Characterization of natural organic matter (NOM) derived from sewage sludge compost. Part 1: Chemical and spectroscopic properties. *Bioresour. Technol.* **2005**, *96*, 471–478. [CrossRef] [PubMed]
80. D'andrilli, J.; Foreman, C.M.; Marshall, A.G.; Mcknight, D.M. Characterization of IHSS Pony Lake fulvic acid dissolved organic matter by electrospray ionization Fourier transform ion cyclotron resonance mass spectrometry and fluorescence spectroscopy. *Org. Geochem.* **2013**, *65*, 19–28. [CrossRef]
81. Jardé, E.; Mansuy, L.; Faure, P. Organic markers in the lipidic fraction of sewage sludges. *Water Res.* **2005**, *39*, 1215–1232. [CrossRef] [PubMed]
82. Ljung, K.; Maley, F.; Cook, A.; Weinstein, P. Acid sulfate soils and human health—A Millennium Ecosystem Assessment. *Environ. Int.* **2009**, *35*, 1234–1242. [CrossRef] [PubMed]
83. Jayalath, N.; Mosley, L.M.; Fitzpatrick, R.W.; Marschner, P. Addition of organic matter influences pH changes in reduced and oxidised acid sulfate soils. *Geoderma* **2016**, *262*, 125–132. [CrossRef]
84. Kolbl, A.; Marschner, P.; Fitzpatrick, R.; Mosley, L.; Kogel-Knabner, I. Linking organic matter composition in acid sulfate soils to pH recovery after re-submerging. *Geoderma* **2017**, *308*, 350–362. [CrossRef]

Appendix F: Co-author contributions to Insecticide Spatial Distribution Study

Reprinted from Rehberg, R. A.; Trivedi, P.; Bahureksa, W.; Sharp, J. L.; Stokes, S. C.; Menger, R. F.; Borch, T. Quantification of Insecticide Spatial Distribution within Individual Citrus Trees and Efficacy through Asian Citrus Psyllid Reductions under Different Application Methods. *Pest Manag. Sci.* **2021**, *77* (4), 1748–1756.

My co-author contributions towards this work included data processing, visualization, investigation, and writing/reviewing/editing.

Research Article

Received: 14 September 2020 Revised: 17 November 2020 Accepted article published: 24 November 2020 Published online in Wiley Online Library: 24 December 2020

(wileyonlinelibrary.com) DOI 10.1002/ps.6195

Quantification of insecticide spatial distribution within individual citrus trees and efficacy through Asian citrus psyllid reductions under different application methods

Rachelle A Rehberg,[a] Pankaj Trivedi,[b] William Bahureksa,[a] Julia L Sharp,[c] Sean C Stokes,[d] Ruth F Menger[a] and Thomas Borch[a,d*]

Abstract

BACKGROUND: Citrus greening disease (Huanglongbing, HLB) has infected >90% of Florida's oranges and thus growers are desperate to improve pest management strategies. In this field study, insecticide application efficacy was investigated with liquid chromatography mass spectrometry to determine if insecticide concentration and distribution were effective at killing the target pest Asian citrus psyllids (ACP). Sample discs attached to leaves were sprayed with imidacloprid and malathion at a field site in Florida. Application method, canopy height and depth, cardinal side of tree, and leaf side were considered to assess the spatial distribution of insecticides throughout citrus trees. Furthermore, ACP were inspected before and after insecticide applications to quantify psyllid population response.

RESULTS: Our findings show that although insecticide concentrations were high enough to kill ACP, the spatial distribution of insecticides throughout individual trees was highly variable and live ACP were detected after insecticide application. The top side of leaves received significantly more insecticide than the underside of leaves. Additionally, inadequate distribution to different areas of the tree canopy was observed for all application methods tested (aerial, ground speed-sprayer, and ground side-sprayer). Inspections of ACP populations before and after insecticide applications resulted in reductions of 85% (malathion) and 48–80% (imidacloprid).

CONCLUSIONS: The variability in insecticide spatial distribution due to application method allows remaining ACP to continue spreading citrus greening disease to unprotected trees. Further research is needed to improve insecticide application methods and technology for citrus trees in order to implement effective pest management strategies and fully target ACP to eliminate HLB.

Supporting information may be found in the online version of this article.

Keywords: Huanglongbing; *Candidatus* Liberibacter asiaticus (CLas); citrus greening disease; pesticide efficacy; *Diaphorina citri* Kuwayama; pest management

1 INTRODUCTION

Citrus greening disease, or Huanglongbing (HLB), continues to spread throughout citrus groves globally, plummeting citrus production and profits. Brazil, China and the United States (US), the largest citrus producers worldwide, are struggling the most with devastation to the citrus industry due to HLB.[1, 2] Since detection in Florida in 2005, citrus production has decreased by 74%.[3, 4] As one of the largest citrus-producing states in the US, Florida has experienced a decline of about 5000 jobs and $1 billion annually since 2015.[2, 5, 6] HLB causes citrus trees to develop weakened root systems, discolored leaves, and greener fruit that prematurely falls off the tree, leading to lower crop yields.[7, 8] Chemical changes in fruit due to HLB infection results in distinctly bitter juice that lacks sweetness and fruity/orange flavor.[6]

* *Correspondence to: T Borch, Department of Soil and Crop Sciences, Colorado State University, 1170 Campus Delivery, Fort Collins, CO 80523, USA. E-mail: thomas.borch@colostate.edu*

a *Department of Chemistry, Colorado State University, Fort Collins, CO, USA*

b *Department of Agricultural Biology, Colorado State University, Fort Collins, CO, USA*

c *Department of Statistics, Colorado State University, Fort Collins, CO, USA*

d *Department of Soil and Crop Sciences, Colorado State University, Fort Collins, CO, USA*

The causative agent of HLB in the US, *Candidatus* Liberibacter asiaticus (CLas) is vectored in fields by the Asian citrus psyllid (ACP) *Diaphorina citri* Kuwayama as it feeds on the citrus phloem.[8] Currently no cure exists for HLB despite several research efforts of potential treatments and management strategies.[2] Insecticides are widely used to control ACP populations and prevent further spread of the disease.[7, 9, 10]In order to halt transmission of HLB, effective insecticides must quickly kill ACP or interrupt the feeding processes by which they infect the phloem.[11] Since ACP prefer new flush,[11] or new foliar growth, effort is made to have full coverage of insecticides to the outermost parts of the tree; and spraying prior to new flush growth is critical in managing ACP populations to prevent reproduction.[7, 10] In addition, it is recommended to apply insecticides in rotation to citrus groves in order to prevent insect resistance.[7] This rotation is determined from alternating chemical classes, modes of action, and recommended application types.

The most practiced management techniques involve combining systemic drenching on younger trees with foliar applications to quickly kill ACP. Newer management strategies include removing infected trees and implementing area-wide management, coordinating spraying 10–50 thousand-acre areas in order to combat the spread of ACP from 'bad neighbors'[9, 12] with less frequent management practices.[9, 12] Overall, insecticide application is an expensive HLB management strategy that has significantly increased in cost due to HLB.[13] Additionally, with insecticide costs around 25% of total citrus production, and increasing with current ACP infestation rates, the area of insecticide application has a lot of potential for optimization.[14]

Previous studies have evaluated the spatial distribution of insecticides when applied at different application rates, sprayer types, spray volumes and droplet sizes, ground speed, and weather conditions in the laboratory and field, often using water sensitive papers or fluorescent dyes.[14–17] Currently, the most common ways to assess insecticide coverage to crops in the field is to implement fluorescent dyes or water-sensitive papers that change color when contacted with water. Water-sensitive papers and dyes allow growers to visually see the sprayed droplets on a leaf.[18] This presence of dye or color change is assumed to translate to the presence of insecticide.[14, 19–21] Citrus trees have large total foliar surface areas[20] and leaves are often wet in humid environments, like Florida's conditions. Therefore, distributing large water-sensitive papers throughout a wet citrus tree often results in misrepresentations of insecticide presence.[18] Some studies investigated spatial distribution in more depth, exploring canopy penetration to a variety of crops including wheat, peppers, onion, tomatoes, oat, and bay laurel. These spatial distribution results of insecticides may be especially inadequate for citrus trees due to their larger canopies and total foliar surface area.[22–26] Few studies have investigated canopy penetration in citrus with metal or fluorescent tracers and have reported that outer canopy receives more spray deposition than inner canopy regions.[14, 20, 27, 28] Therefore, inner canopy leaves could risk receiving an inadequate amount of insecticide necessary to target ACP populations.[14] These studies have not fully investigated all aspects of a citrus tree, including the side of the leaf, which is critical to consider when investigating different kinds of insecticides (contact or systemic) and their application approach. Most studies have not quantified insecticide active ingredient (a.i.) concentrations in sprayer tank mixtures and on leaves while simultaneously inspecting ACP population responses by, for instance, mass spectrometry, which provides more accurate quantification.[13–16, 19–21] Due to volatilization or degradation, the insecticide a.i. concentration could become too low to kill ACP or prevent pest resistance.

Previous studies investigating ACP response to insecticides in the laboratory and field conclude that insecticides are effective at killing psyllids.[11, 29–34] The few studies assessing both insecticide application efficacy with ACP inspections either lacked the variety of application methods commonly used in high management groves or an effective ACP inspection method.[11, 29–31] To date, no studies have thoroughly examined insecticide efficacy by quantifying insecticide concentrations and spatial distribution, extensively sampling entire citrus trees while simultaneously quantifying ACP population response, from multiple insecticide spray methods in a high-management commercial field.

It is clear how insecticides should be applied, kill target pests, and impact ACP at specific concentrations in laboratory studies.[14–17] However, it is not yet known how well insecticides actually distribute and kill ACP among multiple application methods and insecticides when applied to citrus trees in the field. Our objective was to evaluate insecticide application effectiveness by quantifying the concentration and distribution of insecticides applied and their resulting ACP population counts before and after various foliar application methods. We hypothesized that the concentrations of insecticides applied would be high enough to kill ACP, but the spatial distribution would be inconsistent due to larger citrus canopies.

2 MATERIALS AND METHODS

The following methods were used in order to collect and analyze field samples. Our goal was to effectively sample trees to quantify both the concentration of insecticide active ingredients and ACP present throughout citrus trees after application to better understand the coverage and effectiveness of the insecticides applied.

2.1 Sample site and collection

Two field studies were conducted at a citrus grove in Venus, FL, USA in October 2018 and July 2019. This large-scale and high-management grove is 8567 acres and consists of ~60 blocks of citrus trees (Fig. S1). The ambient grove weather conditions (from a weather station on site) range from 29 to 33° C with an average of 81 to 185 mm of rainfall (in October and July, respectively), with wind typically blowing from East to West.

Pilot experiments were performed to test various chemical and inexpensive sorbent materials for samplers as well as methods of attaching samplers to the citrus leaves and trees. After optimizing sampling materials and methods, it was observed that laser-cut Whatman filter (WF) discs clipped to the tops and bottoms of citrus leaf surfaces with mini binder clips (9/16″) were the most effective and representative method for field sampling of insecticide residues. The WF sampling discs were precut from WF paper #1 with an Epilog Zing CO_2 laser (Fort Collins, CO, US) cutter into 47-mm diameter circles, including sample number labels. The cardinal-direction side of the tree, canopy depth and height, and side of the leaf were examined. The WF discs were labeled and attached in specific sampling locations to best encompass the entire tree equally. The labeling scheme included four letters for the four location identifiers (Fig. 1).

(1) Cardinal direction: North (N), South (S), East (E) or West (W)
(2) Canopy depth: outer (O) or inner (I)
(3) Canopy height: upper (U), middle (M) or lower (L))
(4) Side of leaf: top (T) or bottom (B)

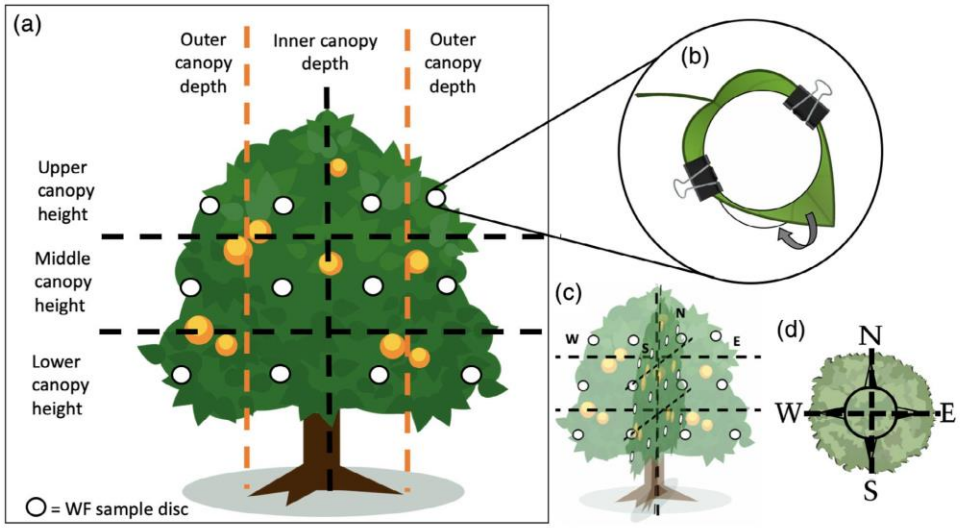

Figure 1. Tree location labeling scheme for field sampling. Trees were divided to investigate canopy depth (inner and outer) and height (upper, middle, and lower) (A). Each sample location had a WF paper disc attached on the top and bottom of a leaf in each canopy height and depth section (B), along with this scheme repeated on each cardinal side of the tree (North, South, East and West) (C). The top view looking down upon the tree is shown (D) to better understand where samples were located within the tree. This scheme generated 48 samples plus 3 field blank samples per tree ($n = 255$ samples per block test). Example of labeling: NUOT = North side, upper-outer canopy, top side of leaf.

Field study #1: In October 2018, five trees were sampled for both ages of trees (old *versus* young) (3 and 1 year old, respectively) and application type (aerial *versus* ground spray) for a total of 20 trees (Figs S1, S2, Table S1). The tree canopy sizes are about 1.1 m × 1.4 m (1 year) and 1.4 m × 1.7 m (3 year). Tree age was provided by our industry partner and identified by sprayer type; ground sprayed with a speed (older) or side (young) sprayer (Fig. S3, Table S1, Text S1). Trees around 2 -years-old and younger are typically small enough to be sprayed with the side sprayer (Fig. S4). Field blanks were also collected for each tree by exposing the WF discs to the air and leaves on their respective tree and storing them in the freezer prior to insecticide application. Three field blanks and 48 samples were collected per tree, totaling 1,020 samples collected altogether for the four age (old *versus* young) and application type (ground *versus* aerial) combination block tests (Table S1). All samples were collected within 30 min after application, stored separately in Ziploc bags and foil, and stored in the freezer. Samples were shipped cold overnight from Florida to Colorado State University.

The insecticides, Admire (a.i. imidacloprid) and Malathion (a.i. malathion), were prepared per label instructions and applied via ground and aerial applications, respectively. Ground applications were carried out with side- and speed-sprayers to young (1-year-old) and old (3-years-old) citrus trees, respectively (Text S1, Table S1).

Tank mix samples from each insecticide mixture applied were collected to quantify the actual concentration of insecticide active ingredient applied to the samples collected. The tank mix solution was mechanically agitated for ≥10 min before sample collection to ensure proper mixing and homogeneity. Samples were collected by the certified pesticide handler in 40-mL amber vials with Teflon cap and stored at 4 °C.

Field Study #2: In July 2019, Admire and Malathion were applied via ground and aerial spraying along with ACP counting practices pre- and post-spray to compare insecticide applications with ACP reduction. Select sample locations from field study #1 were repeated to determine reproducibility. WF samples included 21 samples per block test (3 field blanks and 18 samples). Tank mix samples again were collected by the aforementioned method (Table S1).

2.2 ACP counting

The ACP data were obtained by a professional psyllid inspector in the grove. For each block test, 30 rows were inspected for ACP and sprayed with insecticide. ACP were inspected in three trees in each row (the North border, middle, and south border) totaling $n = 90$ trees inspected for each block test (Fig. S5). The inspector surveyed the entire tree, thoroughly counting ACP adults and nymphs. During the aerial application of malathion in field study #2, the pilot only sprayed rows 1–15, therefore only ACP data for rows #1–15 ($n = 45$ trees) were included for analysis. Psyllid inspectors counted ACP the day before and the day after insecticide application. All ACP counted post-application were confirmed as alive.

Along with the ACP counting methods performed prior to and post insecticide application, sticky traps (AlphaScents ACP Traps, 46.75 in^2 area) were implemented in order to benchmark our counting method (developed with our industry partner) with traditional sticky trap surveying methods. The sticky traps were attached with wire to the first, middle, and last trees in the 1st,

15th, and 30th rows each ($n = 9$ per block test). Sticky traps were exposed for 4 h then collected and inspected.

2.3 Chemicals and standards

Acetonitrile (ACN) and acetone (Thermo Fisher Scientific, Waltham, MA, USA) were used for sample preparation. The following insecticide standards were used for quantification of extraction recovery rates and field samples. Imidacloprid and malathion were purchased as neat materials (purity >98%) from Sigma-Aldrich (St Louis, MO, USA). Individual standard solutions containing 100 μg mL^{-1} imidacloprid or malathion in ACN were prepared for calibration standards and recovery tests. Eight calibration levels were prepared ranging from 0.001 to 20 μg mL^{-1} for each set of standards.

2.4 Sample preparation

The sample discs (WF) were rolled and inserted into 12-mL amber vials (Teflon cap liner), extracted with 10 mL ACN, and shaken at 170 rpm at 5 °C for 20 min (Text S2). Sample discs were removed from solution and 0.5-mL aliquots prepared in autosampler vials for instrumental analysis. Each tank mix sample was diluted with ACN in 10-mL volumetric flasks and prepared for liquid chromatography–tandem mass spectrometry (LC–MS/MS) analysis.

2.5 LC–MS/MS analysis

Sample analysis was carried out with a Waters Xevo UPLC–MS/MS triple quadrupole with MassLynx software for instrumental control and data acquisition. The instrument was operated in the positive ion electrospray mode. An Aquity UPLC BEH C18 column (1.7 μm), maintained at 40 °C, was used for chromatic separation. Mobile phase A consisted of LC–MS grade Optima water with 5% formic acid and mobile phase B was ACN. An elution was applied at a flow rate of 0.4 mL min^{-1} with a cycle time of 4 min. The sample injection volume was 1 μL. The electron spray ionization (ESI) source settings were as follows: desolvation temperature 300 °C; gas flow desolvation 800 L h^{-1} and cone 1 L h^{-1}; source temperature 150 °C; extractor 3 V; RF lens 2.5 V. Mass spectra were recorded in the *m/z* range of 50 to 1200. For imidacloprid: capillary 3.5 kV; cone 15 V; transition masses were 256 *m/z* for the parent ion, and 175 and 209 *m/z* for the quantifier and qualifier daughter product ions, respectively. Dwell time was 0.4 s with a collision energy of 12 V for both. For malathion: capillary 3 kV; cone 25 V; transition masses were 331 *m/z* for the parent ion, and 99 and 126.9 *m/z* for the quantifier and qualifier daughter product ions, respectively. The dwell time was 0.083 s with a collision energy of 10 V and 5 V for the 99 and 126.9 *m/z* masses, respectively (Text S3).

2.6 Method validation

Extraction recovery tests were performed by pipetting 50-μL droplets of 100 μg mL^{-1} standard onto five replicates of WF sample discs. The extraction recovery test samples were extracted and analyzed by the aforementioned method. Percent recoveries were calculated to be 73.6 and 94.5% for imidacloprid and malathion, respectively (Table S2).

Ten ACN blank samples were analyzed to determine limits of detection (LOD) and quantification (LOQ). For imidacloprid, the LOD and LOQ were both determined to be 0.001 μg mL^{-1} and the correlation coefficient was 0.999. For malathion, the LOD and LOQ were 0.007 and 0.01 μg mL^{-1} respectively with a correlation coefficient of 0.998 (Table S2).

2.7 Statistical analysis

Calibration curves, extraction recovery methods, and the sample area (17.35 cm^2) were taken into account to determine the concentration of insecticide present on each sample disc. Statistical analysis was conducted using the lmer function in the R/LMER4 package. Observations that were < LOQ and field blanks were removed before statistical analysis. Due to violation of the normality assumption, the log concentration was used for analysis. Concentrations of zero value were replaced with 0.0000001 prior to the log transformation. Summary statistics were calculated for the log concentration of each insecticide by the sampling location and application spray method. (Table S3). A mixed model analysis was utilized to compare canopy height, canopy depth, cardinal side of the tree, side of leaf, and application method and all two-way interactions (fixed effects) with individual leaf within tree as random effect for individual leaf within tree and tree to account for filters being attached to the top and bottom of the same leaf (i.e. measurements within a tree and on a leaf are correlated). Tukey's multiple comparison adjustment was used for all follow-up comparisons. A significance level of 0.05 was used for statistical significance in all analyses.

3 RESULTS AND DISCUSSION

3.1 Insecticide concentrations in the field

All insecticide tank mixture samples collected during field experiments were confirmed to have high enough (160–56, 900 μg mL^{-1} range) concentrations to kill ACP based on recommended mixing instructions provided by the manufacturer's product labels (Table S3).

3.2 Spatial distribution and application method impacts

3.2.1 Side of citrus leaf

Results of a.i. measured on the WF sample discs from various locations throughout the citrus trees and multiple insecticide applications reveal large variability in coverage within citrus trees of different canopy size and application method. The data especially show a large range in the amount of insecticide that contacts the top *versus* the bottom side of each leaf (Fig. 2). The top side of the leaf receives significantly more insecticide than the underside regardless of application method, canopy height, canopy depth

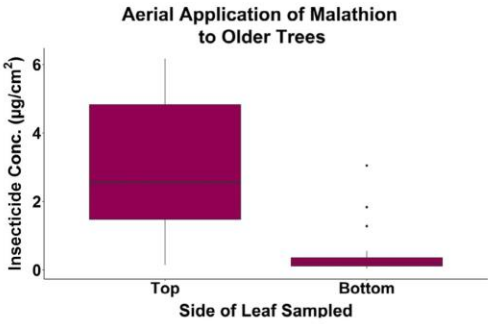

Figure 2. Concentration of Malathion (μg cm^{-2}) detected on aerially sprayed Whatman filter sample discs from the top and bottom sides of the leaf collected from various locations within a citrus tree. Data comprised of five older-aged tree replicates during the October 2018 field experiment ($n = 255$ samples). Additional top/bottom plots demonstrating trend in Figs S6–S8.

or cardinal side (Figs S6–S12, Table S3). This variation has a substantial impact on the insecticide's ability to effectively kill ACP, especially with contact insecticides.[7, 9, 35] Therefore, the ACP, which are primarily located on the underside of leaves, are less likely to be exposed to contact insecticides. However, the use of systemic insecticides that absorb into and throughout the entire leaf would expose ACP feeding anywhere on the leaf to the insecticide.[9, 36] This may help control ACP populations and limit reproduction over time, but still allows for ACP to transfer CLas and infect the tree with HLB in the short term because these modes of action are not immediately lethal to the ACP.[30]

Additionally, comparing imidacloprid concentrations on both sides of leaf between ground (side- and speed-sprayer) application methods revealed that bottom sides of leaves were not statistically different ($diff_{conc}$ = 0.01 μg cm^{-2}, diff = 0.39, P = 0.162), while top sides of leaves were statistically different ($diff_{conc}$ = 0.14 μg cm^{-2}, diff = 1, P < 0.001). Results also showed a greater difference between top and bottom leaf samples for the side-sprayer than the speed-sprayer ground application methods. The side-sprayer resulted in higher concentrations on top side of leaf samples (conc = 0.19 μg cm^{-2}) than the speed-sprayer (conc = 0.05 μg cm^{-2}), whereas the speed-sprayer produced higher concentrations on bottom side of leaf samples (conc = 0.03 μg cm^{-2}) than the side-sprayer (conc = 0.02 μg cm^{-2}). The speed-sprayer, with potentially lower nozzle alignment (Fig. S3) and a higher application pressure (Text S1), may allow for a more direct spray angle and disturbance of leaves during application to produce better coverage to both top and bottom sides of the leaf. Moreover, the design of each sprayer does impact the spray deposition onto citrus trees, with the side-sprayer covering the tops of leaves better and the speed-sprayer producing better coverage to the bottoms. This ultimately impacts the ability of insecticide applications to effectively control ACP populations and manage HLB disease.

3.2.2 *Citrus tree canopy depth and height*

There was large variability in the insecticide distribution with varying canopy depth, canopy height, and cardinal side of the tree (Fig. 3). Our results showed that outer canopy depth, and middle and upper canopy height regions of the tree receive more imidacloprid insecticide than inner and lower areas (Figs 3, S13–S15). For instance, the middle canopy heights sampled contained about 7 times higher concentrations on the outer canopy region (0.26 μg cm^{-2}) compared to the inner canopy region (0.04 μg cm^{-2}) for all cardinal sides [median differences (μg cm^{-2}): N = 2, S = 1.7, E = 0.3, W = 0.9] (Fig. 3). Statistically, outer canopy samples received three times more insecticide than inner canopy samples regardless of application method (concentration range 0.02–0.17 μg cm^{-2}, diff = 1.05, P < 0.001). This supports the proposition that citrus tree foliage hinders insecticide spray from penetrating through to inner canopy regions.

Furthermore, interesting differences between canopy heights were observed with varying application method (P = 0.012) and cardinal side of the tree (P = 0.017). For instance, when comparing

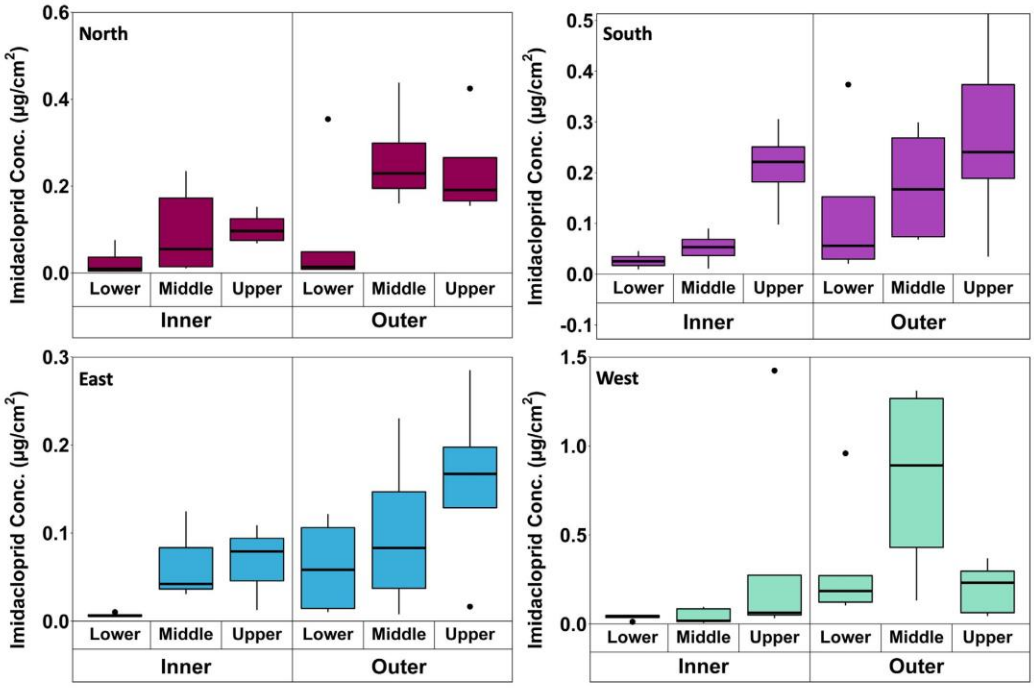

Figure 3. Concentration of Imidacloprid (μg cm^{-2}) detected on ground-sprayed Whatman filter sample discs from various locations within a citrus tree. Data comprised of five younger-aged tree replicates (top of leaf samples only) during the October 2018 field experiment. Each cardinal side of the tree is colored separately: North (red); South (purple); East (blue); and West (green). The North and South sides of the tree touch its neighboring trees, whereas the East and West sides have ~10 ft between the rows of trees. Trees were sprayed with the side-sprayer.

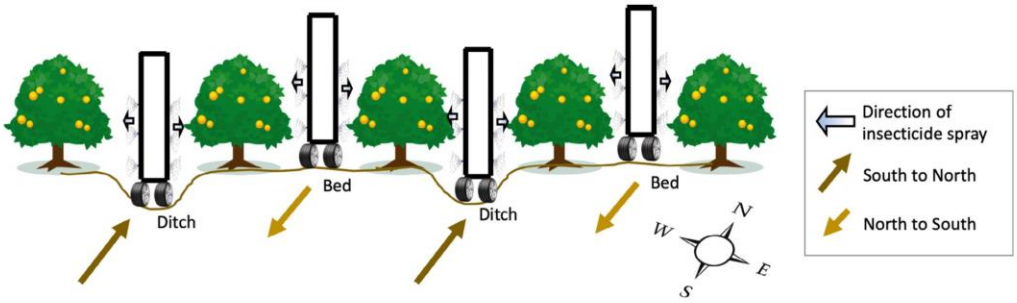

Figure 4. Schematic showing raised beds and irrigation draining ditches that tractor sprayers drive down while applying insecticides. Tractors drive North and South while applying to the East and West sides of the tree.

the ground sprayer application methods, the speed-sprayer had higher concentrations in the lower canopy height (diff = 0.03 μg cm^{-2}), but the middle and upper heights had lower concentrations (diff = 0.11and 0.09 μg cm^{-2}, respectively) than the side-sprayer (Fig. S8-A). There was no statistical difference in the insecticide concentrations between the lower heights and middle heights, but a statistical difference was reported between the upper canopy heights for varying spray method, with the side-sprayer upper regions receiving three times more insecticide than the speed-sprayer upper regions. For the side-sprayer, differences were reported between upper, middle, and lower canopy heights. For the speed-sprayer, although only a statistical difference was determined between the lower and upper canopy heights (diff = 0.64, $P = 0.040$), similar trends of the side-sprayer were observed, with the middle greater than the lower regions. On average, insecticide concentrations increased with canopy height (Fig. S8). After aerial application, canopy height results showed concentrations at the lower height (0.77 μg cm^{-2}) statistically lower than the middle (1.16 μg cm^{-2}, diff = 0.41, $P = 0.005$) and upper (1.40 μg cm^{-2}, diff = 0.99, $P < 0.001$) heights. In addition, ground-sprayed bottom side of leaf samples were similar at lower-middle canopy heights ($diff_{conc}$ = 0 μg cm^{-2}, diff = 0.36, $P = 0.585$) and statistically different for lower-upper ($diff_{conc}$ = 0.02 μg cm^{-2}, diff = 1.45, $P < 0.001$) and upper-middle comparisons ($diff_{conc}$ = 0.02 μg cm^{-2}, diff = 1.09, $P < 0.001$). Relatedly, the top side of leaf samples had statistically similar concentrations at upper-middle canopy heights ($diff_{conc}$ = 0.04 μg cm^{-2}, $P = 0.999$) with statistical differences for the lower-middle ($diff_{conc}$ = 0.1 μg cm^{-2}, $P = 0.021$) and lower-upper comparisons ($diff_{conc}$ = 0.06 μg cm^{-2}, $P = 0.006$). In another investigation into spatial distribution of imidacloprid to citrus trees via systemic drenching application,[29] little to no differences in various canopy depths were reported. This is important for HLB management to identify common ground-spraying techniques that cause unequal insecticide distribution and supports the explanation of how ground-sprayer designs of nozzle angles, placement, and application pressure can lead to uneven distribution throughout the entire citrus tree.

3.2.3 *Cardinal side of citrus trees*

In order to better understand how application method impacts distribution throughout the entire citrus tree, comparisons between cardinal sides were investigated (Fig. 1). Additional statistical analyses of ground-sprayed samples from each cardinal side showed similar trends for canopy heights previously reported, with the exception of the North side middle-height which received slightly more insecticide than the upper region and the West side middle-height which received slightly less than the lower areas (Fig. 3). There was no evidence of statistical difference between cardinal sides at the middle and upper heights, but there were statistical differences at the lower canopy height between the West and North, East, and South sides with much higher insecticide concentrations in the west (W-N: diff = 1.40, $P < 0.001$; W-E: diff = 1.04, $P = 0.02$; W-S: diff = 1.21, $P = 0.004$). As a whole, the West side (0.14 μg cm^{-2}) was statistically different from the East (0.05 μg cm^{-2}) ($diff_{conc}$ = 0.09 μg cm^{-2}, $P = 0.003$) as well as the North (0.05 μg cm^{-2}, $diff_{conc}$ = 0.09 μg cm^{-2}, $P < 0.001$). All other cardinal sides (North, East, South) comparisons were statistically similar, including comparisons between the North and South. This suggests that the arrangement of citrus trees in the field, with trees planted in rows North to South, and the application motion of the sprayers directed down the rows (Fig. 4), encourages lower spray deposition to both the North and South sides of trees that touch their neighboring trees, and could cause greater hinderance due to foliage. The grove arrangement also instigates inconsistencies on the East and West tree sides. For the ground-spraying methods, these differences between the East and West sides of the trees could be due to varied distance to the sprayer, larger 10 ft spaces between the East and West sides of trees across rows, or whether the tractor drives down a lower ditch or raised bed between the rows of trees. The sprayer nozzles align lower or higher in relation to the tree canopy when sprayed from a ditch or bed, respectively (Fig. 4). The ground side-sprayer design allows for more nozzles to spray at a closer distance (0–12 in) on three sides of the tree (East, West and top). The ground speed-sprayer used on older, larger foliage trees, only sprays insecticides from a further distance (1–2 ft) to the East and West sides of the trees, thus increasing distance to the sprayer and foliage that potentially block spray droplets. However, the opposite was observed between the East and West sides during aerial application, with the East cardinal side receiving more insecticide on average than the West (Figs S14, S15). The North and South side concentrations (not significantly different from each other) fell between the range of East and West results. This could be due to application flying patterns (spraying in rows North to South, while starting East and working towards the West) or the wind direction during application (typically East to West wind). Increased distance to sprayer, nozzle alignments, and wind

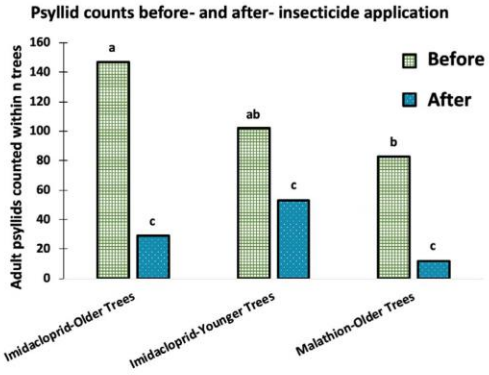

Figure 5. The total number of adult psyllids counted in all trees before- and after-insecticide application during field study #2. Imidacloprid was ground-sprayed with the speed- and side-sprayers to old and young trees, respectively (n = 90 trees included). Malathion was applied aerially to older trees. Only data from the first 15 rows were included (n = 45 trees). Bar plots with the same letter are not statistically different.

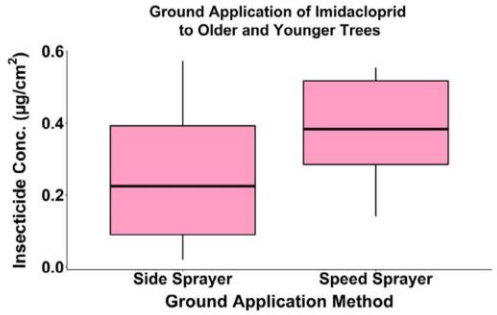

Figure 6. Concentration of Imidacloprid insecticide on samples from older and younger aged trees ground-sprayed with the speed- and side-sprayers (respectively) during field study #2.

direction can all impact drift and effective insecticide application.[37]

3.3 Psyllid inspections and application efficacy

In comparison to the traditional sticky trap method, our modified ACP counting protocol, adopted by our industry partner, allowed for better quantification of ACP before and after insecticide applications. For the purpose of our experiment, we discovered the sticky traps poorly represented the actual amount of ACP in the citrus trees, as we counted only three ACP on the traps compared to hundreds counted by our psyllid inspector (Table S4). For each block test, the ACP count decreased after initial insecticide application, but live ACP always were detected in the trees post- application of insecticide (Fig. 5). ACP population responses to the insecticide applications resulted in percent reductions of 85% for aerial application of malathion, 48% for ground application of imidacloprid with the side-sprayer (smaller trees), and 80% for imidacloprid ground sprayed with the speed-sprayer (larger trees) (Fig. 5). Although it was predicted the side-sprayer, with more nozzles, a smaller distance between the nozzles and leaves, and application to more sides of the tree, would have better insecticide effectiveness than the speed-sprayer, this was not the case. As demonstrated with spatial distribution results, the speed-sprayer which had higher concentrations (Figs 6, S16, S17) and better coverage to undersides of leaves, was more effective at reducing the ACP population (Fig. 5). Although it is possible that new ACP migrated into the blocks within 24 h after application, we suspect that the ACP observed post-application in all block tests either had not come into contact with the insecticide due to poor coverage or had not yet experienced the full effect of the insecticide and thus still alive.[30, 32, 38, 39] The high-management commercial citrus groves that implement large-scale insecticide spray applications resembling those investigated in this field study could witness a rapid regeneration of ACP from the ~50% population remaining post-application.[7] It has been found that ACP populations at higher levels or with higher resistance in the field are more likely to repopulate.[9] In addition, infected adult ACP have increased pathogen transmission when they contracted CLas pathogen as nymphs rather than as adults, thus improved control and reduction of ACP populations is critical. Our results also agree with imidacloprid control of adult ACP populations (reductions of 50–90%).[9] These results also agree with recent findings for imidacloprid (44%) applied to Kinnow mandarin plants via a knapsack sprayer.[30] However, several studies recommend repeated insecticide applications within a week in order to reach effective percent reductions (73% imidacloprid).[30, 40, 41] Although these findings reaffirm the percent reductions obtained during our field studies and align with previous studies showing initial ACP response to the a.i., they do not all fall within the effective percent reductions limit (73%) or offer realistic pest management improvements for a large commercial grove located in regions with specific US Environment Protection Agency (EPA) regulations.[42, 43] High-management commercial citrus groves cannot use fitted knapsack sprayers, which may offer a more targeted application to individual trees in smaller farms or research facilities.[30] In addition, recommended rotations of insecticide types to prevent ACP insecticide resistance development and meet EPA regulations inhibit high-management groves from repeated applications of the same insecticide within a week of the previous application.[44–46] Therefore, suggestions to increase application frequency or concentration do not offer realistic options for some of the large citrus producers. In addition, laboratory studies show a 94–100% mortality rate of ACP with direct spray of imidacloprid, even though the same percent reductions are not generated in the field.[30, 32, 47] Thus, exploring ways to enhance current application sprayer methods with increased agitation to canopy foliage or additional nozzles to spray upward from lower angles and increase deposition onto undersides of leaves, could provide improved distribution and efficacy of insecticide applications to citrus crops. Additionally, limitations in this study include variability of field conditions, seasonal impacts, and short-term psyllid population responses. More research is needed to understand psyllid response over time as a result of seasonal impacts, field conditions, insecticide mode of action and degradation.

4 CONCLUSION

The results presented in this paper clearly show unequal spatial distribution of insecticides applied to citrus trees with varying application methods. On average, outer canopy depths and middle–upper canopy heights received more insecticides than

inner and lower canopy locations, whereas the top of leaves received significantly more insecticide than the bottom. This lack of insecticide coverage to inner canopy regions and undersides of leaves could greatly impact the insecticide's effectiveness at killing ACP, especially as ACP are found primarily on undersides of leaves or on interior leaves to stay cooler when not feeding. The statistical interactions observed between side of leaf, cardinal side, and application method demonstrate the need for optimization of current insecticide application methods in citrus in order to more effectively control the spread of pests. This insufficient spatial distribution is of even greater importance in citrus groves combatting the spread of HLB because since it only takes one ACP to permanently infect a tree with HLB, ACP population reductions of <100% leave trees vulnerable to infection. This greatly impacts the ability to control ACP populations, protect crops, and slow the spread of citrus greening disease.

ACKNOWLEDGEMENTS

We would like to thank Cutrale Citrus Juices USA, Inc. for funding this project, and the entire team at Cutrale Farms in Venus, FL for their support and assistance on this project. We acknoweldge Dr. Hannah Miller, Dr. Paul Ode and Dr. Chuck Henry for their help and support with field experiments, and Dr. Claudia DeBoot at the Central Instrument Facility at Colorado State University for her help with instrumental method development and analysis.

SUPPORTING INFORMATION

Supporting information may be found in the online version of this article.

REFERENCES

1 Wang N and Trivedi P, Citrus huanglongbing: a newly relevant disease presents unprecedented challenges. *Phytopathology* **103**:652–665 (2013).
2 Li S, Wu F, Road C, Duan Y and Singerman A, Citrus greening: management strategies and their economic impact. *HortScience* **55**:1–9 (2020).
3 Florida Citrus Statistics, Florida Department of Agriculture and Consumer Services, Tallahassee, FL, Nichole Fried, Comissioner and USDA, Florida Citrus Statistics 2017-2018, 117 (2019). [November 2019].
4 Singerman A and Rogers ME, The economic challenges of dealing with citrus greening: the case of Florida. *J Integr Pest Manage* **11**:1-7 (2020). https://doi.org/10.1093/jipm/pmz037
5 Court CD, Hodges AW, and Stevens TJ, Economic contributions of the Florida Citrus industry in 2015–16 (2017). Available: https://fred.ifas.ufl.edu/pdf/economic-impact-analysis/Economic_Impacts_of_the_Florida_Citrus_Industry_2015_16.pdf [1 March 2020].
6 Dala-Paula BM, Plotto A, Bai J, Manthey JA, Baldwin EA, Ferrarezi RS *et al.*, Effect of huanglongbing or greening disease on orange juice quality, a review. *Front Plant Sci* **9**:1–19 (2019).
7 Grafton-Cardwell EE, Stelinski LL and Stansly PA, Biology and management of Asian citrus psyllid, vector of the Huanglongbing pathogens. *Annu Rev Entomol* **58**:413–432 (2013).
8 Mead F and Fasulo TR, *Asian Citrus Psyllid, Diaphorina citri Kuwayama (Hemiptera: Psyllidae)*. Univ Florida IFAS Ext, Gainesville, FL (2011).
9 Boina DR and Bloomquist JR, Chemical control of the Asian citrus psyllid and of huanglongbing disease in citrus. *Pest Manage Sci* **71**: 808–823 (2015).
10 Halbert SE and Manjunath KL, Asian citrus psyllids (sternorrhyncha: psyllidae) and greening disease of citrus: a literature review and assessment of risk in Florida. *Florida Entomol* **87**:330–353 (2004).
11 Costa MG, Barbosa JC, Yamamoto PT and Leal RM, Spatial distribution of *Diaphorina citri* Kuwayama (Hemiptera: Psyllidae) in citrus orchards. *Sci Agric* **67**:546–554 (2010).
12 Martini X, Pelz-Stelinski KS and Stelinski LL, Absence of windbreaks and replanting citrus in solid sets increase density of Asian citrus psyllid populations. *Agric Ecosyst Environ* **212**:168–174 (2015).
13 Farnsworth D, Grogan KA, van Bruggen AHC and Moss CB, The potential economic cost and response to greening in Florida Citrus. *Choices* **29**:1–6 (2014).
14 Whitney JD, Salyani M, Churchill DB, Knapp JL, Whiteside JO and Littell RC, A field investigation to examine the effects of sprayer type, ground speed, and volume rate on spray deposition in Florida citrus. *J Agric Eng Res* **42**:275–283 (1989).
15 Pergher G and Gubiani R, The effect of spray application rate and airflow rate on foliar deposition in a hedgerow vineyard. *J Agric Eng Res* **61**:205–216 (1995).
16 Salyani M and Fox RD, Evaluation of spray quality by oil and water-sensitive papers. *Trans ASAE* **42**:37–43 (1999).
17 Brusselman E, Beck B, Pollet S, Temmerman F, Spanoghe P, Moens M *et al.*, Effect of spray volume on the deposition, viability and infectivity of entomopathogenic nematodes in a foliar spray on vegetables. *Pest Manage Sci* **68**:1413–1418 (2012).
18 Menger R, Bontha M, Beveridge R, Borch T and Henry C, Fluorescent-based method for assessment of pesticide coverage on leaves and trees: a citrus grove case study. *J Agric Food Chem* **68**:14009–14014 (2020). https://doi.org/10.1021/acs.jafc.0c01835.
19 Jensen PK and Olesen MH, Spray mass balance in pesticide application: a review. *Crop Prot* **61**:23–31 (2014).
20 Juste F, Sanchez S, Ibanëz R, Val L and Garcia C, Measurement of spray deposition and efficiency of pesticide application in citrus orchards. *J Agric Eng Res* **46**:187–196 (1990).
21 Strand TM, Rolando CA, Richardson B, Gous S, Bader MKF and Hammond D, An aerial spot-spraying technique: a pilot study to test a method for pest eradication in urban environments. *SpringerPlus* **3**: 750 (2014).
22 Atkinson R, Guicherit R, Hites RA, Palm W-U, Seiber JN and De VP, *Transformations of Pesticides in the Atmosphere: A State of the Art, in Fate of Pesticides in the Atmosphere: Implications for Environmental Risk Assessment, ed. by Van Dijk HFG, Van Pul WAY and De Voogt P.* Springer, Dordrecht, pp. 219–243 (1999).
23 MacIntyre-Allen JK, Tolman JH, Scott-Dupree CD and Harris CR, Confirmation by fluorescent tracer of coverage of onion leaves for control of onion thrips using selected nozzles, surfactants and spray volumes. *Crop Prot* **26**:1625–1633 (2007).
24 Foqué D, Pieters JG and Nuyttens D, Spray deposition and distribution in a bay laurel crop as affected by nozzle type, air assistance and spray direction when using vertical spray booms. *Crop Prot* **41**: 77–87 (2012).
25 Olivet JJ, Val L and Usera G, Distribution and effectiveness of pesticide application with a cold fogger on pepper plants cultured in a greenhouse. *Crop Prot* **30**:977–985 (2011).
26 Ferguson JC, Chechetto RG, Hewitt AJ, Chauhan BS, Adkins SW, Kruger GR *et al.*, Assessing the deposition and canopy penetration of nozzles with different spray qualities in an oat (*Avena sativa* L.) canopy. *Crop Prot* **81**:14–19 (2016).
27 Farooq M and Salyani M, Modeling of spray penetration and deposition on citrus tree canopies. *Trans ASAE* **47**:619–628 (2004).
28 Salyani M, Farooq M and Sweeb RD, Spray deposition and mass balance in citrus orchard applications. *Trans ASABE* **50**:1963–1969 (2007).
29 Castle SJ, Byrne FJ, Bi JL and Toscano NC, Spatial and temporal distribution of imidacloprid and thiamethoxam in citrus and impact on {Homalodisca} coagulata populations. *Pest Manag Sci* **61**:75–84 (2005).
30 Iqbal J, Nazeer Hussain H, Latif M, Barjees Baig M, Owayss AA, Raweh HS *et al.*, A field study investigating the insecticidal efficacy against *Diaphorina citri* Kuwayama on Kinnow mandarin, *Citrus reticulata* Blanco trees. *Saudi J Biol Sci* **27**:1237–1241 (2020).
31 Grafton-Cardwell EE and Doria S, Insecticides for citrus Leafminer control, 2019. *Arthropod Manage Tests* **45**:2020 (2020).
32 Khan AA, Afzal M, Raza AM, Khan AM, Iqbal J, Tahir HM *et al.*, Toxicity of botanicals and selective insecticides to Asian citrus psylla, *Diaphorina citri* K. (Homoptera: Psyllidae) in laboratory. *Jokull J* **63**:52–72 (2013).
33 Monzo C, Qureshi JA and Stansly PA, Insecticide sprays, natural enemy assemblages and predation on Asian citrus psyllid, *Diaphorina citri* (Hemiptera: Psyllidae). *Bull Entomol Res* **104**:576–585 (2014).
34 McKenzie CL, Brock G, Murphy BC and Llc C-AP, Insecticidal control of Asian citrus psyllid and citrus leafminer on Hamlin oranges, 2003. *Arthr Manage Tests* **29**:D8 (2003).

35 Grafton-Cardwell EE, Lee JE, Robillard SM and Gorden JM, Role of Imidacloprid in integrated Pest Management of California Citrus. *J Econ Entomol* **101**:451–460 (2008).
36 Cloyd RA, Bethke JA and Cowles RS, Systemic insecticides and their use in 40 ornamental plant systems. *Floric Ornam Biotechnol* **5**:1–9 (2011).
37 Fishel FM and Ferrell JA, Managing Pesticide Drift. *UF/IFAS Ext* **PI232**:16 (2010).
38 Kookana RS, Boxall ABA, Reeves PT, Ashauer R, Beulke S, Chaudhry Q *et al.*, Nanopesticides: guiding principles for regulatory evaluation of environmental risks. *J Agric Food Chem* **62**:4227–4240 (2014).
39 Sétamou M and Bartels DW, Living on the edges: spatial niche occupation of asian citrus psyllid, *Diaphorina citri* kuwayama (Hemiptera: Liviidae), in citrus groves. *PLoS One* **10**:e0131917 (2015).
40 Farmanullah HB and Gul R, Evaluation of six different groups of insecticides for the control of citrus psylla *Diaphorina citri* (Hemiptera: Psyllidae). *Songklanakarin J Sci Technol* **27**:17–23 (2005).
41 Arora PK and Sharma DR, Bio-efficacy of some neonicotinoids against citrus psylla, *Diaphorina citri* Kuwayama on kinnow mandarin. *J Insect Sci* **24**:399–401 (2011).
42 Keigwin R, Imidacloprid Amended Final Work Plan, 8 (2010). [1 May 2020].
43 Bayer, Admire pro ®, Bayer Crop Science (2013). https://s3-us-west-1.amazonaws.com/agrian-cg-fs1-production/pdfs/Admire_Pro_Systemic1e_Protectant_MSDS.pdf
44 Cao X, Yan C, Yang X, Zhou L, Zou W and Xiu G, Photolysis-induced neurotoxicity enhancement of Chlorpyrifos in aquatic system: a case investigation on *Caenorhabditis elegans*. *J Agric Food Chem* **68**:461–470 (2020).
45 Naeem A, Freed S, Jin FL, Akmal M and Mehmood M, Monitoring of insecticide resistance in *Diaphorina citri* Kuwayama (Hemiptera: Psyllidae) from citrus groves of Punjab, Pakistan. *Crop Prot* **86**:62–68 (2016).
46 EPA, Reregistration Eligibility Decision (RED) for Malathion. *EPA 738-R-06-030* (2009). Available: https://archive.epa.gov/pesticides/reregistration/web/pdf/malathion-red-revised.pdf [1 May 2020].
47 Qasim M and Hussian D, Efficacy of insecticides against citrus Psylla (*Diaphorina citri* Kuwayama) in field and laboratory conditions. *Cercet Agron Mold* **48**:91–97 (2015).

Appendix G: Co-author contributions to Enhanced Speciation of Pyrogenic Organic Matter Study

Reprinted from Roth, H. K.; Borch, T.; Young, R. B.; Bahureksa, W.; Blakney, G. T.; Nelson, A. R.; Wilkins, M. J.; McKenna, A. M. Enhanced Speciation of Pyrogenic Organic Matter from Wildfires Enabled by 21 T FT-ICR Mass Spectrometry. *Anal. Chem.* **2022**, *94* (6), 2973–2980.

My co-author contributions towards this work included conceptualization, visualization, investigation, and writing/reviewing/editing.

analytical chemistry

pubs.acs.org/ac Article

Enhanced Speciation of Pyrogenic Organic Matter from Wildfires Enabled by 21 T FT-ICR Mass Spectrometry

Holly K. Roth, Thomas Borch, Robert B. Young, William Bahureksa, Greg T. Blakney, Amelia R. Nelson, Michael J. Wilkins, and Amy M. McKenna*

Cite This: https://doi.org/10.1021/acs.analchem.1c05018 Read Online

ACCESS | Metrics & More | Article Recommendations | Supporting Information

ABSTRACT: Wildfires affect soils through the formation of pyrogenic organic matter (pyOM) (e.g., char and soot). While many studies examine the connection between pyOM persistence and carbon (C) composition, nitrogen (N) transformation in wildfire-impacted systems remains poorly understood. Thermal reactions in wildfires transform biomass into a highly complex, polyfunctional, and polydisperse organic mixture that challenges most mass analyzers. High-field Fourier transform ion cyclotron resonance mass spectrometry (FT-ICR MS) is the only mass analyzer that achieves resolving powers sufficient to separate species that differ in mass by the mass of an electron across a wide molecular weight range (m/z 150−1500). We report enhanced speciation of organic N by positive-ion electrospray ionization (ESI) that leverages ultrahigh resolving power ($m/\Delta m_{50\%}$ = 1 800 000 at m/z 400) and mass accuracy (<10−100 ppb) achieved by FT-ICR MS at 21 T. Isobaric overlaps, roughly the mass of an electron (M_{e^-} = 548 μDa), are resolved across a wide molecular weight range and are more prevalent in positive ESI than negative ESI. The custom-built 21 T FT-ICR MS instrument identifies previously unresolved mass differences in $C_cH_hN_nO_oS_s$ formulas and assigns more than 30 000 peaks in a pyOM sample. This is the first molecular catalogue of pyOM by positive-ion ESI 21 T FT-ICR MS and presents a method to provide new insight into terrestrial cycling of organic carbon and nitrogen in wildfire impacted ecosystems.

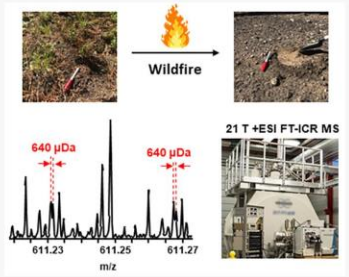

INTRODUCTION

Forests provide a myriad of ecosystem services, including the storage of ~30−40% of terrestrial carbon (C),[1] but are highly susceptible to ecosystem disturbances (e.g., wildfires) that dramatically change foliage and landscape, and produce 256 Tg of pyrogenic C per year.[2] Although fires occur naturally across many ecosystems,[3] wildfire size, frequency, and severity has substantially increased in recent decades in forested ecosystems.[4,5] Incomplete combustion of soil organic matter (SOM) during wildfires forms byproducts (e.g., char and soot)[6] that can impact the quantity and quality of soil C and nitrogen (N).[7,8] Pyrogenic organic matter (pyOM) exists as a continuum that spans from macroscopic (i.e., char and soot) to microscopic scales (i.e., condensed polycyclic aromatic molecules)[6] across a range of physical and chemical properties. The composition of pyOM is determined by the type and amount of biomass and burn conditions (e.g., intensity, moisture, fuel density).[9,10] Collectively, pyOM is characterized by increased hydrophobicity, lower C/N ratios, coarser soil textures, increased pH, and higher electrical conductivity compared to nonfire impacted soil.[9,11]

Nitrogen is an essential and often limiting nutrient,[12,13] and inherent heating and postfire ecosystem dynamics change N lability and bioavailability.[14,15] In unburned/low temperature-impacted soils, N is in the form of a slightly acidic compound (e.g., pyrrole, a ring structure composed of four C atoms and one N atom). As temperature increases, pyridinic structures (aromatic, basic functional groups) have been reported.[16] Although many studies focus on the connection between pyOM persistence and C composition,[16] there are limited reports on the connection between N composition and pyOM mineralization in fire-impacted soil.

The compositional complexity, polydispersity, and polyfunctionality of complex organic mixtures (SOM, pyOM, dissolved organic matter) challenge all analytical techniques. Fourier transform ion cyclotron resonance mass spectrometry (FT-ICR MS) routinely achieves resolving power sufficient to identify species that differ in mass by less than the mass of an electron, prevalent in natural organic matter (NOM).[17−20] The most widely used FT-ICR MS analytical approach for NOM combines solid-phase extraction (SPE) to enrich NOM from aqueous samples and negative-ion electrospray ionization (−ESI) to selectively ionize highly abundant carboxylic acids

Received: November 18, 2021
Accepted: January 12, 2022

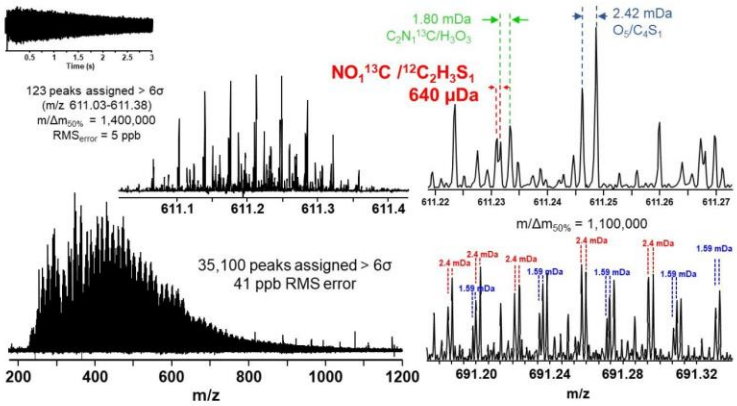

Figure 1. Positive-ion ESI 21 T FT-ICR mass spectrum of a pyOM extract. Bottom left: Broadband FT-ICR mass spectrum containing more than 35 000 assigned mass spectral peaks (m/z 200−1200) with a root-mean-square mass error of 41 ppb, each with a signal magnitude greater than 6σ of baseline noise, with $m/\Delta m_{50\%}$ = 1 800 000 at m/z 400. Top left: 350 mDa mass scale-expanded segment, showing resolution of more than 120 mass spectral peaks at m/z 611. Bottom right: mass scale-expanded segment across m/z 691.1−691.4, showing the increase in the number of isobaric overlaps at higher m/z. Top right: ∼60 mDa mass scale-expanded segment, showing resolution of three isobaric overlaps: 2.42 mDa, 1.80 mDa, and 640 μDa (mass of an electron is 548 μDa).

in NOM.[21] However, studies that compare analyte selectivity in different ionization modes for pyOM remain limited.[22,23]

The first step in all mass spectral techniques is ionization to yield pseudomolecular ions, and it is selected on the basis of the analyte of interest. Negative-ion electrospray yields deprotonated molecular ions based on the ionization efficiency of acidic functional groups.[22,24,25] In −ESI, stronger acids are efficiently ionized,[22] and the most abundant peaks correspond to low pK_a carboxylic acids (see Table S1 for the pK_a's of common soil functional groups), followed by phenolic groups that form as lignin degradation products.[26] Negative ESI is also sensitive to chemical contamination (i.e., linear alkylbenzene surfactants), which causes suppression of analyte ions and results in a mass spectrum dominated by chemical noise.[27] Ionization in −ESI is primarily dominated by low molecular weight carboxylic acids, and basic species and those with lower acidity can be detected by positive-ion ESI (+ESI). The pK_b distribution of basic functional groups in pyOM (e.g., pyridines and amides) results in less ion suppression due to more equal charge competition. Each ionization mode selectively ionizes a subset of species in a single SOM sample,[28] and no one soft ionization technique can equally access all of the compositional windows of SOM species. Ohno et al. benchmarked the field by comparing ±ESI for unburned SOM and reported that the combination of elemental compositions from both modes increased the number of assignments by 43% compared to −ESI alone.[21] In addition, while other studies compare ±ESI composition for soil- or water-derived SOM and refinery wastewater,[21,29−31] this study focuses on detailed characterization of pyOM, an understudied system in the field.

The unparalleled resolving power, high dynamic range, and increased sensitivity of the 21 T FT-ICR MS system identifies previously unresolved mass differences in $C_cH_hN_nO_oS_s$ formulas within pyOM at high mass ranges (>m/z 750).[32,33] The combination of high magnetic field, unique custom hardware, internal mass calibration, and absorption mode data processing available on the custom-built 21 T FT-ICR mass spectrometer achieves high resolving power ($m/\Delta m_{50\%}$ = 2 000 000 at m/z 200), subppm mass accuracy (20−80 ppb), and high dynamic ranges that allow the assignment of more than 30 000 species in a single mass spectrum.[32] Here, we leverage the 21 T FT-ICR MS to illuminate the unique compositional window detected by +ESI, compare the same speciation to −ESI, and expand the compositional window of wildfire-impacted SOM. This is the first study to probe the molecular complexity of pyOM in positive-ion mode with 21 T FT-ICR mass spectrometry. We identify species that remain unresolved and thus undetected by lower resolution mass spectrometers and highlight the minimal resolving power requirements necessary to accurately assign elemental compositions. For the first time, more than 35 000 species are assigned at 30 ppb RMS error by +ESI 21 T FT-ICR MS, a new record for pyOM characterization.

■ EXPERIMENTAL METHODS

Soil Sampling and Preparation. Soil was sampled in a lodgepole pine (*Pinus contorta*)-dominated region of the Medicine Bow National Forest, which burned in the 2018 Ryan fire. A high severity burned site was identified according to the amount of organic matter cover (<20%) and sampled from the organic horizon approximately one year after the fire's containment (for additional information, see Nelson et al.[34] (Sample # R89)). All solvents were HPLC grade and purchased from Sigma-Aldrich Chemical Co., St. Louis, MO, USA. Soil samples were weighed in acid-washed and combusted 250 mL Erlenmeyer flasks. A volume (in mL) of Milli-Q water twice the mass (in grams) was added to each flask and shaken (170 rpm for 10 h). Subsequently, the liquid was transferred into 50 mL centrifuge tubes and centrifuged for 10 min at 7500 rpm followed by filtering through a 0.2 μm poly(ether sulfone) filter. 50 mL of each water sample was acidified to pH 2 with trace-metal grade HCl, followed by SPE with styrene-divinylbenzene (SDVB) polymer modified with a proprietary nonpolar surface (Bond Elut Priority Pollutant,

https://doi.org/10.1021/acs.analchem.1c05018
Anal. Chem. XXXX, XXX, XXX−XXX

Table 1. Isobaric Species Detected in pyOM by +ESI 21 T FT-ICR MS and Theoretical Resolving Power Required as a Function of Mass-to-Charge Ratio (m/z)

			$m/\Delta m_{50\%}$			
	nominal mass (Da)	Δ exact mass (mDa)	m/z 200	m/z 400	m/z 600	m/z 800
$NO_2{}^{13}C/{}^{12}C_2SH_3$	59	0.640	310 000	625 000	930 000	1 200 000
$C_2N_1{}^{13}C/H_3O_3$	51	1.80	110 000	220 000	330 000	440 000
O_5/C_4S_1	80	2.40	83 000	160 000	250 000	330 000
CN_4/H_4O_4	68	1.35	150 000	290 000	440 000	590 000

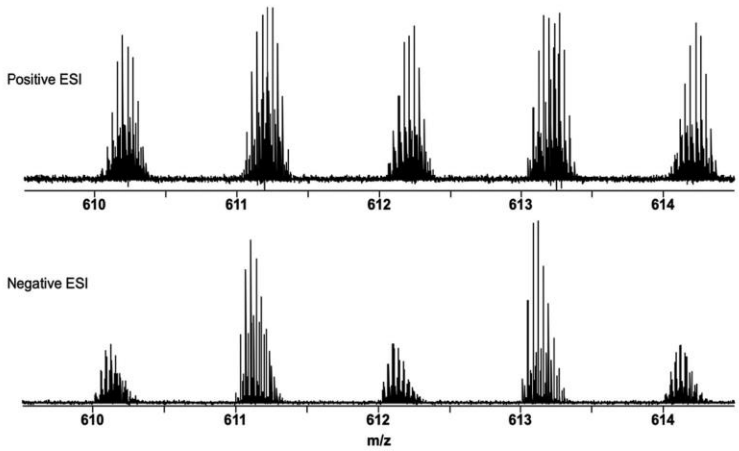

Figure 2. Mass-scale expanded zoom insets for +ESI (top) and −ESI (bottom) across m/z 609.5−614.5 of a pyOM extract.

Agilent Technologies).[29] Water-soluble organics were eluted with HPLC grade methanol and stored in precombusted glass vials at 4 °C in the dark prior to analysis.

21 T FT-ICR Mass Spectrometry. Ions were generated at atmospheric pressure via a microelectrospray source[35] and analyzed by 21 T FT-ICR MS.[32,33] Peaks with signal magnitude greater than 6 times the baseline root-mean-square (RMS) noise at m/z 500 were exported to peak lists, phase-corrected,[36] and internally calibrated on the basis of the "walking" calibration method.[37] Molecular formula assignments were performed with PetroOrg software.[38] Complete experimental details can be found in the Supporting Information. All FT-ICR mass spectra files and assigned elemental compositions are publicly available via the Open Science Framework at https://osf.io/758ux/ (DOI: 10.17605/OSF.IO/758UX).

■ RESULTS AND DISCUSSION

Positive ESI 21 T FT-ICR MS of pyOM Identifies New Isobaric Overlaps. Figure 1 shows the broadband +ESI FT-ICR mass spectrum for a pyOM extract withe more than 35 000 assigned mass spectral peaks (signal magnitude of six times greater than the baseline noise level) between m/z 200 and 1300, centered at m/z 480 (bottom left). The achieved resolving power ($m/\Delta m_{50\%}$, in which $\Delta m_{50\%}$ is the mass spectral peak full width at half-maximum peak height)[17] is 1 800 000 at m/z 400, which enables resolution and assignment of 35 100 peaks at a root-mean-square error of 41 ppb. The mass scale-expanded segment at m/z 611 highlights the immense spectral density with ∼123 peaks within a 0.3 mDa window assigned with a RMS error of 5 ppb (Figure 1 (top left)). The theoretical resolving power required to separate equally abundant species that differ in mass by ∼640 μDa at m/z 600 is 950 000. Here, the achieved resolving power ($m/\Delta m_{50\%}$ = 1 400 000 at m/z 611) enables the separation of species with the same nominal mass (59 Da) that differ in exact mass by 640 μDa ($NO_2{}^{13}C$ versus $^{12}C_2SH_3$), approximately the mass of an electron (548 μDa).[39−41] Table 1 shows isobaric overlaps and minimum achieved resolving power requirements for equally abundant species in pyOM samples by +ESI. Importantly, resolving power requirements will exceed the minimum for species of varying abundances.[17,42,43]

The polyfunctionality and polydispersity in molecular composition and structure of pyOM systems results in a highly complex mass spectrum for all ionization modes, including −ESI. Figure S1 shows the −ESI 21 T FT-ICR mass spectrum with more than 32 000 acidic species assigned between m/z 200 and 1000 with the mass distribution centered at m/z ∼ 375 (Figure S1 (bottom left)). Negative-ion ESI remains dominated by carboxylic acid moieties, yet still results in a highly complex mass spectrum. The mass scale-expanded segment at m/z 611 shows 66 peaks assigned with a RMS error of 7 ppb (Figure S1 (top left)) and highlights the mass spectral complexity in −ESI. However, comparison of the same nominal mass range shows that +ESI detects more than twice the number of peaks (123 peaks) compared to −ESI (66 peaks) and illustrates the dominance of carboxylic acid ionization in negative-ion mode. Improved speciation of pyOM, especially lower abundant species, requires more than

https://doi.org/10.1021/acs.analchem.1c05018
Anal. Chem. XXXX, XXX, XXX−XXX

one ionization mode to more accurately identify compositional trends across a wide molecular weight range.

Ionization Efficiency: +ESI vs −ESI. Efficient ionization of O_x species in −ESI can be rapidly visualized when compared to +ESI for the same sample across the same narrow mass range. Figure 2 shows mass-scale expanded zoom insets for +ESI (top) and −ESI (bottom) across m/z 609.5−614.5. Species in both spectra are composed of singly charged species based on the unit m/z separation between $^{12}C_n$ and $^{13}C_1{}^{12}C_{n-1}$ isotopic variants of the same elemental composition.[44] The most abundant peaks in positive and negative mode correspond to odd nominal mass species (e.g., m/z 611 and 613). Mass spectral peaks with the highest signal magnitude detected by −ESI correspond to O_x species at odd nominal mass and $^{13}C_1O_x$ at even nominal mass.[45] Conversely, +ESI across the same mass window shows approximately equal signal magnitude for even and odd nominal mass species and results in the detection of twice as many species. This is likely due to a combination of the narrow range of basicity in SOM compared to acidity and the relative concentrations of basic functional groups, which leads to more equal ionization in +ESI.

Tables S2 and S3 show m/z, mass error, resolving power, signal-to-noise ratio (S/N), double-bond equivalent (DBE), and neutral elemental composition for all mass spectral peaks detected above 6σ at m/z 611 and 612 by +ESI (Table S2) and −ESI (Table S3). Across the 348 mDa region, >120 peaks are assigned elemental compositions with a RMS mass error of 6 ppb by +ESI (Table S2a) compared to 66 peaks across a similar mass range (RMS error of 6 ppb, error plot in Figure S3) by −ESI for the same sample. The shift of one nominal mass unit higher across each spectrum to m/z 612 (Tables S2b and S3b) shows a similar trend with 96 peaks assigned at a RMS error of 5 ppb by +ESI (across 312 mDa) compared to 54 peaks at a 9 ppb RMS error by −ESI (285 mDa). Positive ESI contains more isobaric species with tighter mass differences (1.59 mDa), which are resolved by 21T FT-ICR MS (Table 1). Additionally, +ESI identifies more N species (56 at m/z 611 and 67 at m/z 612) compared to −ESI (25 at m/z 611 and 31 at m/z 612) and further highlights the increased compositional coverage for +ESI compared to −ESI for pyOM.

Positive-Ion ESI Identifies 12 475 Unique Species Not Observed in Negative-Ion ESI. The differences in spectra result in detection of unique species by each ionization mode, shown in Table 2. Positive ESI results in 24 189 formulas compared to 11 301 by −ESI, a more than 2-fold increase in identified species. Removal of the sodiated adducts from +ESI reduces the number of formulas assigned to 21 010 (only the CHO species resulted in sodiated adducts). For simplicity, further discussion of the elemental assignments will be limited to the nonsodiated fraction. Between −ESI and +ESI, there are 8535 formulas in common to both modes, 4371 CHO and 4164 CHNO, which comprise nearly all the −ESI assignments. Stated another way, ∼76% of the total −ESI formulas and nearly 86% and 91% of the CHO and CHNO are also detected by +ESI. However, common assignments represent only ∼41% of the assignments by +ESI (∼65% of CHO and ∼30% of CHNO).

Table 2. Formula Assignments and Elemental Class Distributions of the CHO and CHNO Fractions of the Negative-Ion and Positive-Ion ESI Spectra of a pyOM Extract

		±		
	−ESI	+ESI	+ESI (no Na)	common
formulas assigned	11 301	24 189	21 010	8535
unique formulas	2766	15 654	12 475	N/A
CHO	5112	9911	6732	4371
unique CHO	741	5540	2361	N/A
CHNO	4568	14 015	14 015	4164
unique CHNO	404	9851	9851	N/A

The unique formulas assigned for each mode were determined by eliminating neutral elemental compositions assigned in both spectra. However, it is important to note that it is possible that structural isomers may be present that have the same elemental composition and thus cannot be differentiated by mass alone. For unique CHO species, only 741 species were assigned in negative mode, whereas 2361 species were assigned in positive mode. However, for CHNO species, 9851 unique species were assigned by +ESI compared to only 404 unique formulas in −ESI, an increase of ∼87% and more than twice the number previously reported.[21] Out of 21 010 nonsodiated species assigned in positive-ion mode, 12 475 are unique; put generally, *+ESI displays more unique formulas than it has in common with negative-ion mode.* Thus, the use of +ESI identifies organic N species in pyOM that remain undetected by −ESI and results in an expansion of the analytical window into complex fire-impacted systems.

Chemical Properties Are Influenced by Ionization Limitations. Chemical property calculations from elemental compositions detected by FT-ICR MS analysis are common in NOM systems for the rapid identification of qualitative trends between samples. For example, the nominal oxidation state of carbon (NOSC) describes a molecule's lability because it is directly related to the Gibbs free energy ($\Delta G°$) of the reduction half-reaction between organic matter as the electron donor and the available terminal electron acceptor (e.g., oxygen) (eq S1).[46] However, calculated properties based on elemental compositions will change based on the number and type of species detected. Table S4 shows average H/C, O/C, N/C, NOSC, and double-bond equivalents (DBEs) (eq S2), plus the average C, H, O, and N number per formula, for both ±ESI spectra. For both polarities, the H/C ratio is ∼1 with ∼10 more C and 12 more H in +ESI than in −ESI. The average number of oxygens is 1.3 higher in −ESI, in agreement with Hertkorn et al.,[47] due to the preferential ionization of O-rich molecules. The differences in average C, H, and N are propagated by differences in DBE, which is four units higher for +ESI, demonstrating how the differences in species detected are propagated through calculated indices. Finally, the distribution of the NOSC assignments displays a distinct shift toward higher oxidation and lower C number in the −ESI sample (Figure S3 (top)). This shift is even more distinct in the CHNO class (Figure S3 (bottom)), which shows a shift toward lower, more reduced NOSC values in +ESI. Together, these properties clearly demonstrate that any calculation based on elemental composition must be evaluated with caution.

Positive ESI at 21 T FT-ICR MS Resolves and Identifies Dissolved Organic Nitrogen. Compared to −ESI, +ESI more efficiently ionizes N-containing species (Table 2). Figure S4 shows the heteroatom class distribution comparison for the same sample of pyOM by ±ESI (see Figure S5 for relative abundances). Nitrogen species detected by +ESI contain a

https://doi.org/10.1021/acs.analchem.1c05018
Anal. Chem. XXXX, XXX, XXX−XXX

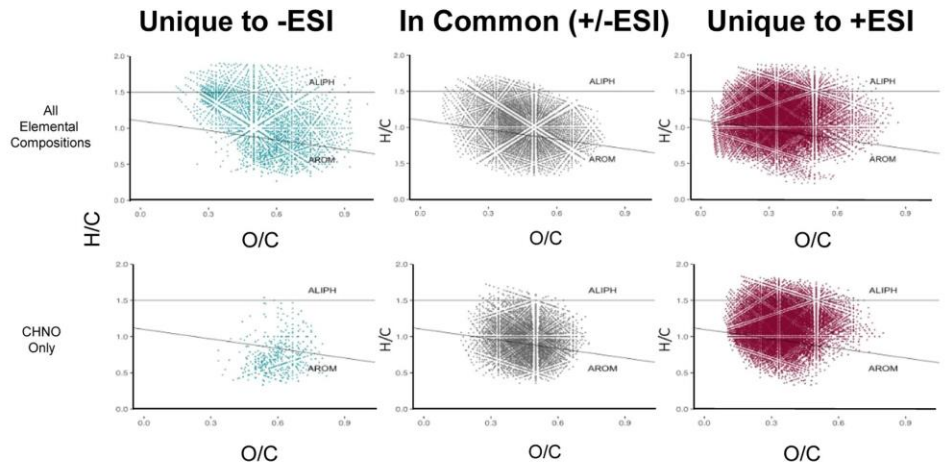

Figure 3. Top: van Krevelen diagrams of all the assigned formulas of the pyOM extract. Bottom: van Krevelen diagrams of only the CHNO class assignments. Unique formulas assigned for −ESI are on the left (blue); formulas in common are in the middle (gray), and formulas unique to +ESI are on the right (red).

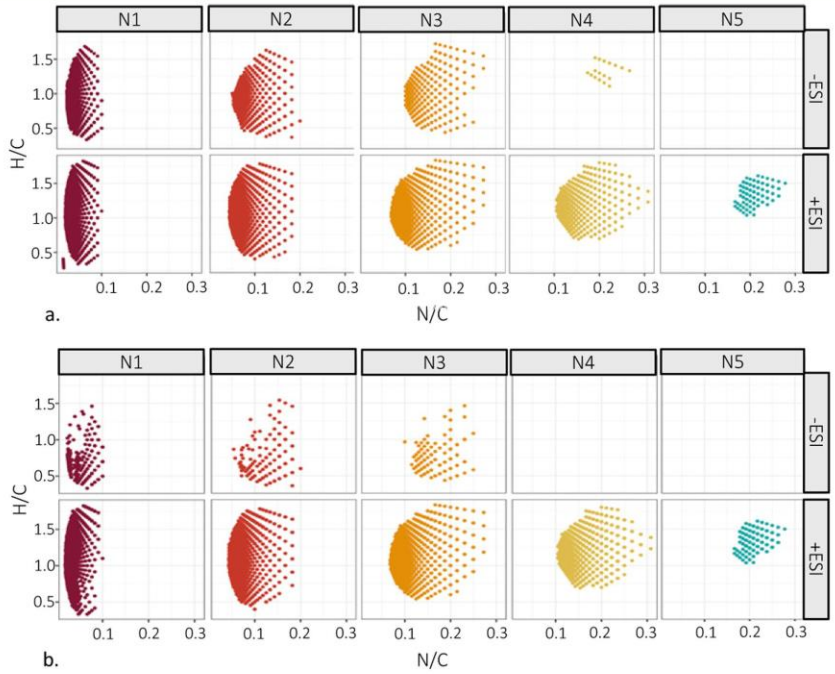

Figure 4. Atomic H/C vs N/C ratios of neutral species detected in a pyOM extract. (a) All CHNO assigned, −ESI assignments on the top row and +ESI assignments on the bottom row. (b) Only the unique CHNO assigned, again with −ESI on the top row and +ESI on the bottom row. Both panels are separated by N number, which increases from left to right.

higher number of N atoms per molecule (i.e., N_3, N_4, and N_5), likely composed of a range of basic functionalities (e.g., pyridines and amides). Species with high N substitution (e.g., N_5) are not detected in −ESI. Additionally, +ESI identifies a higher number of low oxygen-number classes (e.g., O_2 and O_3). In fact, six CHN_1 classes were assigned in +ESI, in addition to CHN_1O_2, CHN_2O_{2-3}, CHN_3O_{2-4}, CHN_4O_{4-6}, and all CHN_5O_x that were not detected by −ESI. This suggests

https://doi.org/10.1021/acs.analchem.1c05018
Anal. Chem. XXXX, XXX, XXX−XXX

that speciation and molecular detection of dissolved organic N in SOM systems could be significantly improved by 21 T FT-ICR MS in positive-ion mode.

Van Krevelen Diagrams Highlight the Increased Compositional Coverage of +ESI at 21 T. van Krevelen diagrams plot the H/C ratio versus the O/C ratio of neutral species, and different regions of the H/C and O/C space correspond to the molar ratios of major biogeochemical precursors (e.g., lignin-like, peptide-like, and lipid-like).[48] Because FT-ICR MS results in tens of thousands of elemental compositions in a single mass spectrum, van Krevelen diagrams are widely applied to rapidly visualize compositional changes between samples.[49] Figure 3 (top) shows van Krevelen diagrams derived from both ionization modes for all assigned species. Elemental compositions unique to −ESI are shown in blue (left); those identified in both spectra are in gray (middle), and species unique to +ESI are shown in red (right). Unique species in −ESI primarily have an O/C between 0.3 and 0.9, whereas species unique to +ESI have an O/C spanning 0.1 to 0.9. As shown in Table 2, 2766 formulas are unique to −ESI and 12 475 are unique to +ESI. These species span similar compositional ranges but are lower in total number of species in −ESI.

Unique Compositional Space of Nitrogen Species by +ESI 21 T FT-ICR MS. Figure 3 (bottom) shows van Krevelen diagrams for unique N-containing species by ±ESI. Importantly, across a wide range of H/C and O/C, positive-ion mode species occupy a much more diverse compositional range compared to −ESI with only 404 peaks in −ESI compared to 9851 peaks in +ESI (more than 24× the formula assignments in −ESI) (Table 2). These figures demonstrate that, across a wide range of compositional and structural classes, +ESI identifies a wide range of N species. Importantly, species that correspond to H/C ratios >1.0 and O/C ratios >0.3 are uniquely detected by +ESI and remain undetected by −ESI. This region of van Krevelen space (H/C > 1.0 and O/C > 0.35) has previously been reported as an indicator for the presence of potential toxicants due to the inhibition of aquatic photosynthetic organisms.[50] Therefore, the characterization of pyOM by +ESI identifies potentially toxic species not detected by −ESI. Differences in the O/C ratio are illustrated in Figure S6, which shows that −ESI identifies more species with a high oxygen content, while +ESI can more efficiently ionize those with a lower oxygen content.

Modified van Krevelen Diagrams: H/C versus N/C. A useful complement to the traditional van Krevelen diagram is the H/C vs N/C plot, shown for the total assigned CHNO fraction (Figure 4a) and the unique CHNO assignments (Figure 4b). Each panel is further divided by ionization mode (−ESI on top) and N number (1−5 from left to right). The compositional space for the total assigned species spans similar compositional ranges for N_1 (N/C > 0.1) and N_2 (N/C > 0.2) species but becomes more evident for N_3−N_5 with only 25 N_4 species identified by negative-ion mode and no N_5 species detected (Figure 4a). For the unique formula assignments, the difference in N/C spans across all N classes. For N_{1-3}, the unique formulas in negative-ion mode are clustered toward lower H/C ratios (H/C < 1.0), while N_4 and N_5 do not display any unique formulas (Figure 4b), further highlighting the increased speciation of CHNO by positive-ion mode. Thus, for research that is focused on changes in N content, +ESI should be utilized as the preferred method. Importantly, previous studies utilizing both negative and positive ESI were not able to provide the level of resolution for the nitrogenated molecules that we report here.[21,23,47] Therefore, this key element for microbial processing and ecosystem productivity is relatively understudied within the field of FT-ICR MS.

CONCLUSIONS

21 T FT-ICR MS in +ESI displayed clear shifts in pyOM composition compared to −ESI, highlighting differences in the ionization mechanism that proliferate into the resulting spectrum. The addition of +ESI resulted in an 87% increase (12 475 additional formulas) in the nonsodiated species compared to the traditional −ESI-only analysis. This included 9851 unique CHNO formulas, which spanned a wider compositional range, and demonstrated that a large fraction of organic N is overlooked with analysis only by −ESI. Additionally, it was shown that the biases associated with calculating chemical parameters by any ionization mechanism (e.g., NOSC) must be fully understood for proper use in C and N cycling models. Finally, while no one ionization mode can address the complexity of SOM, the combination of ESI in positive- and negative-ion modes substantially expands the analytical window for fire-impacted systems.

ASSOCIATED CONTENT

Supporting Information

The Supporting Information is available free of charge at https://pubs.acs.org/doi/10.1021/acs.analchem.1c05018.

Data tables (ZIP)

Additional experimental details, peak lists, FT-ICR MS spectra and error plots, calculated chemical parameters, and FT-ICR MS images (PDF)

AUTHOR INFORMATION

Corresponding Author

Amy M. McKenna − *National High Magnetic Field Laboratory, Ion Cyclotron Resonance Facility, Florida State University, Tallahassee, Florida 32310-4005, United States; Department of Soil and Crop Sciences, Colorado State University, Fort Collins, Colorado 80523-1170, United States;* orcid.org/0000-0001-7213-521X; Phone: +1 850 644 4809; Email: mckenna@magnet.fsu.edu; Fax: +1 850 644 1366

Authors

Holly K. Roth − *Department of Chemistry, Colorado State University, Fort Collins, Colorado 80523, United States;* orcid.org/0000-0003-2733-517X

Thomas Borch − *Department of Chemistry, Colorado State University, Fort Collins, Colorado 80523, United States; Department of Soil and Crop Sciences, Colorado State University, Fort Collins, Colorado 80523-1170, United States;* orcid.org/0000-0002-4251-1613

Robert B. Young − *Chemical Analysis & Instrumentation Laboratory, New Mexico State University, Las Cruces, New Mexico 88003, United States;* orcid.org/0000-0001-7485-0604

William Bahureksa − *Department of Chemistry, Colorado State University, Fort Collins, Colorado 80523, United States*

Greg T. Blakney − *National High Magnetic Field Laboratory, Ion Cyclotron Resonance Facility, Florida State University, Tallahassee, Florida 32310-4005, United States;* orcid.org/0000-0002-4205-9866

https://doi.org/10.1021/acs.analchem.1c05018
Anal. Chem. XXXX, XXX, XXX−XXX

Amelia R. Nelson − *Department of Soil and Crop Sciences, Colorado State University, Fort Collins, Colorado 80523-1170, United States*

Michael J. Wilkins − *Department of Soil and Crop Sciences, Colorado State University, Fort Collins, Colorado 80523-1170, United States*

Complete contact information is available at: https://pubs.acs.org/10.1021/acs.analchem.1c05018

Notes

The authors declare no competing financial interest.

■ ACKNOWLEDGMENTS

The authors thank Christopher L. Hendrickson, Chad R. Weisbrod, and John P. Quinn for the design and maintenance of the 21 T instrument. This work was supported by NSF Division of Chemistry and Division of Materials Research through DMR-1644779 and the State of Florida. The authors also acknowledge support to T.B. from the National Science Foundation under Grant Number 1512670 and USDA National Institute of Food Agriculture through AFRI grant no. 2021-67019034608. This research was funded by the National Science Foundation (2114868) and AFRI grant no. 2021-67019-33726 from the USDA National Institute of Food and Agriculture.

■ REFERENCES

(1) Bladon, K. D.; Emelko, M. B.; Silins, U.; Stone, M. *Environ. Sci. Technol.* **2014**, *48* (16), 8936−8943.
(2) Jones, M. W.; Santín, C.; van der Werf, G. R.; Doerr, S. H. *Nat. Geosci.* **2019**, *12* (9), 742−747.
(3) Giglio, L.; Randerson, J. T.; van der Werf, G. R. *J. Geophys. Res. Biogeosci.* **2013**, *118* (1), 317−328.
(4) Abatzoglou, J. T.; Williams, A. P. *Proc. Natl. Acad. Sci. U.S.A.* **2016**, *113* (42), 11770−11775.
(5) Dennison, P. E.; Brewer, S. C.; Arnold, J. D.; Moritz, M. A. *Geophys. Res. Lett.* **2014**, *41* (8), 2928−2933.
(6) Bird, M. I.; Wynn, J. G.; Saiz, G.; Wurster, C. M.; McBeath, A. *Annu. Rev. Earth and Planet. Sci.* **2015**, *43*, 273−298.
(7) González-Pérez, J. A.; González-Vila, F. J.; Almendros, G.; Knicker, H. *Environ. Int.* **2004**, *30* (6), 855−870.
(8) Knicker, H. *Biogeochemistry* **2007**, *85* (1), 91−118.
(9) Viedma, O.; Quesada, J.; Torres, I.; de Santis, A.; Moreno, J. M. *Ecosystems* **2015**, *18* (2), 237−250.
(10) Pierson, D. N.; Robichaud, P. R.; Rhoades, C. C.; Brown, R. E. *Int. J. Wildland Fire* **2019**, *28* (10), 814−821.
(11) Santín, C.; Doerr, S. H.; Kane, E. S.; Masiello, C. A.; Ohlson, M.; de la Rosa, J. M.; Preston, C. M.; Dittmar, T. *Glob. Change Biol.* **2016**, *22* (1), 76−91.
(12) Geisseler, D.; Horwath, W. R.; Joergensen, R. G.; Ludwig, B. *Soil Biol. Biochem.* **2010**, *42*, 2058−2067.
(13) Acquisti, C.; Elser, J. J.; Kumar, S. *Mol. Biol. Evol.* **2009**, *26* (5), 953−956.
(14) Adkins, J.; Sanderman, J.; Miesel, J. *Geoderma* **2019**, *333*, 10−22.
(15) Miesel, J. R.; Hockaday, W. C.; Kolka, R. K.; Townsend, P. A. *J.Geophys. Res. G: Biogeosci.* **2015**, *120* (6), 1124−1141.
(16) Torres-Rojas, D.; Hestrin, R.; Solomon, D.; Gillespie, A. W.; Dynes, J. J.; Regier, T. Z.; Lehmann, J. *Geochim. Cosmochim. Acta* **2020**, *276*, 170−185.
(17) Marshall, A. G.; Hendrickson, C. L.; Jackson, G. S. *Mass Spectrom. Rev.* **1998**, *17*, 1−35.
(18) Stubbins, A.; Spencer, R. G. M.; Chen, H.; Hatcher, P. G.; Mopper, K.; Hernes, P. J.; Mwamba, V. L.; Mangangu, A. M.; Wabakanghanzi, J. N.; Six, J. *Limnol. Oceanogr.* **2010**, *55* (4), 1467−1477.
(19) Kujawinski, E. B.; del Vecchio, R.; Blough, N. v.; Klein, G. C.; Marshall, A. G. *Mar. Chem.* **2004**, *92*, 23−37.
(20) Dittmar, T.; Koch, B. P. *Mar. Chem.* **2006**, *102* (3−4), 208−217.
(21) Ohno, T.; Sleighter, R. L.; Hatcher, P. G. *Anal. Bioanal. Chem.* **2016**, *408* (10), 2497−2504.
(22) Kruve, A.; Kaupmees, K.; Liigand, J.; Leito, I. *Anal. Chem.* **2014**, *86* (10), 4822−4830.
(23) Hockaday, W. C.; Purcell, J. M.; Marshall, A. G.; Baldock, J. A.; Hatcher, P. G. *Limnol. Oceanogr.: Methods* **2009**, *7* (1), 81−95.
(24) Whitehouse, C. M.; Dreyer, R. N.; Yamashita, M.; Fenn, J. B. *Anal. Chem.* **1985**, *57* (3), 675−679.
(25) Fenn, J. B.; Mann, M.; Meng, C. K.; Wong, S. F.; Whitehouse, C. M. *Science* **1989**, *246* (4926), 64−71.
(26) Qi, Y.; Fu, P.; Volmer, D. A. *Mass Spectrom. Rev.* **2020**, DOI: 10.1002/mas.21634.
(27) Young, R. B.; Avneri-Katz, S.; McKenna, A. M.; Chen, H.; Bahureksa, W.; Polubesova, T.; Chefetz, B.; Borch, T. *Soil Syst.* **2018**, *2* (1), 14−19.
(28) Brown, T. L.; Rice, J. A. *Anal. Chem.* **2000**, *72* (2), 384−390.
(29) Dittmar, T.; Koch, B.; Hertkorn, N.; Kattner, G. *Limnol. Oceanogr.: Methods* **2008**, *6*, 230−235.
(30) He, C.; Fang, Z.; Li, Y.; Jiang, C.; Zhao, S.; Xu, C.; Zhang, Y.; Shi, Q. *Environ. Sci. Process. Impacts* **2021**, *23*, 1466.
(31) Li, Y.; Xu, C.; Chung, K. H.; Shi, Q. *Energy Fuels* **2015**, *29* (5), 2923−2930.
(32) Hendrickson, C. L.; Quinn, J. P.; Kaiser, N. K.; Smith, D. F.; Blakney, G. T.; Chen, T.; Marshall, A. G.; Weisbrod, C. R.; Beu, S. C. *J. Am. Soc. Mass Spectrom.* **2015**, *26* (9), 1626−1632.
(33) Smith, D. F.; Podgorski, D. C.; Rodgers, R. P.; Blakney, G. T.; Hendrickson, C. L. *Anal. Chem.* **2018**, *90* (3), 2041−2047.
(34) Nelson, A. R.; Narrowe, A. B.; Rhoades, C. C.; Fegel, T. S.; Roth, H. K.; Chu, R. K.; Amundson, K. K.; Geonczy, S. E.; Young, R. B.; Steindorff, A. S.; Mondo, S. J.; Grigoriev, I. V.; Salamov, A.; Borch, T.; Wilkins, M. J. Playing with FiRE: A genome resolved view of the soil microbiome responses to high severity forest wildfire. *BioRxiv*, **2021**; DOI: 10.1101/2021.08.17.456416.
(35) Emmett, M. R.; White, F. M.; Hendrickson, C. L.; Shi, D. H.; Marshall, A. G. *J. Am. Soc. Mass Spectrom.* **1998**, *9* (4), 333−340.
(36) Xian, F.; Hendrickson, C. L.; Blakney, G. T.; Beu, S. C.; Marshall, A. G. *Anal. Chem.* **2010**, *82* (21), 8807−8812.
(37) Savory, J. J.; Kaiser, N. K.; McKenna, A. M.; Xian, F.; Blakney, G. T.; Rodgers, R. P.; Hendrickson, C. L.; Marshall, A. G. *Anal. Chem.* **2011**, *83* (5), 1732−1736.
(38) Corilo, Y. E. *PetroOrg Software*; Florida State University, Omics LLC: Tallahassee, FL, 2014.
(39) Wapstra, A. H.; Audi, G.; Thibault, C. *Nucl. Phys. A* **2003**, *729* (1), 129−336.
(40) Audi, G.; Bersillon, O.; Blachot, J.; Wapstra, A. H. *Nucl. Phys. A* **2003**, *729* (1), 3−128.
(41) Mohr, P. J.; Taylor, B. N.; Newell, D. B. *RMP* **2008**, *80* (2), 633−730.
(42) Marshall, A. G.; Rodgers, R. P. *Proc. Natl. Acad. Sci. U.S.A.* **2008**, *105* (47), 18090−18095.
(43) Marshall, A. G.; Blakney, G. T.; Chen, T.; Kaiser, N. K.; McKenna, A. M.; Rodgers, R. P.; Ruddy, B. M.; Xian, F. *Mass Spectrometry* **2013**, *2* (Special_Issue), S0009.
(44) Senko, M. W.; Beu, S. C.; Mclafferty, F. W. *American Society for Mass Spectrometry* **1995**, *6*, 52−56.
(45) Kujawinski, E. B.; Freitas, M. A.; Zang, X.; Hatcher, P. G.; Green-Church, K. B.; Jones, R. B. *Org. Geochem.* **2002**, *33*, 171−180.
(46) LaRowe, D. E.; van Cappellen, P. *Geochim. Cosmochim. Acta* **2011**, *75* (8), 2030−2042.
(47) Hertkorn, N.; Frommberger, M.; Witt, M.; Koch, B. P.; Schmitt-Kopplin, P.; Perdue, E. M. *Anal. Chem.* **2008**, *80* (23), 8908−8919.
(48) Kim, S.; Kramer, R. W.; Hatcher, P. G. *Anal. Chem.* **2003**, *75* (20), 5336−5344.

(49) Rivas-Ubach, A.; Liu, Y.; Bianchi, T. S.; Tolić, N.; Jansson, C.; Paša-Tolić, L. *Anal. Chem.* **2018**, *90* (10), 6152−6160.
(50) Smith, C. R.; Sleighter, R. L.; Hatcher, P. G.; Lee, J. W. *Environ. Sci. Technol.* **2013**, *47* (23), 13294−13302.

https://doi.org/10.1021/acs.analchem.1c05018
Anal. Chem. XXXX, XXX, XXX−XXX